Probing With Low Frequency Electric Currents

A thesis
submitted for the degree of
Doctor of Philosophy in Electrical Engineering
from the
University of Canterbury,
Christchurch, New Zealand

A. D. SEAGAR, B.E.(Hons)

1983

ABSTRACT

Four aspects of probing with low frequency electric currents are considered.

Applications of probing with electric currents in geophysics and medicine are reviewed. The theory of conservative fields is reviewed, and is discussed in relation to low frequency electric currents and other physical phenomena to which it applies.

The resolution with which a conductivity distribution can be reconstructed from electrical measurements is examined. Relationships are derived which relate the accuracy of the measurements to both the spatial resolution and conductivity resolution of the distribution. These relationships are obtained for conductivity distributions within both circular and half plane regions. It is found that the spatial resolution and conductivity resolution at any point depend on both the location and the conductivity of that point. It is experimentally verified that the best theoretical value of spatial resolution, for measurements having a particular accuracy, can be closely approached in practice.

The relationship between two-dimensional circularly symmetric conductivity distributions and electrical probing measurements performed on them is studied. Two approaches are employed. One treats these distributions as smooth and the other treats them as piecewise constant. Two techniques are developed for reconstructing the conductivity distributions from the measurements. One technique is iterative whereas the other is direct. Examples are given in which these techniques are applied to a variety of simulated and experimental measurements. These examples show how well conductivity distributions, reconstructed by these techniques, can be expected to represent the actual conductivity distributions.

The relationship between electrical probing measurements and general two-dimensional conductivity distributions is examined. These distributions are represented both as being smooth and piecewise continuous. Equations are developed relating the measurements on the boundary of a region to the conductivity distribution therein. The conditions on such measurements, for them to fully characterise the electrical response of the region, are established. The circumstances are identified under which coupling between

different portions of the region can be neglected. These circumstances are experimentally verified. A direct technique is developed for interpreting measurements in terms of a particular type of conductivity distribution. This technique is applied successfully to both experimental and simulated measurements.

A model is developed to interpret changes in limb volume measured during venous occlusion plethysmography. The parameters of the model are chosen to represent, as closely as possible, physiological variables of the limb. Experiments are reported in which these changes in volume are inferred from measurements of the electrical resistance of limbs. It is shown that the model can accurately mimic such changes in volume. An experiment is described which demonstrates how changes in the model parameters can be used to monitor changes in the circulatory system within the limb. The model is used to show that significant changes in the limb circulation can occur during surgery. Such changes have particular relevance to the formation of peri-operative venous thrombosis.

ACKNOWLEDGEMENTS

I wish to express my sincere gratitude to my supervisor, Professor R. H. T. Bates, for all the support and encouragement he has provided throughout the course of this study. The benefit of his experience has contributed significantly to all stages of the work involved. I also wish to offer special thanks to Professor J. M. Gibbs and Dr. F. M. Davis of the Department of Anaesthesia of the Christchurch Clinical School of Medicine. Their guidance, insight and assistance was of great value to the medical aspects of this study.

Many thanks also to Dr. G. C. McKinnon, S. Fountain, L. S. Chan and M. J. Henderson for contributions to various aspects of the work reported in this thesis. I am also grateful to my colleagues at the Electrical Engineering Department who have provided companionship and shown interest in my research. In particular I wish to thank Don Mackay, Dr. Brent Robinson, Dr. Phil. Bones, Dr. Rick Millane, Richard Fright and Kathy Garden, with whom I have had helpful discussions.

Throughout this study I have been financially supported by a Post-graduate Scholarship from the University Grants Committee, and for this I am especially thankful. My gratitude extends also to the National Heart Foundation for their support of the medical aspects of this study.

PREFACE

Information about a physical system is often obtained by interacting some form of energy with the system and measuring the resulting effects. Different forms of energy may be chosen according to the particular system being observed and the particular information desired about that system. The measurements themselves do not usually present the information in a manner which is readily understood, so that some form of processing is needed to uncover the wanted information. This thesis is concerned with obtaining information by interacting low frequency electric currents with physical systems. Two types of system are considered.

The first type of system is one which can be represented as a two-dimensional region in which the electrical conductivity is a function of position. This type of system is of particular relevance for geophysical prospecting and medicine. For the former, the conductivity distribution throughout a region of the earth is related to the minerals, rocks, liquids and gases of which the region is composed. Similarly, in medical applications, the conductivity distribution throughout a region of the human body is related to the tissues and fluids of which the region is composed. In both geophysics and medicine the objective of making electrical measurements is to obtain the conductivity distribution, and then from that to infer the material composition of the region. In geophysics this information may be used to locate regions of particular interest, such as certain geological structures or types of rock. In medicine the information is potentially useful as an aid to diagnosis of certain medical conditions.

The second type of system is one which can be represented as a three-dimensional region whose electrical resistance varies with time. Particular attention is paid here to a limb of the human body. Changes in the volume of the limb, which occur when using a technique called venous occlusion plethysmography, are sensed by monitoring the longitudinal resistance of the limb. The changes in volume are of particular significance in the detection of a medical condition called venous thrombosis. They may also be used to monitor limb bloodflow. Reduction in bloodflow is one of the factors which induces the formation of venous thrombosis. Therefore, apart from just being able to detect venous thrombosis, these volume changes can also be used to indicate the likelihood of its occurrence.

Chapter 1 of this thesis contains a review of the different electrical probing techniques used in both geophysics and medicine. The literature indicates that in both of these areas there is at present an interest in imaging two-dimensional conductivity distributions from electrical measurements. Chapter 2 contains a review of the theory pertaining to conservative fields. It is this theory which describes flow of low frequency electrical currents through conductive regions. Conservative field theory applies to a wider range of situations than just electrical measurements on conductive regions, as is explained in detail in Chapter 2. The original work presented in this thesis is described in Chapters 3 to 6.

The accuracy to which a conductivity distribution can be imaged is the main factor determining the practical usefulness of an image of the distribution. This accuracy is always limited by experimental errors in the measurements. In Chapter 3 the manner in which such errors limit both the spatial resolution and conductivity resolution of an image are examined. These limits are determined for conductivity distributions existing within regions whose shapes are either circles or half planes. The limits applying to the former type of region are of particular relevance to medical probing, whereas those applying to the latter region are of particular relevance to geophysical probing. The imaging accuracy may also be limited by incompleteness of measurements or assumptions about the geometry of the conductive region. These limits are also investigated in Chapter 3.

Two methods for imaging two-dimensional circularly symmetric conductivity distributions are examined in Chapter 4 as a precursor to the study of general two-dimensional conductivity distributions. One of the methods is iterative and the other is direct. These methods are used to image distributions from both simulated and experimental measurements. Using such measurements, case studies are performed in order to evaluate the effects which different factors have on the images. The effects of premature termination of the iterative method and the effect of noise in the measurements are examined.

The relationship between a general two-dimensional conductivity distribution and measurements made on its surface is developed in Chapter 5. The conductive region is taken to be circular. This type of region is of direct relevance to medical probing. Conditions are identified for electrical measurements to fully characterise the electrical response of such

regions. It is important to ensure that these conditions are fulfilled when making probing measurements, otherwise it is not possible to uniquely determine the conductivity distribution being probed. A series of case studies are examined in order to draw useful conclusions about the relationship between the conductivity distribution and the measurements. In particular, the effects of neglecting coupling between different regions within the distribution are examined. A direct technique is developed for imaging a particular type of conductivity distribution. This technique is applied to measurements obtained both from experiments and simulations.

In Chapters 3, 4 and 5 results based on both simulations and experiments are presented. The simulations were performed using the theory derived in the earlier sections of those chapters. The experiments were performed using a system developed for that purpose. This system is described in Appendices 1 and 2.

Venous occlusion plethysmography is a technique which is a useful aid in the diagnosis of peripheral venous disease. This technique involves interrupting the venous bloodflow out of a limb without affecting the arterial bloodflow into the limb. The limb increases in volume as blood collects in it. After 30 to 60 seconds the interruption is removed and the volume of the limb returns to normal. In Chapter 6 a model is developed for interpreting these changes in limb volume. The model is designed so that it has parameters which are related as closely as possible to the physiology of the circulatory system within the limb. This approach allows the values of the model parameters, for which the model mimics a particular change in limb volume, to be readily interpreted in terms of limb circulation. The model is also designed to be sufficiently simple for the values of the model parameters to be uniquely determined from such changes in volume. The model is shown to be related to alternative methods of interpreting the changes in limb volume, and it is discussed in relation to these methods. The experimental measurements reported in this chapter were made using an impedance plethysmograph, which was designed and built as part of this study. The impedance plethysmograph is described in Appendix 2. The plethysmograph also forms part of the measurement system referred to above.

In Chapter 7 conclusions from the research reported in this thesis are presented. The significance of the reported results is discussed, and suggestions are made for further research which would be useful.

During the course of the work presented in this thesis the following papers and presentations were prepared.

R. H. T. Bates, G. C. McKinnon and A. D. Seagar. 1980.
"A Limitation on Systems for Imaging Electrical Conductivity". IEEE. Transactions on Biomedical Engineering, V27 #7 July pp418-420.

A. D. Seagar, J. M. Gibbs and R. H. T. Bates. 1980.
"Impedance Imaging and Plethysmography". Presented at the 20th Conference on Physical Sciences and Engineering in Medicine and Biology, Christchurch, New Zealand, August 1980. Abstract: Conference Proceedings p49.

K. L. Garden and A. D. Seagar. 1982.
"Low Frequency Electrical Current Measurements as an Aid to Medical Diagnosis". Presented at NZIE Annual Conference, Christchurch, New Zealand, February 1982. Abstract: Conference Papers p17.

R. H. T. Bates, J. H. T. Bates, P. J. Bones, R. P. Millane and A. D. Seagar. 1982.
"Computational Aspects of Physiological System Modelling". Presented at the Australian National Bio-Medical Engineering Conference, Melbourne, Australia, November 1982. Abstract: Book of Abstracts p4.

J. H. T. Bates, W. R. Fright, R. P. Millane, A. D. Seagar, A. E. McKinnon and R. H. T. Bates. 1982.
"Subtractive Image Restoration III: Some Practical Applications". Optik, V62 #4 pp333-346.

A. D. Seagar, J. M. Gibbs and F. M. Davis. 1982.
"Interpretation of Venous Occlusion Plethysmographic Measurements using a Simple Model". Submitted to Medical and Biological Engineering and Computing.

F. M. Davis, J. A. Floate, V. G. Laurenson, W. J. Gillespie and A. D. Seagar. 1982.
"Calf Blood Flow during Total Hip Replacement Surgery".

TABLE OF CONTENTS

		PAGE
ABSTRACT		(i)
ACKNOWLEDGEMENTS		(iii)
PREFACE		(v)
CHAPTER 1	PROBING WITH ELECTRIC CURRENTS	1
1.1	Introduction	1
	1.1.1 Probing	1
1.2	Geophysical Probing	2
	1.2.1 Electrical Properties of the Earth	2
	1.2.2 Measurements on the Earth	3
	1.2.3 Simplified Models	7
	1.2.4 Interpretation of Measurements	9
	1.2.5 Uniqueness and Resolution	11
1.3	Medical Probing	11
	1.3.1 Electrical Properties of Tissue	11
	1.3.2 Impedance Plethysmography	14
	1.3.3 Medical Uses of Plethysmography	16
1.4	Impedance Imaging	19
	1.4.1 Projection Images	19
	1.4.2 Back Projection	22
	1.4.3 Iterative Model Fitting	23
1.5	Discussion	23
CHAPTER 2	CONSERVATIVE FIELDS	27
2.1	Introduction	27
2.2	Potential, Flux and Sources	27
2.3	Electric and Magnetic Fields	30
	2.3.1 Static Electric Field in a Dielectric	30
	2.3.2 Static Magnetic Field	31
	2.3.3 Static Electric Field in a Conductor	31
	2.3.4 Quasi-static Electric and Magnetic Fields	32
	2.3.5 Current Flow in a Quasi-static Electric Field	34

PAG

2.4 Other Kinds of Fields 3
2.4.1 Fluid Flow 3
2.4.2 Diffusion and Heat Conduction 3
2.4.3 Gravitation 3
2.5 Tabulated Summary 3
2.6 Integral Equation Representation 3
2.6.1 Greens Function for Poisson's Equation 3
2.6.2 Equation for Continuously Varying Regions 4
2.6.3 Equation for Piecewise Homogeneous Regions 4
2.7 Laplaces Equation 4
2.7.1 Separation of Variables 4
2.7.2 Conformal Mapping 5

CHAPTER 3 LIMITATIONS ON IMPEDANCE IMAGING
3.1 Introduction
3.2 The Circularly Symmetric Conductivity Distribution
3.2.1 Visibility and Spatial Resolution
3.2.2 Sensitivity and Conductivity Resolution
3.3 Conformal Transformation to Other Conductivity Distributions
3.3.1 Ideal Electrode Positions
3.3.2 Maximum Visibility and Sensitivity
3.3.3 Visibility Attained in Practice
3.4 Further Limitations of the Flat Geometry
3.4.1 Incomplete Measurements
3.4.2 Approximation to a Curved Geometry
3.5 Discussion

CHAPTER 4 CIRCULARLY SYMMETRIC CONDUCTIVITY DISTRIBUTIONS
4.1 Piecewise Constant Distributions
4.1.1 Comparison Between Experimental and Simulated Measurements
4.1.2 Multiple Ring Models for Iterative Modelling
4.2 Smooth Conductivity Distributions
4.2.1 Comparison of Smooth and Piecewise Constant Distributions
4.2.2 Imaging Smooth Distributions

		PAGE
4.3	Case Studies	100
4.3.1	Model Sensitivity to Data Fit	100
4.3.2	Effect of Random Noise in Measurements	103
4.3.3	Alternative Choice of Models	105
4.3.4	Measurement Noise in Practice	108
4.3.5	Experimental Measurements Interpreted Using Three Models	110
4.4	Discussion	111
CHAPTER 5	GENERAL CONDUCTIVITY DISTRIBUTIONS	115
5.1	Smooth Distributions	116
5.1.1	Description of Approach	116
5.1.2	Manipulating Poisson's Equation	118
5.1.3	Matching the Voltage Boundary Conditions	121
5.1.4	Matching the Current Density Boundary Conditions	121
5.1.5	Relation Between Boundary Voltage and Current Density	123
5.1.6	Calculating the Transfer Impedances from Measurements	125
5.1.7	Receprocity in Relation to the Transfer Impedances	126
5.1.8	Simple Current Distributions for Making Measurements	127
5.2	Piecewise Constant Distributions	129
5.2.1	The Multiple Offset Anomaly Distribution	129
5.2.2	Relation Between Boundary Voltage and Current Density	131
5.2.3	Three Components Contributing to Boundary Voltage	134
5.2.4	The Single Offset Anomaly Distribution	135
5.2.5	Direct Inversion for a Single Offset Anomaly	136
5.3	Case Studies	138
5.3.1	Voltage Measurements and Transfer Impedances	139
5.3.2	Transfer Impedances and Visibilities	142
5.3.3	Coupling Effects Between Two Anomalies	144
5.3.4	Multiple Offset Anomalies and Coupling	148
5.4	Single Offset Anomaly Reconstructions	150
5.5	Discussion	154

		PA
CHAPTER 6	MODELLING LIMB VOLUME CHANGES MEASURED DURING VENOUS OCCLUSION PLETHYSMOGRAPHY	15
6.1	Venous Thrombosis and Pulmonary Embolism	15
6.2	The Model of the Limb Circulation	15
6.2.1	Using the Model to Represent Measurements	16
6.3	Experimental Studies	16
6.3.1	Comparison of Model of Limb Circulation with Human Limbs	16
6.3.2	Relating the Model Parameters to Physiological Quantities	16
6.3.3	Modelling Limb Bloodflow, Compliance and Resistance	16
6.4	Discussion	16
CHAPTER 7	CONCLUSIONS AND SUGGESTIONS FOR FUTURE RESEARCH	17
7.1	Limitations on Impedance Imaging	17
7.2	Circularly Symmetric Conductivity Distributions	17
7.3	General Conductivity Distributions	17
7.4	Conservative Field Imaging	17
7.5	Modelling Limb Volume Changes Measured During Venous Occlusion Plethysmography	17
APPENDIX 1	SYSTEM FOR ELECTRICALLY PROBING CONDUCTIVITY DISTRIBUTIONS	18
APPENDIX 2	INSTRUMENTATION	18
A2.1	Impedance Plethysmograph	18
A2.1.1	Specifications	18
A2.1.2	Circuitry	18
A2.2	Analogue Multiplexer	19
APPENDIX 3	TECHNIQUES EMPLOYED FOR MODEL FITTING	19
A3.1	Newton Methods	19
A3.2	The Moore Penrose Generalised Inverse	19
A3.3	Orthogonal Decomposition	19
A3.4	The Procedures Employed	19
APPENDIX 4	A POWER SERIES REPRESENTATION FOR THE QUOTIENT OF TWO POWER SERIES	20

		PAGE
APPENDIX 5	DETAIL OF SECTION 5.1.2	203
APPENDIX 6	A DIRECT METHOD FOR ESTIMATING A SINGLE EXPONENTIAL CURVE FROM MEASUREMENTS	209
REFERENCES		211

1. PROBING WITH ELECTRIC CURRENTS

1.1 INTRODUCTION

Probing and sensing techniques are used in many areas of scientific and technical importance to gain useful or interesting information. This thesis is concerned with using low frequency electric currents to determine useful information from the spatial or temporal variation of conductivity. (Low frequency means low enough for a conservative field approach to be applicable. See §2.3.4). Two areas in which electrical probing finds major application are geophysical prospecting and medical diagnosis.

Usually, the conductivity is only a convenient intermediary from which some other property is inferred. Where this is the case electrical probing may be only one of a variety of possible techniques. In geophysical prospecting the subsurface composition of the earth is sought, and an alternative method to probing with electric currents is to drill a hole and collect rock samples for analysis. One difference between the electrical method and such an alternative is that the former is non-invasive. This is not necessarily an advantage in geophysical prospecting, but it is very much an advantage in medical diagnosis, where patient welfare is of paramount importance. This chapter serves as an introduction to, and a review of, electrical probing techniques used in geophysical prospecting and in medical diagnosis.

1.1.1 Probing

The generalised probing (or scattering) problem (cf. Bates and McKinnon 1980) is conveniently described with reference to figure 1.1. An incident emanation ψ_i, which is generated by a source (transmitter) impinges upon and interacts with a region R of unknown physical properties λ, giving rise to a perturbed ("scattered" is often an appropriate term) emanation ψ_s. The total emanation $\psi = \psi_i + \psi_s$ is measured with a receiver (detector) and contains all of the observable information about λ. Forward probing involves finding ψ when ψ_i and λ are known. Inverse probing involves finding λ when ψ_i and ψ are known. When the source is within R the measurement of ψ is called sensing. This special situation is often referred to as a source problem, as opposed to the more general probing problem.

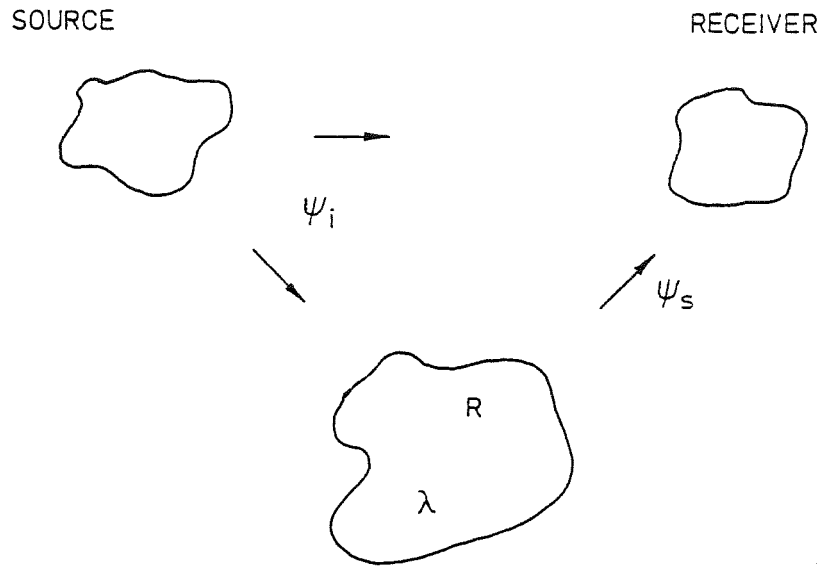

Figure 1.1: Generalised Probing (Scattering) Problem. Incident emanation ψ_i interacts with region R, which has physical characteristics λ, and gives rise to scattered wavefunction ψ_s.

Inverse probing is mathematically more difficult to solve than forward probing. This is because the mathematical descriptions of physical phenomena are usually based on forward probing, and in many situations it is not clear how to manipulate such descriptions to solve inverse problems.

1.2 GEOPHYSICAL PROBING

1.2.1 Electrical Properties of the Earth

Electromagnetic fields can be useful for probing in geophysics because different earth materials exhibit significant differences in conductivity (or resistivity ρ), permittivity and permeability. The various minerals found in the earth allow metallic conduction (e.g. native metals, $\rho = 10^{-7}$ to 10^{-4} Ωm), semiconductor conduction (e.g. sulphides, $\rho = 10^{-4}$ to 10^{4} Ωm) and solid electrolytic conduction (e.g. silicates, $\rho > 10^{4}$ Ωm) (cf. Keller 1971 §2.1; Keller and Frischknecht 1966 §§1.1-1.3). The relative permittivity and relative permeability of naturally occurring minerals lie in the ranges 1 to 10 and 1 to 5 respectively. However, for most rocks near the earth's surface, conduction is due to salts dissolved in groundwater permeating the pores in the rock, and because of this the resistivity is usually between

The electrical properties of the earth are seldom isotropic. Rock which is composed of a sequence of layers of isotropic constituents is effectively anisotropic because the current passes through a parallel combination of the constituents when flowing parallel to the layers, but passes through a series combination when flowing perpendicular to the layers. The ratio of perpendicular to parallel resistivity ranges from 1 to 25 (Keller 1971 §4.1). Even when rock is not composed of layers it may be anisotropic because of some preferred orientation of texture.

1.2.2 Measurements on the Earth

The electrical techniques used to determine the electrical properties of the earth may be classed according to (i) the types of incident and perturbed emanations used to perform the probing, (ii) the information contained in the measurements, and (iii) the particular source-receiver geometry used to obtain the measurements. There are many alternatives in each of these classifications, with any particular measurement technique comprising one alternative from each of (i), (ii) and (iii) above. Therefore there are many different measurement techniques.

Alternative Choices of Emanation

The types of emanation used to perform geophysical probing fall into 3 groups. There are conservative emanations (i.e. low frequency conduction currents), natural source non-conservative emanations (i.e. telluric electromagnetic fields), and man made non-conservative emanations (i.e. man made electromagnetic fields).

Direct current and induced polarisation (also called overvoltage) techniques employ low frequency electric currents passed through the earth using suitable electrodes. Frequencies below 100 Hz are used because this enables a conservative field approach to be adopted (see §2.3.4). Direct current techniques use either a direct current source which is periodically reversed in polarity, or a low frequency sinusoidal waveform (Keller and Frischknecht 1966 §16). Their purpose is to measure the spatial distribution of the electrical characteristics of the material beneath the earth's surface. Induced polarisation techniques make use of either the transient behaviour in the time domain (cf. Seigel 1959) or the steady state behaviour in the frequency domain (cf. Wait 1959, 1981a) in order to obtain the spatial distribution of a parameter called the "chargeability". The latter is a

and conduction current. Alternative parameters called the "metal factor" and the "frequency effect" are also used.

Magnetotelluric and telluric methods make use of the currents induced in the earth by the natural variations in the earth's magnetic field. At frequencies above 1 Hz the variations are primarily caused by lightning strokes, and below 1 Hz are thought to be caused by the interaction between radiation or particulate matter from the sun and the earth's atmosphere and magnetosphere (Keller and Frischknecht 1966 §28). In turn, the currents induced in the earth give rise to time varying electric and magnetic fields. Using the magnetotelluric method the variations in the magnetic field and electric field are measured at one site. In contrast, when using the telluric method the electric field alone is measured at a number of sites. The former method allows the conductivity at a given site to be determined (cf. Larsen 1981; Oldenburg 1979), while the latter allows the conductivity at various sites to be compared. When the conductivity at one site is known by some independent means it can be used as a reference, in which case the telluric method also permits the conductivity to be measured (Yungul 1966).

Electromagnetic methods are those in which artificially generated time varying electromagnetic fields are used to probe the earth. These methods are further subdivided according to whether the receiver is in the near field or far field of the source. Induction methods are those in which the fields are transmitted and received by coils, and the wavelength of the fields in air exceeds the source-receiver spacing. Frequencies between 100 Hz and 5 kHz are used (cf. Keller and Frischknecht 1966 §34). Radio wave methods use electric dipoles for source and receiver, with wavelengths in air being less than the source-receiver spacing (cf. Keller and Frischknecht 1966 Ch.7). Both conductivity and permittivity can be estimated by electromagnetic methods (the permeability is usually 1) since the frequencies used are high enough for displacement current flow in the earth to be significant in comparison with conductive current flow. This is in contrast to the telluric and magnetotelluric methods, where only the conduction current in the earth is significan

There are many different electromagnetic techniques which measure diffe ent characteristics of the electric and magnetic fields. The wave tilt metho uses the vertical and horizontal electric fields at one site (cf. Lytle et al 1976), whereas the ground wave attenuation method uses the amplitude of a trav elling electric field measured at different sites (cf. Maley 1971 §2.4). Propagation delay time and attenuation measurements between boreholes are used (Dines and Lytle 1979; Lytle and Dines 1980), and there are many variations of

Spatial Information Content

Measurements of the total emanation ψ, are made in order to determine the spatial distribution of the earth's electrical characteristics. Often the spatial distribution is assumed to vary only in one dimension. Measurement techniques which are used to derive information which depends solely on the electrical characteristics as a function of depth, are called sounding techniques. Similarly, profiling techniques are those used for estimating lateral variations of the electrical characteristics. Those measurement techniques used to derive information about the electrical characteristics varying in at least two dimensions are called imaging techniques.

Source-Receiver Geometry

The conductivity distribution and the geometrical relationship between the transducers (i.e. electrodes or antennas) used for injecting signals into the earth and for sensing their effects are both intimately related to the effects measured. The injecting transducers are called sources, and the sensing transducers are called receivers. Several source-receiver configurations have become standard, and they are referred to as arrays. Figure 1.2 shows the Wenner, Schlumberger, Eltran and dipole-dipole arrays, which are examples of arrays used for the direct current and induced polarisation techniques. The dipole-dipole array also applies to the electromagnetic methods which employ electric and/or magnetic dipoles.

Apparent Resistivity

The apparent resistivity ρ_a is a quantity often inferred from measurements made using the various electrical probing techniques (cf. Keller and Frischknecht 1966 §17). The values actually obtained for the apparent resistivity depend upon both the resistivity of the earth and the particular technique employed. It is defined as the resistivity of a uniform region which would give rise to the same measurements as those obtained over the actual region being probed. The relationship between the apparent resistivity and the measurements is defined differently for each measurement technique. For the direct current technique it is written as

$$\rho_a = KV/I, \tag{1.1}$$

where V and I are defined in Figure 1.2 and K is called the geometrical factor.

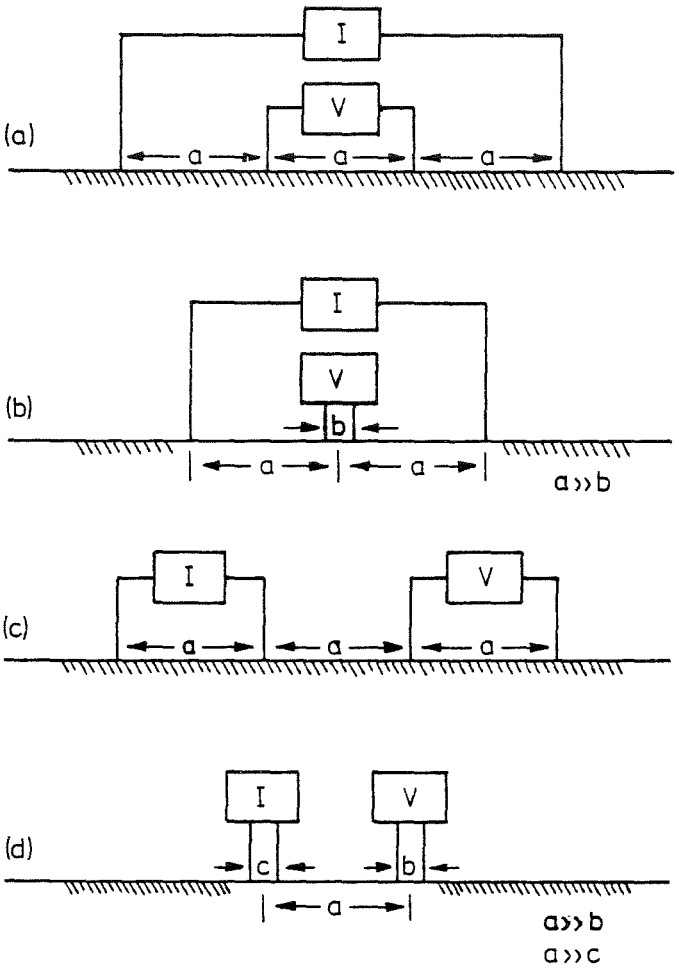

Figure 1.2: Arrays for Direct Current and Induced Polarisation geophysical probing. 'I' is a current source and 'V' is a voltage detector. The distance 'a' is called the array spacing.

(a) Wenner array
(b) Schlumberger array
(c) Eltran array
(d) Dipole-Dipole array.

The apparent resistivity calculated from measurements over a uniform region is equal to the actual resistivity of that region. When the region is not uniform, the apparent resistivity is a convenient way of characterising the measurements. However it is worth emphasising that the apparent resistivities obtained using different measurement techniques over the same nonuniform region are not necessarily the same.

Depending on whether measurements are being made for sounding, profiling or imaging, the apparent resistivity is measured with respect to one or more independent variables. Suitable variables are the frequency of the source (when time dependent emanations are used), the array spacing (which

is defined in figure 1.2) and the lateral position of the array on the earth's surface.

1.2.3 Simplified Models

In order to calculate the apparent resistivity of a region of the earth having a particular conductivity distribution, it is necessary in general to be able to solve Maxwell's Equations (see §2.3) in a nonhomogeneous anisotropic medium. As a mathematical simplification it is often assumed that the earth conducts electricity isotropically. To further simplify the mathematics the conductivity distribution is often modelled in a simple manner. Models with particular geological significance are the horizontally stratified earth and the isolated orebody with an overburden (see figure 1.3).

Many methods are available for calculating the apparent resistivity from conductivity distributions. These are divided here into 4 categories of modelling: (i) explicit, (ii) approximate, (iii) integral equation, and (iv) scale.

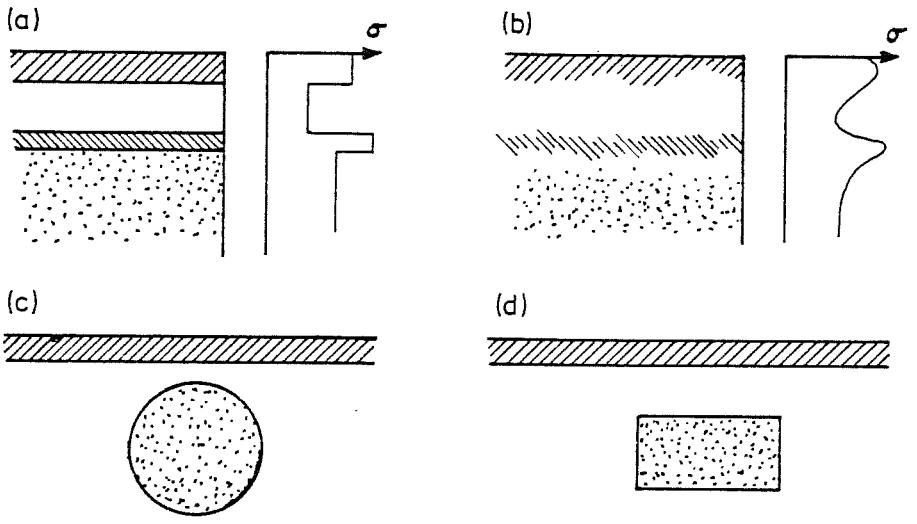

Figure 1.3: Conductivity distribution models used in the interpretation of geoelectric measurements.

(a) discrete strata.
(b) continuous strata.
(c) ore body with overburden.
(d)

Explicit Models

Explicit solutions of Maxwell's Equations are limited to relatively simple models. Nevertheless many useful solutions are known. The forward solution for direct current techniques over horizontally stratified media was originally developed for discrete strata (Stefanesco et al 1930; Keller and Frischknecht 1966 §23a) and has since been extended to allow for transition layers having a linear change in resistivity with depth (Mallick and Roy 1968; Koefoed 1979). Forward solutions for plane electromagnetic waves incident on stratified media have been developed for the calculation of magnetotelluric and telluric model data (Cagniard 1953; Wait 1981b Ch. 2,3). The electromagnetic responses to various magnetic and electric sources over stratified media (Wait 1962 Ch.2; Dey and Ward 1970), over orebody models (Ogunade 1981) and over laterally inhomogeneous earth models (Hill and Wait 1981) have been calculated to help with the interpretation of data gathered using electromagnetic methods.

Approximate Models

Smooth conductivity distributions are often approximated by piecewise constant distributions, as in finite element modelling (Coggon 1971; Kisner and Della Torre 1974; Pridmore 1981). The alternative finite difference modelling technique approximates the differential equation for the voltage (see §2.3) by a difference equation (Mufti 1976, 1978; Dey and Morrison 1979). Transmission line (or network) modelling represents a multi-dimensional continuous conductivity distribution as a multi-dimensional mesh (or network) of one-dimensional resistors (Johns and Rowbotham 1981, Dines and Lytle 1981). The so-called alpha centre approach (which applies only to conservative fields) models the square root of the conductivity as a sum of continuous functions (Stefanescu 1974; Petrick et al 1981). Solutions to the forward problem are facilitated by choosing these functions from appropriate sets.

Integral Equation Models

The integral equation approach (see §2.6) expresses the voltage, at any point, in terms of an integral of contributions from all other points (Metz and Pilkington 1969; Snyder 1976; Lee et al 1981; Ting and Hohmann 1981). For simple models explicit formulas may be derived from the integral equation, but most often it can only be solved numerically. When the integral equation approach is applied to regions for which the resistivity is piecewise homogeneous, the resulting volume (or area) integrals reduce to area (or line) integrals, thus reducing computational requirements (see §2.6.3).

Scale Models

Electromagnetic scale modelling involves building a model of the conductivity distribution and performing measurements on the model (cf. Frischknecht 1971). The model may be as complicated as desired. Scale modelling is particularly useful for providing experimental data to compare with calculated values obtained from any of the other three modelling methods discussed above.

1.2.4 Interpretation of Measurements

Curve Matching

The earliest method developed for the interpretation of sounding measurements is called curve matching (cf. Keller and Frischknecht 1966 §20). The apparent resistivity is plotted as a function of the array spacing (defined in figure 1.2), and the graph is compared to apparent resistivity curves for various stratified earth models (see figure 1.3a). The earth model with the apparent resistivity most closely matching that measured is taken to represent the region of the earth which is being sounded. In practice the curve matching technique is only capable of predicting two or three strata, since the number of possible models increases rapidly as the number of strata is increased.

Iterative Model Fitting

Any of the methods suitable for calculating the forward problem may be used as the basis of an iterative inverse method. Interpretation is performed indirectly by solving for the apparent resistivity for many parameter values of a particular model. The set of parameters for which the apparent resistivity best fits the measurements is taken to be the solution. Any of the techniques available for function minimisation (cf. Gill and Murray 1974) are suitable for finding such a solution by minimising the difference (perhaps in a least squares sense) between the measured and calculated values for the apparent resistivity. The choice of minimisation technique is largely arbitrary.

Often there is insufficient independence in the data (perhaps due to noise) to arrive at a unique model. Regularisation techniques help to overcome this by selecting a solution subject to predetermined constraints (cf. Backus and Gilbert 1968; Deschamps 1972; Jupp and Vozoff 1975; Marquardt 1963; Noble 1976). The constraints are chosen so as to select a model with

Stable iterative techniques have been developed for interpreting measurements in terms of stratified (i.e. one-dimensional) earth models. The models represent either continuous strata (Oldenburg 1978, 1979) or discrete strata (Parker 1971; Wu 1968; Glenn et al 1973; Rijo et al 1977; Meinardus 1970; Petrick et al 1977; Inman 1975; Vozoff 1958; Inman et al 1973). These models are able to represent any earth stratification. Iterative techniques which interpret measurements in terms of two and three-dimensional models have also been developed (Brass et al 1981; Pelton et al 1978; Petrick et al 1981), but they can only be applied to very simple kinds of conductivity distributions.

Ray Approximations

When the wavelength of an electromagnetic signal is small compared to any inhomogeneities in the refractive index, the propagation can be usefully approximated in terms of rays. Using this approach the reconstruction of two-dimensional cross sections is achieved in X-ray computed tomography (cf. Lewitt and Bates 1978a,b,c; Lewitt et al 1978; Kak 1979), ultrasound transmission tomography (Greenleaf et al 1974, 1975; Kak 1979), and in geophysical probing (Lytle and Dines 1980, Dines and Lytle 1979). In the latter situation it is more difficult to obtain the necessary data, since access to the entire circumference of the region being probed is not possible. Where ray curvature is important, due to changes in refractive index, correction schemes can be devised, although it is far from clear at present whether they can be expected to be generally useful (cf. McKinnon and Bates 1980).

Direct Interpretation

Langer (1933) derives an analytical solution for the conductivity of a continuously stratified earth by relating a series representation of the conductivity to a function derived from the measurements. Slichter (1933) uses Langer's solution to compare the interpretation of some examples of conductivity distributions. Langer's solution has been extended to allow for discontinuities in either the conductivity or its derivative (Langer 1936).

Pekeris (1940) develops a direct graphical technique to determine the conductivity of a discretely stratified earth. This technique is based on the asymptotic behaviour of the measurements at high spatial frequency (small array spacing). Beginning at the earth's surface and progressing downward each stratum is determined sequentially. This method has been automated (Koefoed 1976) and modified to make it more able to cope with noisy data (Szarniec 1980).

A third method, fundamentally different from the two described above, is that devised by Coen et al (1981) and Weidelt (1972). Nonlinear transformations are used to change the problem into an inverse scattering problem for the Schrodinger Equation. This can then be solved by the method of Gelfand and Levitan (1955).

1.2.5 Uniqueness and Resolution

The accuracy to which a conductivity distribution can be estimated, from data measured to a given accuracy, is not well understood. Often many significantly different conductivity distributions can be found, all of which are consistent with the measured data according to the accuracy of the measurements. This has been referred to as "non-uniqueness" or "equivalence".

Several methods are available for estimating the accuracy of the solution. Inman (1975) estimates the standard deviations of the model parameters from the effect on the data of perturbations in the model. Alternatively, Backus and Gilbert (1968) consider all solutions which when convolved with a point spread function are still consistent with the data. The maximum width of the point spread function indicates the resolution. Roy and Apparao (1971) compare for different electrode arrays the contribution to the measurements given by a thin horizontal stratum (layer). This provides a measure of the relative ability of the various arrays to detect horizontal strata as a function of both depth and array spacing, thereby indicating the vertical resolution. Apparao and Gangadhara Rao (1974) use the same technique for linear (as opposed to point) electrodes.

The accuracy to which a conductivity distribution is estimated can be improved when two different measurement techniques are used. This is achieved by interpreting both sets of measurements jointly, rather than each set separately (Vozoff and Jupp 1975).

1.3 MEDICAL PROBING

1.3.1 Electrical Properties of Tissue

Electrical conduction in living organisms is due to the movement of ions in solution. Within tissue the movement of ions is restricted by cellular membranes, so that different tissues have different conductivities. The measured resistivity of biological materials varies widely from one reported value to another (Geddes and Baker 1967). Body fluids have the

lowest resistivity, e.g. 64 to 65 Ωcm for cerebrospinal fluid, and 61 to 67 Ωcm for blood plasma (blood without the red blood cells). Amongst the poorest conductors are lung (140 to 2400 Ωcm), fat (1000 to 5000 Ωcm) and bone (2000 to 16000 Ωcm).

Materials of particular interest are skeletal muscle and blood. The resistivity of blood depends on the hematocrit (percentage of red blood cells) and on the velocity of the blood flow. It also depends on whether measurement is perpendicular or parallel to the direction of flow (Frewer 1974), apparently being related to the spatial distribution and orientation of the red blood cells in the blood vessel. Typically the resistivity of blood is from 150 to 170 Ωcm. In contrast the resistivity of skeletal muscle is from 1 to 15 times higher than that of blood. Skeletal muscle is composed of many long parallel cells. Measured parallel with the long axis of the cells the resistivity is from 150 to 408 Ωcm, while in the perpendicular direction it is from 675 to 2300 Ωcm.

The cells of nerve and muscle tissue have membranes which are said to be electrically excitable (Katz 1966). In the resting state an excitable cell maintains an ionic concentration gradient across the cell membrane. This results in a resting potential difference, so that the membrane is said to be polarised. When the membrane is electrically stimulated its ionic permeability changes and allows the ionic concentrations to equilibrate across the membrane. The resting potential disappears and the membrane is said to have depolarised. After a refractory period, during which the membrane is not excitable, or at least relatively insensitive to excitation, the cell membrane restores the ionic concentration difference and the resting potential returns. The variation with respect to time of the transmembrane potential, during the depolarisation and repolarisation of the membrane, is called the action potential.

Nerve tissue propagates action potentials around the body as part of normal bodily function. Muscle tissue uses action potentials to perform synchronous (and thereby useful) contraction of the individual muscle cells. The bulk electrical activity of the body resulting from all the individual action potentials may be measured on the surface of the body, or below the surface. In the latter situation the potentials are measured either with needle electrodes or during surgery. Potentials of primary interest to clinicians are the electrocardiogram (ECG or EKG) and the electroencephalogram (EEG), which are recordings of the electrical activity of the heart and of the brain respectively. Other potentials

found to be useful are the electromyogram (from skeletal muscle), the electroretinogram (being the response of the retina to visual stimulus), the electrooculogram (which is the variation in corneal-retinal potential accompanying eye motion), and the electrogastrogram (from the peristaltic movements of the gastrointestinal tract). These biologically produced potentials range from 10 μV to 4 mV and from direct current to 100 Hz; or for the electromyogram up to 3 kHz (Cromwell et al 1973 Ch.3).

It is important that artificial electric potentials generated within the body for determining tissue conductivity do not interfere with the normal function of the body. Interference can cause effects such as ventricular fibrillation, where the muscle cells forming the ventricular chambers of the heart depolarise asynchronously so that the heart does not pump sufficient blood to maintain bodily function. Experiments on humans and other animals indicate that the threshold current required to elicit observable effects (such as the threshold of sensation, slowing of the heart due to interference with the vagus nerve, and ventricullar fibrillation) increases with the frequency of the applied current (Geddes et al 1969).

Electrical currents which do interfere with bodily functions can also induce beneficial effects. A large current pulse through the heart depolarises all ventricular tissue simultaneously allowing a heart undergoing ventricular fibrillation to return to normal synchronous operation. Electrodes placed near nerves can be used to block the propagation of action potentials and induce an anaesthesia-like state (Geddes 1965).

The conductive properties of tissue can be measured in a variety of ways. Magnetic induction (cf. Tarjan and McFee 1968; McDonald 1979 Ch. 9), the attenuation of radio waves (Maini et al 1980) and the voltage resulting from current flowing through the tissue can all be used to find the conductivity. The latter method requires electrodes to be connected to the tissue, and is widely applied in plethysmography (see §§ 1.3.2 and 1.3.3).

When using electrodes the useful frequency range of currents is limited, apart from the need for patient safety, by chemical effects at the electrode-electrolyte (tissue) boundary. A transfer of ions from the electrode into solution creates a static voltage, which in equilibrium balances the tendency of further ions to enter solution. This ionic reaction appears electrically to have both a capacitive and resistive impedance (Baker 1971 § 1.4). When measuring low frequency voltages it is important to carefully prepare the electrode tissue interface, such as using an elect-

rode connected via its saturated ionic solution to an abraded patch of tissue, to reduce the resistive component of impedance. When measuring high frequency voltages the capacitive component is negligible (Nowotny and Nowotny 1980) and electrode preparation is not so important.

1.3.2 Impedance Plethysmography

Plethysmography is the name given to any technique used for measuring those volume changes of the human body which are associated with some physiological event. Plethysmography is used on either a particular body segment (e.g. limb, digit, torso) or on the whole body. There are many alternative plethysmographic techniques. The changes in volume can be measured by enclosing the body segment in a rigid box and measuring changes in volume or pressure of the fluid within the box, or flow of the fluid from the box (Sumner 1978). Alternatively a strain gauge can be used around the circumference of the body segment, or the electrical resistance of the body segment can be monitored (see figure 1.4a). The latter method is called impedance plethysmography (Nyober 1970), and is convenient to apply in practice.

The relationship between the electrical resistance measured during impedance plethysmography and the volume changes of a body segment, is derived from the assumption that the body segment is composed of cylindrical sections that have constant resistivity (figure 1.4b). The longitudinal resistance R of each section is

$$R = \rho \ell^2 / V \qquad (1.2)$$

where ρ is the resistivity, ℓ is the length and V is the volume of the sectio Assuming that the electrodes cover the end surfaces, the total longitudinal resistance is

$$R = \rho_t \rho_b \ell^2 / (V_b \rho_t + V_t \rho_b) \qquad (1.3)$$

where the subscripts t and b stand for tissue and blood respectively.

When some physiological change causes a small change in blood volume ΔV, without changing the length of the section, the change in resistance ΔR is

$$\Delta R/\Delta V_b \simeq \partial R/\partial V_b = -(\rho_t/\rho_b) R/(V_b \rho_t/\rho_b + V_t) . \qquad (1.4)$$

Assuming that the total volume V ($= V_t + V_b$) is approximately equal to $V_b \rho_t/\rho_b +$ (which is true when $\rho_t \simeq \rho_b$ or $V_b << V_t$), the change in volume is given by

$$\Delta V/V \simeq -(\rho_b/\rho_t)\,\Delta R/R \ . \qquad (1.5)$$

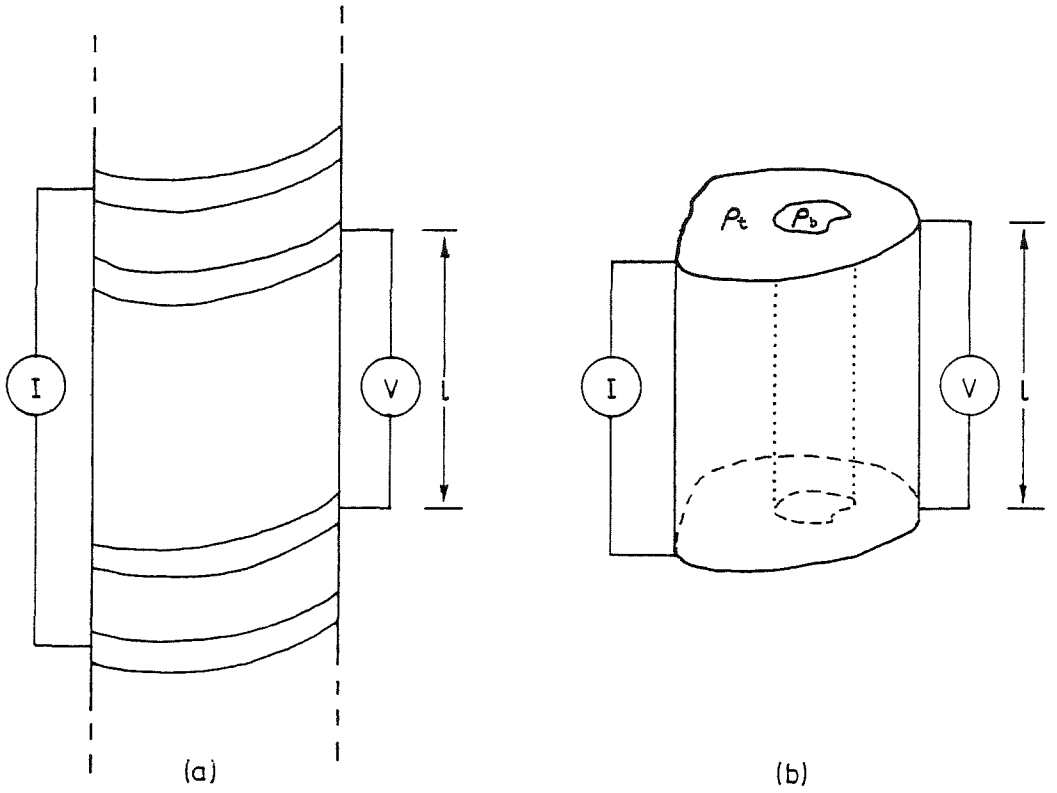

Figure 1.4: (a) Impedance plethysmography performed on limb by passing current between one pair of circumferencial electrodes and monitoring voltage on another pair.

(b) Assumed electrical model of limb with end electrodes causing parallel current flow along cylindrical sections of constant resistivity.

Whereas the geometry of limbs, fingers and toes is reasonably approximated by cylinders, the torso of the body has many isolated inhomogeneities (e.g. heart, lungs) and is not well approximated by a cylinder. Furthermore, electrodes are usually applied to the body segment as circumferential bands (see figure 1.4a). When using band electrodes the effect which a localised perturbation in conductivity (or volume) has on the change in resistance depends on the position of the perturbation in relation to the position of the electrodes (Penney et al 1979; Anderson et al 1980). However it is possible to choose the position of the electrodes to minimise the dependence of the change in resistance on the position of the perturbation.

When the section expands longitudinally instead of radially, its longitudinal resistance increases (Brown et al 1975). Depending on the ratio of longitudinal to radial stretching, the magnitude of the measured change in resistance is somewhat smaller than that given by (1.5). On average the measured value of $\Delta R/R$ is 20% lower than if no longitudinal stretching were present (Jaffrin and Vanhoutte 1979), but the effect can be reduced by mounting the electrodes on an inextensible frame. The change in conductivity of blood with blood velocity contributes to the measured change in resistance (Swanson and Webster 1976), and can contribute as much as 10% of $\Delta R/R$ as do volume changes (Peura et al 1978).

1.3.3 Medical Uses of Plethysmography

Venous Occlusion Plethysmography

Venous occlusion plethysmography is the measurement of volume changes of a body segment during an interval when the venous bloodflow is first occluded and then subsequently restored. A convenient way to achieve venous occlusion is to inflate a pneumatic cuff encircling the limb to a pressure in excess of venous pressure but lower than arterial pressure (see figure 1.5a). The body segment increases in volume as blood collects in the veins. On release of the pressure within the cuff, the limb volume returns to its previous level (see figure 1.5b).

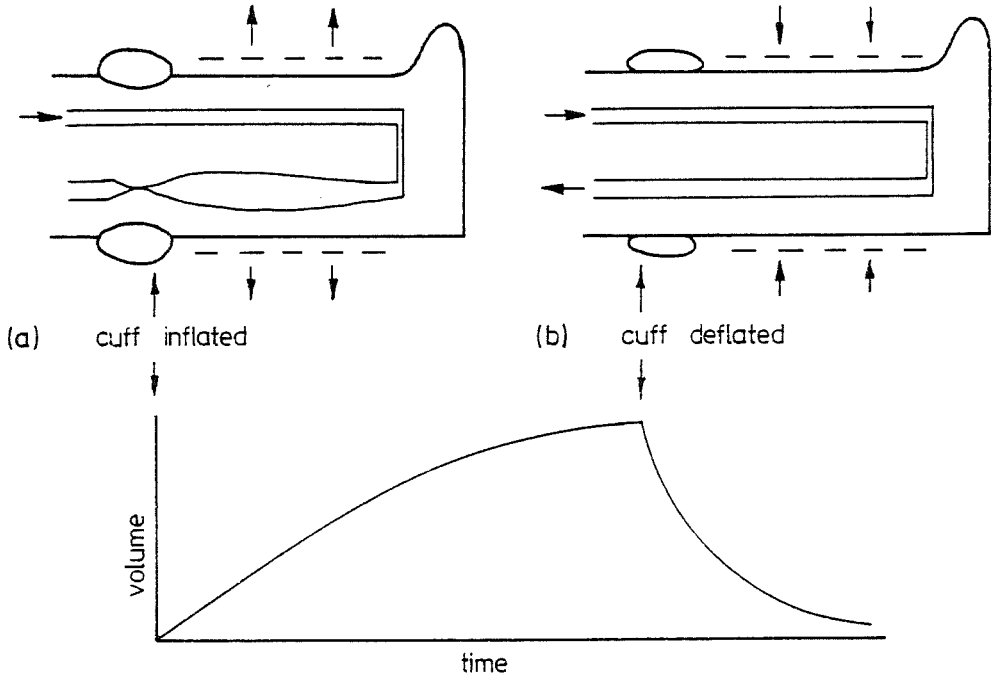

Figure 1.5: Volume changes measured during venous occlusion plethysmography.

(a) Limb volume increases as blood collects in the veins while cuff is inflated

The volume change is about 1% of the volume of the body segment, and contains two diagnostically important pieces of information. The slope of the curve immediately after occlusion is proportional to the bloodflow into the limb (cf. Sumner 1978). The shape of the volume decay following the release of occlusion is useful in the diagnosis of venous thrombosis, which is the blockage of veins due to blood clots.

Several methods have been developed in order to diagnose venous thrombosis from the limb volume change measured during venous occlusion plethysmography (cf. Barnes et al 1972; Johnson & Kakkar 1974; Wheeler et al 1974). These methods involve deducing one or two parameters from the volume change (see figure 1.6), and using the parameters as an aid to diagnosis.

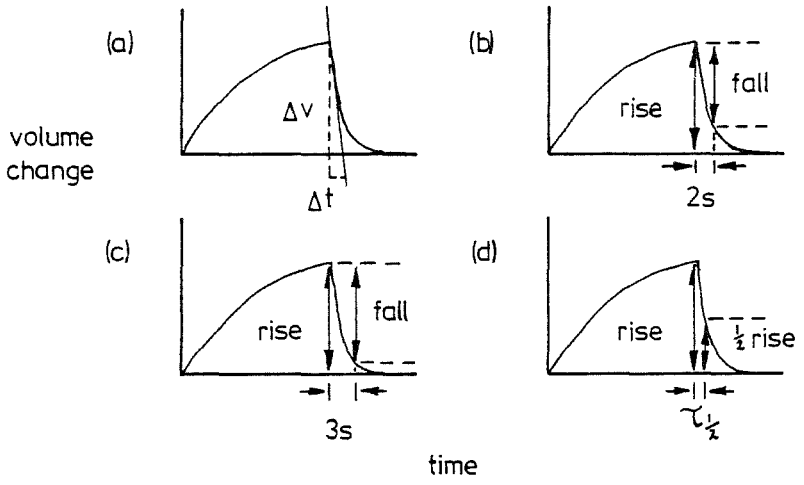

Figure 1.6: Alternative parameters used to interpret venous occlusion volume changes for venous thrombosis.

(a) the rate of decrease in volume at cuff release (Barnes et al 1972),

(b) the ratio of the fall in volume in the 2 seconds following cuff release to the total rise in volume (Johnson & Kakkar 1974),

(c) the fall in volume in the 3 seconds following cuff release together with the rise in volume (Wheeler et al 1974),

(d) the half life of the decrease in volume following cuff release (Jaffrin 1976).

Pulse Plethysmography

Pulsatile volume changes of body segments are observed every time the heart beats. The volume change is due to periodic fluctuations in the arterial blood pressure, and is about 0.1% of the volume of the body segment

(excluding the torso) (see figure 1.7). The pressure pulse originates at the heart and travels towards the peripheral parts of the body. As the pulse travels down the arterial tree, its shape and amplitude change according to the physiological state of the vessels through which it passes. The shape of the volume change at the extremities is useful in the diagnosis of arterial occlusive conditions (arteriosclerosis) (cf. Raines 1978).

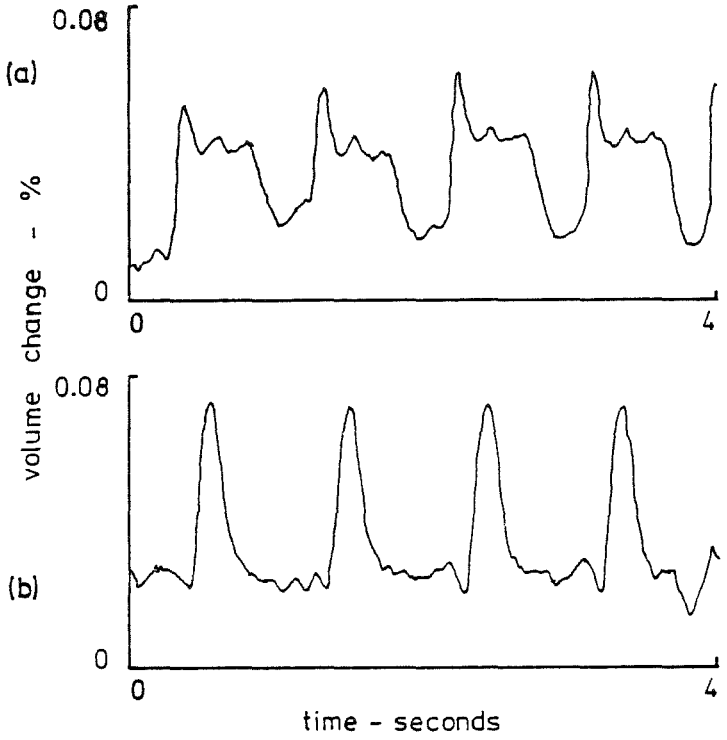

Figure 1.7: Pulsatile volume changes measured simultaneously on the

(a) upper arm, and

(b) lower leg (calf).

Quantitative interpretaion of the pulsatile volume change is complicated by two factors. Firstly, non-pulsatile bloodflow has no effect on the measured volume change, so that absolute bloodflow cannot be determined (Brown et al 1975). Secondly, differences between the pressure pulse at the heart amongst different individuals necessitates the use of some form of normalisation of peripheral pulse shape against pulse shape at the heart.

Modelling the arterial tree as a passive linear network, in which the components are independent of pressure, provides a good representation of the actual arterial system (de Pater and vandenBerg 1964; Avolio 1980). The transfer function between two points in such a model of the arterial tree is therefore independent of the pressure pulse at the heart. Hence

logical state of the vessels (Skidmore and Woodcock 1980; Brown et al 1978; Li et al 1980).

Cardiac Output

Pulsatile volume and impedance changes of the torso occur as the heart beats. It is clear that the changes are in some way related to the function of the heart and vascular system (Rubal et al 1980). This has led to attempts at relating the impedance changes directly to the cardiac output (flow of blood through the heart) (cf. Baker 1971 §1.6). It is not clear, when using impedance plethysmography to calculate the cardiac output, whether the assumptions about the origin of the impedance changes are valid. The cardiac output measured by the impedance technique can overestimate that measured by alternative techniques by up to 20% (cf. Case 1980), however the impedance technique does have the advantage of being noninvasive. In view of such large discrepancies the technique is of more value for monitoring changes in the cardiac output of a particular individual, rather than for making absolute estimates of cardiac output (cf. Case 1980; Hill and Lowe 1973; Miyamoto et al 1981).

1.4 IMPEDANCE IMAGING

Impedance imaging is any procedure whereby measurements of electric current and voltage on the surface of a region are used to derive an estimate of the conductivity within the region. Other names for impedance imaging and related terms in various fields are
"impedance camera" (Henderson and Webster 1978; Lytle and Dines 1978),
"electric current computed tomography" (Schomberg 1980),
"electrical impedance computed tomography" (Price 1979),
"electrical conductivity imaging" (Dines and Lytle 1981), and
"computerised geophysical tomography" (Dines and Lytle 1979).

1.4.1 Projection Images

The simplest impedance imaging procedure is to pass a known electric current through a body and to measure the voltage difference from one side of the body to the other. The measured voltage gives some idea of the conductivity of the body.

Consider figure 1.8a where $\rho(x,y)$ is the resistivity within the region R (i.e. the body). A coordinate system ξ,η is inclined at an angle θ to the coordinate system x,y. A constant current I is simultaneously passed between pairs of electrodes having the same η coordinate. Each such pair of electrodes must have a separate current source, which is electrically isolated from all others to ensure the current flows between the chosen pairs of electrodes. The current flows parallel to the streamlines (dashes) along the paths which depend upon the conductivity distribution within R. Perpendicular to the streamlines are the equipotentials (solid lines). A curvilinear coordinate system α,β coincides with the streamlines (α) and equipotentials (β).

The voltage difference V between a pair of electrodes with the same coordinate η_o, is

$$V(\eta_o\theta) = \int_{\alpha_1}^{\alpha_2} \rho(\alpha,\beta_o,\theta)\,|\underset{\sim}{J}(\alpha,\beta_o,\theta)|\,d\alpha\ , \qquad (1.6)$$

where $\underset{\sim}{J}$ is the current density, and β_o is the streamline which meets the surface of R at η_o. An impedance projection $V(\eta,\theta)$ is obtained by measuring the voltage difference between all pairs of electrodes with the same coordinate.

Projections of the body may also be formed using X-rays. A projection formed using X-rays is known as an X-ray picture or X-ray shadowgram. One difference between using X-rays to form a projection and using electric currents is that the X-rays travel in straight lines whereas the current streamlines are curvilinear. An X-ray picture appears blurred due to the integration (i.e. averaging) of the X-ray absorptivity along the ray paths. The impedance projection $V(\eta,\theta)$ has the same blurring, but also contains geometrical distortions due to current flow along curved paths. Poor spatial resolution, due to the blurring and curvilinear current flow, has been noted by Henderson and Webster (1968) when using an imaging system similar to that shown in figure 1.8a.

It is interesting to note that it is possible to form another kind of impedance projection which is different to $V(\eta,\theta)$. This is achieved by taking the voltage gradient as the independent variable and the current as the dependent variable. Consider figure 1.8b. A constant voltage difference ΔV is simultaneously applied between adjacent electrodes, equally spaced in the ξ coordinate. The polarity of the voltage difference is chosen such that the equipotentials meet the surface of R at electrodes having the same

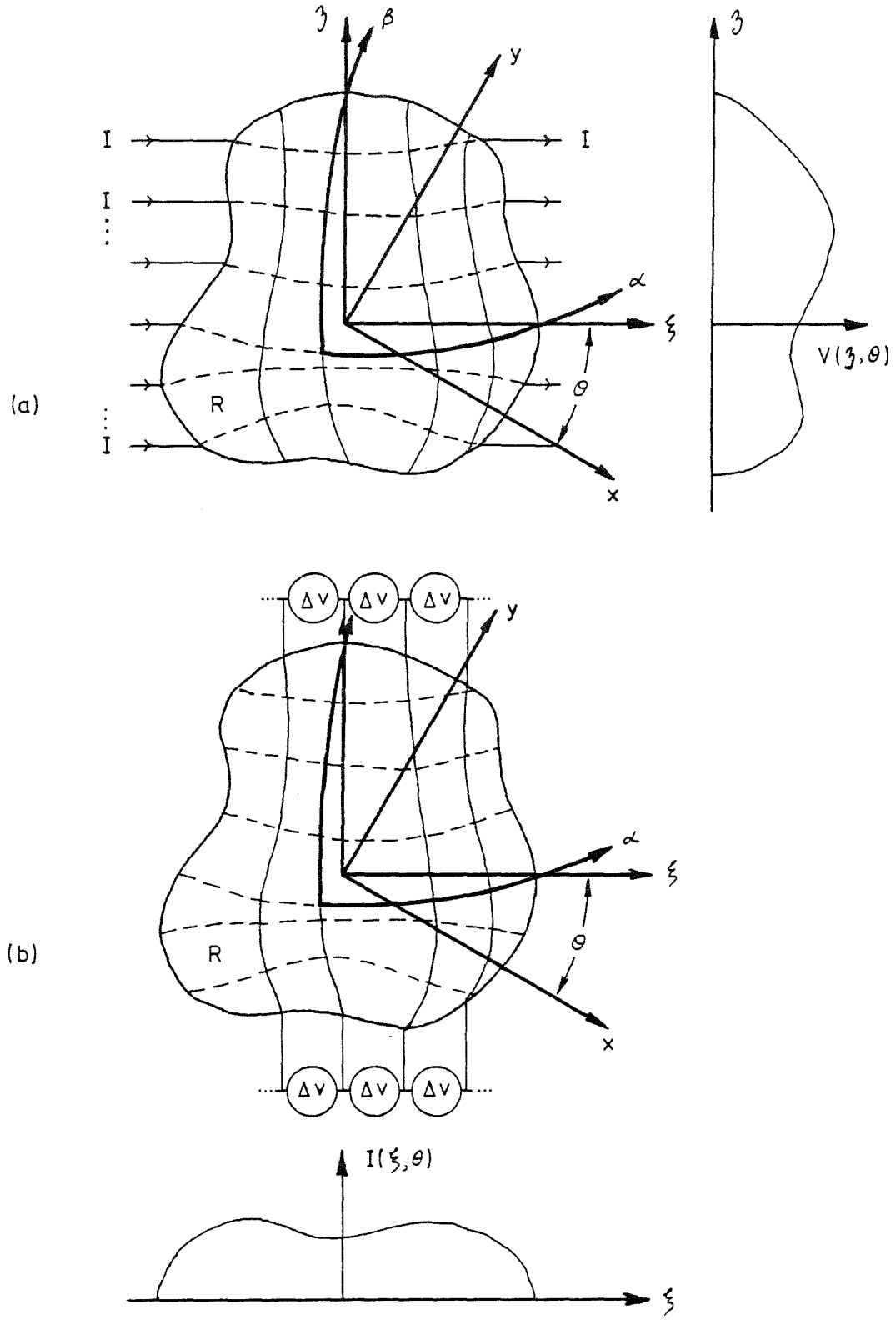

Figure 1.8: Impedance projections $V(\eta,\theta)$ and $I(\xi,\theta)$ along (a) current lines (dashes) and (b) equipotentials (solid) respectively. (see text).

ξ coordinate. Curvilinear coordinates α,β coincide with the streamlines and equipotentials as before.

The total current crossing the equipotential which meets the surface at ξ_o is

$$I(\xi_o, \theta) = \int_{\beta_1}^{\beta_2} \sigma(\alpha_o, \beta, \theta) \left| \nabla V(\alpha_o, \beta, \theta) \right| d\beta, \qquad (1.7)$$

where σ is the conductivity, ∇V is the gradient of the voltage and α_o is the equipotential which meets the surface of R and ξ_o. $I(\xi_o, \theta)$ is measured as the total injected current for $\xi < \xi_o$ (or $\xi > \xi_o$). Here an impedance projection $I(\xi,\theta)$ is obtained by measuring the total current crossing all equipotentials.

When the conductivity is the same throughout all of R then the coordinates α,β coincide with the rectangular coordinates ξ,η, and the integrals in (1.7) and (1.6) are straight line integrals. However, suppose that current or voltage distributions other than those described here are used to make the measurements. Depending on the particular distributions chosen, the current streamlines and equipotentials may not coincide with the rectangular coordinates ξ,η for any conductivity distribution within R, and it may not be possible to interpret the measurements in terms of projections.

Measuring a single projection $V(\eta,\theta)$ or $I(\xi,\theta)$ for only one angle of θ does not uniquely characterise the conductivity distribution within R. Similarly an X-ray picture does not fully characterise the X-ray absorptivity of the body on which it was taken. Nevertheless, single X-ray pictures are particularly useful. It is therefore conceivable that in some situations single impedance projections may also be useful.

1.4.2 Back Projection

It has been suggested (Price 1979) that a back projection approach similar to that used for X-ray computed tomography (cf. Lewitt et al 1978) might be suitable for reconstructing the conductivity distribution from electrical measurements. Such an approach would appear particularly appropriate in view of the successful reconstruction of distributions of refractive index and attenuation from ultrasonic transmission measurements (Greenleaf et al 1974, 1975), and the reconstruction of distributions of attenuation from measurements using high frequency electromagnetic waves (Lytle and

Dines 1980; Dines and Lytle 1979). Unfortunately a back projection approach based on the impedance projections $V(\eta,\theta)$, or $I(\eta,\theta)$, measured for many angles θ does not unambiguously determine $\sigma(x,y)$ (Bates et al 1980; Schomberg 1980). The problem is that many of the projections $V(\eta,\theta)$, or $I(\xi,\theta)$, are linearly dependent and thus insufficient information is obtained to uniquely reconstruct $\sigma(x,y)$ (see §5.1.6).

1.4.3 Iterative Model Fitting

Rather than treating impedance imaging conceptually in terms of line integrals it is equally appropriate to adopt an iterative model fitting approach. The basis of such an approach is to iteratively adjust a model of the conductivity distribution until the measurements predicted by the model mimic those which are obtained experimentally (cf. §1.2.4).

Iterative modelling, using a finite difference modelling approach, has been used to interpret simulated data (Lytle and Dines 1978). The resulting reconstructions are of low resolution. Similar results are also achieved when using a discrete network representation to model the conductivity distribution (Dines and Lytle 1981).

Iterative modelling has also been used to interpret experimental measurements. Simple models representing two-dimensional (Pelton et al 1978) and three-dimensional (Petrick et al 1981) conductivity distributions have been fitted to data obtained from geophysical probing. These particular two and three-dimensional models are not capable of representing arbitrary conductivity distributions.

1.5 DISCUSSION

All methods for estimating distributions of conductivity within bodies involve injecting electric currents into the regions which it is desired to probe. The currents may be generated either by using electrodes to apply potential differences across the region, or by forcing time-dependent electric and magnetic fields to interact with the region. Whereas both of these techniques are used in geophysics, only the former is used extensively in medical diagnostic applications.

In geophysics, the sole purpose of the measurements is to determine the spatial distribution of the conductivity in order to find the material composition beneath the surface of the earth. Similarly in medical practice it is of interest to determine the tissue composition as a function of position, but it is also valuable to monitor changes in electrical resistance associated with particular physiological events in order to derive information about them. The latter has no parallel in geophysics because the conductivity of the earth is assumed constant over the period of the measurements. Quantitative interpretation of measurements is based on Maxwell's Equations (see §2.3). These equations describe the interaction between electric and magnetic fields and the electrical properties of the region in which the fields exist. Whereas numerous techniques exist for calculating the measurements from the physical properties of the region (§1.2.3), the converse is not true (§1.2.4).

The analytical techniques for determining the conductivity distributions, which vary only in one direction (Langer 1933; Pekeris 1940; Coen 1981), are particularly interesting, but it is not clear how they may be extended to two or more dimensions. The most successful two-dimensional impedance imaging techniques are those which use high frequency electromagnetic waves and assume ray propatation (Dines and Lytle 1979; Lytle and Dines 1980). A back projection approach similar to that used in X-ray computed tomography and ultrasonic computed tomography is then appropriate for reconstructing images of conductivity distributions. However when conservative electric fields are used, a simple back projection approach analagous to that used in X-ray computed tomography is not suitable (Bates et al 1980). It is therefore not clear how to image a conductivity distribution from measurements of its interaction with conservative or low frequency electromagnetic fields. Perhaps this is why there is an abundance of iterative model fitting techniques used to interpret measurements. Clearly there is ample scope for the further investigation of two-dimensional impedance imaging.

The purpose of this thesis is to examine different aspects of probing with electric currents. The probing is performed using alternating currents which have frequencies low enough for a conservative field approach to be adopted. The mathematical description of conservative fields and the physical situations in which they are useful are reviewed in Chapter 2. The three particular aspects of probing with electric currents which are examined in this thesis are summarised below.

Firstly, particular classes of conductivity distribution are examined in order to obtain limits on the spatial and conductivity resolution of impedance imaging systems (Chapter 3). Such limits are valuable because most techniques used for impedance imaging are iterative, so that the accuracy of the conductivity distribution thereby deduced may not be well defined.

The second aspect of probing is concerned with determining the conductivity distribution within a region from measurements on the surface of the region. It is by no means immediately clear how to calculate the conductivity distribution. Two approaches, developed for dealing with such problems, are reported in this thesis. The first approach is to iteratively adjust a model representing the conductivity distribution until it is consistent with the measurements (Chapter 4). The second approach is to use a simple model to represent the conductivity distribution. Provided the model is simple enough, the mathematical description of the problem can often be manipulated to give a direct solution for the model in terms of the measurements (Chapters 4 and 5).

The third consideration is how to make use of changes in electrical resistance in order to monitor changes in significant physiological parameters. A simple model is introduced in Chapter 6 for interpreting the limb volume changes which are measured during venous occlusion plethysmography (see §1.3.3). The model parameters are chosen to relate as closely as possible to the physiology of the limb.

2. CONSERVATIVE FIELDS

2.1 INTRODUCTION

Fields in physics and engineering are physical constructs which facilitate the description of various physical phenomena. The properties attributable to fields are directly observable, which means the fields have physical existence (e.g. electric and magnetic fields). Many phenomena can be described in terms of vector fields (i.e. fields having both direction and magnitude), with any particular field depending upon the physical situation under consideration. The physical situation of interest in this study is steady state electric current flow in a region with spatially varying isotropic conductivity. This situation is described by a conservative field, which is a vector field having the particular properties outlined in §2.2.

Fields may be described mathematically as a set of functions of the coordinates of a point in space, and this allows the power of mathematics to be applied to fields. The same mathematical description may also be applied to some physical phenomena in which no physical field is directly observable, such as in heat conduction. In this case a field exists only in concept but this does not make the mathematical description any less useful.

In this chapter the various phenomena which can be described by conservative fields are reviewed, as are the mathematical expressions which are used in later chapters to represent the fields.

2.2 POTENTIAL, FLUX AND SOURCES

Any vector field $\underset{\sim}{F}$ can be represented as the sum of the gradient of a scalar function Φ and the curl of a divergenceless vector $\underset{\sim}{A}$ (cf. Morse and Feshbach 1953 §1.5):

$$\underset{\sim}{F} = \nabla\Phi + \nabla\times\underset{\sim}{A} \tag{2.1}$$

with

$$\nabla\cdot\underset{\sim}{A} = 0, \tag{2.2}$$

where ∇ is the gradient operator, $\nabla\times$ is the curl operator and $\nabla\cdot$ is the divergence operator. Φ is called the scalar potential of $\underset{\sim}{F}$, and $\underset{\sim}{A}$ is the vector potential.

A conservative field is one for which the integral over any closed path C within the field is zero, i.e.

$$\int_C \underset{\sim}{F}\cdot\underset{\sim}{t}\, dC = 0 \tag{2.3}$$

where '·' is the vector scalar product and $\underset{\sim}{t}$ is the unit tangent to C (see figure 2.1). Stokes's Theorem equates this line integral to the surface integral over the enclosed surface S by

$$\int_C \underset{\sim}{F}\cdot\underset{\sim}{t}\, dC = \int_S \nabla x\underset{\sim}{F}\cdot\underset{\sim}{n}\, dS \tag{2.4}$$

where $\underset{\sim}{n}$ is the unit normal to S (see figure 2.1).

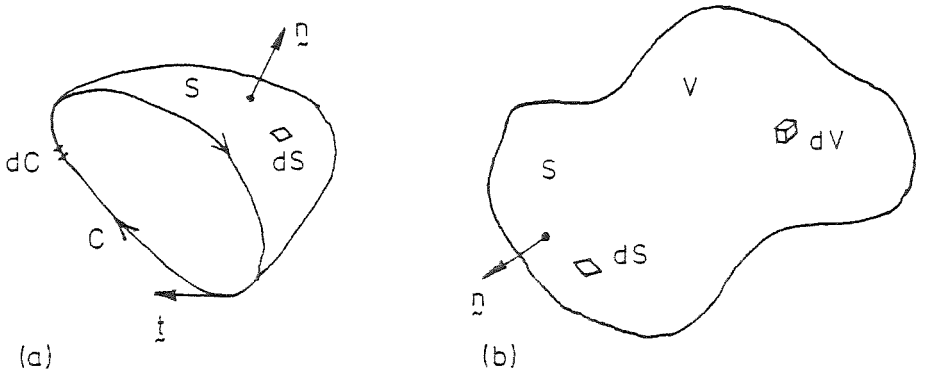

Figure 2.1 Definition of symbols used in 3 dimensions

(a) Open surface S is enclosed by curve C. The unit normal to S is $\underset{\sim}{n}$, and the infinitesimal area is dS. C has unit tangent $\underset{\sim}{t}$ and infinitesimal arc length dC.

(b) Closed surface S encloses volume V. $\underset{\sim}{n}$ and dS are the same as in (a). The infinitesimal volume is dV.

Substituting (2.1) into (2.4) and using (2.3) determines the constraints placed on a general vector field for it to be conservative; i.e.

$$\int_S (\nabla x\nabla\phi + \nabla x\nabla x\underset{\sim}{A}).n\, dS = 0. \tag{2.5}$$

Since curl(grad(.)) is identically zero, (2.5) requires that $\nabla x\underset{\sim}{A}$ must itself be a conservative field. Thus any conservative field may be represented as the sum of a scalar potential and another conservative field (which may of course be zero). As a matter of convention a conservative field is represented as the negative gradient of a scalar potential. Putting $\Phi = -\phi$ gives

$$\underset{\sim}{F} = -\nabla\Phi, \tag{2.6}$$

which uniquely defines $\underset{\sim}{F}$ in terms of Φ although not the converse, as Φ plus an constant defines the same $\underset{\sim}{F}$. $\underset{\sim}{F}$ is called the field intensity and Φ is called

the potential. (Potential is always used here to mean scalar potential, when any other type of potential is considered it is named differently).

In physical situations it is frequently meaningful to define another field $\underset{\sim}{D}$ which is related to the field intensity by

$$\underset{\sim}{D} = \lambda \underset{\sim}{F}. \tag{2.7}$$

$\underset{\sim}{D}$ is called the flux density and λ is a function of the space over which $\underset{\sim}{F}$ is defined. If the space is isotropic then λ is a scalar function, otherwise it must be a tensor relating the components of $\underset{\sim}{F}$ to those of $\underset{\sim}{D}$. λ is called the constitutive parameter and (2.7) is called the constitutive relation. The divergence of the flux density is a scalar function, s, called the source density, i.e.

$$\nabla \cdot \underset{\sim}{D} = s. \tag{2.8}$$

Integrating s over a volume V and using the Divergence Theorem gives

$$\int_V s \, dV = \int_S \underset{\sim}{D} \cdot \underset{\sim}{n} \, dS \tag{2.9}$$

where $\underset{\sim}{n}$ is the unit normal to the closed surface S which encloses the volume (see figure 2.1). Remember that lower case s represents the source density, while upper case S represents the closed surface in figure 2.1b. Equation (2.9) is called Gauss's Theorem and states that the net flux emerging from a closed surface is equal to the total amount of source enclosed.

Substituting (2.6) and (2.7) into (2.8) yields

$$\nabla . (\lambda \nabla \phi) = -s, \tag{2.10}$$

or on rearranging

$$\nabla^2 \phi = -(s + \nabla \lambda . \nabla \phi)/\lambda. \tag{2.11}$$

where ∇^2 (= div(grad)) is the Laplacian operator. It is convenient to regard the right hand side of (2.11) as a generalised source density. Equation (2.11) is Poisson's Equation and relates the Laplacian of the potential to the generalised source density. Whereas the flux density has associated with it only one source term s, the gradient of the potential (field intensity) has two source terms: s/λ and $\nabla \lambda \cdot \nabla \phi / \lambda = (\nabla \ln \lambda) . \nabla \phi$. The former source density is independent of the field intensity and is called the independent source density. The latter source density depends upon the interaction between the field intensity and spatial variations in λ and is called the dependent source density. There are no dependent sources in regions where λ does not vary. When there are no sources at all (2.11) reduces to

$$\nabla^2\phi = 0 \tag{2.12}$$

which is called Laplace's Equation.

2.3 ELECTRIC AND MAGNETIC FIELDS

The set of equations governing classical (non-quantum) electromagnetic phenomena are called Maxwell's Equations. These may be written as (cf. Ramo, Whinnery and van Duzer 1965 §4.06)

$$\nabla\cdot\underset{\sim}{D} = \rho \ , \tag{2.13a}$$

$$\nabla\cdot\underset{\sim}{B} = 0 \ , \tag{2.13b}$$

$$\nabla\times\underset{\sim}{E} = -\dot{\underset{\sim}{B}} \tag{2.13c}$$

and

$$\nabla\times\underset{\sim}{H} = \underset{\sim}{J} + \dot{\underset{\sim}{D}} . \tag{2.13d}$$

$\underset{\sim}{D}$, $\underset{\sim}{B}$, $\underset{\sim}{E}$, $\underset{\sim}{H}$, $\underset{\sim}{J}$ and ρ are the electric flux density, magnetic flux density, electric field intensity, magnetic field intensity, conduction current density and charge density respectively, and the dot over a variable indicates the derivative with respect to time. In linear isotropic dielectrics, ferromagnetics and conductors the following constitutive relations hold:

$$\underset{\sim}{D} = \varepsilon\underset{\sim}{E} \ , \tag{2.14a}$$

$$\underset{\sim}{B} = \mu\underset{\sim}{H} \tag{2.14b}$$

and

$$\underset{\sim}{J} = \sigma\underset{\sim}{E} \tag{2.14c}$$

where ε, μ, and σ are the permittivity, permeability and conductivity respectively. Equation (2.14c) is called Ohm's Law. Equations (2.13) and (2.14) combine to yield three conservative fields, each appropriate to a different physical situation.

2.3.1 Static Electric Field in a Dielectric

The time dependent electric field $\underset{\sim}{E}$ is not conservative because curl $\underset{\sim}{E}$ is not zero by (2.13c) and hence the closed line integral of (2.4) is not in general zero. When $\underset{\sim}{E}$ is not time dependent then neither is $\underset{\sim}{B}$, so curl $\underset{\sim}{E}$ is zero and $\underset{\sim}{E}$ is conservative. Defining the electric potential as ϕ with

$$\underset{\sim}{E} = -\nabla\phi \ , \tag{2.15}$$

then (2.13a) and (2.14a) give

$$\nabla^2\phi = -(\rho + \nabla\varepsilon.\nabla\phi)/\varepsilon, \tag{2.16}$$

which is Poisson's Equation (2.11).

2.3.2 Static Magnetic Field

As with the time dependent electric field, the time dependent magnetic field $\underset{\sim}{H}$ is not conservative. Furthermore even the static magnetic field is not conservative in regions of current flow $\underset{\sim}{J}$. Provided the magnetic field is neither time dependent nor encloses any regions of current flow it is conservative and is represented by the magnetic scalar potential ϕ_m where

$$\underset{\sim}{H} = -\nabla\phi_m. \tag{2.17}$$

Equations (2.13b) and (2.14b) then combine to produce Poisson's Equation involving magnetic quantities:

$$\nabla^2\phi_m = -\nabla\mu.\nabla\phi_m/\mu. \tag{2.18}$$

Equation (2.18) is different from (2.16) in that it has no independent sources, which is equivalent to saying that magnetic monopoles do not exist.

2.3.3 Static Electric Field in a Conductor

The static electric field is conservative in a conductor just as it is in a dielectric (cf §2.3.1). In a conductor the electric potential ϕ is often written as V, in which case it is called the voltage. Substituting (2.15) with (2.14c) into (2.13d) with $\dot{\underset{\sim}{D}} = 0$ and taking the divergence of the resulting expression gives (using div(curl(·)) = 0 and putting $\phi = V$)

$$\nabla^2 V = -\nabla\sigma.\nabla V/\sigma \ . \tag{2.19}$$

In contrast with an electric field in a dielectric which has independent sources ρ, there are no independent sources in a conductor because any free charge is conducted away down the potential gradient.

It is at times convenient to imagine that there are fixed current sources which are not dependent on the field. In particular this is true for excitable tissue in physiological conductors. In this case (2.14c) is modified to

$$\underset{\sim}{J} = \sigma\underset{\sim}{E} + \underset{\sim}{J}_i \tag{2.20}$$

where $\underset{\sim}{J}_i$ is the independent source density. Substituting as before yields

$$\nabla^2 V = (-\nabla\sigma.\nabla V + \nabla.\underset{\sim}{J}_i)/\sigma \ , \tag{2.21}$$

which is again Poisson's Equation. Modifying the constitutive relations for the magnetic field (2.14b) and electric field in a dielectric (2.14a) in an analagous manner allows independent magnetic dipole and electric dipole sources to be represented. Magnetic and electric dipole sources are found in ferromagnetic and ferroelectric substances respectively. These substances are said to have residual magnetic and electric polarisation.

2.3.4 Quasi-static Electric and Magnetic Fields

There are circumstances under which time dependent magnetic and electric fields are so closely approximated by conservative fields that it is sensible to represent them thus. In homogeneous isotropic media Maxwell's Equations (2.13) and the constitutive relations (2.14) may be re-expressed as (cf. Ramo, Whinnery and van Duzer 1965 §4.16)

$$\nabla^2\phi - \mu\varepsilon\ddot{\phi} = -\rho/\varepsilon \ , \tag{2.22a}$$

$$\nabla^2\underset{\sim}{A} - \mu\varepsilon\ddot{\underset{\sim}{A}} = -\mu\underset{\sim}{J} \ , \tag{2.22b}$$

$$\underset{\sim}{B} = \nabla x\underset{\sim}{A} \tag{2.22c}$$

and

$$\underset{\sim}{E} = -\nabla\phi - \dot{\underset{\sim}{A}} \tag{2.22d}$$

where ϕ is the scalar electric potential as before, and $\underset{\sim}{A}$ is the vector potent of the magnetic field. Equations (2.22a) and (2.22b) define ϕ and $\underset{\sim}{A}$. When solved in three dimensions over a volume V, they give (Ramo, Whinnery and van Duzer 1965 §4.17)

$$\phi = \int_V \left[\rho(t-r/v)/4\pi\varepsilon r\right] dV \tag{2.23a}$$

and

$$\underset{\sim}{A} = \mu\int_V \left[\underset{\sim}{J}(t-r/v)/4\pi r\right] dV. \tag{2.23b}$$

Time is represented by t, r is the Euclidean distance from the point at which ρ (or $\underset{\sim}{J}$) is being evaluated in the integrand to the point at which ϕ (or $\underset{\sim}{A}$) is being calculated, and v is the velocity of propagation of the electromagnetic fields and is given by

$$v = (\mu\varepsilon)^{-\frac{1}{2}}. \tag{2.24}$$

Equations (2.23a) and (2.23b) express the potentials ϕ and $\underset{\sim}{A}$ in terms of contributions to those potentials from all sources ρ or J within the volume being considered. The contributions weaken with distance by the factor r in the denominator, and are delayed in time by r/v due to the finite velocity of propagation. Because of the latter effect ϕ and $\underset{\sim}{A}$ are called retarded potentials.

Expanding the numerators of (2.23a) and (2.23b) in their Taylor series gives

$$\rho(t-r/v) = \rho(t) + \rho'(t)(-r/v) + \rho''(t)(-r/v)^2/2! + \ldots \qquad (2.25)$$

When r/v is very small (as it often may be since $v \simeq 3 \times 10^8$ m/s in free space) all terms other than the first on the right hand side of (2.25) are negligible, giving

$$\phi_q = \int_V \rho(t)/4\pi\varepsilon r \, dV \qquad (2.26a)$$

and

$$\underset{\sim}{A}_q = \mu \int_V \underset{\sim}{J}(t)/4\pi r \, dV. \qquad (2.26b)$$

ϕ_q and $\underset{\sim}{A}_q$ are called <u>quasi-static potentials</u> and vary with time but have no retardation effect. When the fields do not vary with time there is neither retardation nor time variation and both (2.23a) and (2.26a), and both (2.23b) and (2.26b) reduce respectively to

$$\phi_s = \int_V \rho/4\pi\varepsilon r \, dV \qquad (2.27a)$$

and

$$\underset{\sim}{A}_s = \mu \int_V \underset{\sim}{J}/4\pi r \, dV \qquad (2.27b)$$

where ϕ_s and $\underset{\sim}{A}_s$ are called the <u>static potentials</u>.

Comparing (2.26) with (2.27) it is apparent that the quasi-static potentials at a particular instant are the same as static potentials. Therefore it is possible to approach the quasi-static situation as though it were a continuous sequence of static problems, the solution to each of which gives the solution to the quasi-static situation at a particular instant. This means a conservative field approach is applicable to quasi-static problems.

The only difference between the retarded potentials and the quasi-static potentials is in the term in the numerator of the integrands of (2.23) and (2.26). In order to estimate the difference between the quasi-static and retarded potentials consider the error e(t) in the numerator when assuming the quasi-static approach is valid, i.e.

$$e(t) = \rho(t) - \rho(t-r/v). \qquad (2.28)$$

(It clearly makes little difference whether it is $\underset{\sim}{J}$ or ρ which is considered). Let the charge density at the point $\underset{\sim}{r}$, for which the error is being calculated, be decomposed into a sum of Fourier components of which one component has a frequency ω and has its magnitude normalised to unity. Then

$$e_\omega(t) = \cos\omega t - \cos\omega(t-r/v) \tag{2.29}$$

where e_ω means the error in the ω frequency component. The error varies with time. To gain a representative value for the error consider $\bar{e}_\omega$, the RMS (root mean square) value of the error as a fraction of the RMS value of the variation in charge density, i.e.

$$\bar{e}_\omega = \left\{ \int_0^T \left[\cos\omega t - \cos\omega(t-r/v)\right]^2 dt \Big/ \int_0^T \left[\cos^2\omega t\right] dt \right\}^{\frac{1}{2}} \tag{2.30}$$

where $T = 2\pi/\omega$. The denominator is readily evaluated as π/ω and the use of trignometric identities shows that the numerator is $(4\pi/\omega)\sin^2(\omega r/2v)$. Thus

$$\bar{e}_\omega = 2\sin(\omega r/2v). \tag{2.31}$$

The smaller the value of $\bar{e}_\omega$ over all frequencies and coordinates $\underset{\sim}{r}$ the better does the quasi-static potential represent the retarded potential. This is true when the frequency ω, the distance r and the reciprocal of the wave velocity v are small enough. From (2.24) the latter constraint implies low permittivity and low permeability.

The experiments reported in this thesis employed a saline solution (resistivity ≈ 150 Ω cm) for which $\varepsilon \simeq 78\ \varepsilon_o$ and $\mu \simeq \mu_o$, where ε_o and μ_o are the values of permittivity and permeability of free space. The maximum dimension was 0.1 and operating frequency f (= $2\pi/\omega$) was 62.5 kHz. These figures yield a value for $\bar{e}_\omega$ of 0.0023. As this is much less than unity it is evident, for the purposes of this thesis, that the retarded potential is well represented by the quasi-static potential, and therefore a conservative field approach is justified.

2.3.5 Current Flow in a Quasi-static Electric Field

The identification of a conservative field approach as a valid method of treating quasi-static electric fields means the previous discussion (cf. §2.3.3) of the static electric field in a conductor can be elaborated. Maxwell's Equations may be written in yet another form different from (2.13) and (2.22). For electric and magnetic fields varying sinusoidally with time (i.e. $\underset{\sim}{E}(t) = \underset{\sim}{E}\, e^{j\omega t}$, etc.) equation (2.13) gives (Ramo, Whinnery and van Duzer 1965 §4.08)

$$\nabla.\underset{\sim}{D} = \rho\ , \tag{2.32a}$$

$$\nabla.\underset{\sim}{B} = 0\ , \tag{2.32b}$$

$$\nabla\times\underset{\sim}{E} = -j\omega\underset{\sim}{B} \tag{2.32c}$$

and

$$\nabla\times\underset{\sim}{H} = \underset{\sim}{J} + j\omega\underset{\sim}{D}\ , \tag{2.32d}$$

where j is the square foot of -1.

Equations (2.31a-d) express Maxwell's equations in the frequency domain, and to emphasize the distinction it is often said that the term $e^{j\omega t}$ is "understood". The constitutive relations (2.14), when written in the frequency domain, are identical to (2.14) with $e^{j\omega t}$ understood.

Substituting the constitutive relations for $\underset{\sim}{J}$ and $\underset{\sim}{D}$ into (2.32d) and taking the divergence of both sides as in §2.3.3 yields

$$\nabla^2 V = -\nabla(\sigma+j\omega\varepsilon)\cdot\nabla V/(\sigma+j\omega\varepsilon), \tag{2.33}$$

where V is the voltage as before. It is important to realise that the field must be quasi-static to be able to put $\underset{\sim}{E} = -\nabla V$ and arrive at (2.33). This is the same as (2.19) but with the conductivity σ replaced by the complex conductivity $\sigma+j\omega\varepsilon$. Both conduction current and displacement current are allowed. Similar manipulations of (2.32c) lead directly to (2.18).

The conduction part of the complex conductivity is often compared to the displacement (imaginary) part to determine whether a particular medium is more like a conductor or a dielectric. For the experiments performed in this study (using the values for resistivity, permittivity and frequency given in §2.3.4), $\sigma = 0.67\ (\Omega m)^{-1}$ and $\omega\varepsilon = 0.00027$ Farads/metre-sec. Clearly the saline solution is almost totally resistive (the M.k.s. units of $(\Omega m)^{-1}$ and Farads/metre-sec are equivalent). This is also found in physiological systems at frequencies of interest (cf. Plonsey 1969 §5.2; Baker 1971 §1.3).

2.4 OTHER KINDS OF FIELDS

The conservative field equations derived in §2.2 can be applied to physical phenomena other than the electric and magnetic fields introduced in §2.3. In the following subsections the treatment of fluid flow, diffusion, heat conduction and gravitation is outlined.

2.4.1 Fluid Flow

In fluid mechanics consideration of the interaction between the normal and shear (tangential) stresses due to viscosity, the hydrostatic pressure, and the body forces on the fluid (gravity) yields a representation for the motion of the fluid (cf. Kaufmann 1963 §II.B.15). This is

$$\dot{\underset{\sim}{v}} = \underset{\sim}{F} - (\nabla p - \mu\nabla^2\underset{\sim}{v})/\rho\ , \tag{2.35}$$

where $\underset{\sim}{v}$, $\underset{\sim}{F}$, p, μ and ρ are the fluid velocity, body force per unit mass, pressure, viscosity and density respectively. $\underset{\sim}{\nabla}^2$ is the vector Laplacian operator which produces a vector whose components are the ordinary (scalar) Laplacians of the components of $\underset{\sim}{v}$. Equation (2.35) is called the Navier-Stokes Equation. It assumes that the flow is laminar (as opposed to turbulent) and that the fluid is incompressible, i.e.

$$\nabla.\underset{\sim}{v} = 0. \tag{2.36}$$

Laminar flow is assured in straight pipes if the Reynolds number (Re) is below 2,320 (Kaufmann 1963 §I.B.13). The Reynolds number is defined as

$$Re = \bar{v}\rho d/\mu \tag{2.37}$$

where $\bar{v}$ is the average velocity and d the pipe diameter. Thus low velocity and density, and high viscosity encourage laminar flow, but in practice flow i often not laminar. The restriction that the fluid be incompressible is a special case of the conservation of mass,

$$\rho + \nabla.(\rho\underset{\sim}{v}) = 0 , \tag{2.38}$$

when the density is kept constant. Liquids are very nearly incompressible, and in gasses the density variations are negligible provided the relative velo city of the gas near a solid is considerably smaller than the velocity of soun in the gas. This condition excludes sound waves.

The velocity $\underset{\sim}{v}$ given by (2.35) is not a conservative field because combining the identity

$$\underset{\sim}{\nabla}^2\underset{\sim}{v} = \nabla x\nabla x\underset{\sim}{v} - \nabla(\nabla.\underset{\sim}{v}) \tag{2.39}$$

with (2.35) and (2.36) shows that curl $\underset{\sim}{v}$ is not zero. Nevertheless, if the theory of laminar flow is applied to a circular pipe it is found that the aver velocity of flow, being the flow rate divided by the cross-sectional area, is proportional to the pressure gradient along the pipe (Kaufmann 1963 §I.8.12). (This is in contrast to turbulent flow where the mean velocity is nearly propor tional to the square root of the pressure gradient). The proportionality between mean velocity and pressure gradient is observed experimentally for the diffusion of fluid through a permeable medium (e.g. sand) and is expressed as (cf. Baden Fuller 1973 §9.8)

$$\underset{\sim}{v} = -k\nabla p \tag{2.40}$$

where $\underset{\sim}{v}$ is the superficial velocity (i.e. that observed outside the medium, k i the permeability and p the pressure. Equation (2.40) is called Darcy's Law and is normally valid for velocities less than 0.003 m/s (Kaufmann 1963 II.B.1 which is in accordance with the criteria for a low Reynolds number. Darcy's I

may be looked upon as representing the bulk properties of a fluid passing through many small interconnected vessels under conditions of laminar flow.

Substituting (2.40) into (2.36) gives

$$\nabla^2 p = -\nabla k.\nabla p/k \ , \tag{2.41}$$

which is again Poisson's Equation with dependent sources.

2.4.2 Diffusion and Heat Conduction

The transfer of heat by conduction and the diffusion of molecules from areas of high to low concentration are processes which are both due to random molecular motions. The relations governing these processes, which were originally determined from experimental observations on steady state systems (cf. Croft and Lilley 1977 §2.1; Crank 1970 §1.2), are

$$\underset{\sim}{q} = -k\nabla T \tag{2.42}$$

and

$$\underset{\sim}{F} = -D\nabla C. \tag{2.43}$$

T, k and $\underset{\sim}{q}$ are temperature, thermal conductivity and heat flow per unit area respectively, and $\underset{\sim}{F}$, D and C are rate of molecular transfer per unit area, diffusion coefficient and concentration of diffusing substance. Equation (2.42) is called Fourier's Law and (2.43) is Fick's 1st Law of Diffusion.

Consideration of conservation of energy in (2.42) and conservation of molecules in (2.43) yields (Croft and Lilley 1977 §2.2; Crank 1970 §1.3)

$$\nabla^2 T = (-H - \nabla k.\nabla T + \rho C_p \dot{T})/k \tag{2.44}$$

and

$$\nabla^2 C = (-\nabla D.\nabla C + \dot{C})/D \ , \tag{2.45}$$

where H, ρ and C_p are heat source density, mass density and specific heat at constant pressure. Equations (2.44) and (2.45) are called the Heat Conduction Equation and the Diffusion Equation respectively. In the steady state ($\dot{T} = \dot{C} = 0$) both of these reduce to Poisson's Equation, as given by (2.11). The Heat Conduction Equation contains the density of independent heat sources, which may arise for example from a chemical reaction in the material or from electromagnetic radiation interacting with the material and generating heat. There is no independent source density contained in the Diffusion Equation, as mass is conserved.

2.4.3 Gravitation

The magnitude of the force f of gravitation between two point masses m_1 and m_2 is given according to Newton's Law of Gravitation (cf. Wang 1979 §43) by

$$f = -Gm_1m_2/r^2 \ , \tag{2.46}$$

where f, G and r are the magnitude of the force, the gravitational constant and the separation of the masses respectively. The gravitational field $\underset{\sim}{g}$ is the force per unit mass and is given for a continuous medium by (cf. Wang 1979 §43)

$$\underset{\sim}{g} = \int_V -(G\rho/r^3)\underset{\sim}{r}\, dV \tag{2.47}$$

where ρ is the density of matter. The vector $\underset{\sim}{r}$ is directed from the point at which $\underset{\sim}{g}$ is being evaluated to the point in the intergrand, and r is the magnitude of $\underset{\sim}{r}$. The gravitational field is conservative since it is represented by the (negative) gradient of a scalar U, i.e.

$$\underset{\sim}{g} = -\nabla U \ , \tag{2.48}$$

where

$$U = -\int_V G\rho/r \, dV \tag{2.49}$$

and U is called the gravitational potential.

A flux density D may be defined by

$$\underset{\sim}{D} = -\underset{\sim}{g}/4\pi G. \tag{2.50}$$

The divergence of $\underset{\sim}{D}$, evaluated by substituting (2.47) into (2.50), taking the divergence and using the Divergence Theorem, is

$$\nabla\cdot\underset{\sim}{D} = \rho \ . \tag{2.51}$$

Combining (2.48), (2.50) and (2.51) gives

$$\nabla^2 U = 4\pi\rho G \ . \tag{2.52}$$

Equation (2.52) is Poisson's Equation, but in contrast to all of the previous examples there are no dependent sources. The difference here is that in Newtonian mechanics the gravitational constant G is indeed constant over all space, whereas in the previous examples the constitutive parameter depends on position. This makes (2.52) much more amenable to solution than the versions of Poisson's Equation with dependent sources.

2.5 TABULATED SUMMARY

The various equations encountered in §2.1 to §2.4 are tabulated in Table 2.1 for convenient comparison. The equations for one physical situation differ from another in only two ways (apart from the obvious use of different symbols):

(1) the source density is identically zero in some cases while not so in others, and

(2) the gravitational constant does not vary as a function of space whereas the other constitutive parameters often do.

2.6 INTEGRAL EQUATION REPRESENTATION

Poisson's differential equation (2.11) may be manipulated into an integral equation formulation which explicitly specifies the potential at one point as the sum (integral) of the contributions to that potential from all sources. This concept is used in §2.3.4 with the integral representation of the retarded potentials. The integral equation representation relies on the linearity of (2.11) with respect to potential, and of the knowledge of a solution to (2.11) when the source term consists only of a single point source. A general source distribution is then formed as a linear combination of suitable point sources, and the corresponding potential by the sum of the potentials due to the individual sources. This approach is called the Greens Function technique (cf. Morse and Feshbach 1953 §7).

2.6.1 Greens Function for Poisson's Equation

Consider that a point source is located at some point Q, and that the solution to (2.11) is required at some point P. Equation (2.11) is then written

$$\nabla^2 g(P,Q) = -\delta(P-Q) \quad . \tag{2.53}$$

P is called the observation point, Q is called the source point, δ is an n-dimensional delta function, and g(P,Q) is called a Greens Function. The actual form of g(P,Q) depends upon the equation for which it is chosen (in this case (2.53)). In two dimensions (n=2) the solution to (2.53) is (Morse and Feshbach 1953 §7.2).

$$g(P,Q) = -(1/2\pi)\ \ln R \tag{2.54}$$

where R is the distance between P and Q (see figure 2.2).

TABLE 2.1 SUMMARY OF CONSERVATIVE FIELDS AND THEIR EQUATIONS

		Electro-statics	Magneto-statics	Current Flow	Fluid Diffusion	Heat Flow	Molecular Diffusion	Gravitation
Field Intensity	$\underset{\sim}{F} = -\nabla\phi$	$\underset{\sim}{E} = -\nabla\phi$ electric field	$\underset{\sim}{H} = -\nabla\phi_m$ magnetic field	$\underset{\sim}{E} = -\nabla V$ electric field	$-\nabla p$ pressure gradient	$-\nabla T$ thermal gradient	$-\nabla C$ concentration gradient	$\underset{\sim}{g} = -\nabla U$ gravitational field
Potential	ϕ	ϕ electric potential	ϕ_m magnetic potential	V voltage	p pressure	T temperature	C concentration	U gravitational potential
Flux Density	$\underset{\sim}{D} = \lambda F$	$\underset{\sim}{D} = \varepsilon E$ electric flux density	$\underset{\sim}{B} = \mu H$ magnetic flux density	Ohm's Law $\underset{\sim}{J} = \sigma E$ current density	Darcy's Law $\underset{\sim}{v} = -k\nabla p$ velocity	Fourier's Law $\underset{\sim}{q} = -k\nabla T$ thermal flux density	Fick's 1st Law $\underset{\sim}{F} = -D\nabla C$ diffusion flux density	$\underset{\sim}{D} = -\underset{\sim}{g}/4\pi G$ gravitational flux density
Source Density	$\nabla.\underset{\sim}{D} = s$	$\nabla.\underset{\sim}{D} = \rho$ charge density	$\nabla.\underset{\sim}{B} = 0$	$\nabla.\underset{\sim}{J} = 0$	$\nabla.\underset{\sim}{v} = 0$	$\nabla.\underset{\sim}{q} = Q$ heat source density	$\nabla.\underset{\sim}{F} = 0$	$\nabla.\underset{\sim}{D} = \rho$ mass density
Constitutive Parameter	λ	ε permittivity	μ permeability	σ conductivity	k permeability	k thermal conductivity	D diffusion coefficient	G gravitational constant

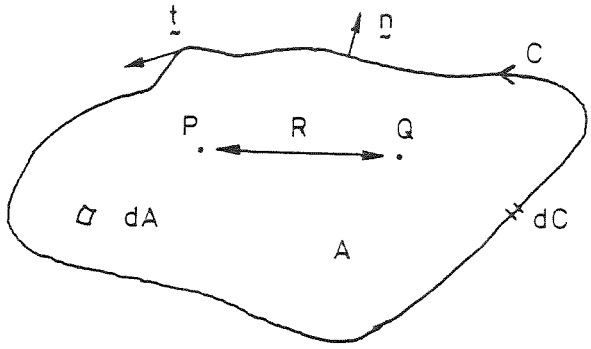

Figure 2.2 Definition of symbols used in 2 dimensions. Region A is enclosed by curve C. The unit normal to C is $\underset{\sim}{n}$, the unit tangent is $\underset{\sim}{t}$, and infinitesimal arc length is dC. The infinitesimal area in A is dA. P and Q are observation and source point respectively, separated by R and both anywhere in A.

This is readily verified by the folowing steps. Expanding the left hand side of (2.53) expanded in polar coordinates (r,θ) about P gives (cf. Ramo, Whinnery and van Duzer 1965 endpaper)

$$\nabla^2 g = (1/r)\,\partial(r\partial g/\partial r)/\partial r + (1/r^2)\,\partial^2 g/\partial\theta^2. \qquad (2.55)$$

Substituting (2.54) into (2.55) the term $\partial g/\partial r$ reduces to $-1/2\pi r$, and $\partial^2 g/\partial\theta^2$ is zero. Therefore, for $r\neq 0$ (2.55) reduces to zero. Thus for $Q\neq P$ (2.54) is the solution to (2.53).

Integrating the left hand side of (2.53) with respect to area and using the Divergence theorem gives

$$\int_A \nabla^2 g \; dA = \int_C \nabla g.\underset{\sim}{n} \; dC. \qquad (2.56)$$

The curve C and the area A it encloses are shown in figure 2.3. The vector $\underset{\sim}{n}$ is the unit normal to C, and is called $\underset{\sim}{n}_1$ on C_1 and so on. The choice of the area A to be a sector is not restrictive because the integral over A only has a value other than zero when Q coincides with P, in which case (integrating the right hand side of (2.53)) it should equal -1. Along C_1 and C_3 ∇g is perpendicular to $\underset{\sim}{n}_1$ and $\underset{\sim}{n}_3$ respectively and the contributions to the total integral along C is zero. Along C_2 the scalar product $\nabla g.\underset{\sim}{n}$ is $\partial g/\partial r$, which is $-1/2\pi r$ as before. Finally the arc length along C_2 is $rd\theta$, all of which gives

$$\int_A \nabla^2 g \; dA = \int_0^\alpha (-1/2\pi r)\,rd\theta. \qquad (2.57)$$

The right hand side reduces to $-\alpha/2\pi$.

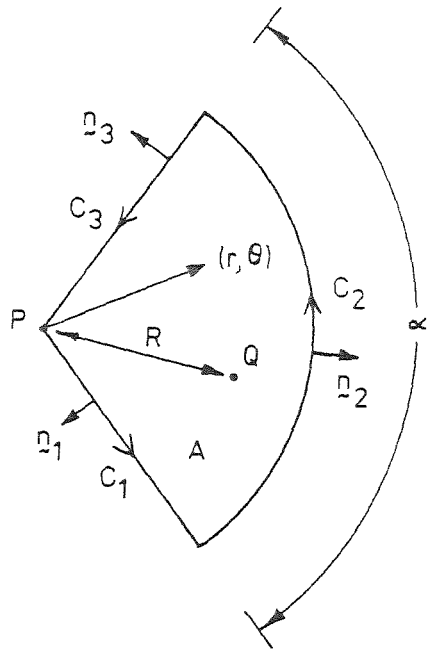

Figure 2.3 Sector shaped region A of angle α contains fixed observation point P and variable source point Q, separated by distance R.

Equation (2.57) only has unity magnitude if α is 2π and P is totally enclosed by A. In this case (2.54) is the solution to (2.53) when Q=P. If P is on the boundary of A the integral on the left hand side of (2.57) has magnitude less than unity. This is important when using the Greens Function approach to evaluate the potential on boundaries, since the Greens Function which is valid inside A must be multiplied by a constant for it to be valid on the boundary of A. If for instance the boundary is smooth at P then $\alpha = \pi$ and the right hand side of (2.57) reduces to $-\frac{1}{2}$, indicating that the Greens Function in (2.54) must be multiplied by the factor 2.

2.6.2 Equation for Continuously Varying Regions

The integral equation representation for the potential at P using the Greens Function approach is obtained by substituting the Greens Function and Poisson's Equation (2.11) into Greens Theorem (also called Greens 2nd Identity, cf. Morse and Feshbach 1953 §7.2). Greens Theorem is derived from the Divergence Theorem, and like the Divergence Theorem relates volume (area) integrals to closed surface (line) integrals. Consider the region A bounded by the curve C in figure 2.2 Applying the Divergence Theorem to the expression "$g\nabla\phi - \phi\nabla g$" in the region A gives

$$\iint_A \nabla.(g\nabla\phi-\phi\nabla g)\,dA = \int_C (g\nabla\phi-\phi\nabla g).\underset{\sim}{n}\,dC. \qquad (2.58)$$

Alternatively, expanding out the left hand side of (2.58) gives

$$\iint_A (\nabla g.\nabla\phi+g\nabla^2\phi-\nabla\phi.\nabla g-\phi\nabla^2 g)\ dA = \iint_A (g\nabla^2\phi-\phi\nabla^2 g)\ dA. \qquad (2.59)$$

Greens Theorem is obtained by equating the right hand of (2.57) with that of (2.58).

Substituting now for $\nabla^2\phi$ from Poisson's Equation into Greens Theorem gives

$$\iint_A \left\{-g(P,Q)\ \left[s(Q)+\nabla\lambda(Q).\nabla\phi(Q)\right]/\lambda(Q)\ -\ \phi(Q)\nabla^2 g(P,Q)\ \right\} dA$$

$$= \int_C \left[g(P,Q)\,\partial\phi(Q)/\partial n\ -\ \phi(Q)\,\partial g(P,Q)/\partial n\right] dC, \qquad (2.60)$$

where integrals over A and along C are with respect to source points Q. $\nabla\phi.\underset{\sim}{n}$ and $\nabla g.\underset{\sim}{n}$ have been written as $\partial\phi/\partial n$ and $\partial g/\partial n$ where n is the measure of length along the vector $\underset{\sim}{n}$. Rewriting (2.60) with the area integral separated into two terms gives

$$-\iint_A \phi(Q)\nabla^2 g(P,Q)\ dA = \iint_A g(P,Q)\left[s(Q)+\nabla\lambda(Q).\nabla\phi(Q)\right]/\lambda(Q)\ dA$$

$$+\int_C \left[g(P,Q)\,\partial\phi(Q)/\partial n\ -\ \phi(Q)\,\partial g(P,Q)/\partial n\right] dC. \qquad (2.61)$$

Substituting for $\nabla^2\ g(P,Q)$ from (2.53) means the left hand side becomes

$$\iint_A \phi(Q)\,\delta(P-Q)\ dA = \phi(P). \qquad (2.62)$$

Care must be taken when P is on the boundary C. Either a Greens Function different (by a multiplicative constant) from that valid within A must be used, or it must be realised that (2.61) will yield some fraction of $\phi(P)$. (see §2.6.1). When the correct Greens Function is chosen (2.61) simplifies to:

$$\phi(P) = \iint_A g(P,Q)\left[s(Q)+\nabla\lambda(Q).\nabla\phi(Q)\right]/\lambda(Q)\ dA$$

$$+\int_C \left[g(P,Q)\,\partial\phi(Q)/\partial n\ -\ \phi(Q)\,\partial g(P,Q)/\partial n\right] dC. \qquad (2.63)$$

In this way the potential at a point P is given as an integral of contributions to that potential from all sources within an area A, plus the contributions

from the potential and the normal gradient of the potential on the boundary C of region A.

It is not immediately clear that the integrals on the right hand side of (2.63) are well defined since they include a singularity at Q=P. Consider first the area integral of the circular region A of radius α centred on P as shown in figure 2.4.

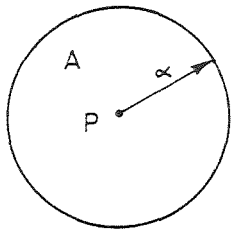

Figure 2.4: Small region A of radius r=α centred on the observation point P.

When the radius α is very small, the sources do not change appreciably over A. The total source term is then suitably represented by an average source densit $\bar{S}$, which can be taken outside the integral. Substituting from (2.54) for g(P,Q) and writing dA as rdrdθ, the integral becomes

$$-(\bar{S}/2\pi)\int_0^{2\pi}\int_0^{\alpha} r\ln r\ dr d\theta. \qquad (2.64)$$

The angular integral is 2π, and the radial integral remains bounded as r approaches zero (Spiegel 1968 §15.90) so (2.64) is well defined at the singularity.

Consider now the contour integral in (2.63) with reference to figure 2.5. Consider the integral along the curve C over the angle θ up to and including the singularity at P. Since θ is small, the curve is well represented by a circular arc, and the potential and normal gradient of potentia along the arc are suitably approximated by averages $\bar{\phi}$ and $\partial\bar{\phi}/\partial n$ respectively. Substituting these averages and the Greens Function into the contour integral and using the chain rule to expand the factor $\partial g/\partial n$ gives

$$(1/2\pi)\left\{-\partial\bar{\phi}/\partial n\int_C [\ln r]\, dC+\bar{\phi}\int_C [(\partial \ln r/\partial r)\partial r/\partial n]\, dC\right\}. \qquad (2.65)$$

From the geometry of figure 2.5, $r = 2\alpha\sin(\theta/2)$ which means $\partial r/\partial n = \partial r/\partial\alpha = 2\sin(\theta/2) = r/\alpha$. Substituting for r in the 1st integral of (2.65) and using $dC = \alpha d\theta$ gives

$$\int_{\theta_1}^{\theta_2} \ln\left[2\alpha\sin(\theta/2)\right] d\theta, \tag{2.66}$$

which remains bounded as θ_1 goes to zero (Spiegel, 1968, §15.102).

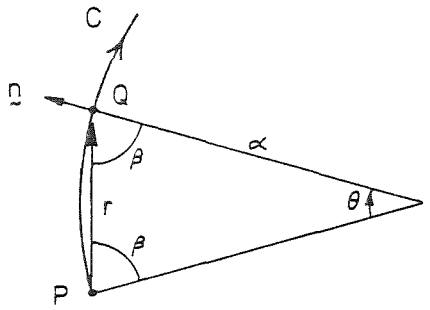

Figure 2.5: Small segment of curve C, close to observation point P, which is well represented by an arc of radius α.

Substituting similarly into the second integral of (2.65) gives

$$\int_{\theta_1}^{\theta_2} (1/r)(r/\alpha)\alpha d\theta = \int_{\theta_1}^{\theta_2} d\theta \tag{2.67}$$

which is also bounded as θ_1 approaches zero. Thus all the integrals on the right hand side of (2.63) are well behaved at Q=P even though the Greens Function has a singularity there.

2.6.3 Equation for Piecewise Homogeneous Regions

Frequently it is convenient to consider an inhomogeneous region to be composed of a number of smaller regions, each homogeneous but with a different value of the constitutive parameter (λ) than the others. This situation occurs both in geophysical applications where the earth is at times considered as horizontally stratified (cf. Keller and Fischknecht 1966 §23), and in biophysical applications where the various organs, tissues and fluids have differing conductivities (Plonsey 1969 §6.14; Geddes and Baker 1967). In these cases (2.63) simplifies, since the contribution to the potential from current flowing across conductivity variations only occurs at the discontinuities in conductivity, and not over the total region.

Consider the region A bounded by the curve C_1 in figure 2.6. Region A is separated by the curve C_2 into two homogeneous regions A_1 and A_2. The constitutive parameter in A_1 is λ_1 and in A_2 is λ_2. Unit vectors tangential and normal to C_2 are $\underline{t}$ and $\underline{n}$ respectively. P and Q (not shown) are the source and observation point respectively, each anywhere in A. The potential due to the dependent sources in (2.63) is

$$\phi_d(P) = \iint_A g(P,Q)\,\nabla\lambda(Q)\,.\,\nabla\phi(Q)/\lambda(Q)\;dA. \tag{2.68}$$

λ varies only in the direction $\underset{\sim}{n}$ so that

$$\nabla\lambda(Q)\,.\,\nabla\phi(Q) = (\partial\lambda(Q)/\partial n)(\partial\phi(Q)/\partial n)\,. \tag{2.69}$$

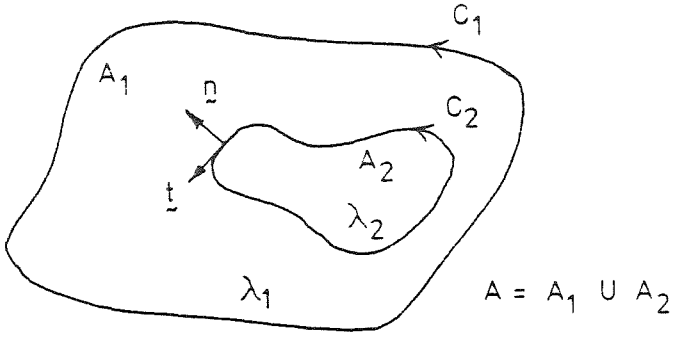

Figure 2.6: Piecewise homogeneous region A composed of two homogeneous regions A_1 and A_2. C_1 encloses A and C_2 encloses A_2. $\underset{\sim}{n}$ and $\underset{\sim}{t}$ are the unit normal and tangential to C_2.

In the vicinity of C_2 the element of area dA is conveniently written as dndt. Combining this with (2.68) and (2.69) gives

$$\phi_d(P) = \int_{C_2}\int_n g(P,Q)\left[1/\lambda^2(Q)\right]\partial\lambda(Q)/\partial n\left[\lambda(Q)\,\partial\phi(Q)/\partial n\right]\,dndt, \tag{2.70}$$

where the factor $1/\lambda$ has been written as λ/λ^2.

Here only the dependent sources are being considered so Gauss's Theore (2.9) gives

$$\int_\ell \underset{\sim}{D}.\underset{\sim}{\nu}\,d\ell = 0 \tag{2.71}$$

where $\underset{\sim}{D}$ is only the flux density due to dependent sources. Applying (2.71) to the curve ℓ enclosing a small region A' through which C_2 passes (see figure 2.7), gives

$$\int_{\ell_1} \underset{\sim}{D}.\underset{\sim}{\nu}_1\,d\ell_1 = \int_{\ell_2} \underset{\sim}{D}.\underset{\sim}{\nu}_2\,d\ell_2. \tag{2.72}$$

Using (2.6) and (2.7), $\underset{\sim}{D}$ is written as $-\lambda_1\nabla\phi_1.\underset{\sim}{\nu}_1$ in A_1 and $-\lambda_2\nabla\phi_2.\underset{\sim}{\nu}_2$ in A_2. Substituting these into (2.72) and allowing A' to shrink about C_2 yields at the boundary

$$\lambda_1\nabla\phi_1.\underset{\sim}{n} = \lambda_2\nabla\phi_2.\underset{\sim}{n}\ , \tag{2.73}$$

which says that the normal flux density is constant across the boundary (in the absence of independent sources). Thus the term $\lambda(Q)\partial\phi(Q)/\partial n$ is independent of n and can be removed from the integral over n in (2.70), so that

$$\phi_d(P) = \int_{C_2} \lambda(Q)\partial\phi(Q)/\partial n \int_n g(P,Q)\left[1/\lambda^2(Q)\right]\partial\lambda(Q)/\partial n \, dndt \qquad (2.74)$$

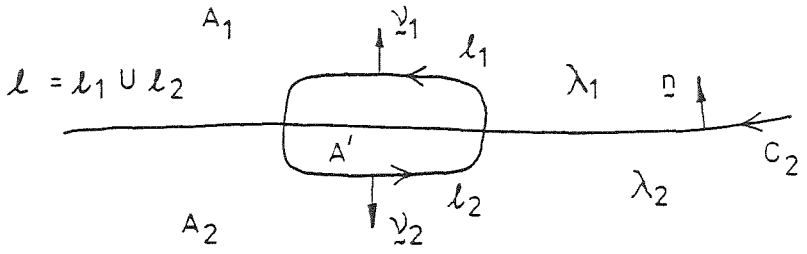

Figure 2.7: Small area A' through which boundary C_2 passes. Curve ℓ with normal $\underset{\sim}{\nu}_1$ in A_1 and $\underset{\sim}{\nu}_2$ in A_2 encloses A'.

The normal integral in (2.74) is simplified further when it is realised that $\left[1/\lambda^2(Q)\right]\partial\lambda(Q)/\partial n$ is a delta function, although not of unity magnitude. Clearly, for Q not on C_2, this term is zero because $\partial\lambda(Q)/\partial n = 0$ everywhere except on C_2, i.e.

$$\left[1/\lambda^2(Q)\right]\partial\lambda(Q)/\partial n = 0 \; ; \; Q \notin C_2 \; . \qquad (2.75)$$

The integral across C_2 in the normal direction is

$$\int_{n\in A_2}^{n\in A_1} \left[1/\lambda^2(Q)\right]\partial\lambda(Q)/\partial n \, dn \qquad (2.76)$$

which on change of variable of integration from n to λ gives

$$\int_{\lambda_2}^{\lambda_1} 1/\lambda^2(Q) \, d\lambda(Q) = (\lambda_1-\lambda_2)/\lambda_1\lambda_2 \; . \qquad (2.77)$$

Equations (2.75) to (2.77) show that $\left[1/\lambda^2(Q)\right]\partial\lambda(Q)/\partial n$ is a delta function with value only when Q is on C_2 and with magnitude $(\lambda_1-\lambda_2)/\lambda_1\lambda_2$. Thus the normal integral becomes $g(P,Q)(\lambda_1-\lambda_2)/\lambda_1\lambda_2$. Substituting this into (2.74) and putting arc length $dC_2 = dt$ gives

$$\phi_d(P) = (\lambda_1-\lambda_2)/\lambda_1\lambda_2 \int_{C_2} g(P,Q)\lambda(Q)\partial\phi(Q)/\partial n \, dC_2 . \qquad (2.78)$$

Clearly if $\lambda_1=\lambda_2$ there is no dependent source term and $\phi_d(P) = 0$.

The total potential from all sources in A is now given from (2.63) by

$$\phi(P) = \iint_A g(P,Q)s(Q)/\lambda(Q)\ dA + \int_{C_1} \left[g(P,Q)\partial\phi(Q)/\partial n - \phi(Q)\partial g(P,Q)/\partial n\right] dC_1 + (\lambda_1-\lambda_2)/\lambda_1\lambda_2 \int_{C_2} g(P,Q)\lambda(Q)\partial\phi(Q)/\partial n\ dC_2. \quad (2.79)$$

There is no limit to the number of subregions like A_2 that could be included within A. Each additional subregion adds another expression like (2.78) (with appropriate changes to the subscripts) onto (2.79). When there are no independent sources (2.79) reduces to contour integrals alone (surface integrals if operating in three dimensions). This reduction in dimensionality is a great advantage when evaluating the potential numerically as the computational effort is substantially lessened.

There is an interesting alternative derivation of (2.79). It makes use of the integral equation (2.63) with $\nabla\lambda=0$, which is applied to the regions A_1 and A_2 in turn. Continuity of normal current (2.73) and voltage at the boundary between the regions leads to two equations which combine to give (2.79). Such treatments are given by Plonsey (1969 §5.12), Metz and Pilkington (1969) and Martin and Pilkington (1972).

2.7 LAPLACES EQUATION

Laplace's Equation (2.12) is much easier to solve than Poisson's Equation (2.11) because there are neither dependent nor independent sources. In many practical situations the region under consideration may be divided into subregions in each of which Laplace's Equation holds. In §2.6.3 this approach leads to a simplification of the equations involved. One of the greatest advantages of using Laplace's Equation is that much is already known of general solutions in many coordinate systems. Also, conformal mapping techniques allow (in two dimensions) the solutions applicable to simple geometries to be utilised in more complicated geometries.

2.7.1 Separation of Variables

The method of solution of partial differential equations known as separation of variables depends not only upon the equation being solved but

also upon the coordinate system in which separation is being performed. The method breaks the single partial differential equation into more than one ordinary differential equation. Each ordinary differential equation must then be solved. When such a separation is possible in a particular coordinate system the partial differential equation is called separable in that coordinate system. Many equations arising from the mathematical description of physical systems are separable in more than one coordinate system. Laplace's Equation is separable in thirteen three-dimensional coordinate systems (Morse and Feshback 1953 Ch.5 tables) and in two dimensions is separable in any coordinate system which is derived from rectangular coordinates by a conformal transformation. Conformal transformations are discussed in §2.7.2.

In the following chapters the analysis of current flow in conductors is performed exclusively in two dimensions. In a two-dimensional polar coordinate system, with radial component r and angular component θ (see figure 2.8), Laplace's Equation becomes (cf. Ramo, Whinnery and van Duzer 1965 endpaper)

$$\nabla^2\phi = (1/r)\partial(r\partial\phi/\partial r)/\partial r + (1/r^2)\partial^2\phi/\partial\theta^2 = 0 \qquad (2.80)$$

Postulating a solution in the form $\phi(r,\theta) = R(r)\,\Theta(\theta)$ and substituting into (2.80) yields on rearrangement

$$(r/R)\partial R/\partial r + (r^2/R)\partial^2 R/\partial r^2 + (1/\Theta)\partial^2\Theta/\partial\theta^2 = 0, \qquad (2.81)$$

which separates as a result of the independence of Θ and R, giving

$$(r/R)\partial R/\partial r + (r^2/R)\partial^2 R/\partial r^2 = m^2 \qquad (2.82)$$

and

$$(1/\Theta)\partial^2\Theta/\partial\theta^2 = -m^2 . \qquad (2.83)$$

The value of the separation constant m^2 is arbitrary, which means the solutions to the ordinary differential equations (2.82) and (2.83) vary according to the value chosen for m. Calling these solutions R_m and Θ_m, it follows that (Morse & Feshback 1953 §6.3)

$$\Theta_m(\theta) = A_m \cos m\theta + B_m \sin m\theta, \qquad (2.84)$$

$$R_o(r) = a_o + b_o \ln r \qquad (2.85a)$$

and

$$R_m(r) = a_m r^m + b_m r^{-m} \quad ; \; m>0. \qquad (2.85b)$$

There is a multiplicity of solutions to (2.81) in the form $\phi_m(r,\theta) = R_m(r)\Theta_m(\theta)$. The $\phi_m(r,\theta)$ are <u>particular solutions</u> and the general solution is written as a linear combination of them, i.e.

$$\phi(r,\theta) = A_o(a_o+b_o \ln r) + \sum_{m=1}^{\infty} (a_m r^m + b_m r^{-m})(A_m \cos m\theta + B_m \sin m\theta). \qquad (2.86)$$

For a physically reasonable solution $\phi(r,\theta)$ must be analytic. This imposes constraints determining which of the particular solutions can be used in specific situations. Consider figure 2.8 where the origin O is enclosed in the region A, for which the solution is required. At the origin, $R_m(r)$ remains analytic only if all the b_m are zero. Similarly $\Theta_m(\theta)$ is analytic only if $\Theta(\alpha) = \Theta(\alpha+2\pi)$, which means m must be an integer. Thus the particular solutions which give an analytic solution are

$$\phi_o(r,\theta) = a_o A_o \qquad (2.87a)$$

and

$$\phi_m(r,\theta) = a_m r^m (A_m \cos m\theta + B_m \sin m\theta) \quad ; m \varepsilon N, \qquad (2.87b)$$

and the analytic solution is

$$\theta(r,\theta) = a_o A_o + \sum_{m=1}^{\infty} a_m r^m (A_m \cos m\theta + B_m \sin m\theta). \qquad (2.88)$$

The $\phi_m(r,\theta)$ in (2.87) are called the <u>eigenfunctions</u> for the situation represented in figure 2.8. However if the solution is required only in the region A_1 (i.e. excluding r=0) then the b_m are not constrained to be zero and the eigenfunctions contain terms in $\ln r$ and r^{-m}. In this situation the analytic solution is given by (2.86).

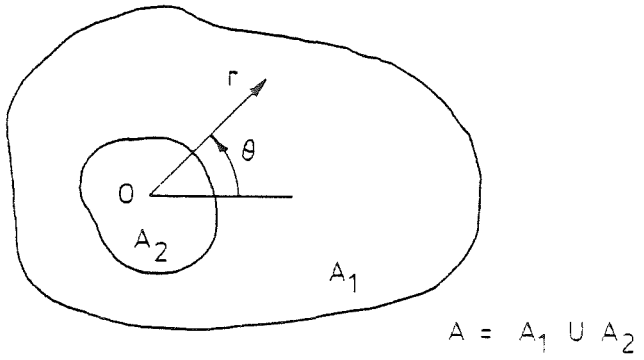

Figure 2.8: Polar coordinates r,ϑ in 2 dimensions. The origin O is in A_2.

The solution $\phi(r,\theta)$ for any specific situation is found by requiring the solution to match the boundary conditions which apply to that situation. In this way the coefficients a_m, b_m, A_m and B_m are evaluated and $\phi(r,\theta)$ is uniquely determined. Either Dirichlet or Neumann boundary conditions on a closed boundary specify a unique solution to Laplace's Equation (Morse and Feshbach 1953 §6.2).

2.7.2 Conformal Mapping

Conformal mapping is of particular use for the solution of Laplace's Equation in two dimensions since it allows the solutions formulated for simple geometries to be transformed and applied to more complicated geometries. It arises from the theory of analytic functions of a complex variable. A function of a complex variable is said to be analytic at a point if its derivative there is independent of the direction in which it is taken (cf. Kreyszig 1972 §11.2). As a direct consequence of analyticity the real and imaginary parts of the analytic function

$$w(z) = u(x,y) + iv(x,y) \tag{2.89}$$

satisfy the partial differential equations called the Cauchy Riemann Equations (Kreyszig 1972 §11.3), i.e.

$$\partial u/\partial x = \partial v/\partial y \tag{2.90a}$$

and

$$\partial u/\partial y = -\partial v/\partial x. \tag{2.90b}$$

Here 'i' is the square root of -1. Any analytic function which has a finite derivative not equal to zero is called a conformal mapping (Kreyszig 1972 §12.2). The condition that the derivative is not zero is sufficient to ensure the mapping is one to one (injective) within a small enough neighbourhood around a point. This means that in that neighbourhood the inverse mapping

$$z(w) = x(u,v) + iy(u,v) \tag{2.91}$$

also exists, is conformal and satisfies the Cauchy Riemann Equations as

$$\partial x/\partial u = \partial y/\partial v. \tag{2.92a}$$

and

$$\partial x/\partial v = -\partial y/\partial u. \tag{2.92b}$$

Consider the effect on a curve C in the z-plane (figure 2.9) when conformally mapped onto the curve C' in the w-plane (cf. Kreyszig 1972 §12.2). A parameter t defines C, along which z=z(t). The tangent at some point $z_o=z(t_o)$ on C is $dz/dt\big|_{t_o}$. In the w-plane the corresponding curve C' is given by w=w(z(t)) and the tangent at $w(z_o)$ is, by the chain rule,

$$dw/dt\big|_{t_o} = (dw/dz)(dz/dt)\big|_{t_o} . \tag{2.93}$$

dw/dz is not zero so C' has a unique tangent. Expressing each of the terms of (2.93) in polar form ($dw/dt\big|_{t_o} = \rho e^{i\phi}$; $dw/dz\big|_{z_o} = \alpha e^{i\psi}$; $dz/dt\big|_{t_o} = re^{i\theta}$) gives

$$\rho e^{i\phi} = \alpha r e^{i(\theta+\psi)} . \tag{2.94}$$

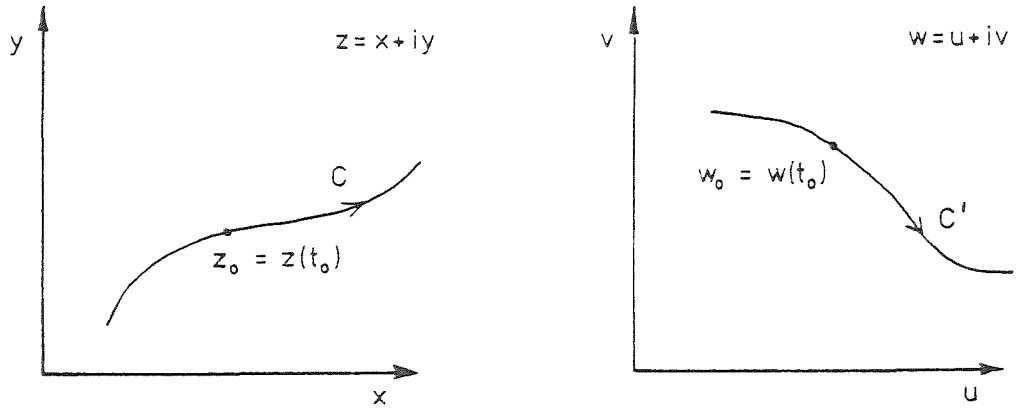

Figure 2.9: Curve C in the z-plane conformally maps to curve C' in the w-plane. z_o on C maps to w_o on C'.

Thus the curve C maps onto C' at t_o by undergoing a local rotation of ψ and a local stretch of α. The curve C is arbitrary. So any curve going through z_o is mapped (only at z_o) with the same rotation and stretch. Therefore the angle between two curves intersecting at z_o is preserved under the transformation.

Consider now the effect of conformally mapping two adjacent regions A_1 and A_2 in figure 2.10 from the z-plane into A_1' and A_2' in the w-plane. The boundary between A_1 and A_2 is cut perpendicularly at z_o by a curve C. C and z_o map to C' and w_o. In each region in the z-plane there is a functior h(x,y) which satisfies Laplace's Equation; i.e.

$$\nabla^2 h_1(x,y) = \nabla^2 h_2(x,y) = 0. \qquad (2.95).$$

The functions h_1 and h_2 are found by some unspecified means (perhaps separatic of variables) and at the common boundary satisfy the boundary equations for continuity of potential and continuity of normal flux (2.73), i.e.

$$h_1(z_o) = h_2(z_o) \qquad (2.96a)$$

and

$$\lambda_1 dh_1/dt\big|_{t_o} = \lambda_2 dh_2/dt\big|_{t_o}, \qquad (2.96b)$$

where the parameter t defines C as before. The regions A_1 and A_2 map conform ally by the same transformation w=w(z) onto A_1' and A_2' in the w-plane, in which the functions g(u,v) corresponding to h(x,y) are

$$g_1(u,v) = h_1(x,y) \tag{2.97a}$$

and

$$g_2(u,v) = h_2(x,y). \tag{2.97b}$$

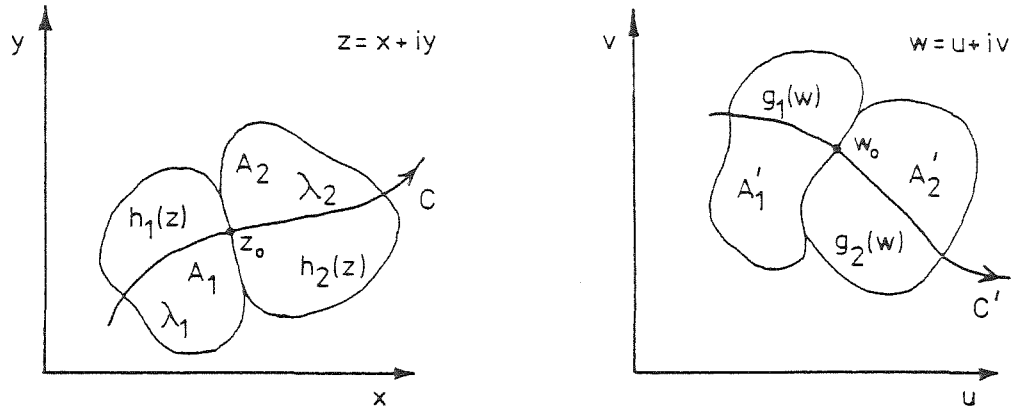

Figure 2.10: Regions A_1 and A_2 in the z-plane map to A_1' and A_2' respectively in the w-plane. C cuts perpendicularly the boundary between A_1 and A_2 at z_o. C maps to C' and z_o maps to w_o.

In the w-plane

$$\nabla^2 g(u,v) = \partial^2 h(x,y)/\partial u^2 + \partial^2 h(x,y)/\partial v^2 \tag{2.98}$$

where g represents g_1 in region A_1' and g_2 in A_2'. Substituting $x = x(u,v)$ and $y = y(u,v)$ from (2.91), and differentiating using chain and product rules, yields on rearrangement

$$\nabla^2 g(u,v) = \frac{\partial^2 h}{\partial x^2}\left(\frac{\partial x}{\partial u}\right)^2 + \frac{\partial^2 h}{\partial y^2}\left(\frac{\partial y}{\partial u}\right)^2 + \frac{\partial^2 h}{\partial x^2}\left(\frac{\partial x}{\partial v}\right)^2 + \frac{\partial^2 h}{\partial y^2}\left(\frac{\partial y}{\partial v}\right)^2$$

$$+ \frac{\partial h}{\partial x}\left(\frac{\partial^2 x}{\partial v^2} + \frac{\partial^2 x}{\partial u^2}\right) + \frac{\partial h}{\partial y}\left(\frac{\partial^2 y}{\partial u^2} + \frac{\partial^2 y}{\partial v^2}\right) . \tag{2.99}$$

The last two parentheses of (2.99) are identically zero, which is verified by suitably differentiating the Cauchy Riemann Equations (2.92). Rearranging the remaining terms and substituting for $\partial y/\partial u$ and $\partial y/\partial v$ from (2.92) gives the term

$$\left[\partial^2 h/\partial x^2 + \partial^2 h/\partial y^2\right]\left[(\partial x/\partial u)^2 + (\partial x/\partial v)^2\right] . \tag{2.100}$$

But $\nabla^2 h(x,y)$ is identically zero because it satisfies Laplace's Equation (2.95) by definition. Hence all terms on the right hand side of (2.99) are zero and

$$\nabla^2 g(u,v) = 0. \tag{2.101}$$

Thus $g_1(u,v)$ and $g_2(u,v)$ also satisfy Laplace's Equation (2.101).

Since the same conformal mapping is used for both A_1 and A_2, it follows from (2.97) that the values of $g(u,v)$ at w_o are

$$g_1(w_o) = h_1(z_o) \tag{2.102a}$$

and

$$g_2(w_o) = h_2(z_o). \tag{2.102b}$$

Use of the Dirichlet boundary condition (2.96a) shows that

$$g_1(w_o) = g_2(w_o). \tag{2.103}$$

Thus $g_1(u,v)$ and $g_2(u,v)$ satisfy the same Dirichlet boundary condition as $h_1(x,y)$ and $h_2(x,y)$.

Also, the curve C remains normal to the boundary under the transformation. Using (2.93) the normal derivatives of $g(u,v)$ at w_o are

$$dg_1/dt\big|_{t_o} = (dw/dz)(dh_1/dt)\big|_{t_o} \tag{2.104a}$$

and

$$dg_2/dt\big|_{t_o} = (dw/dz)(dh_2/dt)\big|_{t_o}. \tag{2.104b}$$

Use of the Neumann boundary condition (2.96b) shows that

$$\lambda_1 dg_1/dt\big|_{t_o} = \lambda_2 dg_2/dt\big|_{t_o}. \tag{2.105}$$

Thus $g_1(u,v)$ and $g_2(u,v)$ satisfy the same Neumann boundary condition as $h_1(x,y)$ and $h_2(x,y)$.

Equations (2.101), (2.103) and (2.105) imply that $g_1(u,v)$ and $g_2(u,v)$ are the solutions to Laplace's Equation in A_1' and A_2' which satisfy the same boundary conditions between the regions as the solutions $h_1(x,y)$ and $h_2(x,y)$ do between A_1 and A_2. Notice however that if the Neumann boundary condition is artificially imposed upon some part of A_1 it must be scaled by dw/dz before being imposed upon A_1'. Otherwise the solutions g_1 and g_2 mapped from h_1 and h_2 are not the correct solutions in the w-plane. However with a little care piecewise solutions to Laplace's Equation, satisfying a given set of boundary conditions, can be conformally mapped to a new set of coordinates and a new geometry. In the new geometry the piecewise solutions of Laplace's Equation

which satisfy the conformally mapped boundary conditions are exactly the same as the solutions conformally mapped from the original geometry. This enables a complicated geometry to be mapped to a simple geometry, the solution to Laplace's Equation to be found, and then mapped back to apply to the original geometry.

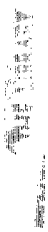

3. LIMITATIONS ON IMPEDANCE IMAGING

It is important to understand the limitations on impedance imaging in order that it can be used to the best possible advantage. The accuracy to which the conductivity can be found is limited because in practice all measurements contain some experimental error. Examined in this chapter are how limitations on the conductivity resolution and the spatial resolution are related to experimental error. The spatial resolution and conductivity resolution are each examined for three particular classes of conductivity distribution. The first of the classes is examined in §3.2, and conformal transformations are used in §3.3 to derive the latter two classes from the first.

3.1 INTRODUCTION

It is necessary to first define what is meant here by the limits on the conductivity resolution and spatial resolution. Consider therefore the conductivity distribution shown in figure 3.1. The region R is divided into two subregions R_a and R_b, in which the conductivity is σ_a and σ_b respectively. R_a is called the anomaly. The surface of R is S. The voltage at point P on S is V(P), and the current density normal to S is J(P). Individually V(P) and J(P) are referred to as the voltage distribution and current density distribution respectively. Collectively V(P) and J(P), or any useful parameters derived from them (such as the apparent resistivity), are called the measurements.

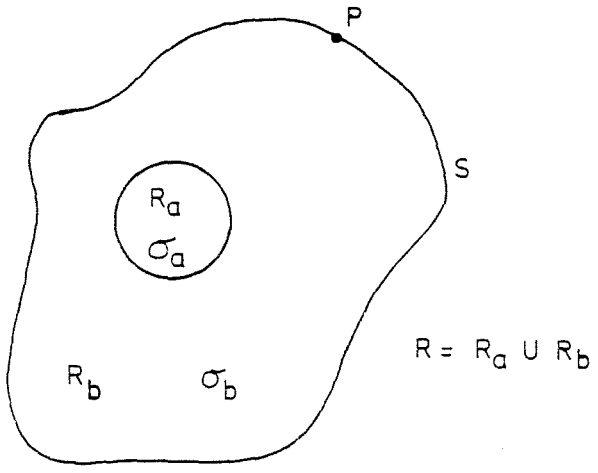

Figure 3.1: Conductivity distribution in region R. Subregion R_a (the anomaly) has conductivity σ_a, and subregion R_b has conductivity σ_b. P is a point on the surface S along which measurements are made.

Suppose that two sets of measurements are taken; one when σ_a is differe from σ_b, and one when σ_a equals σ_b. If the difference between the two sets o measurements is smaller than the experimental error then it is not possible to determine from the measurements whether or not there is an anomaly within R. maximum size of anomaly at which this occurs represents the limit on the spati resolution.

Suppose now that two more sets of measurements are taken; one when σ_a = and one when σ_a has been changed slightly to $\sigma_a = \sigma+\Delta\sigma$. If the difference be the two sets of measurements is less than the experimental error then the two different values of conductivity cannot be resolved. The maximum change in ductivity $\Delta\sigma$ for which this occurs represents the limit of the conductivity r ution.

The anomaly may be of any size and conductivity, and may be anywhere i The spatial resolution and conductivity resolution are therefore functions of position and conductivity of the anomaly.

3.2 THE CIRCULARLY SYMMETRIC CONDUCTIVITY DISTRIBUTION

Shown in figure 3.2 is a circularly symmetric conductivity distributic The circular region R has radius r_b, and has its centre at the origin O. Pc in R have radial and angular coordinates r and θ respectively. Within R is circular region R_a (the anomaly). The centre of R_a is at O, and the radius is r_a. The annular region between r_a and r_b is called R_b. Regions R_a and have conductivities σ_a and σ_b respectively.

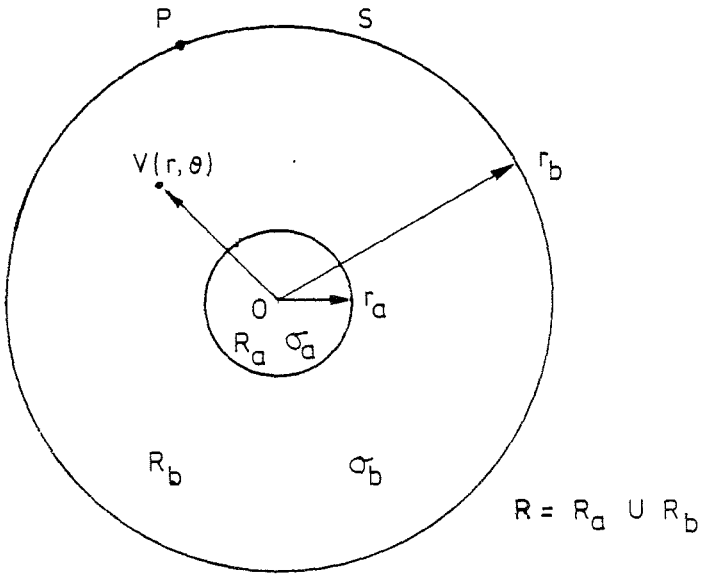

Figure 3.2: Simple circularly symmetric conductivity distribution. Polar coordinates r,θ with origin O are used within R. The voltage in R is V(r,θ).

Laplace's Equation (2.12) describes the voltage $V(r,\theta)$ in each of R_a and R_b. On the boundary S (i.e. at $r=r_b$) Fourier series are introduced to represent the voltage V(P), and the current density normal to S, J(P). These are

$$V(P) = V(r_b, \theta) = \sum_{n=o}^{\infty} U_n \cos n\theta + V_n \sin n\theta \qquad (3.1)$$

and

$$J(P) = J(r_b, \theta) = \sum_{n=o}^{\infty} I_n \cos n\theta + J_n \sin n\theta \qquad (3.2)$$

respectively. There are no current sources in R and the voltage must remain finite everywhere in R.

On appealing to the general solution for Laplace's Equation (2.86), it is seen that

$$V(r,\theta) = \sum_n A_n r^n \cos n\theta + A'_n r^n \sin n\theta \; ; \qquad r \leq r_a \qquad (3.3)$$

and

$$V(r,\theta) = \sum_n (B_n r^n + C_n r^{-n}) \cos n\theta + (B'_n r^n + C'_n r^{-n}) \sin n\theta \; ; \; r_a \leq r \leq r_b . \qquad (3.4)$$

The boundary conditions (3.1) and (3.2) at $r=r_b$, and the conditions for continuity of both the normal current density and the voltage across the boundary at $r=r_a$ allow the unknown coefficients $A_n, A'_n, B_n, B'_n, C_n$ and C'_n in (3.3) and (3.4) to be eliminated. The result is

$$z_{nn} = V_n/J_n = U_n/I_n = -(r_b/n\sigma_b)\left[(1+\alpha)+(1-\alpha)\beta^n\right]/\left[(1+\alpha)-(1-\alpha)\beta^n\right] \qquad (3.5)$$

where the "impedance" z_{nn} has been introduced for later convenience, and $\alpha=\sigma_a/\sigma_b$ and $\beta=(r_a/r_b)^2$. Here α is called the conductivity contrast.

Equation (3.5) can be written as

$$V_m = \sum_{n=1}^{\infty} z_{mn} J_n \qquad (3.6)$$

where in the particular situation represented by (3.5), the z_{mn} are zero except for m=n. Suppose V_m and J_n in (3.6) represented the node voltages and node currents respectively of a discrete electric network, then the z_{mn} would be transfer impedances for $m \neq n$, and would be driving point impedances for m=n (cf. Skilling 1974 Ch.9). It is convenient to use the terminology of discrete electric networks, thus the z_{nn} in (3.5) and (3.6) are called driving point impedances, and the z_{mn}, for $m \neq n$, in (3.6) are called transfer impedances Whereas with discrete networks the nodes are physically separated, here each of the "nodes" is distributed over the entire surface S. Instead of the

physical position it is the linear independence of the voltage and current density distributions represented by V_m and J_m which separate one "node" from another.

It is important to note in (3.5) that a particular Fourier component of voltage (V_n or U_n) equals the same Fourier component of current density (I_n or J_n) multiplied by the driving point impedance z_{nn}. The inverse Fourier transform of a product of two functions is equal to the convolution of the inverse Fourier transforms of each function separately. Therefore the voltage distribution $V(r_b, \theta)$ is equal to the current distribution $J(r_b, \theta)$ convolved with the inverse Fourier transform of the driving point impedances. Furthermore, from a single voltage distribution and current distribution, all of the driving point impedances can be found. Once the z_{nn} are known the electrical response of the region to any voltage or current distribution impressed on S is fully characterised.

3.2.1 Visibility and Spatial Resolution

When making measurements on a conductivity distribution it is important to know the minimum size of anomaly which can be detected by the measurements within the accuracy to which they are made. This size defines the limit of spatial resolution of the measurement system.

Suppose that measurements are made at the boundary S shown in figure 3.2 when the anomaly is not present (i.e. $\sigma_a=\sigma_b$). Equation (3.5) reduces to

$$z_{nn}|_1 = -r_b/n\sigma_b, \tag{3.7}$$

where "$|_1$" means evaluated for $\alpha=1$. Define now the visibility Q_{mn} of the anomaly as

$$Q_{mn} = (z_{mn}-z_{mn}|_1)/(z_{kk}+z_{kk}|_1), \tag{3.8}$$

where k is the lesser of m and n. Q_{mn} is a measure of the difference betwe the measurements when the anomaly is present and when it is not present. Q_{mn} therefore represents the effect the presence of the anomaly has on the measurements.

When $m\neq n$ and the Fourier components V_m and J_n are independent it foll from (3.6) and (3.8), that the corresponding z_{mn} and Q_{mn} are zero. For thi reason it is only necessary here to examine the Q_{nn}. Furthermore, when V_m and J_n are independent for $m\neq n$ and a current boundary condition $J(r_b, \theta)$ is maintained on S irrespective of the conductivity in R, (3.8) reduces to

$$\left.\begin{aligned} Q_{mn} &= (V_n - V_n|_1)/(V_n + V_n|_1) \quad ; \quad m=n \\ Q_{mn} &= 0 \quad ; \quad m\neq n \end{aligned}\right\} \tag{3.8a}$$

Similarly, when a constant voltage boundary condition $V(r_b, \theta)$ is maintained on S, (3.8) reduces to

$$\left.\begin{aligned} Q_{mn} &= (J_n|_1 - J_n)/(J_n|_1 + J_n) \quad ; \quad m=n \\ Q_{mn} &= 0 \quad ; \quad m\neq n \end{aligned}\right\} \tag{3.8b}$$

When these constant boundary conditions apply it is easier to use (3.8a) or (3.8b) to calculate to Q_{mn}, since it is not necessary to calculate the z_{mn} first. It is worth keeping in mind that for the situations treated in Chapter 5 the Q_{mn} are not necessarily zero for $m\neq n$, which complicates matters appreciably.

In practice the z_{mn} cannot be determined exactly from measurements. Let $\hat{z}_{mn}$ be an estimate gained from experiment of the value of z_{mn}. The upper bound on the error in the experimental value is $\Delta\hat{z}_{mn}$, so that $-\Delta\hat{z}_{mn} < z_{mn} - \hat{z}_{mn} < \Delta\hat{z}_{mn}$. When the anomaly has little effect on the measurements it may not be possible, within the limits set by experimental error, to distinguish $\hat{z}_{mn}$ from $z_{mn}|_1$. Assume that the surface conductivity is known so that $z_{mn}|_1$ can be determined exactly. Then the difference between the actual visibility (i.e.(3.8)) and that calculated using $\hat{z}_{mn}$ as an estimate of z_{mn} is given approximately by

$$\Delta\hat{Q}_{mn} \simeq \Delta\hat{z}_{mn}/2\hat{z}_{kk}. \tag{3.9}$$

Equation (3.9) gives an estimate of the error in the visibility calculated from measurements. When the visibility Q_{mn} of the anomaly is less than $\Delta\hat{Q}_{mn}$ it is not possible, within the accuracy of the measurements, to distinguish the region R from a region with uniform conductivity.

For the simple conductivity distribution shown in figure 3.2 the visibility (for m=n) is found in terms of the size and conductivity of the anomaly by substituting (3.5) and (3.7) into (3.8). This gives

$$Q_{nn} = (1-\alpha)\beta^n/(1+\alpha). \tag{3.10}$$

Figure 3.3 shows Q_{11} and Q_{22} for different sizes and conductivities of anomaly. The visibility of the anomaly increases as the size of the anomaly increases ($\beta\to 1$) and as the conductivity contrast increases ($\alpha\to 0$, $\alpha\to\infty$).

The anomaly is also more visible at the lowest spatial frequencies (n→1), when the highest current density passes through the anomaly.

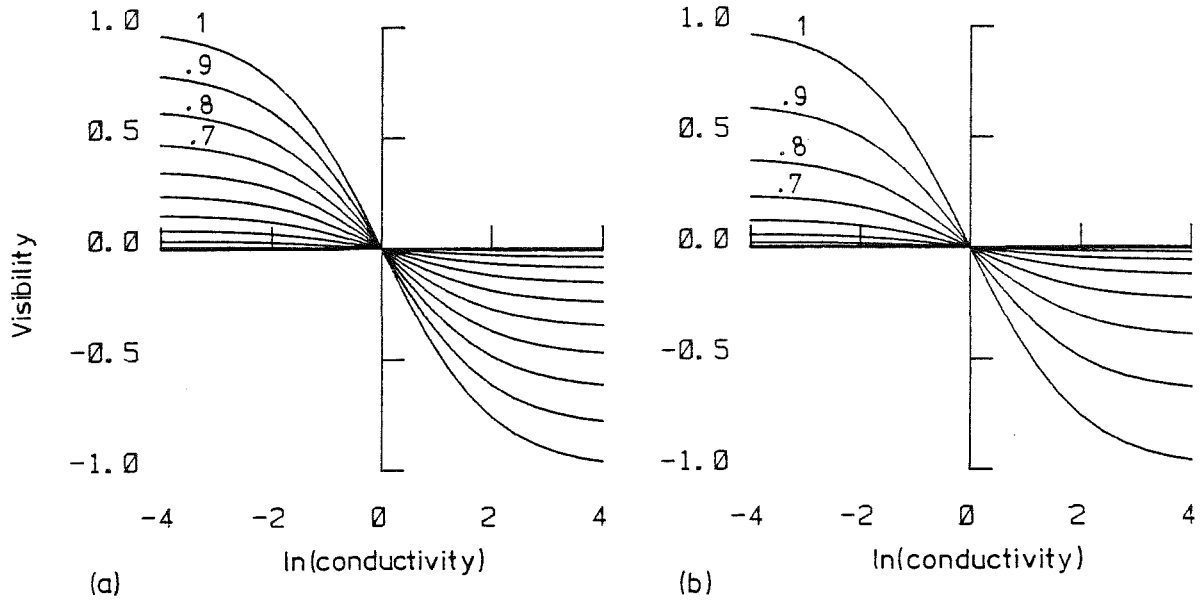

Figure 3.3: Visibility of the anomaly shown in figure 3.2. The curves shown are for the normalised radius of the anomaly (r_a/r_b) from 1.0 to 0.0 in steps of 0.1, plotted against the natural log of the conductivity contrast (σ_a/σ_b).

(a) Visibility to 1st order Fourier component, Q_{11}

(b) Visibility to 2nd order Fourier component, Q_{22}.

The maximum visibility possible for a particular size of anomaly is finite. This occurs when n=1 and α=0 or α=∞. The maximum visibility puts an absolute limit on the spatial resolution which can be obtained with impedance imaging systems. For instance, if the accuracy of measurements allows $\hat{z}_{11}$ to be obtained to within 2% then using (3.9) gives $\Delta\hat{Q}_{11}$ = 0.01. Thus (3.10) shows that the normalised radius r_a/r_b of the anomaly must exceed 0.1 for the anomaly to be detected, even if it is of infinite or zero conductivity.

3.2.2 Sensitivity and Conductivity Resolution

It is important to know not only the best spatial resolution which can be achieved when imaging conductivity distributions, but also the best conductivity resolution. This allows the accuracy to which the conductivity can be imaged to be estimated.

Consider therefore changes in the transfer impedances z_{mn} (see (3.5), (3.6) in §3.2) with respect to the conductivity contrast α. Let the

sensitivity S_{mn} of changes in z_{mn} to changes in α be defined by

$$S_{mn} = (\partial z_{mn}/z_{kk})/(\partial\alpha/\alpha) = (\alpha/z_{kk})\partial z_{mn}/\partial\alpha, \tag{3.11}$$

where k is the lesser of m and n. The partial differential notation "∂" is used to represent infinitesimal differences since the z_{mn} are also functions of the radius of the anomaly (see (3.5)). As with Q_{mn} in §3.2.1 it is only necessary here to examine S_{mn} for m=n. When $m\neq n$ and the Fourier components V_m and J_n are independent, and either a fixed current distribution or a fixed voltage distribution is maintained on S, then (3.11) reduces respectively to

$$S_{nn} = (\partial V_n/V_n)/(\partial\alpha/\alpha) \tag{3.11a}$$

or

$$S_{nn} = -(\partial J_n/J_n)/(\partial\alpha/\alpha). \tag{3.11b}$$

Suppose, for a small finite change in conductivity $\Delta\alpha$, that the corresponding changes in the transfer impedances are Δz_{mn}. For small changes in conductivity (i.e. $|\Delta\alpha/\alpha|<<1$) $\partial z_{mn}/\partial\alpha \simeq \Delta z_{mn}/\Delta\alpha$. When the errors $\Delta\hat{z}_{mn}$ in the estimates of the transfer impedances are small then $\hat{z}_{mn} \simeq z_{mn}$. The range over which the conductivity can vary without $\hat{z}_{mn}$ varying by more than $\Delta\hat{z}_{mn}$ is therefore

$$\Delta\alpha/\alpha \simeq (\Delta\hat{z}_{mn}/\hat{z}_{kk})/S_{mn}. \tag{3.12}$$

Equation (3.12) expresses the accuracy to which the conductivity can be determined in relation to the accuracy of the measurements.

For the conductivity distribution shown in figure 3.2, S_{nn} can be found by differentiating (3.5) with respect to α and substituting it into (3.11). This gives

$$S_{nn} = -4\alpha\beta^n/\left[(1+\alpha)^2-(1-\alpha)^2\beta^n\right]. \tag{3.13}$$

Figure 3.4 shows S_{11} and S_{22} for anomalies having various sizes and conductivities. The sensitivity of the measurements to changes in conductivity of the anomaly increases as the size of anomaly increases ($\beta\to1$), and as the conductivity contrast decreases ($\alpha\to1$). The sensitivity is also greatest at low spatial frequencies ($n\to1$).

The maximum sensitivity possible for a particular size of anomaly, which is found when n=1 and α=1, is finite. This puts a limit on the conductivity resolution which can be obtained for a particular spatial

spatial resolution (i.e. size of anomaly). For instance, suppose the accuracy of the measurements allows z_{11} to be obtained to within 2%, and the radius of the anomaly is known to be 0.5. Then $\Delta z_{11}/z_{11}$ is 0.02 and $\beta = 0.25$. Putting $\beta = 0.25$ and $\alpha=1$ in (3.13) gives the sensitivity $S_{11} = -0.25$. It then follows from (3.12) that the conductivity ratio is only accurate to within 8%.

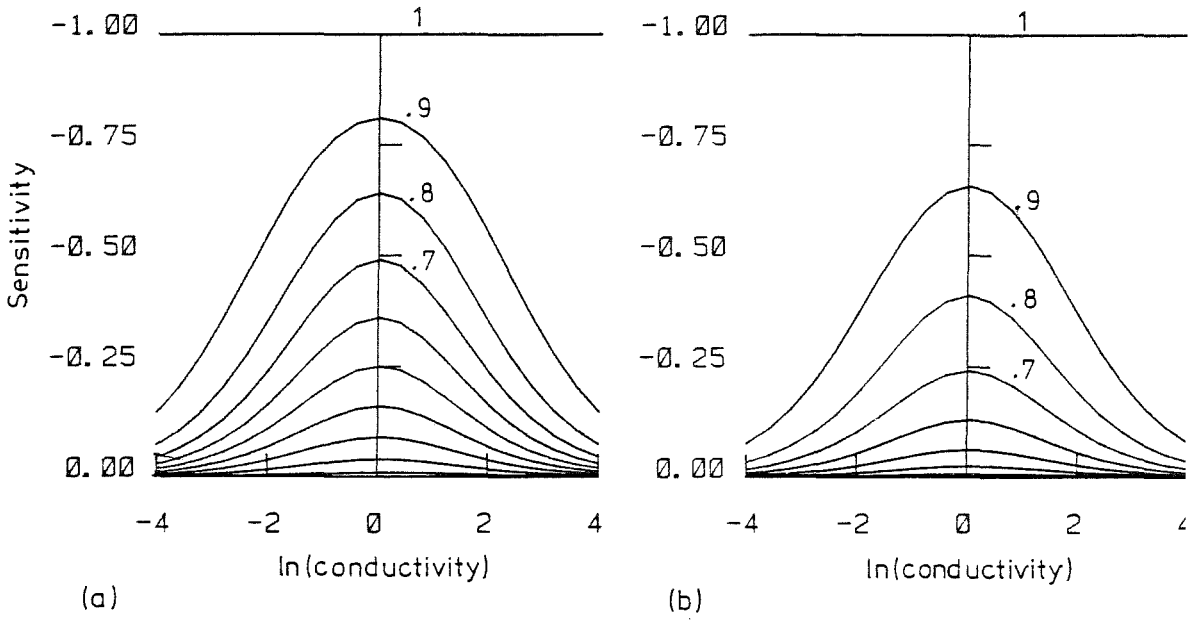

Figure 3.4: Sensitivity of measurements to changes in conductivity of the anomaly shown in figure 3.2. The curves shown are for the normalised radius of the anomaly (r_a/r_b) from 1.0 to 0.0 in steps of 0.1 plotted against the natural log of the conductivity contrast (σ_a/σ_b).

(a) Sensitivity to 1st order Fourier component, S_{11}.

(b) Sensitivity to 2nd order Fourier component, S_{22}.

3.3 CONFORMAL TRANSFORMATION TO OTHER CONDUCTIVITY DISTRIBUTIONS

In this section conformal transformations are used to relate the circularly symmetric class of conductivity distributions (see §3.2) to two further classes of conductivity distribution. In this way the sensitivity and visibility, and hence the conductivity resolution and spatial resolution, are found for the latter two classes.

Figure 3.5 illustrates the three classes of conductivity distribution. The "offset" conductivity distribution shown in figure 3.5b is of interest in medical imaging, where the total circumference of the region being imaged is accessible. The anomaly can be positioned at any radial coordinate.

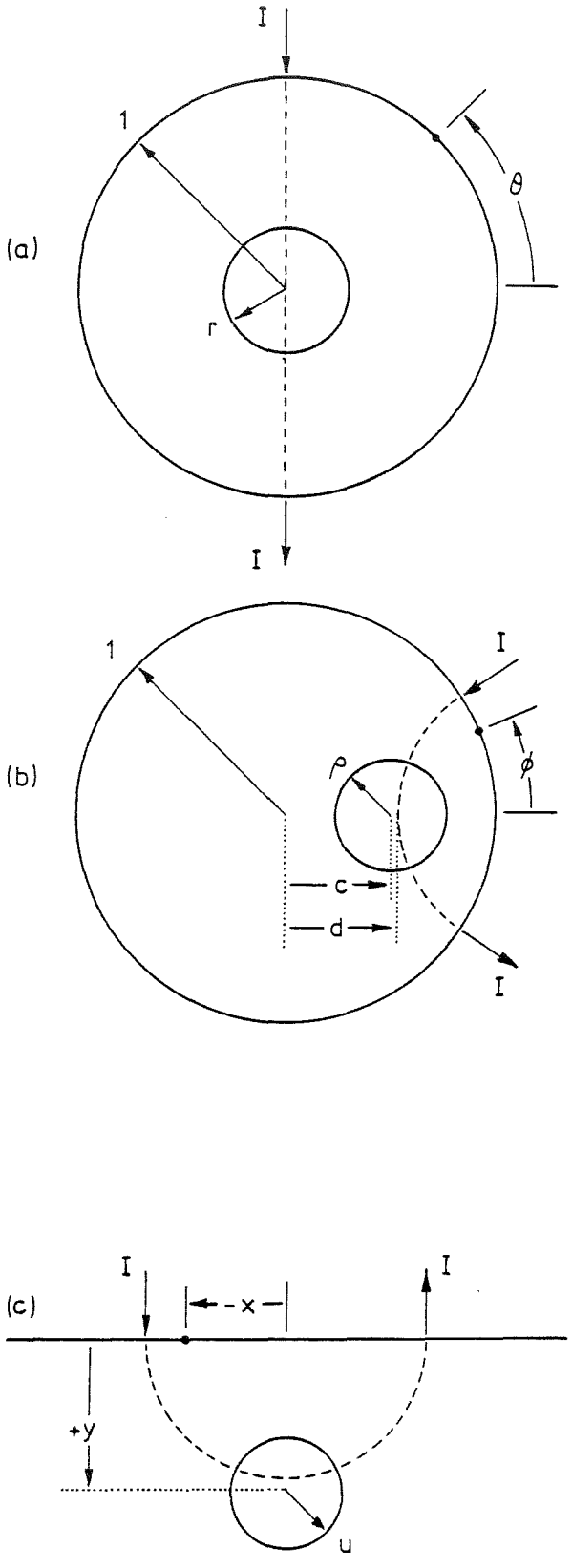

Figure 3.5: Two dimensional conductivity distributions related by conformal transformation.
(a) symmetric geometry, complex z-plane,
(b) offset geometry, complex w-plane,
(c) flat geometry, complex t-plane.

Point current sources and sinks are indicated by arrows labelled 'I'. The dashed lines are current streamlines.

The "flat" conductivity distribution shown in figure 3.5c is of interest in geophysical probing. The anomaly can be positioned at any depth.

The conformal transformations used here to map between the various classes of conductivity distribution are bilinear (or linear fractional) transformations. Such transformations have the useful property that all circles and straight lines map to circles and straight lines (cf. Kreyszig 1972 §12.3; Ahlfors 1953 §3.2). One transformation is used to map between the symmetric conductivity distributions in the complex z-plane and the offset conductivity in the complex w-plane. A further transformation is used to map between the w-plane and the flat conductivity distributions in the complex t-plane.

Parameters of particular importance which are affected by the transformations are the radius and position of the anomaly, and the position of the electrodes on the surface of the conductive region. The transformations between the z and w-planes and the w and t-planes, and the effect they have on the parameters mentioned above, are summarised in table 3.1. For convenience the configurations characterised by the z, w and t-planes are referred to as the symmetric geometry, the offset geometry and the flat geometry respectively.

3.3.1 Ideal Electrode Positions

From the arguments presented in §3.2.1 and §3.2.2 it is clear that the maximum sensitivity and visibility occur for the low spatial frequencies of voltage and current density distributions (i.e. when n=1). One current density distribution which may be used on the symmetric geometry is a point current source and point current sink at $\theta = 90^{\circ}$ and $\theta = -90^{\circ}$ respectively (see figure 3.5a). It is a particularly suitable current density distribution because it is simple (i.e. it uses only 2 electrodes), and it has the largest fundamental component (n=1) of all current density distributions which use only 2 electrodes. For these reasons $\theta = 90^{\circ}$ and $\theta = -90^{\circ}$ are termed here the "ideal" electrode positions.

The visibility of an anomaly is highest for the fundamental Fourier component of current density (see §3.2.1). Of all current density distributions which use only 2 electrodes, that with electrodes at the ideal electrode positions has the highest fundamental component. Hence the differences between the voltages measured when an anomaly is present and those when no anomaly is present, is the largest when the ideal electrode positions are chosen.

Table 3.1: Conformal Transformations between the conductivity distributions shown in figure 3.5. $i = \sqrt{-1}$. Other symbols are defined in figure 3.5.

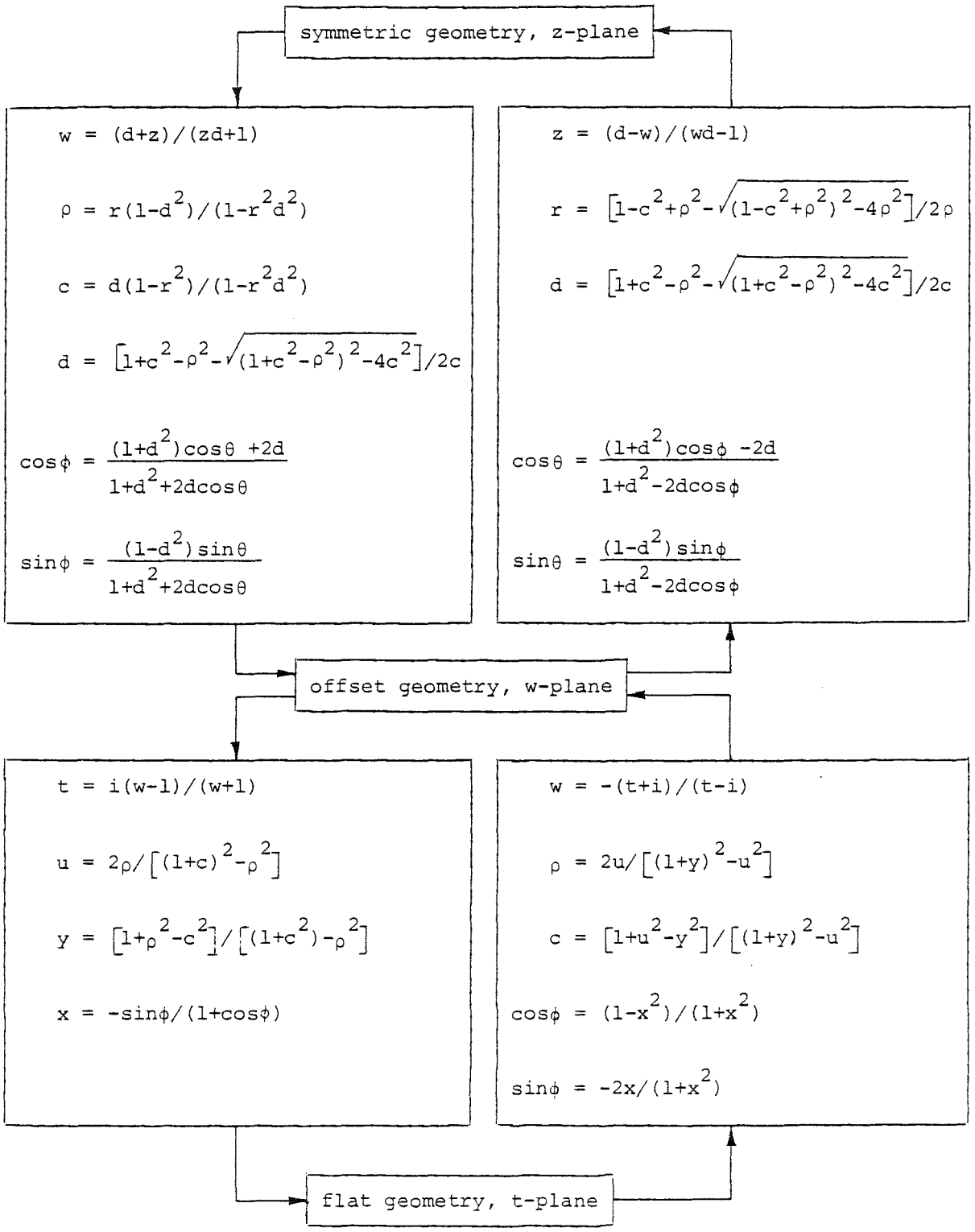

The corresponding ideal electrode positions for the offset and flat geometries can be found by conformal transformation. For the offset geometry the ideal electrode positions vary almost linearly with the offset of the anomaly (see figure 3.6a). For the flat geometry the ideal electrode separation for small or deep anomalies (i.e. radius/depth $<<$ 1) is twice the depth of the anomaly, and otherwise is somewhat less (see figure 3.6b).

3.3.2 Maximum Visibility and Sensitivity

When any particular conductivity distribution in the offset or flat geometry is mapped into the symmetric geometry, equations (3.10) and (3.13) give the visibility and sensitivity respectively. Of primary interest are the maximum visibility and maximum sensitivity, since it is these which limit the spatial and conductivity resolution. The magnitude of the maximum visibility ($n=1$, $\alpha=0$ or ∞) and the magnitude of the maximum sensitivity ($n=1$, $\alpha=1$) are both equal to r^2, where r is the radius of the anomaly as shown in figure 3.5a. Thus only a single graph is needed to show both maximum visibility and maximum sensitivity. Figure 3.7 shows the maximum visibility and sensitivity for each of the three geometries.

It is interesting to notice in figure 3.7b that the visibility and sensitivity of an anomaly of fixed size increases only slowly as the offset of the anomaly increases, until the surface of the anomaly is about 0.9 of the distance towards the outer surface of the conductive region. This indicates that an impedance imaging system operating on a closed region can be expected to have both spatial and conductivity resolutions which are almost independent of position. The visibility and sensitivity only approach zero as the size of the anomaly approaches zero, so that any arbitrarily small anomaly can be detected, provided the measurements are accurate enough. In practice, measurements are not arbitrarily accurate so that resolution is limited.

Figure 3.7c shows that both visibility and sensitivity decrease as the depth of the anomaly increases. To maintain visibility at increased depth the ratio u/y (radius per unit depth) must be kept constant. The spatial resolution is then inversely proportional to depth, and conductivity resolution is independent of depth. There is a tradeoff between spatial resolution and conductivity resolution, and if a fixed spatial resolution is chosen for all depths then the conductivity resolution must necessarily worsen as depth increases. In contrast to the offset geometry,

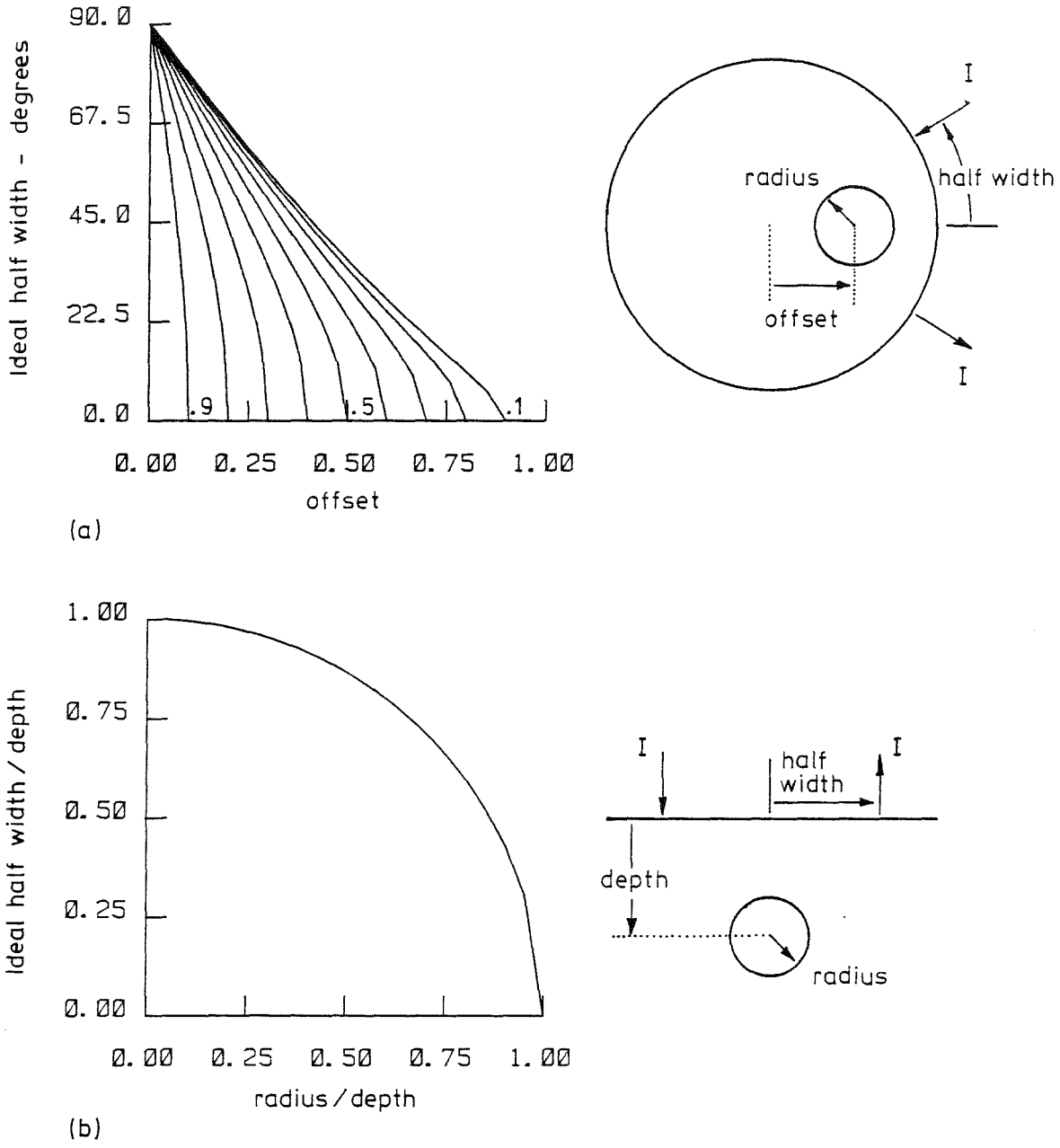

Figure 3.6: Ideal electrode positions for (a) offset and (b) flat geometries. The curves in (a) are shown for the radius of the anomaly from 0.9 to 0.1 in steps of 0.1.

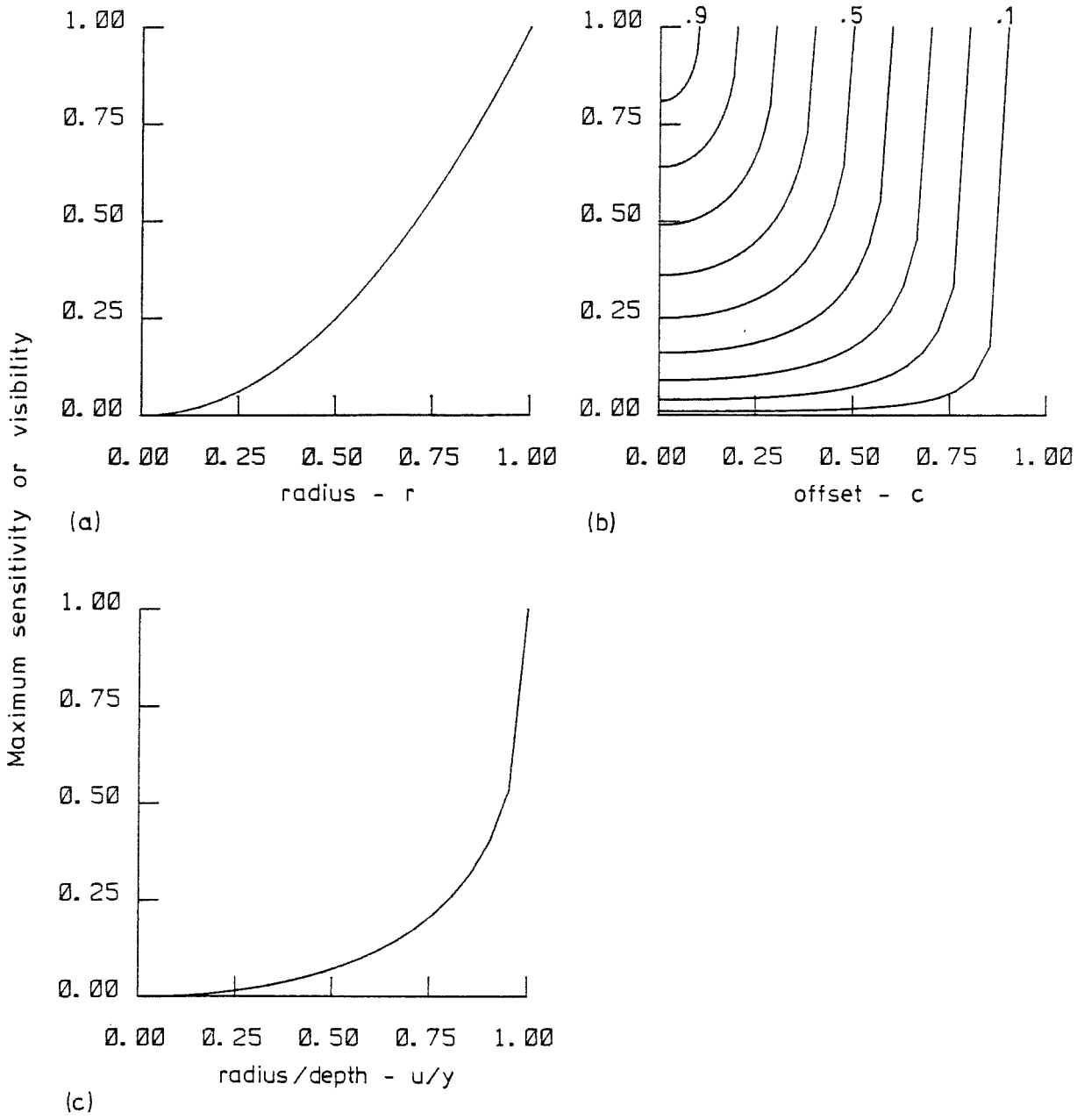

Figure 3.7: Maximum visibility and sensitivity for (a) the symmetric geometry, (b) the offset geometry, and (c) the flat geometry (see figure 3.5). The curves in (b) are shown for normalised radius of the anomaly (i.e. ρ) from 0.9 to 0.1 in steps of 0.1.

the visibility and sensitivity of any anomaly approaches zero as its depth increases regardless of the size of the anomaly.

Figures 3.7b and 3.7c show only the maximum visibility (or sensitivity) for offset and flat geometries. The maximum is not reached unless the conductivity of the anomaly is either zero or infinite (see §3.2.1). However the visibility (or sensitivity) for anomalies of arbitrary conductivity can be found by mapping the anomaly to an equivalent anomaly in the symmetric geometry using figure 3.7a, and then using figures 3.3a and 3.4a. The following example serves as a demonstration.

Assume it is known that a buried concrete pipe carrying water has a radius of 1 m and is centred 1.8 m below the earth's surface. The water is 2.72 times as conductive as the pipe and the earth. It is desired to locate the pipe by probing with a single current source and current sink as shown in figure 3.5c. What is the ideal spacing to use between the current electrodes, and how accurate do the measurements need to be?

Firstly, the ideal electrode spacing is independent of the conductivity of the anomaly. From figure 3.6b with $u/y = 0.57$, the half spacing per unit depth is 0.83, so that the full electrode spacing for 1.8 m depth is $2 \times 1.8 \times 0.83 = 3.0$ m.

From figure 3.7c the maximum visibility when $u/y = 0.57$, is 0.09. The equivalent anomaly in the symmetric geometry, with a maximum visibility of 0.09, is found from figure 3.7a to have a radius of 0.3. From figure 3.2a an anomaly with radius of 0.3 and conductivity contrast 2.72 (or $\ln\alpha = 1$) has a visibility of 0.04. Reference to (3.9) now indicates that the measurement accuracy must exceed $2 \times 100 \times 0.04 = 8\%$.

3.3.3 Visibility Attained in Practice

The limits on spatial and conductivity resolution derived in §§3.2.1 and 3.2.2 are useful, provided that the values of visibility and sensitivity calculated from measurements agree with the corresponding theoretical values. A simple experiment to measure the maximum values of visibility is described here.

Depicted in figure 3.8 is a round insulating tank containing a saline solution (i.e. an electrolyte). In the tank is placed an anomaly of effectively zero or infinite conductivity. Current electrodes are attached at the ideal electrode positions, which can be found by referring to figure 3.6a.

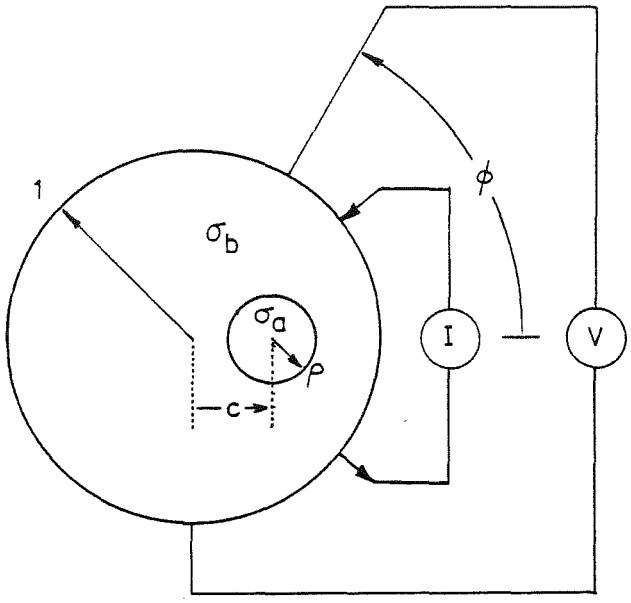

Figure 3.8: Experimental setup to measure the visibility of an anomaly. Current electrodes (I) are located at the ideal electrode positions. Voltage (V) is measured over the entire circumference.

The voltage V is measured as a function of ϕ. It is then conformally mapped back to the symmetric geometry (i.e. $V(\theta)$), and its Fourier transform is calculated to obtain the fundamental harmonic of the voltage on S (i.e. V_1 in (3.1)). The anomaly is then removed and the voltage measurement repeated. Conformally mapping and Fourier transforming as before gives $V_1|_1$, the fundamental harmonic of voltage for the conductivity contrast $\alpha=1$. The visibility is then calculated by substituting V_1 and $V_1|_1$ into (3.8a). The apparatus used to perform these measurements is described in Apprndices 1 and 2, and the results are shown in figure 3.9.

Figure 3.9a shows the measured visibility for the symmetric geometry. The measured values for both highly conducting (x) and nonconducting (o) anomalies closely approach their theoretical values. This indicates that the theoretical maximum visibility is attainable in practice, and is therefore a useful upper limit. Figure 3.9b shows that as expected the visibility increases with the offset of the anomaly (cf. figure 3.7b). The measured values do not, however, increase as much as expected when the anomaly approaches the surface. Furthermore, the measured visibilities for conducting and insulating anomalies of similar size consistently diverge as the offset increases. The visibilities of the insulating anomalies approach the calculated values more closely than the conducting anomalies. There are two sources of experimental error with which these results are consistent.

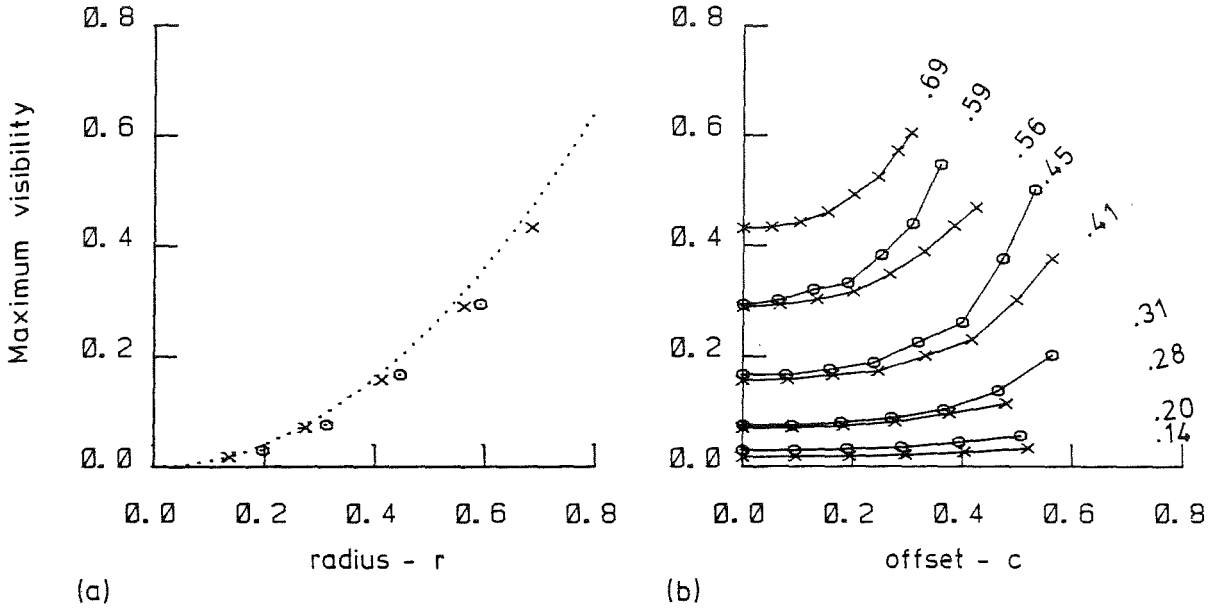

Figure 3.9: Maximum visibility measured experimentally for (a) the symmetric geometry, and (b) the offset geometry. 'x' and 'o' indicate conducting and nonconducting anomalies respectively. The dotted line in (a) shows the theoretical maximum. The curves in (b) have the normalised radius of the anomaly indicated alongside.

The voltage was measured with electrodes equally spaced around the circumference, but when this voltage is conformally mapped to the symmetric geometry the spacing between the voltage samples becomes unequal. The effect is to lower the sampling rate in the symmetric geometry. This permits aliasing to occur when calculating the Fourier components of $V(\theta)$. As the offset is increased the aliasing becomes worse, and the deviation between the measured visibility and the calculated visibility increases. The result is that the visibility near the surface does not in practice reach its maximum theoretical value.

There were 128 electrodes used to measure the voltage around the surface of the tank. The conductivity of the electrodes was high in comparison to that of the saline, so that the effective conductivity close to the surface of the tank was reduced. This means that the two conductivity model (see figure 3.2) used to calculate the theoretical visibility does not fully apply to the experiment described here. For conductive anomalies near the surface most of the current flow is through the anomaly, and the surface shunt due to the electrodes does not contribute significantly to the measurements. However for nonconductive anomalies near the surface

most of the current flow is through the shunt, and the measurements are significantly altered.

The departure of the experimental results from the theoretical values shows that the maximum visibility measured can be limited by the particular measurement system used. Thus in practice it may not be possible to achieve the theoretical value of the maximum visibility. However, the maximum visibility measured when the anomaly is in the centre of the tank does closely approach the theoretical value (see figure 3.9a). Also, the maximum visibility measured when the anomaly is offset, is always greater than the value when the anomaly is at the centre (see figure 3.9b). Therefore the maximum visibility obtained in practice, regardless of the position of the anomaly, is at least as great as the theoretical value when the anomaly is at the centre. Hence an estimate of the spatial resolution of a practical imaging system in which the measurements are collected around the circumference of a circular region can be calculated, as discussed in §§3.3.2 and 3.2.1 using the theoretical value for the visibility at the centre of the region.

3.4 FURTHER LIMITATIONS OF THE FLAT GEOMETRY

3.4.1 Incomplete Measurements

In the flat geometry (figure 3.5c) it is physically impossible to measure the voltage along all of the surface at y=0. It is important to know what error is introduced by incomplete measurement of the voltage since the resolution is limited by errors in the measurements (see §§3.2.1, 3.2.2).

Refer therefore to figure 3.10. Suppose that the voltage V(x) is due to current flow between electrodes located at the ideal electrode position i.e. $x = \pm a$. When no anomaly is present V(x) is called $V_u(x)$. Suppose that the measurements are only made when $|x|<b$. Ideally the value of b should be infinite, so that V(x) is known for all values of x. However, in practice b is always finite, which means that the measurements are incomplete.

Denote by $\hat{V}(x)$ the estimate of V(x) for all values of x. When $|x|<b$, $\hat{V}(x)$ can be found directly from the measured values of V(x). However when $|x| > b$, $\hat{V}(x)$ must be estimated. One simple estimate of V(x) is the value of $\gamma V_u(x)$, where the scaling factor γ is chosen such that $\gamma V_u(b) = V(b)$. This scaling factor ensures that $\hat{V}(x)$ is continuous at $|x| = b$. The estimate of V(x) then becomes

$$\hat{V}(x) = V(x) \; ; \qquad |x|<b \tag{3.14a}$$

and

$$\hat{V}(x) = V_u(x)V(b)/V_u(b) \; ; \qquad |x|>b. \tag{3.14b}$$

When no anomaly is present $\hat{V}(x)$ equals $V(x)$ for all x.

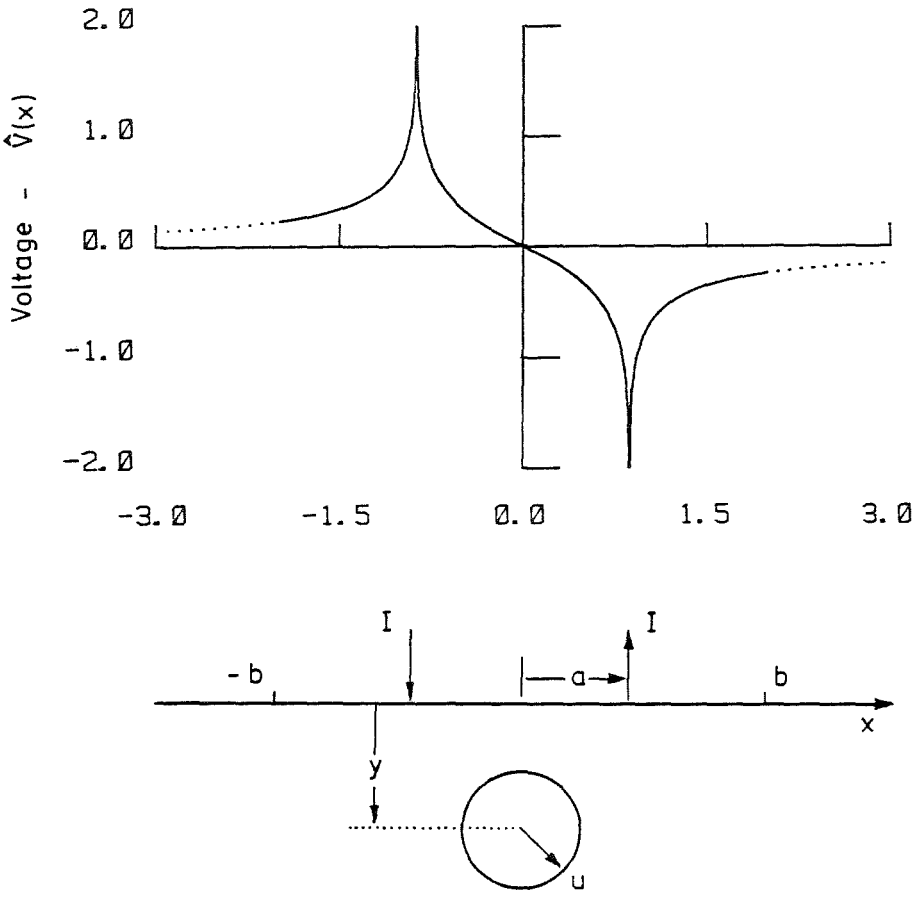

Figure 3.10: Incomplete voltage measurement in the flat geometry. Current electrodes (I) are at $x=\pm a$, and the voltage is measured for $|x|<b$. For $|x|>b$ the voltage $\hat{V}(x)$ is estimated (dotted, see text).

Using the conformal transformations listed in table 3.1 the voltages $V(x)$ and $\hat{V}(x)$ transform to $V(\theta)$ and $\hat{V}(\theta)$ respectively in the symmetric geometry. The first order Fourier components of $V(\theta)$ and $\hat{V}(\theta)$ are V_1 and $\hat{V}_1$ respectively. Therefore the error in the visibility ΔQ_{11} due to the departure of $V(x)$ from $\hat{V}(x)$ is

$$\Delta Q_{11} = \left[(V_1-V_1|_1)/(V_1+V_1|_1)\right]-\left[(\hat{V}_1-V_1|_1)/(\hat{V}_1+V_1|_1)\right] \tag{3.15}$$

where "$|_1$" means evaluated for $\alpha=1$. When the visibility of an anomaly is less than the error in visibility, caused by the incomplete measurement of

V(x), the anomaly cannot be detected.

Figures 3.11a and 3.11b show ΔQ_{11} for anomalies with infinite and zero conductivity respectively. For anomalies with small radius per unit depth (u/y) the conductive region is almost uniform, so $\hat{V}(x)$ in (3.14b) is a good approximation to V(x), which means little error is introduced. For anomalies with u/y approaching unity the ideal electrode positions are much closer together (cf. figure 3.6b), so that the measured part of $\hat{V}(x)$ (i.e. (3.14a)) encompasses a greater proportion of the total circumference when mapped to $V(\theta)$ in the symmetric geometry. Thus the error introduced using (3.14b) tends to zero as u/y approaches unity.

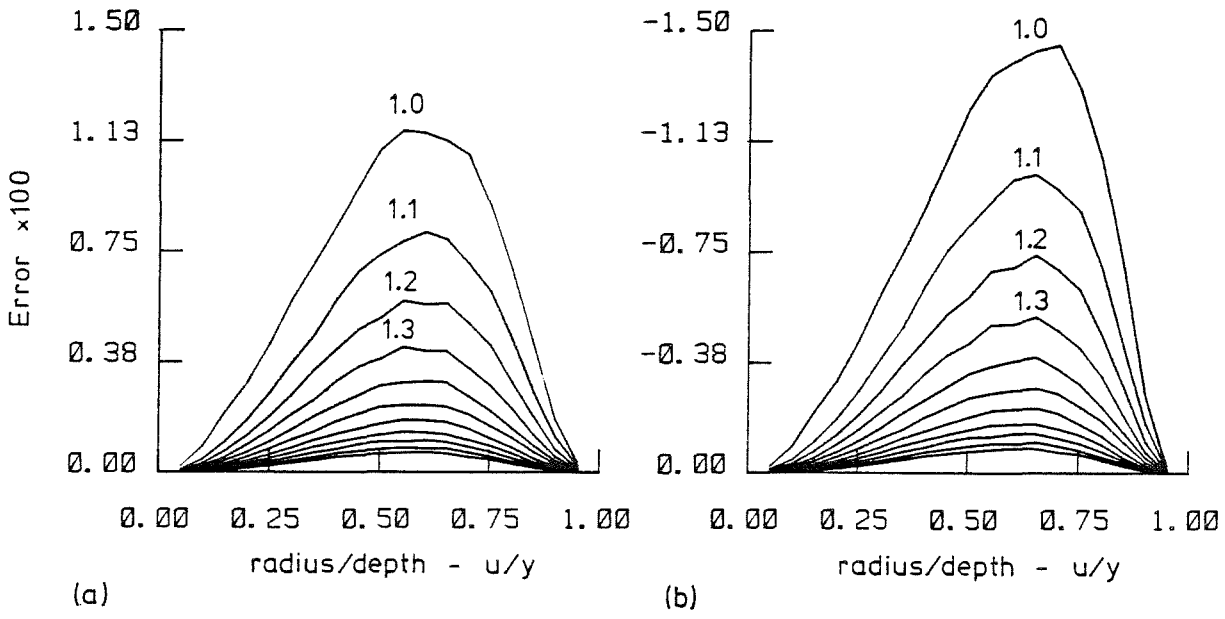

Figure 3.11: Error in visibility due to incomplete measurements on a flat earth (see figure 3.10) for (a) a conducting anomaly, and (b) a nonconducting anomaly. The curves are shown for the extent of measurements (b/y) from 1.0 to 2.0 in steps of 0.1.

For anomalies having u/y values significantly different from either 0 or 1, $\hat{V}(x)$ is not a good approximation to V(x). However the error can be reduced by measuring $\hat{V}(x)$ over more of the surface. For instance, provided b/y is greater than 2 then ΔQ_{11} is less than 0.00075, regardless of the size of the anomaly. This means that the resolution is limited by incomplete measurements only if $\Delta V_1/V_1 < 0.0015$. Unless measurements are made to an accuracy exceeding 0.15% the voltage need only be measured out to twice the depth of the anomaly, and extended using (3.14b).

3.4.2 Approximation to a Curved Geometry

Electrical probing measurements of the earth are often interpreted as though the earth is flat (see §1.2.4). Therefore, it is important to know the error introduced when interpreting measurements made on a curved geometry in terms of a flat geometry. Comparing the geometrical factor K (see (1.1)) for flat and curved earth models is a convenient way of estimating the error.

Consider the flat and circular geometry shown in figure 3.12. The conductivity σ is uniform throughout the lower half plane in figure 3.12a, and throughout the circular region in figure 3.12b. A Wenner electrode array (see figure 1.2), with array spacing a, passes current I through each region and measures the voltage difference ΔV. In the flat geometry the voltage V at a point x' is found, using (2.79), to be

$$\begin{aligned} V(x') &= -\int_{-\infty}^{\infty} (1/\pi)\ln|x'-x|\,(I/\sigma)\{\delta(x+3a/2)-\delta(x-3a/2)\}dx \\ &= (I/\sigma\pi)\{\ln|x'-3a/2|-\ln|x'+3a/2|\}\ . \end{aligned} \tag{3.16}$$

The geometric factor is found by rearranging (1.1), and then calculating $\Delta V = V(-a/2)-V(a/2)$ using (3.16). This gives $K_{flat} = \pi/2\ln 2$. It is interesting to notice that the geometrical factor is independent of electrode spacing in the flat two-dimensional geometry, since in general it is not (cf. Keller and Frischknecht 1966 §17).

In the circular geometry the voltage V at a point θ' on the surface is found, using (2.79), to be

$$V(\theta') = -\int_{-\pi}^{\pi} (1/\pi)\ln|\underset{\sim}{r}'-\underset{\sim}{r}|\,(I/\sigma)\{\delta(\theta+3\omega/2)-\delta(\theta-3\omega/2)\}d\theta \tag{3.17}$$

where $\underset{\sim}{r}$ and $\underset{\sim}{r}'$ are vectors to points with coordinates (r,θ) and (r',θ') respectively on the surface of the circular region. When the factor $\ln|\underset{\sim}{r}'-\underset{\sim}{r}|$ is expanded in terms of r,θ,r' and θ' (cf. Morse and Feshbach 1955 §10.1), and both r and r' are set to 1, equation (3.17) simplifies to give

$$V(\theta') = I/\{\sigma\pi \sum_{n=1}^{\infty} (1/n)\left[\cos n(\theta'-3\omega/2)-\cos n(\theta'+3\omega/2)\right]\} \tag{3.18}$$

where ω is the array spacing measured in radians (see figure 3.11b). Using (1.1), and (3.18) to calculate $\Delta V = V(-\omega/2)-V(\omega/2)$, gives the geometric factor for the circular model, i.e. $K_{round} = \pi/\{2\sum_{n=1}^{\infty}(1/n)\left[\cos 2n\omega-\cos n\omega\right]\}$.

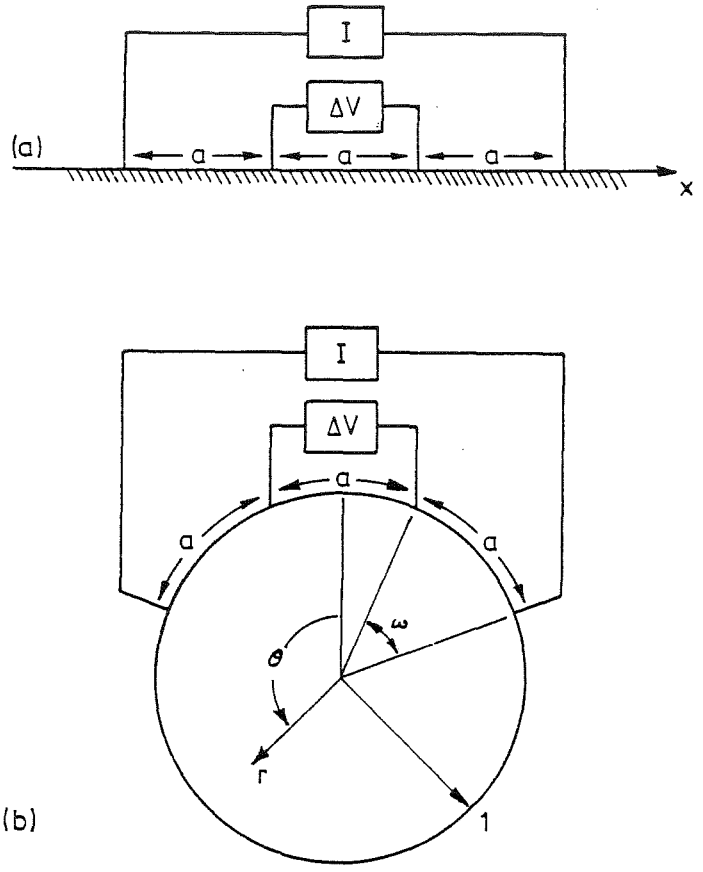

Figure 3.12: Wenner electrode array measurements. Voltage difference (ΔV) due to current flow I is measured.

(a) flat geometry

(b) circular geometry.

Figure 3.13 shows the ratio K_{round}/K_{flat}. This is the correction factor by which the apparent resistivity found in the curved geometry must be multipled to yield the equivalent measurement in the flat geometry. Provided $\omega<15^{\circ}$ the correction needed is less than 1.3%, and for $\omega<5^{\circ}$ the correction is less then 0.14%. These corrections correspond to a maximum array spacing of about 1700 km and 560 km respectively on a two-dimensional earth. An array spacing of 560 km is impracticably large for the Wenner array, since over 2,000 km of wire is needed to inject the current and measu the voltage. Therefore the correction needed in practice is always less than 0.14%.

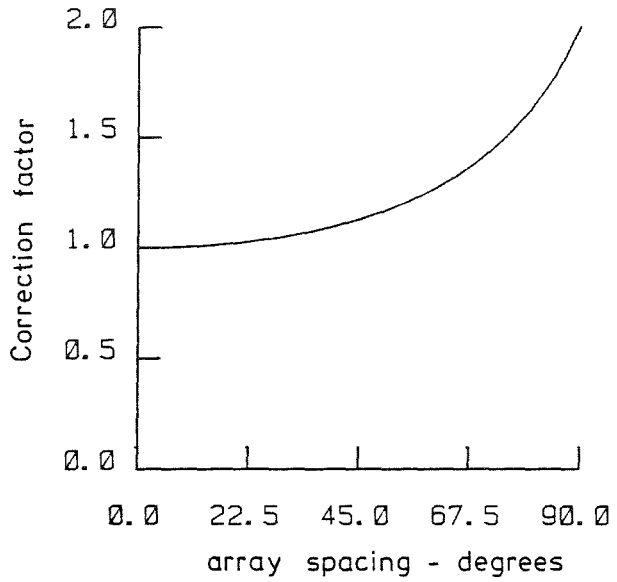

Figure 3.13: Correction to apparent resistivity in order to allow for curvature. The angular array spacing (ω) is defined in figure 3.12.

3.5 DISCUSSION

The visibility and sensitivity, defined in §§3.2.1 and 3.2.2 respectively, enable upper limits on the spatial and conductivity resolution to be found. Alternatively they enable the accuracy of measurements, needed to image a region to a particular spatial and conductivity resolution, to be determined. The spatial resolution is limited by the accuracy of the measurements even when the anomaly has infinite or zero conductivity. The conductivity resolution depends on both the spatial resolution and the accuracy of the measurements. The tradeoff between spatial and conductivity resolution enables the error in the estimated values of the conductivity to be reduced at the expense of the spatial resolution. However, the maximum sensitivity never exceeds unity, so the uncertainty in the conductivity must necessarily exceed the uncertainty in the measurements. The lowest conductivity resolution occurs for anomalies possessing very high or low conductivities.

The limits on spatial and conductivity resolution are different for different imaging system geometries. For the offset geometry shown in figure 3.5b, where the measurements totally encompass the region being

investigated, both spatial and conductivity resolution are essentially independent of position within the region. However the resolution in the flat geometry, shown in figure 3.5c, necessarily decreases with increasing distance from the boundary at which the measurements are made. If the conductivity resolution is chosen constant throughout the lower half plane then the spatial resolution is inversely proportional to depth.

It is important to take advantage of the way in which the spatial resolution varies with position. For instance, finite difference resistivity modelling with nonuniform grid spacings has improved efficiency over the same method with uniform grid spacing (Mufti 1978).

Measurements made on part of the surface of a conducting region, which is assumed flat but is actually curved, have additional errors introduced due to incompleteness of measurement and due to the curvature of the surface. In practice these errors can be avoided.

The error due to incompleteness of measurement can be easily reduced below any desired level by making the measurements over more of the surface (see figure 3.11). If a 0.2% accuracy of measurements is sufficient, then the measurements should cover twice as much of the surface as the maximum depth being probed.

The error due to the curvature of the surface can be significant if the amount of surface on which the measurements are made and the radius of curvature of the surface are approximately the same size (see figures 3.12 and 3.13). Using the two dimensional circular geometry shown in figure 3.13, the error for an array spacing equivalent to 560 km on the earth is less than 0.14%. The curve shown in figure 3.13 is approximately linear for small array spacings ($\omega<5^{o}$), and in this situation the error may equivalently be expressed as 0.00025% per kilometer of array spacing. This error is insignificant for Geoelectric probing methods that employ direct current, because the error in the measurements per kilometer of array spacing is much greater than 0.00025%.

4. CIRCULARLY SYMMETRIC CONDUCTIVITY DISTRIBUTIONS

Circularly symmetric conductivity distributions are those in which the conductivity has rotational symmetry about an origin. The conductivity, expressed in terms of a circular coordinate system about this origin, depends only upon the radial coordinate. In this chapter both iterative and direct techniques are used to interpret measurements from circularly symmetric conductivity distributions. The different techniques are compared using both simulated and experimental measurements.

Two different representations of circularly symmetric conductivity distributions are employed for interpreting measurements in this chapter. These representations are termed here the piecewise constant conductivity distribution and the smooth conductivity distribution (see figure 4.1). The piecewise constant conductivity distribution consists of any number of concentric rings (annuli), each with constant conductivity. The smooth distribution is continuous and has continuous derivatives of all orders with respect to radius, except at the origin where the derivatives may be discontinuous. The background theory relating to the piecewise constant and smooth conductivity distributions is developed in §§4.1 and 4.2 respectively. In §4.3 measurements are interpreted in terms of both types of conductivity distribution.

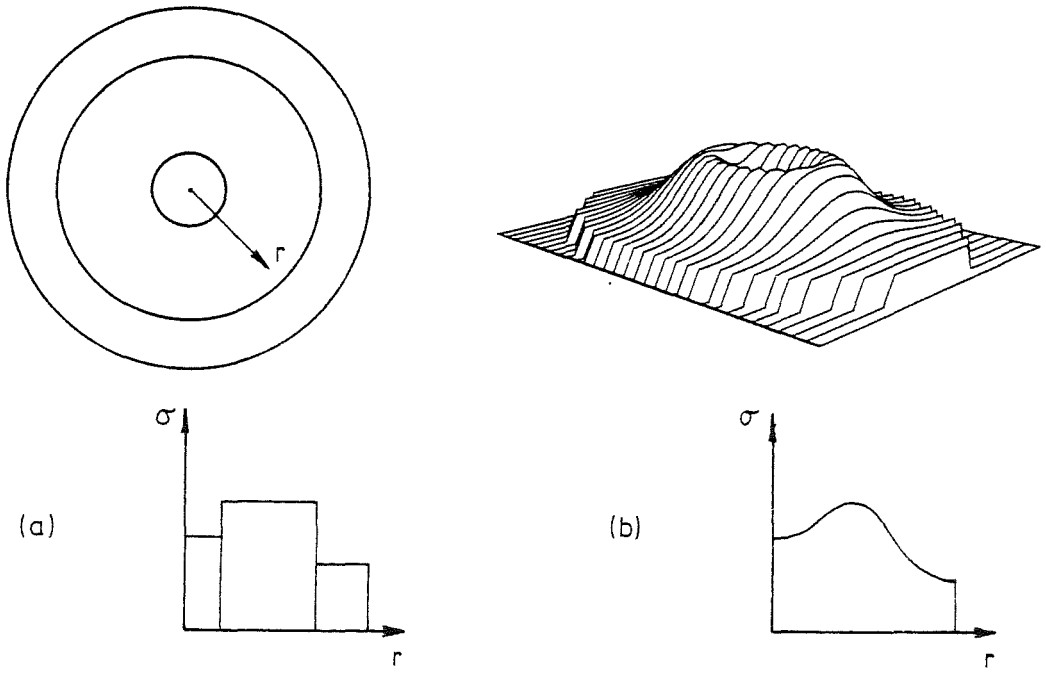

Figure 4.1: Circularly Symmetric Conductivity Distributions.
(a) Piecewise constant.
(b) Smooth.

4.1 PIECEWISE CONSTANT DISTRIBUTIONS

The relationship between the voltage and current density on the boundary of a region having a circularly symmetric piecewise constant conductivity distribution is developed here. The method is based on that used in §3.1 for the symmetric single anomaly conductivity distribution.

Consider the conductivity distribution consisting of N concentric rings within the circular region R shown in figure 4.2. Points in R have radial and angular coordinates r and θ respectively. The kth ring has conductivity σ_k and outer radius r_k. On the boundary S, at $r = r_N$, the Fourier series in (3.1) and (3.2) are used (with r_b replaced by r_N) to represent the voltage, $V(P)=V(r_N,\theta)$, and the current density normal to S, $J(P)=J(r_N,\theta)$ respectively. There are no current sources within R and the voltage must remain finite everywhere in R. In this situation the general solution of Laplace's Equation (2.86) gives the voltage $V(r,\theta)$ within R as

$$V(r,\theta) = \Sigma\, A_n^{(1)} r^n \cos n\theta + B_n^{(1)} r^n \sin n\theta \quad ; \quad r \leq r_1 \,, \tag{4.1a}$$

$$V(r,\theta) = \Sigma\, (A_n^{(k)} r^n + \tilde{A}_n^{(k)} r^{-n}) \cos n\theta + (B_n^{(k)} r^n + \tilde{B}_n^{(k)} r^{-n}) \sin n\theta \quad ; \quad r_{k-1} \leq r \leq r_k \tag{4.1b}$$

and

$$V(r,\theta) = \Sigma\, (A_n^{(N)} r^n + \tilde{A}_n^{(N)} r^{-n}) \cos n\theta + (B_n^{(N)} r^n + \tilde{B}_n^{(N)} r^{-n}) \sin n\theta \quad ; \quad r_{N-1} \leq r \leq r_N \tag{4.1c}$$

where the superscript in parentheses indicates to which ring the coefficients A and B apply.

The boundary conditions (3.1) and (3.2) at $r = r_N$, and the conditions for continuity of both current across and voltage at the boundaries $r = r_k$ (for all k from 1 to N-1) enable the unknown coefficients $A_n^{(k)}$, $\tilde{A}_n^{(k)}$, $B_n^{(k)}$ and $\tilde{B}_n^{(k)}$ to be related to those in the adjacent rings, and the voltage to be related to the current density at the surface. The resulting expressions for the B_n are

$$B_n^{(2)} = \frac{1}{2} B_n^{(1)} (1+\alpha_1) \tag{4.2a}$$

$$\tilde{B}_n^{(2)} = \frac{1}{2} B_n^{(1)} (1+\alpha_1)\beta_1 \tag{4.2b}$$

$$B_n^{(k+1)} = \frac{1}{2}\left[B_n^{(k)}(1+\alpha_k)+\tilde{B}_n^{(k)}(1-\alpha_k)\beta_k^{-n}\right] \tag{4.2c}$$

$$\tilde{B}_n^{(k+1)} = \frac{1}{2}\left[B_n^{(k)}(1-\alpha_k)\beta_k^{n}+\tilde{B}_n^{(k)}(1+\alpha_k)\right] \tag{4.2d}$$

and

$$z_{nn} = V_n/J_n = -(r_N/n\sigma_N)\left[B_n^{(N)}+\tilde{B}_n^{(N)}\right]/\left[B_n^{(N)}-\tilde{B}_n^{(N)}\right] \tag{4.2e}$$

where the conductivity contrast is $\alpha_k = \sigma_k/\sigma_{k+1}$ and $\beta_k = (r_k/r_N)^2$ is the square of the normalised radius of the rings. The resulting expressions for the A_n are the same as (4.2a) to (4.2e) with V_n, J_n, $B_n^{(k)}$ and $\tilde{B}_n^{(k)}$ replaced by U_n, I_n, $A_n^{(k)}$ and $\tilde{A}_n^{(k)}$ respectively. The z_{nn} are the driving point impedances, which are introduced in §3.2.

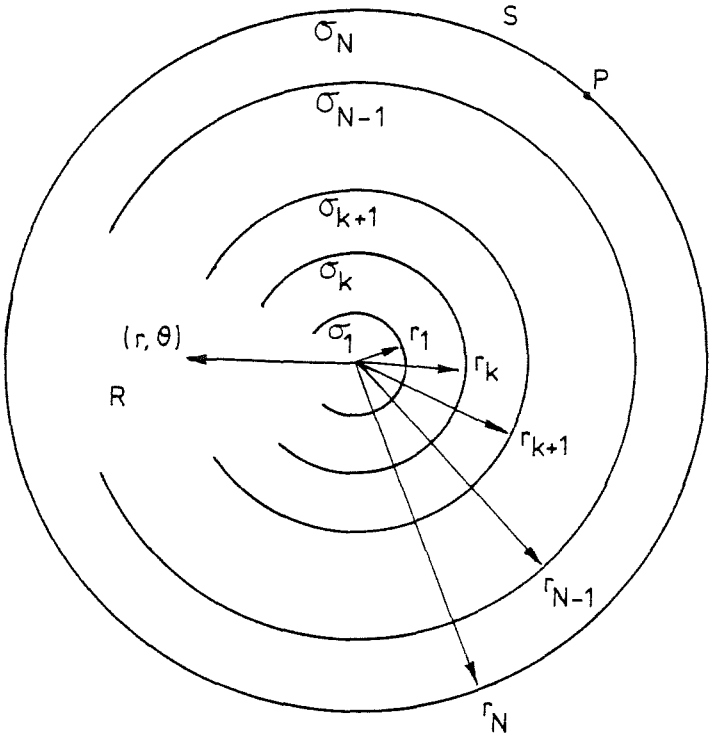

Figure 4.2: Piecewise constant conductivity distribution. N concentric rings of radius r_1 to r_N have conductivities σ_1 to σ_N respectively. P is a point on the surface S.

The recursive relations in (4.2a) to (4.2d) show that any $B_n^{(k)}$ and any $\tilde{B}_n^{(k)}$ is equal to the product of $B_n^{(1)}$ and a factor which depends on the α's, β's, n and k. Thus, when the ratio of the terms in square brackets in (4.2e) is evaluated, the $B_n^{(1)}$ cancel, so that z_{nn} depends only on the conductivities and radii of the rings. Furthermore, a particular Fourier component of voltage V_n is equal to the same Fourier component of current J_n multiplied by the driving point impedance z_{nn}. The significance of this relationship is discussed in detail in §3.1 in relation to (3.5) and the simple circularly symmetric conductivity distribution shown in figure 3.2.

The important points are here summarised briefly, in so far as they apply to the circularly symmetric conductivity distribution shown in figure 4.2. Firstly, the voltage distribution $V(r_N,\theta)$ and the current density distribution $J(r_N,\theta)$ are related by a convolution. Secondly, only a single pair of measurements $V(r_N,\theta)$ and $J(r_N,\theta)$ on the entire boundary of S are necessary to calculate all of the driving point impedances z_{nn}. Finally, the z_{nn} fully characterise the electrical response of conductivity distributions of the kind illustrated by figure 4.2.

Equation (4.2e) is the two-dimensional equivalent for the circularly symmetric geometry of what is called the geophysical kernel function for the three-dimensional flat horizontally stratified geometry (see figure 1.3a) (cf. Keller and Frischknecht 1966 §23a; Szaraniec 1976). The geophysical kernel is often expressed in terms of a set of recursive relations similar to (4.2a) to (4.2d). The similarity is not surprising because the same boundary conditions at the discontinuities in conductivity are used to arrive at both (4.2) and the geophysical kernel. The similarity is further emphasised by the logarithmic conformal transformation illustrated by figure 4.3. The portion of the half plane for x between $-\pi$ and π in the complex z-plane maps to the unit circle in the complex w-plane. Horizontal strata in the z-plane map to concentric rings in the w-plane.

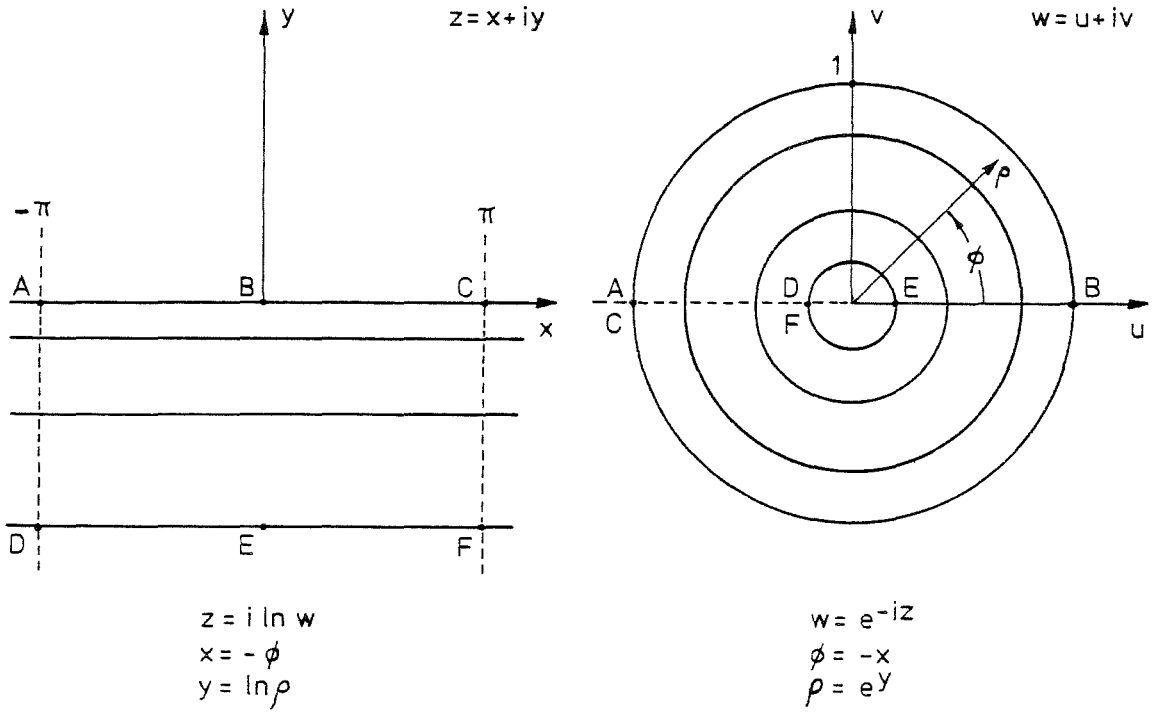

Figure 4.3: Logarithmic conformal transformation relating horizontally stratified flat earth to circularly symmetric region.

4.1.1 Comparison Between Experimental and Simulated Measurements

An experiment is described here in which different current distributions are imposed upon two specimen conductivity distributions, and the corresponding voltage distributions are measured. The driving point impedances are then calculated from the voltage and current distributions and compared to the theoretical values.

Consider first how the driving point impedances may be simply determined from the current and voltage distributions. In §4.1 it is reasoned that the driving point impedances z_{nn} depend only upon the conductivity distribution of the circular region on which measurements are made. Furthermore, (4.2e) shows that the z_{nn} can be calculated from the Fourier components of the voltage and current density distributions on the boundary of the region. In order that a particular z_{nn} can be calculated from measurements it is necessary that the voltage (or current density) distribution applied to the boundary has a corresponding Fourier component V_n (or J_n) which is not zero. The applied distribution should therefore be chosen to contain all Fourier components of interest.

A simple 2-electrode current distribution which induces with equal magnitude, upon the circumference of a circular region, all of the odd sinusoidal Fourier components of current density is shown in figure 4.4a. The arrows labelled "I" indicate point sources and sinks of current. Similarly, the 4-electrode current distribution shown in figure 4.4b induces equally one half of the even sinusoidal Fourier components of current density upon the circumferences of the region.

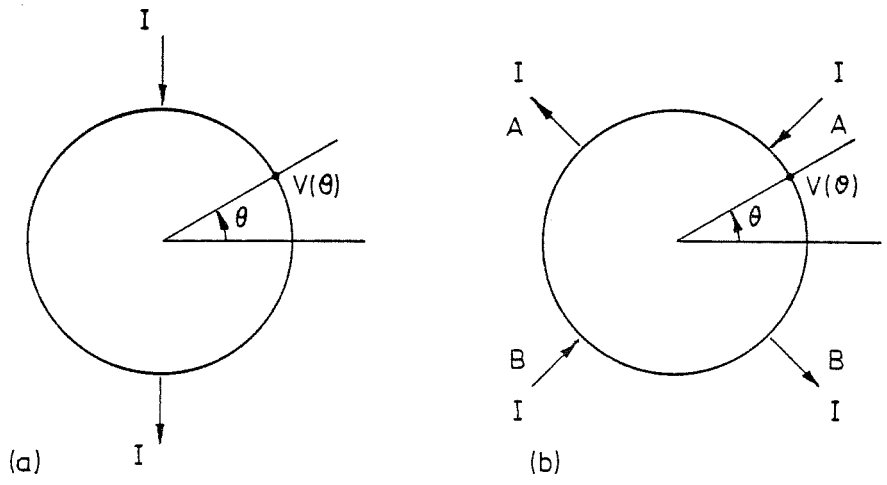

Figure 4.4: Simple current distributions of which the Fourier components are:

(a) all odd sinusoidal components, i.e. n=1,3,5...

(b) even sinusoidal components excluding those which are a multiple of 4, i.e. n=2,6,10,14,...

One difficulty with using point sources of current is that the voltage at the source must be infinite, because the size of the source is infinitesimal. In practice, point sources are approximated by small electrodes (see figure 4.5) and the voltages at the electrodes remain finite. Thus when comparing theoretical values with experimental measurements it is important to allow for the size of the current electrodes.

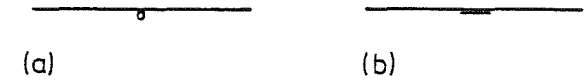

(a) (b)

Figure 4.5: Approximations to point sources lying just under the surface of a conducting region.

(a) cross-section of a wire,

(b) cross-section of an infinitessimally thin strip.

Experimental measurements were obtained on a circularly symmetric conductivity distribution consisting of a single anomaly (see figure 3.2) having effectively zero or infinite conductivity. Current distributions were applied to the boundary of the conductivity distribution as shown in figure 4.4, with small circular electrodes being used (see figure 4.5a) instead of point sources. The voltage distribution (i.e. $V(\theta)$ in figure 4.4) was measured. The particular equipment used to perform these measurements is described in Appendices 1 and 2. Since the equipment used had only one current source and one current sink, the current distribution shown in figure 4b was simulated by using two electrodes, first located at the positions labelled A and then at the positions labelled B. The sum of the voltage distributions measured with the current electrodes at A and B respectively gives the response to all four electrodes simultaneously. This follows since the Fourier components of both the voltage and current density distributions are linearly related (see (4.2)).

For the purpose of determining the theoretical response of the conductivity distributions, the circular electrodes were approximated by flat electrodes lying on the surface of the distributions as shown in figure 4.5b. The average current density over the circular and one side of the flat electrodes was matched. The match is achieved by taking the width of the flat electrode to equal the circumference of the circular electrode.

Figures 4.6a and 4.6b show the measured voltage distributions corresponding to the current distributions shown in figures 4.4a and 4.4b respectively. The crosses and circles indicate the voltages measured for the anomalies of effectively infinite and zero conductivity respectively. The solid lines indicate the theoretical values of the voltage. Shown in figure 4.6c are the driving point impedances calculated from the curves shown in figures 4.6a and 4.6b.

The measured and theoretical voltage distributions are in good accord except very close to the current electrodes. The exception is not surprising since the circular electrodes used in the experiment were approximated by flat electrodes when calculating the theoretical values of the voltage. The driving point impedances calculated from the experimental measurements also agree well with their respective theoretical values.

These results shown in figure 4.6 demonstrate that it is possible to accurately measure the driving point impedances for circularly symmetric conductivity distributions using particularly simple current distributions. However, it is worth noting that only three out of every four consecutive driving point impedances are determined using the method described here. Additional current distributions are needed to obtain the remaining one quarter of the driving point impedances. Such distributions should be chosen to contain Fourier components of current density which correspond to the desired driving point impedances.

In §4.3 driving point impedances deduced from measurements are interpreted in terms of various types of circularly symmetric conductivity distributions. These driving point impedances are obtained using the method described here. Only three out of every four consecutive driving point impedances are measured.

4.1.2 Multiple Ring Models for Iterative Modelling

Iterative modelling is one way of interpreting experimentally measured driving point impedances in terms of a conductivity distribution. The basis of the iterative modelling approach is to adjust parameters of a model which represents the conductivity distribution until the model mimics the experimental measurements as closely as is feasible.

Figure 4.7 shows two models suitable for interpreting measurements in terms of circularly symmetric piecewise constant conductivity distributions (cf. figure 4.1a). The parameters in the fixed-radii model (figure 4.7a)

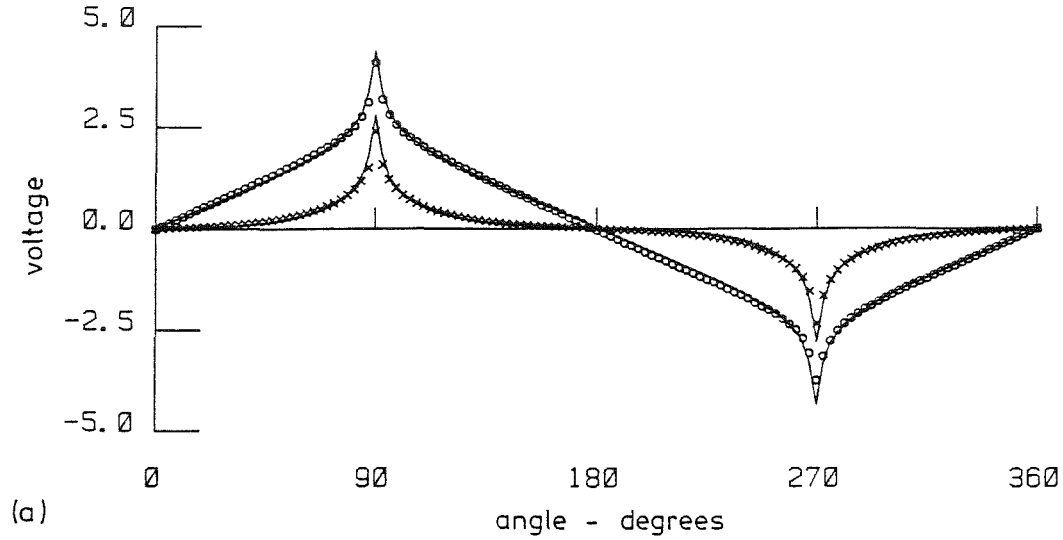

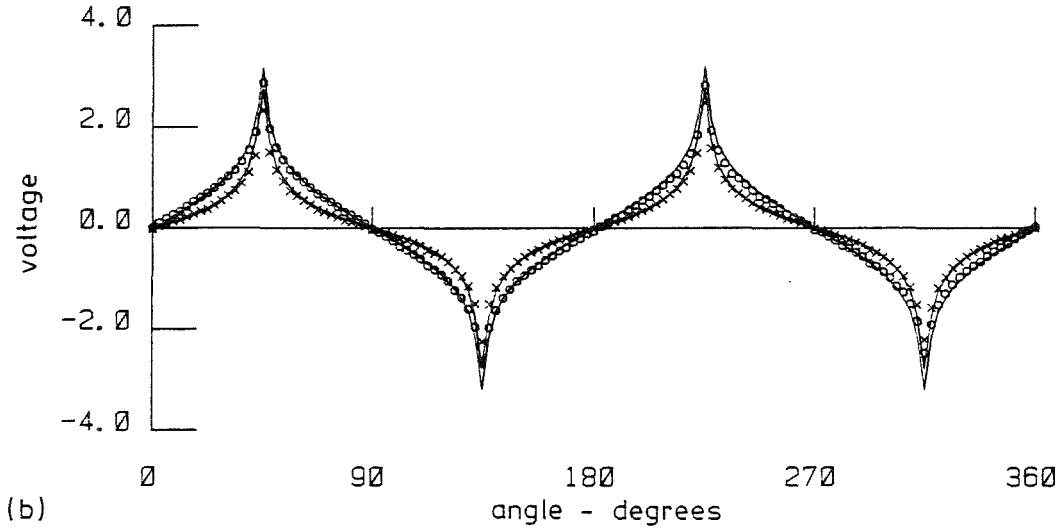

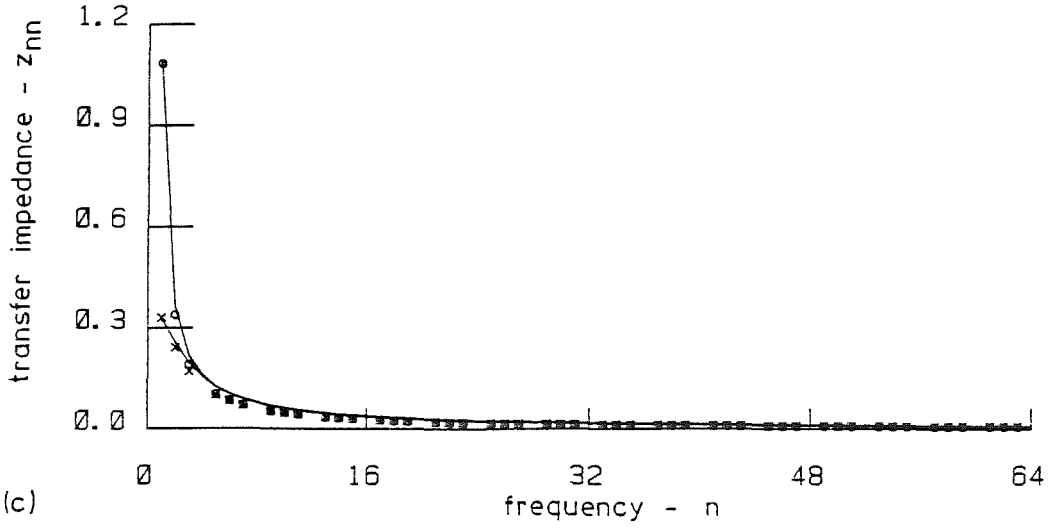

Figure 4.6: (a) and (b) Voltage measurements for the current distributions shown in Figures 4.4(a) and (b) respectively.

(c) Magnitude of driving point impedances calculated from (a) and (b).

"O" and "X" indicate experimental measurements for anomalies with $r=0.59$ and $\sigma=0$, and $r=0.56$ and $\sigma=\infty$ respectively. The solid lines are the calculated values.

are the conductivities of the rings. The radii of the rings are fixed. The parameters in the variable-radii model (figure 4.7b) are both the conductivities and radii of the rings. When sufficient parameters are included in either model, any circularly symmetric conductivity distribution can be represented as closely as desired. The two models are compared with each other in §4.3. In that section both models are used to interpret measurements derived from both continuous and piecewise constant conductivity distributions.

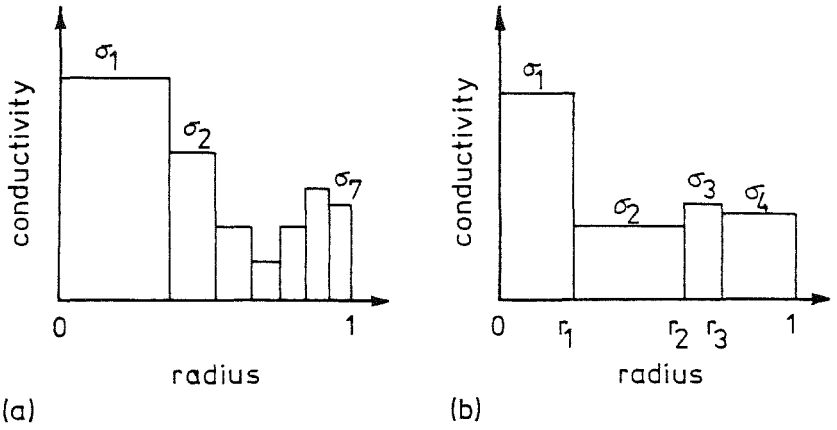

Figure 4.7: Models for interpreting circularly symmetric conductivity distribution.

(a) Fixed-radii model. Seven variables, σ_1 to σ_7.

(b) Variable-radii model. Seven variables, σ_1 to σ_4 and r_1 to r_3.

Practical Considerations

The specific way in which the model parameters and the measurements are represented numerically may significantly affect the efficiency with which any particular iterative procedure can find parameter values for which the model mimics the measurements. The preceding used in §4.3 is a modified Newton algorithm (see Appendix 3). In Newton algorithms, systems of linear equations are solved in order to find new estimates for model parameters. If a system of linear equations is ill-conditioned, the new estimates may not represent any improvement on the proceding estimates. The conditioning of the system of equations depends on the values of the derivatives of the measurements with respect to the model parameters, so that the representation of the measurements and model parameters should be chosen as far as possible to avoid ill-conditioning. Unfortunately, the value of the derivatives are not known a priori in general because they change as the iterative procedure finds new estimates of the parameters. Here, the choice of the represent-

ation of the model parameters and measurements is based on the derivatives obtained for a model having uniform conductivity.

Model Parameters Representing Conductivity

Consider the 3-ring model shown in figure 4.8. The rings with outer radius r_1, r_2 and r_3 have conductivities σ_1, σ_2 and σ_3 respectively. The derivative of the driving point impedances z_{nn} with respect to the conductivity of the inner ring is obtained in §3.2. It is expressed there as the sensitivity of fractional changes in the z_{nn} with respect to fractional changes in the conductivity contrast. In terms of the conductivity distribution shown in figure 4.8 the sensitivity of the z_{nn} to changes in the conductivity of the innermost ring is (from (3.13))

$$(\alpha_1/z_{nn})\,\partial z_{nn}/\partial\alpha_1\big|_{\sigma_2=\sigma_3} = -4\alpha_1\beta_1^n/\left[(1+\alpha_1)^2-(1-\alpha_1)^2\beta_1^n\right] \qquad (4.3)$$

where $\alpha_1 = \sigma_1/\sigma_3$, $\beta_1 = (r_1/r_3)^2$ and "$|_{\sigma_2=\sigma_3}$" means evaluated for σ_2 equal to σ_3. Similarly, the sensitivity of the measurements to simultaneous changes in the conductivity of both the inner rings is

$$(\alpha/z_{nn})\,\partial z_{nn}/\partial\alpha\big|_{\sigma_2=\sigma_3} = -4\alpha\beta_2^n/\left[(1+\alpha)^2-(1-\alpha)^2\beta_2^n\right], \qquad (4.4)$$

where $\alpha = (\alpha_1+\alpha_2)/2$, $\alpha_1 = \sigma_1/\sigma_3$, $\alpha_2 = \sigma_2/\sigma_3$ and $\beta_2 = (r_2/r_3)^2$. The sensitivity to changes in both rings simultaneously is related by partial differentiation to the sensitivity to changes in the innermost ring alone, i.e.

$$\partial z_{nn}/\partial\alpha = (\partial z_{nn}/\partial\alpha_1)(\partial\alpha_1/\partial\alpha) + (\partial z_{nn}/\partial\alpha_2)(\partial\alpha_2/\partial\alpha). \qquad (4.5)$$

Using (4.3), (4.4) and (4.5) gives the sensitivity of the z_{nn} to changes in the conductivity of the second ring provided $\sigma_1 = \sigma_2 = \sigma_3$. This sensitivity is

$$(\alpha_2/z_{nn})(\partial z_{nn}/\partial\alpha_2)\big|_{\sigma_1=\sigma_2=\sigma_3} = \partial \ln z_{nn}/\partial \ln \alpha_2 = \beta_1^n-\beta_2^n \qquad (4.6)$$

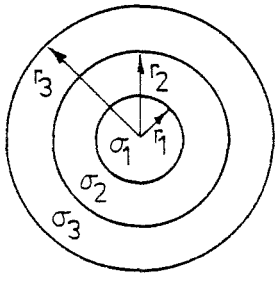

Figure 4.8: Three ring piecewise constant conductivity model. The rings have outer radii r_1, r_2 and r_3, and conductivities σ_1, σ_2 and σ_3 respectively.

Equation (4.6) shows that the magnitude of changes in $\ln z_{11}$ with respect to changes in the logarithm of the conductivity contrast of any ring is proportional to the area of the ring. Choosing the radii in figure 4.2 so that $\beta_k = (r_k/r_N)^2 = k/N$ ensures that changes in $\ln\alpha_k$ of any particular ring has equal effect on $\ln z_{11}$ as do similar changes in any other ring. Therefore, in terms of the single measurement $\ln z_{11}$, all of the parameters $\ln\alpha_k$ may be equally well resolved. Because of this equal sensitivity (or equal resolution) the radii of the fixed-radii model (figure 4.7a) are chosen here to be $r_k/r_N = (k/N)^{\frac{1}{2}}$, and the model parameters and measurements are chosen, for the purposes of the iterative model fitting procedure, to be $\ln\alpha_k$ and $\ln z_{nn}$ respectively.

Model Parameters Representing Radius

The effect on the measurements of changes in radius of a single anomaly is found by differentiating z_{nn} in (3.5) with respect to $\beta(=r^2)$. After rearrangement this gives

$$(1/z_{nn})(\partial z_{nn}/\partial\beta) = \partial \ln z_{nn}/\partial\beta$$

$$= 2(1-\alpha)(1+\alpha)n\beta^{n-1}/\left[(1+\alpha)^2-(1-\alpha)^2\beta^{2n}\right]. \qquad (4.7)$$

The ratio of the effect on the measurements of changes in β for two different values β_1 and β_2 is therefore

$$\beta_1^{n-1}((1+\alpha)^2-(1-\alpha)^2\beta_2^{2n})/\left[\beta_2^{n-1}((1+\alpha)^2-(1-\alpha)^2)\beta_1^{2n}\right].$$

As the conductivity contrast approaches unity, the ratio of the effect at two different radii approaches $(\beta_1/\beta_2)^{n-1}$. Therefore the effect of changes in the β_k (see figure 4.2) on changes in $\ln z_{11}$ is constant regardless of the value of β_k. Hence in terms of the single measurement $\ln z_{11}$, all of the parameters β_k may be equally well resolved. Because of this equal resolution (or sensitivity) it would appear appropriate, for the purposes of the iterative model fitting procedure, to use the parameters β_k rather than the radii of the rings. However when using an unconstrained iterative technique, such as the Newton method, it is numerically possible for β_{k-1} to exceed β_k. This situation is physically meaningless, since it corresponds to the radii of two rings having "crossed over". It makes better sense, therefore, to map the N variables β_k, which are ordered so that $\beta_1 > 0$, $\beta_k > \beta_{k-1}$, and $\beta_N = 1$, onto the N variables γ_k, which can take any real value. When the β_k are related to the γ_k by

$$\beta_k = \beta_{k-1} + \left[1/2 + (1/\pi)\ \tan^{-1}\gamma_k\right](\beta_{k+1}-\beta_{k-1}) \quad ; \quad 0<k<N \tag{4.8}$$

where $\beta_o = 0$ and $\beta_N = 1$ then the β_k remain ordered and within the range from 0 to 1 regardless of the values of the γ_k. The γ_k are found by rearranging (4.8) to be

$$\gamma_k = \tan\{\pi\left[((\beta_k-\beta_{k-1})/(\beta_{k+1}-\beta_{k-1}))-1/2\right]\} \quad ; \quad 0<k<N\,. \tag{4.9}$$

It is easy to calculate the γ_k from the β_k using (4.9), and (4.8) forms a set of linear equations for the β_k in terms of the inverse tangents of the γ_k. Hence, for the purposes of the iterative model fitting procedure, the model parameters representing the radii of the rings are chosen to be the γ_k. As previously, the model parameters representing the measurements and conductivity are chosen to be $\ln z_{nn}$ and $\ln\alpha_k$ respectively.

4.2 SMOOTH CONDUCTIVITY DISTRIBUTIONS

Piecewise constant conductivity distributions of the type described in §4.1 need many rings to represent smooth conductivity distributions (figure 4.1b). For the latter type of conductivity distribution it is more appropriate to use an analytic representation of the conductivity as a function of radius. In this section the relationship between the voltage and current density on the surface of a region having a smooth circularly symmetric conductivity distribution is developed.

Consider the circularly symmetric conductivity distribution shown in figure 4.9. The voltage within R is $V(r,\theta)$ and the conductivity is $\sigma(r)$, where $r(=r'/r_a)$ is the normalised radius. The voltage within R is governed by Poisson's Equation (2.11). The independent source density in R is zero and the conductivity is independent of θ, so that Poisson's Equation reduces

$$\nabla^2 V + (dV/dr)(d\ln\sigma/dr) = 0. \tag{4.10}$$

Expressing the voltage in the form

$$V(r,\theta) = \sum_{m=0}^{\infty} R_m(r)\Theta_m(\theta) \tag{4.11}$$

and then applying the method of separation of variables (see §2.7.1) to (4.1 gives

$$(r/R_m)dR_m/dr + (r^2/R_m)d^2R_m/dr^2 + (r^2/R_m)(dR_m/dr)d\ln\sigma/dr - m^2 = 0 \tag{4.12a}$$

and

$$(1/\Theta_m)d^2\Theta_m/d\theta^2 + m^2 = 0 \ . \qquad (4.12b)$$

The solutions to (4.12b) are the cosine and sine functions (see (2.84)), and are independent of the conductivity.

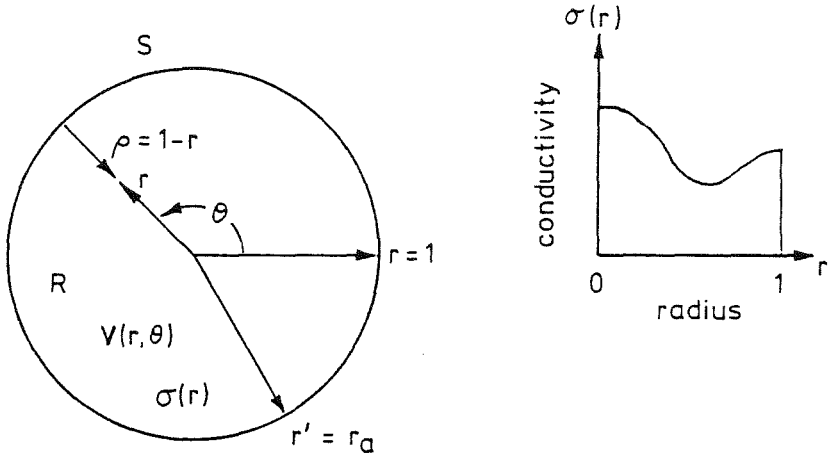

Figure 4.9: Smooth circularly symmetric conductivity distribution. All orders of derivatives of conductivity with respect to radius are continuous for r between 0 and 1. The radius of the distribution is $r' = r_a$. The normalised radial coordinates are $r = r'/r_a$.

Equation (4.12a) is further simplified by making the substitutions

$$Y_m = 1/(d\ln R_m/d\ln r) = (R_m/r)/(dR_m/dr) \qquad (4.13a)$$

and

$$X = d\ln\sigma/d\ln r = (r/\sigma)d\sigma/dr \ . \qquad (4.13b)$$

Using these substitutions gives

$$1 - r(dY_m/dr) + XY_m - m^2Y_m^2 = 0 \ . \qquad (4.14)$$

The voltage and its derivatives must be finite and continuous everywhere within R, which means that $R_m(r) \to r^m$ as $r \to 0$. Substituting $R_m = r^m$ into (4.13a) then shows that $Y_m \to 1/m$ as $r \to 0$. Y_m is therefore suitably expressed by the power series

$$Y_m(r) = (1/m) \sum_{n=0}^{\infty} y_{mn} r^n \ , \qquad (4.15)$$

where y_{m0} is always unity. Putting $Y_m(0) = 1/m$, and $r = 0$ into (4.14) shows that X(0) must be zero. Thus X(r) is suitably expressed by the power series

$$X(r) = \sum_{n=1}^{\infty} x_n r^n . \qquad (4.16)$$

It would be acceptable to use series other than power series (e.g. a sum of Bessel functions) to represent $Y_m(r)$ and $X(r)$. Power series are used here for ease of manipulation.

Using the boundary conditions (3.1) and (3.2) at r=1 ($r'=r_a$), and using (2.84), (4.11), (4.13a), (4.14) and (4.15) gives the relationship between the current density $J(r_a,\theta)$ and voltage $V(r_a,\theta)$ on the boundary S in terms of their Fourier components V_m, U_m, J_m and I_m. The relationship is

$$z_{mm} = V_m/J_m = U_m/I_m = -\left[r_a/m\sigma(1)\right]\sum_{n=0}^{\infty} y_{mn} \quad , \qquad (4.17)$$

where $\sigma(1)$ is the conductivity at r=1, and the z_{mm} are the driving point impedances (see §3.2). The factor r_a appears on the right hand side of (4.17) because $J(r_a,\theta)$ is measured with respect to the unnormalised radial coordinate r'. Here, as with the piecewise continuous conductivity distribution in §4.1, a particular Fourier component of current density is related only to the same Fourier component of voltage. The comments on the significance of this relationship made in §4.1 therefore apply equally well here with respect to the smooth circularly symmetric conductivity distribution, as illustrated by figure 4.9.

It is necessary to relate the y_{mn} to the x_n before (4.17) can be used to evaluate the driving point impedances z_{mm}. This is achieved by substituting (4.15) and (4.16) into (4.14) and rearranging to give

$$y_{m0} = 1 \qquad (4.18a)$$

and

$$y_{mn} = \left[x_n - m\sum_{k=1}^{n-1} y_{mk}y_{m,n-k} + \sum_{k=1}^{n-1} y_{mk}x_{n-k}\right]/(2m+n) . \qquad (4.18b)$$

The y_{mn} can be determined recursively using (4.18b), and summed and substituted into (4.17) to calculate z_{mm}. However the infinite sum in (4.17) may not necessarily converge (see, for instance, §4.2.1).

4.2.1 Comparison of Smooth and Piecewise Constant Distributions

When the number of rings in a piecewise constant conductivity distribution (figure 4.1a) is increased without limit, it can arbitrarily closely approximate any smooth conductivity distribution (figure 4.1b). It is therefore possible to compare numerically the driving point impedances calculated using (4.17) with those calculated using (4.2). Consider therefore the two smooth conductivity distributions $\sigma(r)$ illustrated in figure 4.10. The

smooth distributions are shown approximated by piecewise constant conductivity distributions having 10 rings. The outer radius and the conductivity of the kth ring are $r_k = (k/N)^{\frac{1}{2}}$ and $\sigma_k = \sigma(\left[(k-\frac{1}{2})/N\right]^{\frac{1}{2}})$ respectively, where N is the number of rings.

Figure 4.11 shows the difference between the driving point impedances for the two conductivity distributions shown in figure 4.10a. The difference is shown as the root mean square value of the percentage difference between all of the driving point impedances from $z_{1,1}$ to $z_{64,64}$. As the number of rings is increased the difference between the z_{nn} for the smooth distribution and the z_{nn} for the piecewise constant distribution approaches zero. Thus either (4.17) or (4.2) can be used to accurately calculate the driving point impedances for a smooth circularly symmetric conductivity distribution.

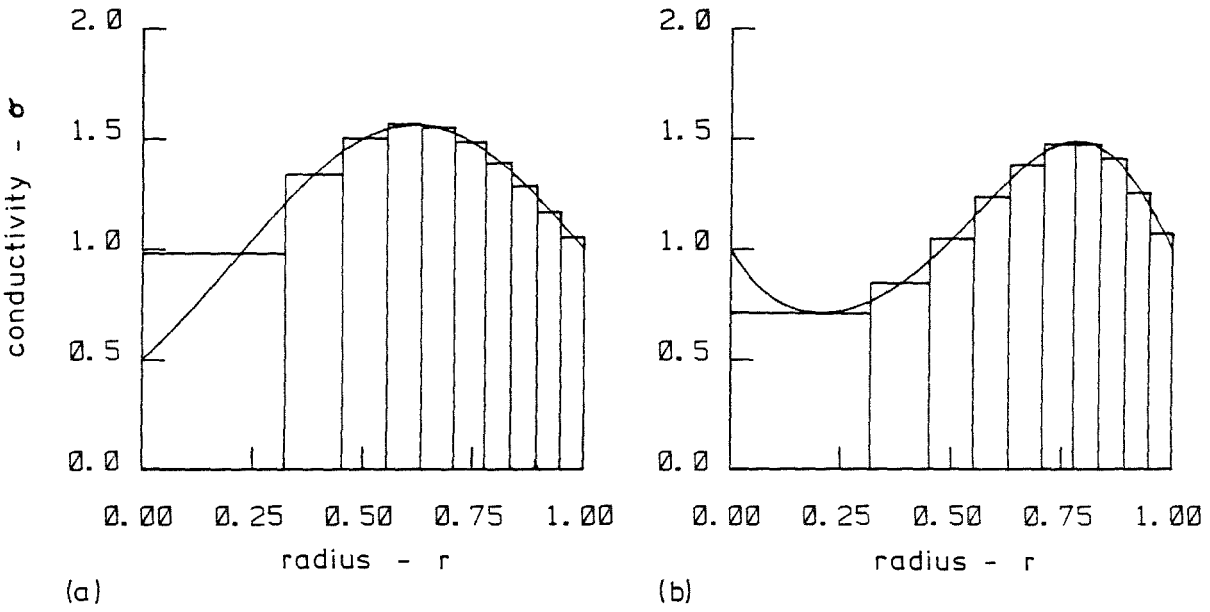

Figure 4.10: Smooth conductivity distributions approximated by piecewise constant models.

(a) $\ln\sigma(r) = -0.693 + 3.701r - 3.008r^2$.

(b) $\ln\sigma(r) = -3.670r + 11.335r^2 - 7.666r^3$.

Table 4.1 lists the z_{nn} calculated for the smooth conductivity distribution shown in figure 4.10b using both (4.17) and (4.2) with 200 rings. In this situation the sum of the y_{mn} in (4.17) does not converge for the lower order driving point impedances (i.e. $n \leq 11$). In order to avoid non-convergence it is therefore advisable to use a many ring approximation to represent a smooth conductivity distribution, and to use (4.2) to calculate the z_{nn} rather than using (4.17).

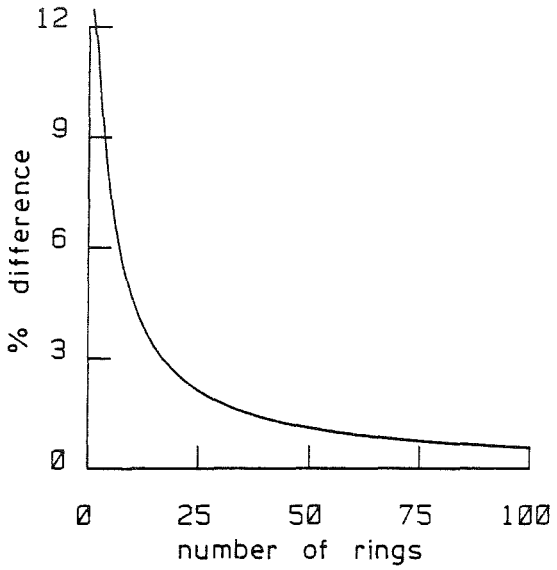

Figure 4.11: Difference in driving point impedances for smooth conductivity distribution in figure 4.10a and piecewise constant approximation. The number of rings in the approximation is shown on the abscissa.

Table 4.1: Transfer impedances z_{nn} calculated for the smooth conductivity distribution shown in figure 4.9b. "Smooth" and "Rings" indicate the values obtained using (4.17) and (4.2) respectively. The difference between the values are also shown. All numbers are rounded in the last digit.

n	Smooth	Rings	Difference
1	-1191036	-0.860	-1191036
2	-749041	-0.395	-749041
3	237184	-0.263	237184
4	-226196	-0.200	-226196
5	131813	-0.163	131813
6	-134217	-0.138	-134217
7	-92223	-0.120	-92223
8	94001	-0.107	94001
9	69634	-0.096	69634
10	53365	-0.087	53365
11	-507	-0.080	-507
12	-3.033	-0.074	-2.959
13	-0.091	-0.069	-0.022
14	-0.064	-0.064	0.000
15	-0.060	-0.060	0.000
16	-0.056	-0.057	0.000
17	-0.053	-0.054	0.000
18	-0.051	-0.051	0.000
19	-0.048	-0.049	0.000
20	-0.046	-0.046	0.000

4.2.2 Imaging Smooth Distributions

In this subsection a simple direct formulation is derived which enables the driving point impedances to be interpreted in terms of a smooth conductivity distribution. In order to derive the formulation it is useful to express $Y_m(r)$ and $X(r)$ (see (4.13)) in terms of $\rho = 1-r$ (see figure 4.9). Substituting $\rho=1-r$, $Y_m(\rho)$ and $X(\rho)$ into (4.14) gives

$$1 + (1-\rho)dY_m/d\rho + XY_m - m^2Y_m^2 = 0 . \qquad (4.19)$$

Rearranging (4.19) to isolate the function X gives

$$X = m^2Y_m + \left[(\rho-1)dY_m/d\rho - 1\right]/Y_m . \qquad (4.20)$$

Here as in §4.2, $Y_m \to 1/m$ as $r\to 0$, which means that $Y_m \to 1/m$ as $\rho\to 1$. Therefore a suitable power series representation for Y_m is

$$Y_m(\rho) = (1/m)\left[y_{m0} + \sum_{n=1}^{\infty} y_{mn}\rho^n\right] \qquad (4.21a)$$

where

$$\sum_{n=0}^{\infty} y_{mn} = 1. \qquad (4.21b)$$

Hence at the boundary $\rho=0$ the Fourier components of the voltage and current density are related by (cf (4.17))

$$z_{mm} = V_m/J_m = U_m/I_m = -\left[r_a/m\sigma(0)\right]y_{m0} \qquad (4.22)$$

where $\sigma(0)$ is the conductivity at $\rho=0$, which is the same remember as $r=1$. Provided $\sigma(0)$ is known then the y_{m0} can be directly inferred from the measurements.

Consider now substituting (4.21a) into (4.20). The derivative $dY_m/d\rho$ can be evaluated term by term, and the ratio $\left[(\rho-1)dY_m/d\rho-1\right]/Y_m$ can be resolved into a single power series in ρ by dividing the denominator into the numerator (see Appendix 4). The coefficients of the resulting series depend upon the coefficients of both the numerator and the denominator, and here are functions of m and y_{mn}. Therefore $X(\rho)$ is of the form

$$X(\rho) = \sum_{n=0}^{\infty} F_n(m, y_{m0}, \ldots, y_{mk})\rho^n \qquad (4.23)$$

where the F_n are nonlinear functions and k is a positive integer.

Equation (4.23) depends upon the voltage within the region R (see figure 4.9). However $X(\rho)$ is only a function of the conductivity within R. In particular at $\rho=0$, $X(\rho)$ and all of the derivatives of $X(\rho)$ are proportional to certain constants x_n, i.e.

$$d^n X(\rho)/d\rho^n = n! x_n \tag{4.24}$$

so that $X(\rho)$ may also be expressed by

$$X(\rho) = \sum_{n=0}^{\infty} x_n \rho^n \ . \tag{4.25}$$

Differentiating (4.23) and evaluating the derivatives at $\rho=0$, and then equating the derivatives to those in (4.24) gives the set of nonlinear equations

$$x_n = F_n(m, y_{mo}, \ldots , y_{mk}) \ . \tag{4.26}$$

All of the y_{m0} are known from measurements so that (4.21b) allows some of the y_{mk} to be eliminated. However it is not clear from (4.26) whether the x_n can be determined.

Suppose for simplicity that the series for $Y_m(\rho)$ is represented to a first approximation by a quadratic (i.e. $y_{mn}=0$ for $n>2$). Substituting $Y_m(\rho)$ into (4.20) and then performing the differentiation and division gives

$$X(\rho) = F_1(m, y_{m0}, y_{m1}) + F_2(m, y_{m0}, y_{m1}, y_{m2})\rho + O(\rho^2) \tag{4.27}$$

where

$$x_1 = F_1(m, y_{m0}, y_{m1}) = m y_{m0} - (m+y_{m1})/y_{m0} \ , \tag{4.28a}$$

$$x_2 = F_2(m, y_{m0}, y_{m1}, y_{m2}) = m y_{m1} + \left[y_{m1} - 2y_{m2} + (m+y_{m1}) y_{m1}/y_{m0}\right]/y_{m0} \tag{4.28b}$$

and $O(\rho^2)$ means terms of order ρ^2 and higher. Using (4.28a) and (4.28b) each for two values of m, say k and ℓ, allows x_1 and x_2 to be eliminated. The resulting expressions are

$$F_1(k, y_{k0}, y_{k1}) = F_1(\ell, y_{\ell 0}, y_{\ell 1}) \tag{4.29a}$$

and

$$F_2(k, y_{k0}, y_{k1}, y_{k2}) = F_2(\ell, y_{\ell 0}, y_{\ell 1}, y_{\ell 2}) \ . \tag{4.29b}$$

Using (4.21b), which now has only three terms because $Y_m(\rho)$ is quadratic, gives for m=k and m=ℓ respectively

$$y_{k0} + y_{k1} + y_{k2} = 1 \tag{4.29c}$$

and

$$y_{\ell 0} + y_{\ell 1} + y_{\ell 2} = 1 \ . \tag{4.29d}$$

Equations (2.29a) to (2.29d) are four equations in four unknowns, since y_{k0} and $y_{\ell 0}$ are inferred from the measurements. Their solutions are

$$b_1 = \frac{2b_0(b_0-a_0)+[pb_0(1-a_0^2)-qa_0(1-b_0^2)][(2pa_0+3)b_0+q(1-b_0^2)]}{qa_0-pb_0+3a_0b_0(pa_0-qb_0)} \qquad (4.30a)$$

and

$$b_2 = 1 - b_1 - b_0 \qquad (4.30b)$$

where two of the unknowns are obtained by putting $a_0 = y_{k0}$, $b_0 = y_{\ell 0}$, $b_1 = y_{\ell 1}$, $b_2 = y_{\ell 2}$, $p = k$ and $q = \ell$, and the other two are obtained by putting $a_0 = y_{\ell 0}$, $b_0 = y_{k0}$, $b_1 = y_{k1}$, $b_2 = y_{k2}$, $p = \ell$ and $q = k$.

Once b_0, b_1 and b_2 are known, x_1 and x_2 are given by (4.28). Unfortunately x_1 and x_2 do not determine $X(\rho)$ because of the terms $O(\rho^2)$ in (4.27). However all of the coefficients x_n can be found by performing the power series division in (4.20) using the recursive relations given in Appendix 4. The conductivity can then be found by solving (4.13b). Putting $r=1-\rho$ and $\sigma=\sigma(\rho)$ into (4.13b) gives

$$X(\rho) = (\rho-1)d\ln\sigma/d\rho \, . \qquad (4.31a)$$

Solving (4.31a) for the conductivity gives

$$\sigma(\rho) = \sigma(0)\exp\left[\int_0^\rho X(\rho)/(\rho-1)\, d\rho\right] \, , \qquad (4.31b)$$

where the constant of integration has been chosen to be $\ln\sigma(0)$.

The conductivity distribution can be deduced from (4.30) using any two different driving point impedances. However this assumes that a quadratic approximation can be a good representation of $Y_m(\rho)$. When more than two driving point impedances are known, the validity of the assumption can be checked. If, in this situation, the conductivity distributions deduced using all possible pairs of driving point impedances are in agreement then the assumption is justified.

In §4.3 $\sigma(\rho)$ is calculated from the driving point impedances $z_{1,1}$ and $z_{2,2}$ using both simulated and experimental data. The conductivity distributions found are compared with those obtained, when interpreting the same data, using the piecewise constant models described in §4.1.

4.3 CASE STUDIES

Case studies are particularly useful for observing the effect of the controlled alteration of variables which have particular bearing on the phenomena being studied. Experimental and simulated studies are both valuable, each often being suited to different situations. In this section various cases of both simulated and experimental measurements are interpreted in terms of both the smooth model (§4.2.2) and the piecewise constant models (§4.1.2).

The experimental measurements used here were obtained using the technique described in §4.1.1 and the equipment described in Appendices 1 and 2. The piecewise constant models were chosen to have either 15 or 10 fixed radii when interpreting simulated or experimental measurements respectively, or 4 variable radii for both types of measurement.

Studies have been made to determine how accurately measurements need be fitted for a model to accurately represent a conductivity distribution. The effect which errors in the fit between the actual measurements and those given by a model have on the modelled conductivity distribution are examined. Errors due to both random noise and premature termination of iterative modelling are examined. Measurements from both smooth and piecewise constant conductivity distributions are interpreted in terms of both the smooth and the two piecewise constant models. The different interpretations are compared to determine if any one type of model is better than the others. Interpretations of experimentally measured data is compared with similar interpretations of simulated data so that the effect of experimental noise can be observed. Finally experimental measurements from each of three conductivity distributions are interpreted in terms of the smooth model and both of the piecewise constant models.

4.3.1 Model Sensitivity to Data Fit

When iterative modelling is used to interpret measurements it is not usually possible to adjust the model so that it exactly mimics the measurements. The error in fit may be due to noise in the measurements or due to premature termination of the iterative procedure. In either case some difference between the conductivity distribution represented by the model and the actual conductivity distribution is unavoidable.

Suppose that there is no error in the measurements so that ideally a model could be found to exactly fit them. It is then possible to study how small the difference between the actual measurements and those given by the model must be made in order for the model to represent the actual conductivity distribution to a particular level of accuracy. Consider, therefore, the 15-ring conductivity distribution shown in figure 4.12a, from which the ideal noise-free measurements $z_{nn}^{(i)}$ are calculated to an accuracy of seven decimal places. Let $z_{nn}^{(m)}$ be the measurements derived from a model fitted to the $z_{nn}^{(i)}$. In order to quantify the error in the data fit the root mean square percentage difference between $z_{nn}^{(i)}$ and $z_{nn}^{(m)}$ is used here, i.e.

$$\text{error} = 100 \left\{ \sum_{n=1}^{N} \left[(z_{nn}^{(m)} - z_{nn}^{(i)}) / z_{nn}^{(i)} \right]^2 / N \right\}^{\frac{1}{2}} .$$

Figures 4.12b to 4.12f show a series of models obtained by iteratively fitting a 15-ring fixed-radii model to the $z_{nn}^{(i)}$. Each of the models (b) to (f) fits the $z_{nn}^{(i)}$ with an error in data fit of about an order of magnitude lower than the preceding one. Figure 4.12b shows that a conductivity distribution which is almost uniform fits the experimental error to within 1%. A 1% error may not seem large yet figure 4.12b is clearly a poor representation of the distribution illustrated in figure 4.12a. As the model is adjusted to minimise the error in data fit (i.e. figures 4.12b to 4.12f), the conductivity distribution represented by the model approaches the actual conductivity distribution (figure 4.12a). The error shown in figure 4.12f is only in the last digit of the seven digit accuracy used for the measurements. However the model contains only the gross detail of the actual conductivity distribution.

The near equality of the measurements derived from two significantly different conductivity distributions, such as those shown in figures 4.12a and 4.12f, is often referred to as the "equivalence" of the distributions (see §1.2.4). This equivalence results from the low sensitivity of the measurements to changes in the conductivity, and means in practice that the model fitting must be continued until no reduction can be made in the error in the data fit. Even then the conductivity distribution represented by the model may not be a good representation of the actual distribution, as is illustrated here by figures 4.12f and 4.12a respectively.

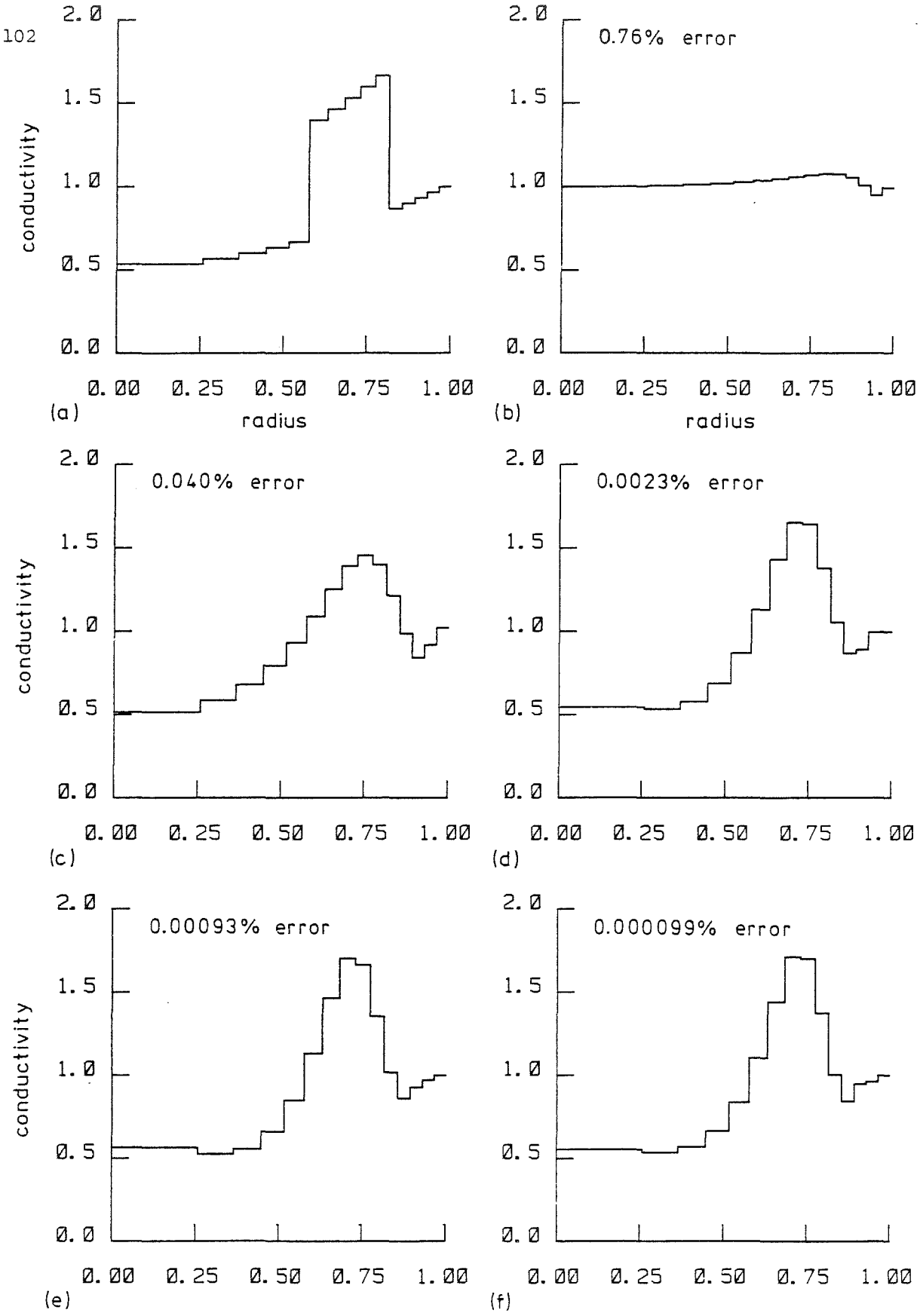

Figure 4.12: Models iteratively fitted to the measurements simulated from the conductivity distribution in (a). The RMS error in data fit is shown.

4.3.2 Effect of Random Noise in Measurements

In practice it is not possible to measure voltage to one part in 10 million, which is the accuracy of the measurements simulated in §4.3.1. Therefore, the conductivity distribution deduced by iterative modelling to fit practical measurements from the conductivity distribution shown in figure 4.12a, differs from that shown in figure 4.12f. The amount of difference depends on the error in the measurements. In order to observe the effects of different amounts of error on the conductivity distribution deduced, different amounts of random noise were added to the measurements. The measurements resulting from adding noise having a Gaussian probability density distribution to the $z_{nn}^{(i)}$ (see §4.3.1) are called here the $z_{nn}^{(n)}$. The amount of noise added is expressed here as a percentage of the root mean square value of the $z_{nn}^{(i)}$, i.e.

noise added = $100 \{\sum_{n=1}^{N}(z_{nn}^{(i)}-z_{nn}^{(n)})^2\}^{\frac{1}{2}}/\{\sum_{n=1}^{N}(z_{nn}^{(i)})^2\}^{\frac{1}{2}}$. A model was iteratively fitted to the $z_{nn}^{(n)}$, as in §4.3.1, with the iterative procedure continuing until no further reduction in the data fit error appeared possible.

Figure 4.13 shows the models fitted to the $z_{nn}^{(n)}$ for various values of added noise. The error in data fit (§4.1.3) is shown. The models illustrated in figures 4.13b to 4.13f become progressively poorer representations of the conductivity distribution shown in figure 4.12a as the noise in the measurements increases. It is interesting to note that the data fit error is consistently the same order of magnitude as the actual noise added to the measurements. It therefore seems that the data fit error can be used as an estimate of the actual noise in the measurements.

It is informative to compare the model having a 0.76% data fit error, shown in figure 4.12b, with the model having a 1.6% error, shown in figure 4.13e. The latter is a significantly better representation of the actual conductivity distribution (figure 4.12a) than is the former. Suppose a predetermined data fit error around 1% is chosen as a termination criterion for the iterative modelling procedure. The model deduced using the noisy data is then a better representation of the actual conductivity distribution than is the model deduced using the noise-free data. It would appear this situation arises because the former model has been chosen only after the iterative procedure has converged, whereas the latter model has been chosen prematurely. It is therefore important to continue the iterative procedure until no further reduction in the difference between the actual measurements and those given by the model can be found.

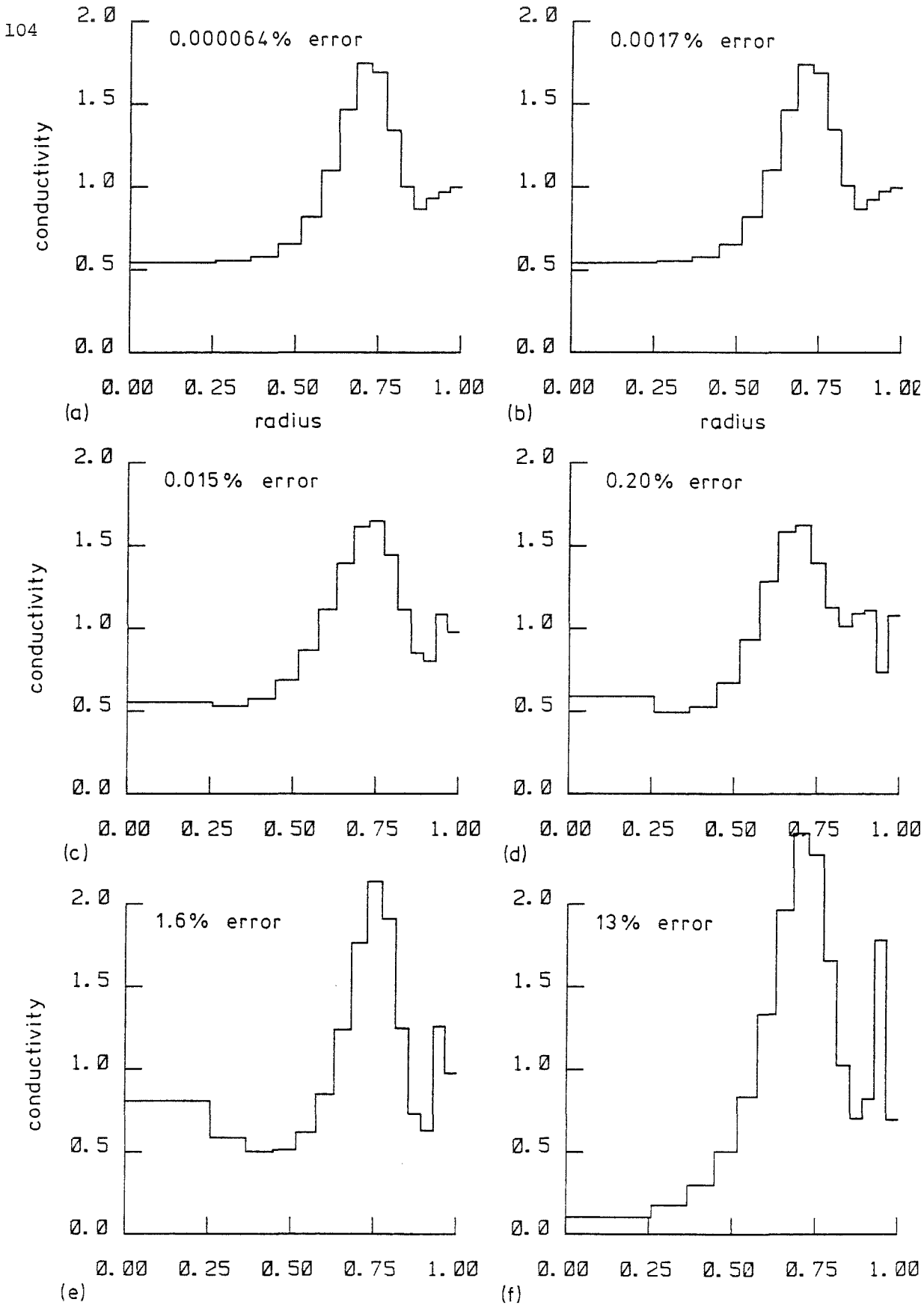

Figure 4.13: Models fitted to data from the conductivity distribution in Figure 4.12a after adding random noise (see text)

(a) no noise, (b) 0.001% noise, (c) 0.01% (d) 0.1%, (e) 1%, (f) 10%.

The RMS error in data fit is shown.

4.3.3 Alternative Choice of Models

It is not in general known whether the conductivity distribution being imaged is best represented by a piecewise constant model or by a smooth model. It is therefore of interest to examine whether there is any advantage in choosing the model used for interpretation of the measurements to be of the same type as the conductivity distribution.

Consider therefore the three conductivity distributions shown in figure 4.14. The distributions (a), (b) and (c) have been chosen so that they can be accurately represented by a fixed-radii piecewise constant model (see figure 4.7a), a variable-radii piecewise constant model (see figure 4.7b) and a smooth model (see figure 4.1b) respectively. Measurements were calculated from each of these distributions and all measurements were interpreted in terms of each of the three types of models. Figures 4.15, 4.16 and 4.17 show respectively the fixed-radii piecewise constant models, the variable-radii piecewise constant models and the smooth models deduced from these measurements. The models (a), (b) and (c) in each of figures 4.15 to 4.17 correspond to the conductivity distributions labelled the same way in figure 4.14.

Two interesting features arise when comparing figures 4.15, 4.16 and 4.17 with figure 4.14. Firstly, all of the models (a), (b) and (c) have the same overall shape as the conductivity distributions (a), (b) and (c) respectively shown in figure 4.14. In this respect each of the three types of models does provide a meaningful interpretation of the measurements from all of the three conductivity distributions. Secondly, the error in the data fit, when the model used to interpret the measurements is of the same type as the conductivity distribution used to generate the measurements, is not necessarily lower than when a different type of model is used. For instance, the error for the model shown in figure 4.16b is significantly greater than that for the model shown in 4.15b. In this situation it would appear sensible to choose the latter model as the better representation of the conductivity distribution shown in figure 4.14b.

It seems that each of the three types of model is suitable for interpreting any of the measurements here, because all of the models deduced represent the gross features of the conductivity distributions. Using the error in data fit as an indication of how closely a particular model represents a conductivity distribution, there does not appear to be any advantage

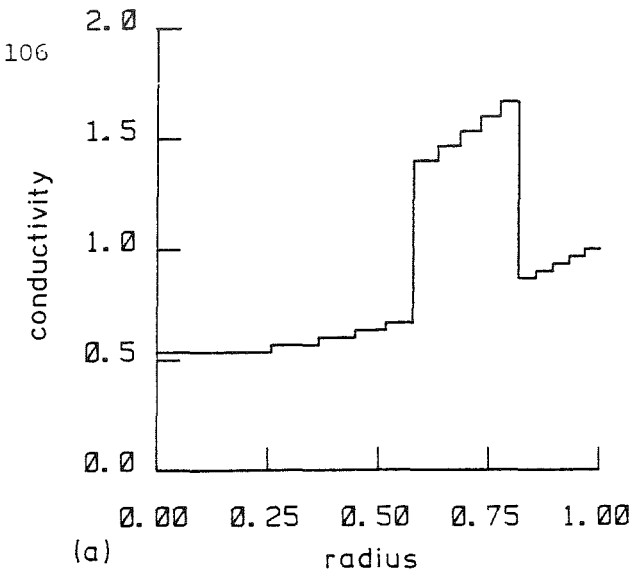

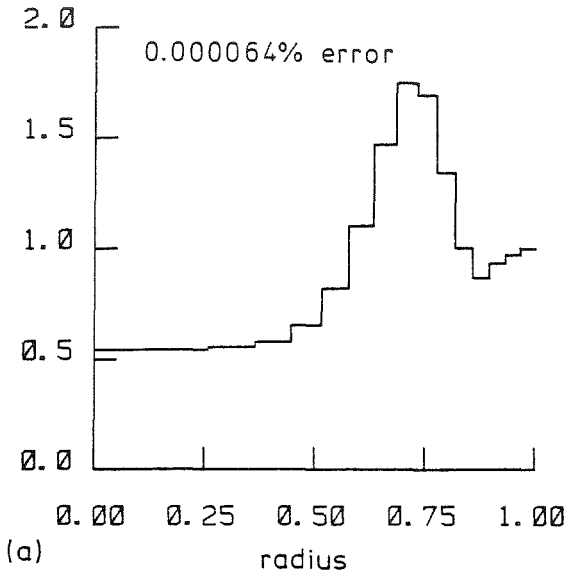

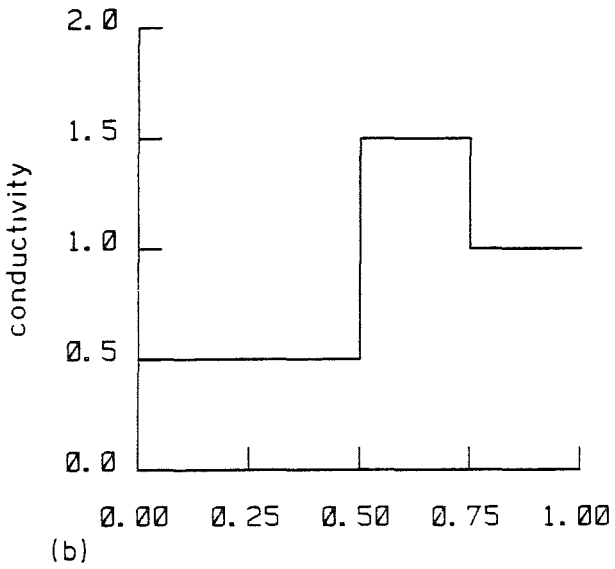

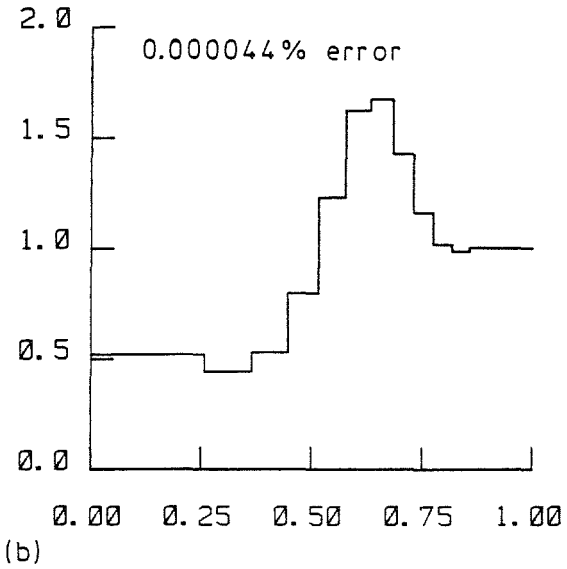

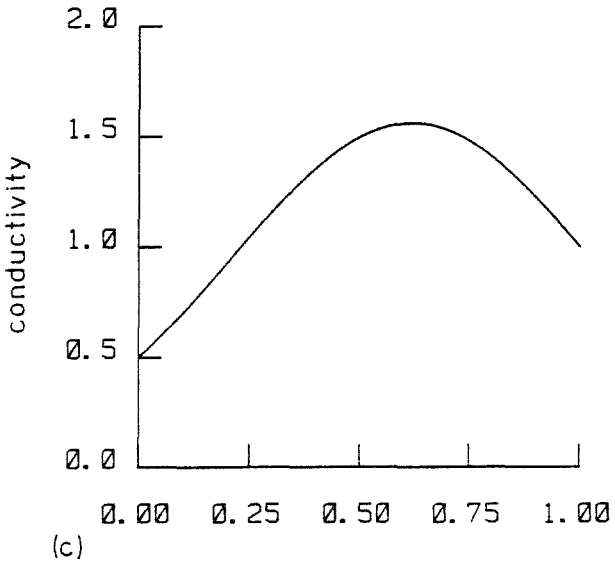

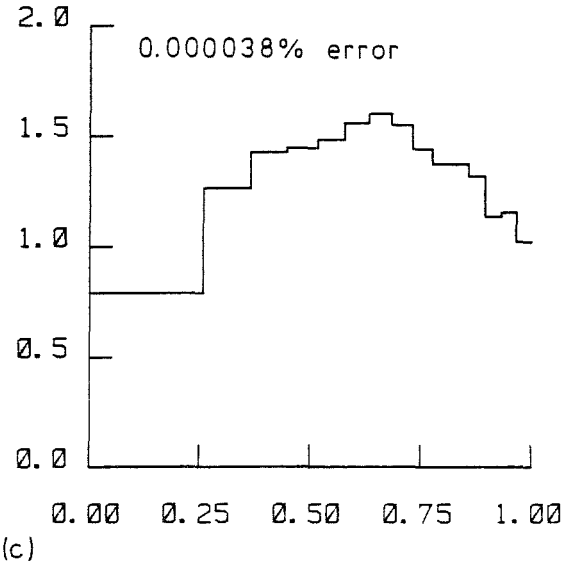

Figure 4.14:

Ideal conductivity distributions used for simulating data for model fitting.

Figure 4.15:

Fixed-radii piecewise constant models fitting data from Figure 4.14. RMS error in data fit is shown.

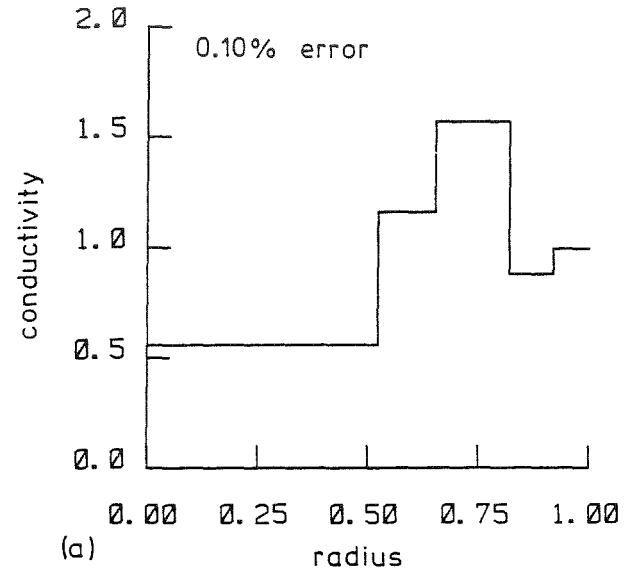

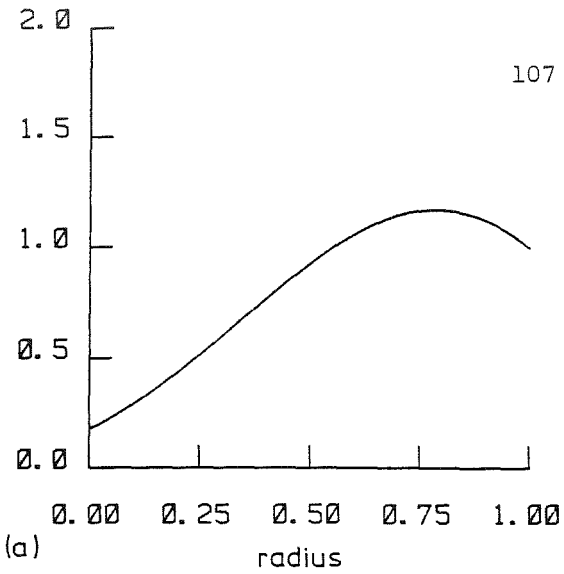

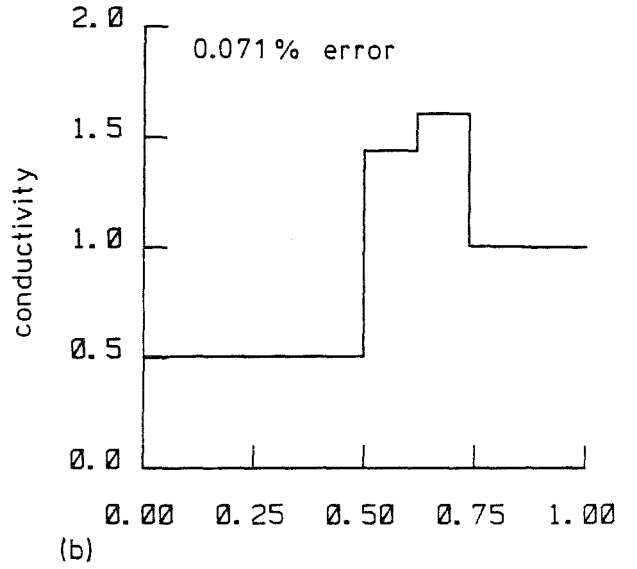

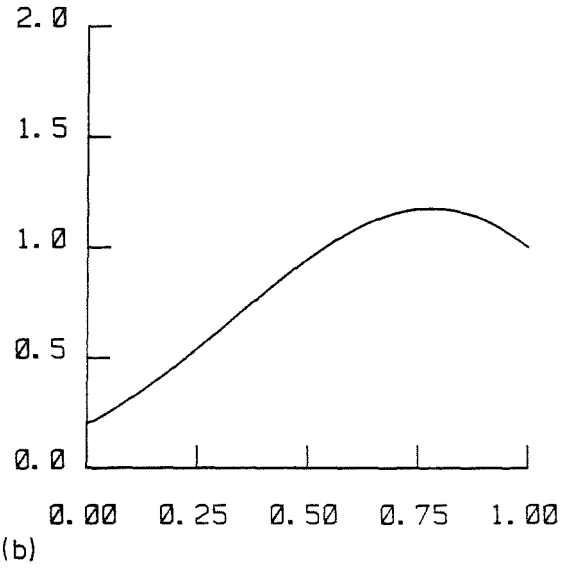

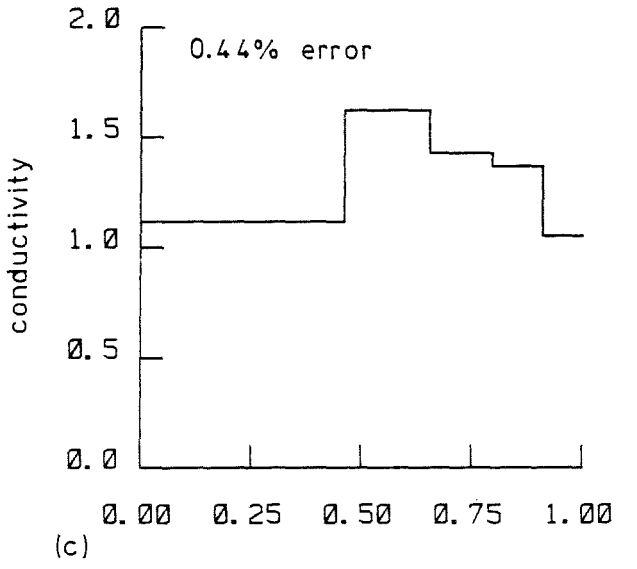

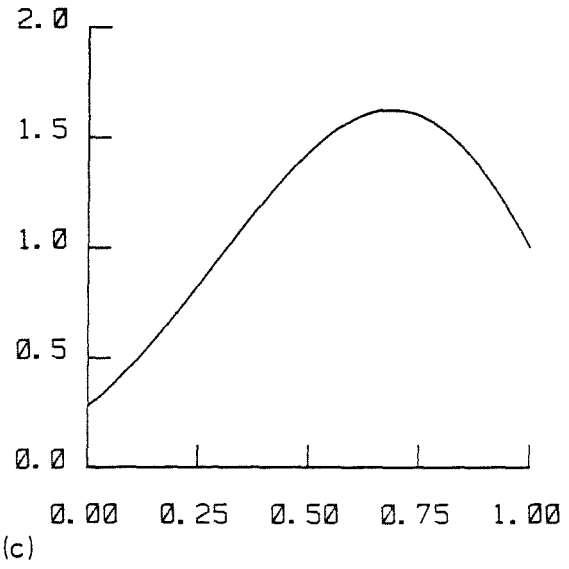

Figure 4.16:

Variable-radii piecewise constant models fitting data from Figure 4.14. RMS error in data fit is shown.

Figure 4.17:

Smooth models fitting the lowest 2 orders of driving point impedances from Figure 4.14.

in choosing the model used for interpretation to be of the same type as the conductivity distribution. This is further demonstration of the practical equivalence of many conductivity distributions for the same measurements.

4.3.4 Measurement Noise in Practice

The usefulness of any imaging technique can only be fully evaluated by determining how well it interprets experimentally measured data. Here, models representing different conductivity distributions are found from experimental measurements. These models are compared with both the actual conductivity distributions, and with models deduced using noise-free simulated measurements.

Measurements were made on conductivity distributions which were uniform apart from a single anomaly (see §3.1) of effectively zero conductivity. A variable-radii piecewise model (cf figure 4.7b) is used here to interpret the measurements. Figure 4.18 shows the actual conductivity distributions (solid lines) and the models deduced using both simulated and experimental measurements (dashes and dots respectively).

The models deduced from experimental and simulated measurements respectively all indicate that there is a region of low conductivity at the centre of the conductivity distributions (see figure 4.18). The radius at which the boundary of this region occurs can be approximately determined from each of the models. However the models shown in figures 4.18a, b and c suggest that there are three regions of different conductivity (i.e. $\sigma=0$, $\sigma=1$, $\sigma=1.5$), whereas there are actually only two.

The models deduced from the noise-free simulated measurements consistently have lower errors in data fit than those deduced from experimental measurements. However, in figures 4.18a, b and c, the former models do not appear to represent the actual conductivity distributions any better than the latter models. This indicates that whatever noise is present in the experimental measurements is not seriously affecting their interpretation. In §4.3.2 it is observed that the error in the data fit is of the same order of magnitude as random noise in the measurements. Based on this observation, it appears, from the errors shown in figure 4.18, that the noise in the experimental measurements reported in this section is between 0.1% and 1%.

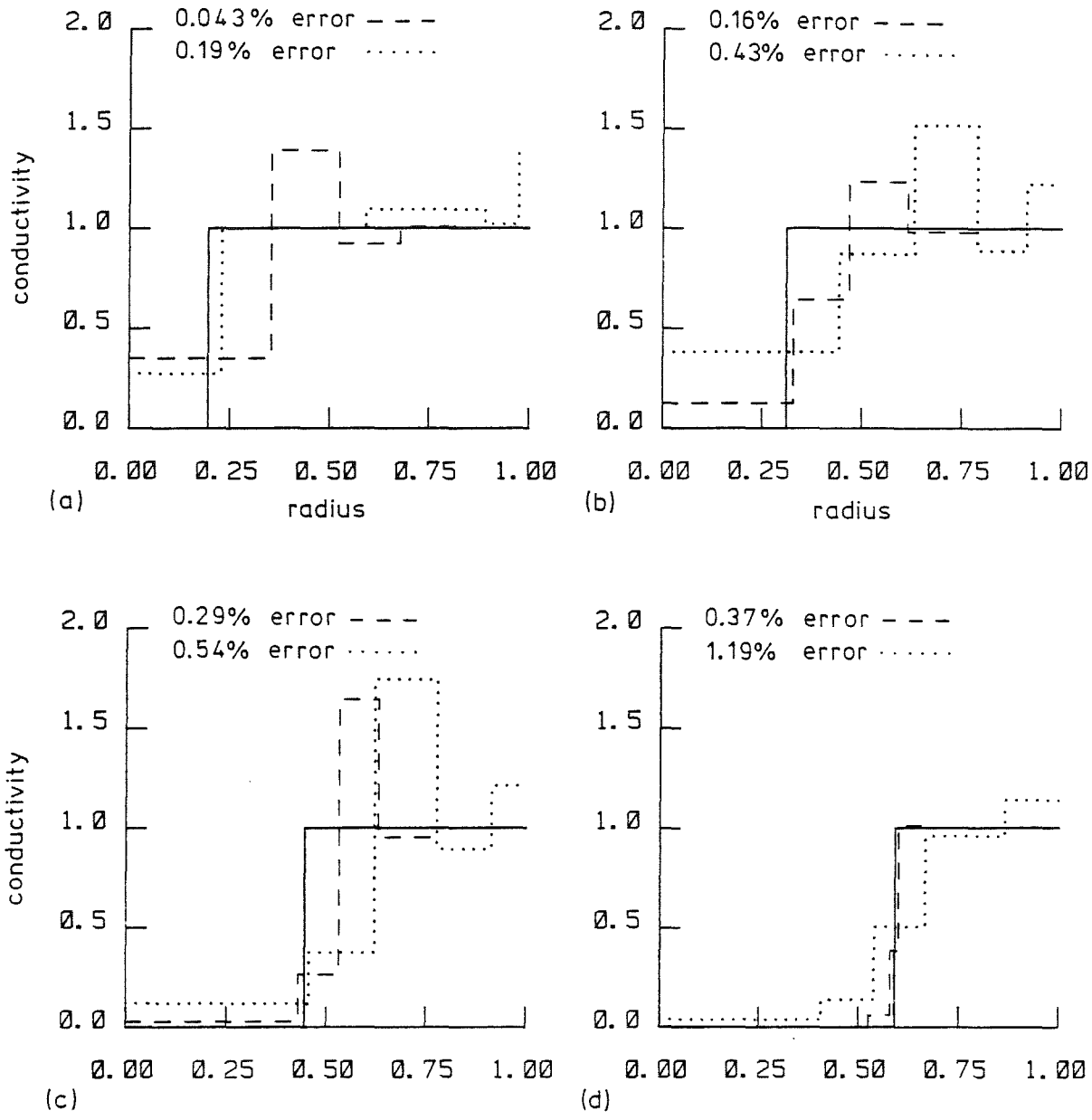

Figure 4.18: Ideal conductivity distributions (solid lines) and models fitted to simulated and experimental measurements (dashes and dots respectively). RMS error in data fit is shown.

4.3.5 Experimental Measurements Interpreted Using Three Models

In §4.3.3 it is shown for noise-free measurements that there is no advantage in choosing the model used to interpret measurements to be of the same type as the conductivity distribution on which the measurements are made. It is of interest here to examine whether this holds true when the measurements are derived from experiment, and therefore contain noise.

In figure 4.19 three conductivity distributions are shown from which experimental measurements were obtained. The conductivity distribution shown in figure 4.19b has uniform conductivity. The other two distributions are uniform apart from anomalies having effectively zero and infinite conductivity respectively (see figures 4.19a and c). Note that the vertical axis in figure 4.19c is in units of resistivity, whereas the vertical axes in figures 4.19a and b are in units of conductivity. Figures 4.20, 4.21 and 4.22 show respectively the fixed-radii piecewise constant, variable-radii piecewise constant, and smooth models fitted to experimental measurements from the distributions shown in figure 4.19. The models labelled (a), (b) and (c) in each of figures 4.20 to 4.22 correspond to the distributions labelled in the same way in figure 4.20.

The models (a), (b) and (c) shown in figures 4.20 to 4.22 have the same overall shape as do the respective conductivity distributions which ideally they should closely resemble (i.e. figures 4.19a, b and c respectively). The models labelled (a) show lower conductivity at the centre (radius = 0) compared to that at the surface (radius = 1). The models labelled (b) have much the same conductivity at all values of radius, and those labelled (c) show a lower resistivity at the centre compared to the surface. None of the three types of model appears better than the others for interpreting the experimental measurements.

The errors in the data fit shown in figures 4.20 and 4.21 are higher than those obtained when using noise-free measurements (see, for instance, figures 4.15 and 4.16 respectively). The higher error indicates the presence of noise in the experimental measurements. Using the value of the error in data fit as an estimate of the noise (see §4.3.2), suggests that the noise here is somewhere between 0.2% and 0.7% of the experimental measurements. This estimate is consistent with that found for the experimental measurements in §4.3.4.

From a practical viewpoint it does not appear important which of the three types of model is chosen to interpret measurements. However it is clear that whatever model is used, the conductivity distribution suggested by the model is not likely to be an accurate representation of the actual conductivity distribution. Therefore any conductivity distribution suggested by any particular model must be considered only as one possible way of interpreting the measurements.

4.4 DISCUSSION

Two distinct types of model have been used in this chapter to represent circularly symmetric conductivity distributions (see §§4.1 and 4.2). Both representations yield the same measurements when representing the same conductivity distribution (§4.2.1). In the models the voltage and current density on the surface of a conducting region are both expressed in terms of their Fourier components (i.e. in the frequency domain). The driving point impedances are defined in terms of these Fourier components and are shown to characterise circularly symmetric conductivity distributions (§§4.1 and 4.2). This approach is in contrast to geophysical electrical measurements where the apparent resistivity, which is a spatial domain representation of the measurements, is used to characterise the conductivity distribution.

A measurement technique is used here which differs from the way the apparent resistivity is measured in geophysics (cf §1.2.2). It is sensible to use a different technique because here voltages and currents are represented in the frequency domain, whereas in geophysics they are represented in the spatial domain. The technique here is to use fixed point current sources and sinks, and to measure the voltage over the entire surface of the region probed (§4.1.1). It is a particularly simple technique to apply in practice. Some methods used to interpret geoelectric measurements do employ a frequency domain approach. One such method assumes that voltage measurements are made over the entire surface of a flat region about a fixed point current source (cf. Langer 1933). These voltage measurements are transformed into the frequency domain for interpretation.

The phenomenon known in geophysics as the "equivalence" of different conductivity distributions (see §1.2.4) is also observed for the distributions examined here (§4.3.1). This observation is not surprising in view of the similarity between the flat stratified model used in geophysics and the

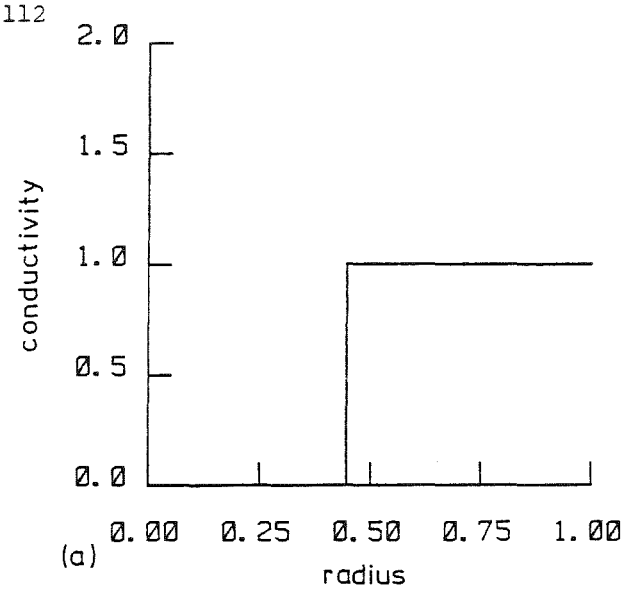

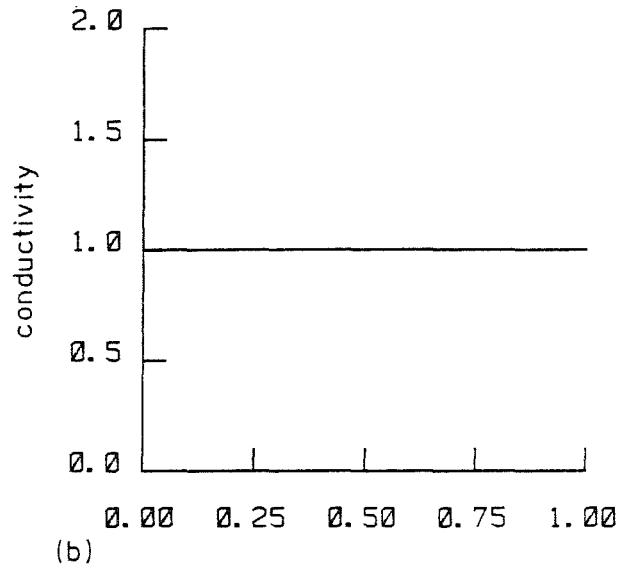

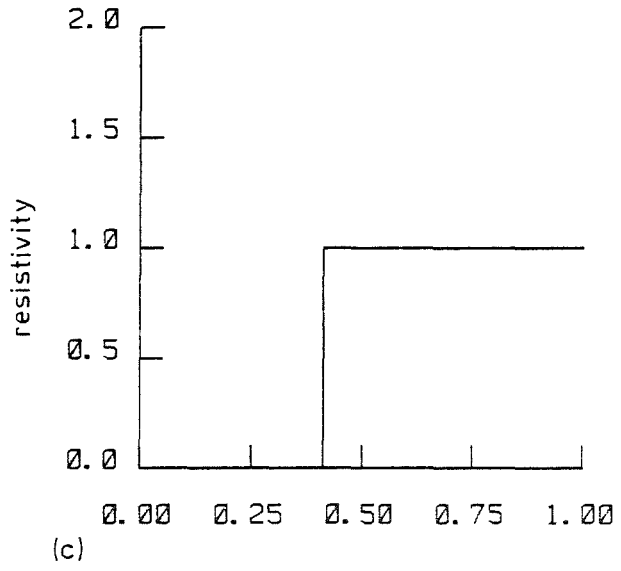

Figure 4.19:

Ideal conductivity distributions from which experimental data was obtained.

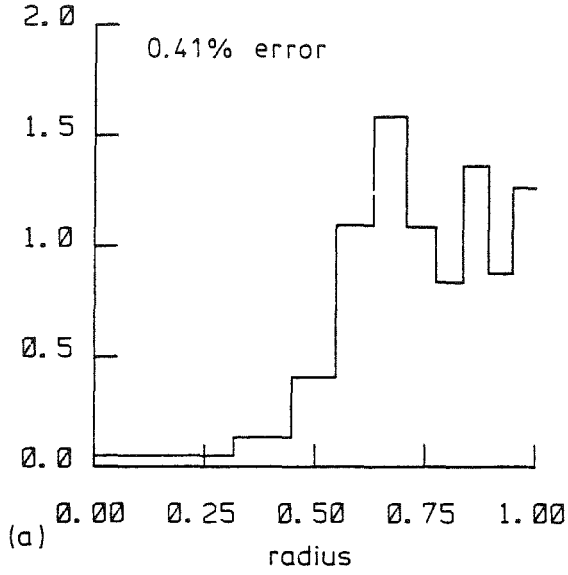

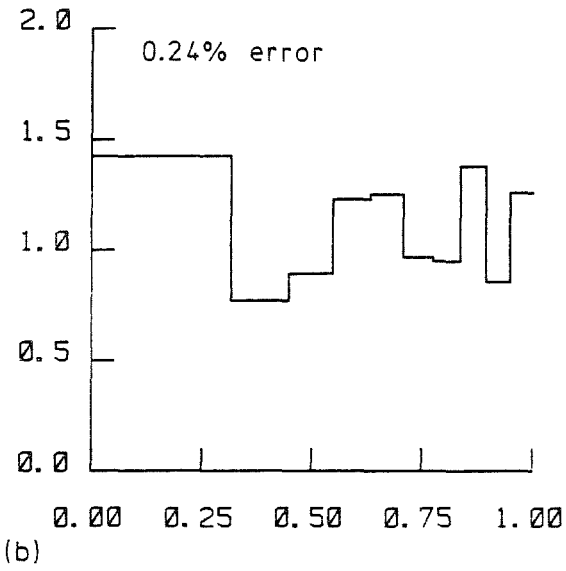

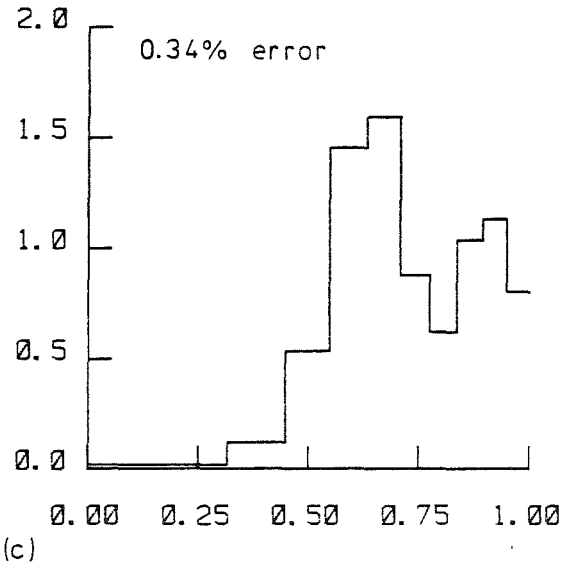

Figure 4.20:

Fixed-radii piecewise constant models fitting experimental data from Figure 4.19. RMS error in data fit is shown.

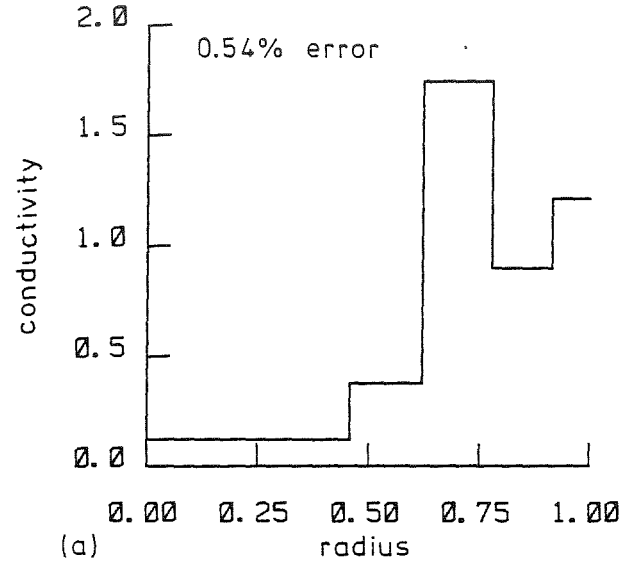

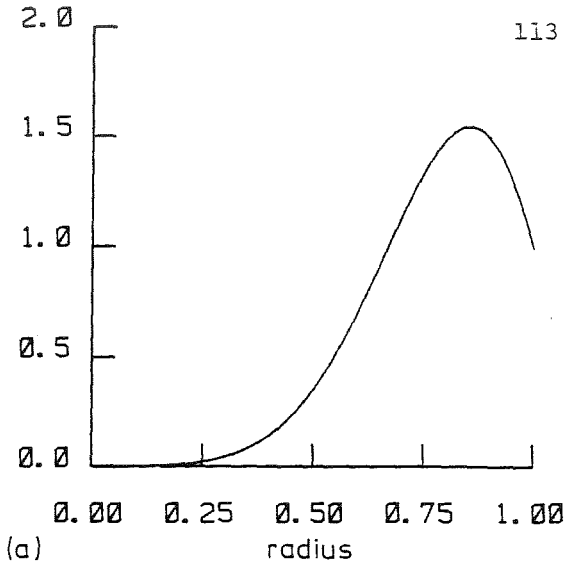

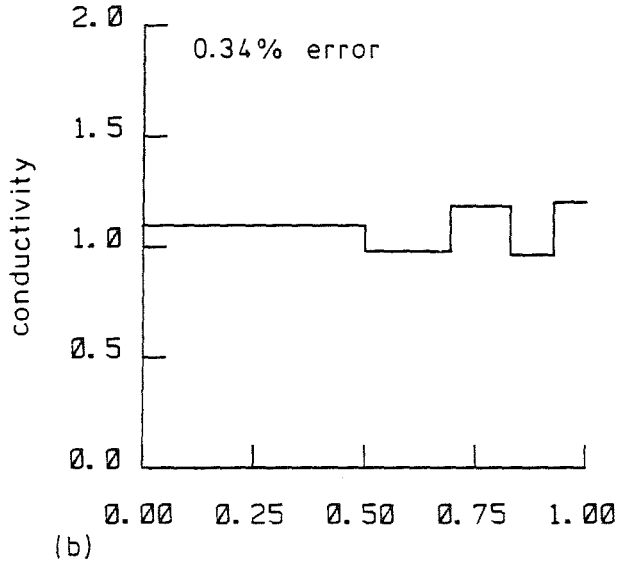

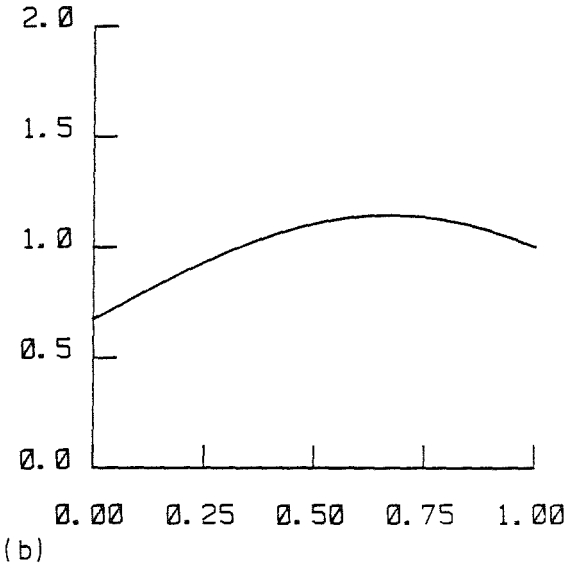

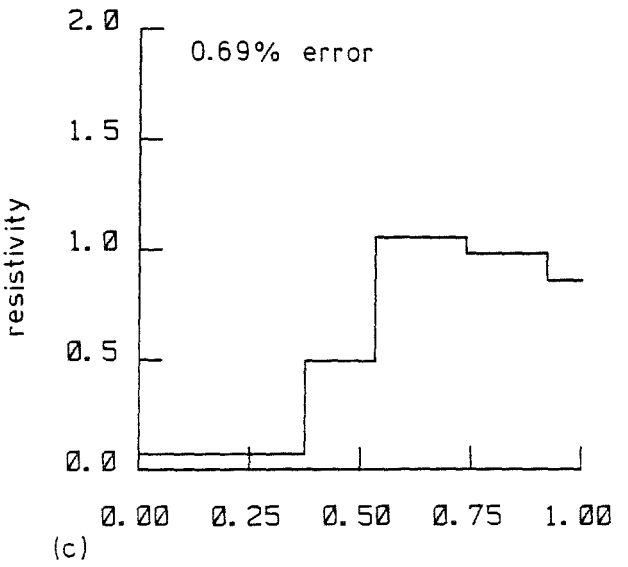

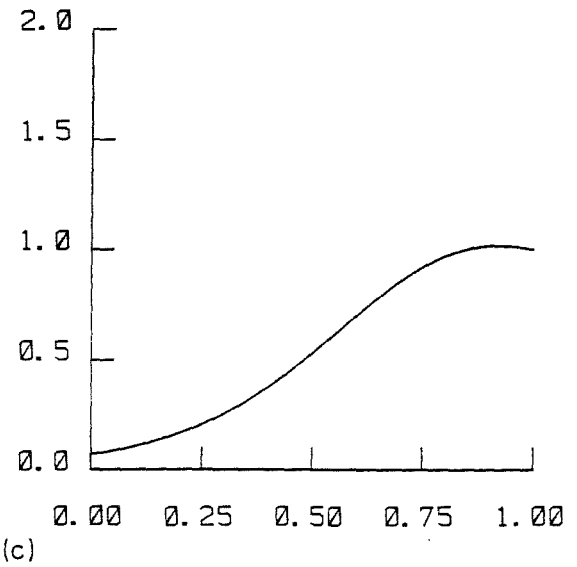

Figure 4.21:

Variable-radii piecewise constant models fitting experimental data from Figure 4.19. RMS error in data fit is shown.

Figure 4.22:

Smooth continuous model fitting the lowest 2 orders of driving point impedances from Figure 4.19.

circularly symmetric models used here (see §4.1). It is not possible to decide which of a number of these equivalent conductivity distributions best represents the conductivity of the region on which measurements are made based on those measurements alone. In §4.3.1 it is shown that seven decimal places of accuracy is not sufficient to avoid this equivalence. In practice it is therefore not important whether a smooth or piecewise constant model is chosen to represent the actual conductivity distribution, because either one can be equally well fitted to the measurements.

The equivalence of conductivity distributions is amply demonstrated here by all of the examples using both experimental and simulated data. Not one of the imaged distributions looks exactly like that from which measurements were made. The cause of this obvious limitation on impedance imaging has previously been encountered in Chapter 3 in terms of the effect the presence of regions of contrasting conductivity has on the measurements, and the sensitivity of the measurements to changes in conductivity. A difficulty in the interpretation of impedance images is posed because of equivalence. In geophysics this difficulty can be overcome by using complementary information derived independently (cf. Vozoff and Jupp 1975). Where possible it would seem sensible to use the same approach when interpreting conductivity distributions such as those imaged here.

CHAPTER 5

GENERAL CONDUCTIVITY DISTRIBUTIONS

General conductivity distributions are those for which the conductivity is a positive real, but otherwise arbitrary, function of position. In this chapter two types of general conductivity distribution are examined. Measurements of voltage and current are identified which are both necessary and sufficient to fully characterise the electrical response of such distributions. A method for representing these measurements is introduced which allows the measurements obtained on different conductivity distributions to be conveniently compared.

Figure 5.1 shows the two types of conductivity distribution examined in this chapter. The smooth distribution (Figure 5.1a) has all orders of derivative continuous with respect to both radius and angle. The multiple offset anomaly distribution (Figure 5.1b) is made up of a circular region having constant conductivity σ_1, in which are imbedded any number N of smaller circular regions. The latter N regions also have constant conductivity, and provided they do not impinge upon one another they are of arbitrary size and position. Both the smooth and the multiple offset anomaly conductivity distributions can represent any two-dimensional conductivity distribution as faithfully as desired.

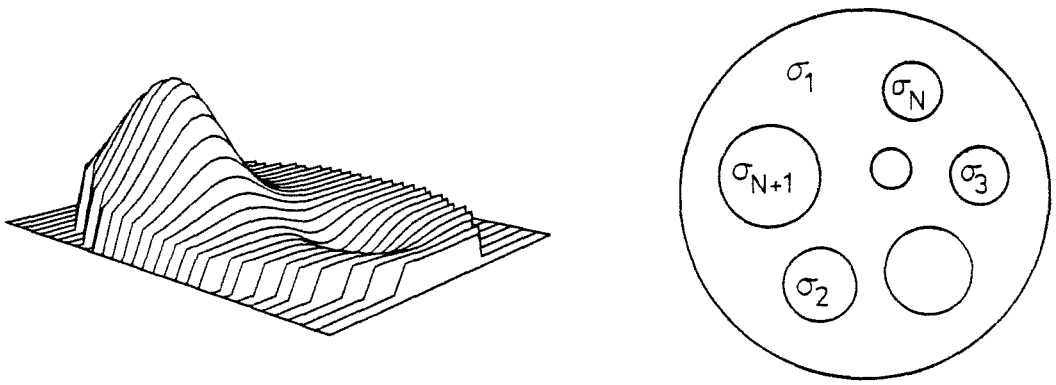

Figure 5.1: General conductivity distributions
(a) Smooth
(b) Multiple offset anomaly.

In order to image a conductivity distribution two steps are usually performed. Firstly a set of measurements is obtained which uniquely characterises the electrical response of the conductive region, and then the measurements are interpreted to yield a representation of the conductivity distribution. Both of these steps are examined in this chapter. Theoretical expressions are derived in order to compare simulated measurements with experimental measurements, and to interpret both simulated and experimental measurements in terms of a simple type of two dimensional conductivity distribution.

5.1 SMOOTH DISTRIBUTIONS

The relationship between the voltage and normal current density on the boundary of a circular region having a smooth conductivity distribution is developed here. This relationship enables a set of measurements to be defined which fully characterises the electrical response of the conductivity distribution.

5.1.1 Description of Approach

Consider the smooth continuous conductivity distribution within the region R shown in Figure 5.2. The voltage and conductivity in R are $V(r,\theta)$ and $\sigma(r,\theta)$ respectively where $r(=r'/r_a)$ is the normalised radius. On the boundary S, at $r' = r_a$, the Fourier series in (3.1) and (3.2) are used (with r_b replaced by r_a) to represent the voltage, $V(P) = V(r_a,\theta)$, and the current density normal to S, $J(P) = J(r_a,\theta)$, respectively. The independent source density in R is zero, so that the voltage in R is given, using Poisson's Equation (2.11), by

$$\nabla^2 V = -\nabla V . \nabla \ln\sigma . \tag{5.1}$$

The voltage and its derivatives must be finite and continuous everywhere within R, hence the voltage is suitably represented by an angular Fourier series. The series used here is

$$V(r,\theta) = \sum_{m=o}^{\infty} \sum_{n=o}^{\infty} A_{mn} r^{m+n} \cos m\theta + B_{mn} r^{m+n} \sin m\theta \ . \tag{5.2}$$

Assuming that the conductivity and its derivatives are both finite and continuous, and also that the conductivity is not zero, then the logarithm of the conductivity can be suitably represented by

$$\ln[\sigma(r,\theta)] = \sum_{p=o}^{\infty} \sum_{q=o}^{\infty} a_{pq} r^{p+q} \cos p\theta + b_{pq} r^{p+q} \sin p\theta. \qquad (5.3)$$

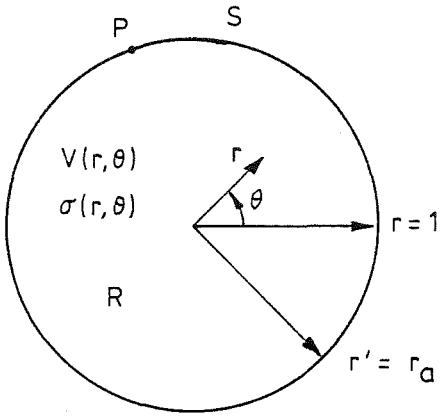

Figure 5.2: Smooth continuous conductivity distribution. The voltage V and conductivity σ are functions of the coordinates r and θ within the circular region R. The radius of R is $r' = r_a$, which is normalised to $r = r'/r_a = 1$. The surface of R is S, on which a point is P.

It is shown in §§4.1 and 4.2 that it is only necessary to use one pair of measurements (or boundary conditions) $V(r_a,\theta)$ and $J(r_a,\theta)$ to fully characterise the electrical response of a circularly symmetric conductivity distribution. However here the situation is different, and one can expect that many pairs of measurements may be needed. Indeed it is shown in §5.1.6 that many pairs of measurements are necessary. Consider therefore a set of paired voltage and current density boundary conditions given by

$$V_\ell(P) = V_\ell(r_a,\theta) = \sum_{n=o}^{\infty} U_{n\ell} \cos n\theta + V_{n\ell} \sin n\theta \qquad (5.4)$$

and

$$J_\ell(P) = J_\ell(r_a,\theta) = \sum_{n=o}^{\infty} I_{n\ell} \cos n\theta + J_{n\ell} \sin n\theta \qquad (5.5)$$

respectively. The subscript ℓ identifies the ℓth pair of boundary conditions in the set. The voltage in R depends upon which of the boundary conditions are imposed upon S, so that the voltage $V(r,\theta)$ and the coefficients A_{mn} and B_{mn} in (5.2) also require an additional subscript ℓ. Equation (5.3) remains unaltered. Having introduced the extra notation required, it is now convenient for the sake of brevity to discard the subscript ℓ until it is needed (§5.1.6). It is, however, to be understood that the relationship between the ℓth pair of a set of voltage and current boundary conditions is being examined.

Using the boundary conditions (5.4) and (5.5) at r = 1 ($r' = r_a$), and (5.1), (5.2) and (5.3), a relationship between the current density and the voltage on S can be obtained. The details are given in §§5.1.2 to 5.1.5. Firstly (5.1), (5.2) and (5.3) are manipulated in order to relate all of the A_{mn} and B_{mn} to the coefficients A_{mo} and B_{mo} (§5.1.2). Using this relationship the voltage and normal current density boundary conditions are then each expressed in terms of the coefficients A_{mo} and B_{mo} (§§5.1.3 and 5.1.4). Finally the voltage and normal current density on S are related to each other, and the A_{mo} and B_{mo} are eliminated (§5.1.5).

5.1.2 Manipulating Poisson's Equation

Expanding (5.1) in terms of the coordinates r,θ (cf Ramo, Whinnery and Van Duzer 1965 endpaper) and using (5.2) and (5.3) gives

$$\nabla^2 V = \sum_{m=o}^{\infty} \sum_{n=o}^{\infty} \left[(m+n)^2 - m^2\right] r^{m+n-2} \left[A_{mn} \cos m\theta + B_{mn} \sin m\theta\right] \qquad (5.6a)$$

and

$$\nabla V . \nabla \ln\sigma = \sum_{m,n,p,q=o}^{\infty} r^{m+n+p+q-2}$$

$$\{(m+n)(p+q)(A_{mn}\cos m\theta + B_{mn}\sin m\theta)(a_{pq}\cos p\theta + b_{pq}\sin p\theta)$$

$$+mp(-A_{mn}\sin m\theta + B_{mn}\cos m\theta)(-a_{pq}\sin p\theta + b_{pq}\cos p\theta)\}. \qquad (5.6b)$$

Using the orthogonality of trignometric functions, and equating the coefficients of the power series in (5.6a) to the negative of the corresponding coefficients in (5.6b), gives (see Appendix 5)

$$4\left[\mu^2 - (\mu+\nu)^2\right] A_{\mu\nu} = 2 \sum_{m,n=o}^{\mu\ \nu} \alpha_{\nu n \mu m} \left[A_{mn} a_{\mu-m,\nu-n} - B_{mn} b_{\mu-m,\nu-n}\right]$$

$$+\varepsilon_\mu \sum_{m=\mu}^{\mu+\nu/2} \sum_{n=o}^{\nu-2m+2\mu} \alpha_{\nu n \mu m} \left[A_{mn} a_{m-\mu,\nu-n-2m+2\mu} + B_{mn} b_{m-\mu,\nu-n-2m+2\mu}\right]$$

$$+\varepsilon_\mu \sum_{m=o}^{\nu/2} \sum_{n=o}^{\nu-2m} \beta_{\nu n \mu m} \left[A_{mn} a_{m+\mu,\nu-n-2m} + B_{mn} b_{m+\mu,\nu-n-2m}\right] \qquad (5.7a)$$

and

$$4\left[\mu^2 - (\mu+\nu)^2\right] B_{\mu\nu} = 2 \sum_{m,n=o}^{\mu\ \nu} \alpha_{\nu n \mu m} \left[A_{mn} b_{\mu-m,\nu-n} + B_{mn} a_{\mu-m,\nu-n}\right]$$

$$+\varepsilon_\mu \sum_{m=\mu}^{\mu+\nu/2} \sum_{n=o}^{\nu-2m+2\mu} \alpha_{\nu n \mu m} \left[-A_{mn} b_{m-\mu,\nu-n-2m+2\mu} + B_{mn} a_{m-\mu,\nu-n-2m+2\mu}\right]$$

$$+\varepsilon_\mu \sum_{m=o}^{\nu/2} \sum_{n=o}^{\nu-2m} \beta_{\nu n \mu m} \left[A_{mn} b_{m+\mu,\nu-n-2m} + B_{mn} a_{m+\mu,\nu-n-2m} \right] \tag{5.7b}$$

where

$$\alpha_{\nu n \mu m} = (m+n)(\mu-m+\nu-n) - m(\mu-m) , \tag{5.7c}$$

$$\beta_{\nu n \mu m} = (m+n)(\mu-m+\nu-n) + m(\mu+m) \tag{5.7d}$$

and $\nu/2$ is truncated to an integer value when ν is odd. ε_μ is the Neumann factor, which equals 1 for $\mu=0$, and 2 for $\mu \neq 0$.

Equations (5.7a) and (5.7b) are more conveniently written by collecting the A_{mn} and B_{mn} under a single summation, i.e.

$$A_{\mu\nu} = \sum_{m=o}^{\mu+\nu/2} \sum_{n=o}^{\nu} \gamma^{(1)}_{\nu n \mu m} A_{mn} + \gamma^{(2)}_{\nu n \mu m} B_{mn} \tag{5.8a}$$

and

$$B_{\mu\nu} = \sum_{m=o}^{\mu+\nu/2} \sum_{n=o}^{\nu} \gamma^{(3)}_{\nu n \mu m} A_{mn} + \gamma^{(4)}_{\nu n \mu m} B_{mn} , \tag{5.8b}$$

where the γ's depend on the α's, β's, a's and b's, and are chosen so that (5.8a) and (5.8b) are consistent with (5.7a) and (5.7b) respectively.
It is also convenient to remove the distinction between the A_{mn} and B_{mn} by putting $C_{2m,n} = A_{mn}$ and $C_{2m+1,n} = B_{mn}$. This gives

$$C_{2\mu,\nu} = \sum_{m=o}^{\mu+\nu/2} \sum_{n=o}^{\nu} \gamma^{(1)}_{\nu n \mu m} C_{2m,n} + \gamma^{(2)}_{\nu n \mu m} C_{2m+1,n} \tag{5.9a}$$

and

$$C_{2\mu+1,\nu} = \sum_{m=o}^{\mu+\nu/2} \sum_{n=o}^{\nu} \gamma^{(3)}_{\nu n \mu m} C_{2m,n} + \gamma^{(4)}_{\nu n \mu m} C_{2m+1,n} . \tag{5.9b}$$

Replacing 2μ, $2m$, $2\mu+1$ and $2m+1$ by p,q,p' and q' respectively then gives

$$C_{p,\nu} = \sum_{n=o}^{\nu} \left\{ \sum_{q=o(2)}^{p+\nu} \gamma^{(1)}_{\nu n k \ell} C_{q,n} + \sum_{q'=1(2)}^{p+\nu} \gamma^{(2)}_{\nu n k \ell'} C_{q',n} \right\} \tag{5.10a}$$

and

$$C_{p',\nu} = \sum_{n=o}^{\nu} \left\{ \sum_{q=o(2)}^{p'+\nu-1} \gamma^{(3)}_{\nu n k' \ell} C_{q,n} + \sum_{q'=1(2)}^{p'+\nu-1} \gamma^{(4)}_{\nu n k' \ell'} C_{q',n} \right\} , \tag{5.10b}$$

where k, ℓ, k' and ℓ' are $p/2$, $q/2$, $(p'-1)/2$ and $(q'-1)/2$ respectively, and the number in parentheses beneath the summation sign indicates increments of 2.

The terms p and q are always even whereas p' and q' are always odd, so that (5.10a) and (5.10b) can be written as the single equation

$$C_{\mu,\nu} = \sum_{n=o}^{\nu} \sum_{q=o}^{\mu+\nu} \gamma_{\nu n \mu q} C_{q,n} \quad , \tag{5.11}$$

where μ = p when even, μ = p' when odd and $\gamma_{\nu n \mu q}$ is either $\gamma^{(1)}_{\nu n k \ell}$, $\gamma^{(2)}_{\nu n k \ell'}$, $\gamma^{(3)}_{\nu n k' \ell}$ or $\gamma^{(4)}_{\nu n k' \ell'}$ in (5.10) depending on whether q and μ are even or odd. Rewriting (5.11) in matrix notation gives

$$\underset{\sim}{C}_{\nu} = \sum_{n=o}^{\nu} \Gamma_{\nu n} \underset{\sim}{C}_{n} \quad , \tag{5.12}$$

where the element in row μ of the vector $\underset{\sim}{C}_{\nu}$ is written as $\left[\underset{\sim}{C}_{\nu}\right]_{\mu}$, and here has the value of $C_{\mu,\nu}$. Similarly the element in row μ and column q of the matrix $\Gamma_{\nu n}$ is written as $\left[\Gamma_{\nu n}\right]_{\mu q}$, and here has the value of $\gamma_{\nu n \mu q}$.

Equation (5.12) can be written as a lower triangular system of linear equations in which the unknowns are the vectors $\underset{\sim}{C}_{n}$, and the coefficients of the unknowns are the matrices $\Gamma_{\nu n}$. This system of equations relates all of the $\underset{\sim}{C}_{\nu}$, for $\nu > 0$, to $\underset{\sim}{C}_{o}$. Since the system is lower triangular it is easily solved by forward substitution. Moving the $n = \nu$ term from the right hand side of (5.12) to the left hand side and rearranging gives

$$\underset{\sim}{C}_{\nu} = (I - \Gamma_{\nu\nu})^{-1} \sum_{n=o}^{\nu-1} \Gamma_{\nu n} \underset{\sim}{C}_{n} \quad , \tag{5.13}$$

where I is the identity matrix. When $\nu = 1$, (5.13) gives $\underset{\sim}{C}_{1}$ in terms of $\underset{\sim}{C}_{o}$, the individual elements of $\underset{\sim}{C}_{1}$ being linear combinations of those in $\underset{\sim}{C}_{o}$. Using this result and (5.13) for $\nu = 2$ then gives $\underset{\sim}{C}_{2}$ in terms of $\underset{\sim}{C}_{o}$. Continuing the forward substitution finally gives

$$\underset{\sim}{C}_{\nu} = G_{\nu} \underset{\sim}{C}_{o} \quad . \tag{5.14}$$

The matrix G_{ν} can be found from the $\Gamma_{\nu n}$ once all of the substitutions have been performed. It is important to realise that the matrix G_{ν} depends solely upon the conductivity distribution (i.e. the a's and b's in (5.3)).

The summation form of (5.14)

$$C_{\mu,\nu} = \sum_{k=o}^{\infty} g_{\nu \mu k} C_{k,o} \quad , \tag{5.15}$$

where $g_{\nu\mu k} = \left[G_\nu\right]_{\mu k}$ and $C_{ko} = \left[\underset{\sim}{C}_o\right]_k$, is used in §§5.1.3 and 5.1.4 to relate the voltage and current density on S (see Figure 5.2) to the coefficients $C_{k,o}$.

5.1.3 Matching the Voltage Boundary Conditions

Matching the voltage boundary conditions given by (5.4) with the voltage given by (5.2) at r = 1 yields

$$U_m = \sum_{n=o}^{\infty} A_{mn} \tag{5.16a}$$

and

$$V_m = \sum_{n=o}^{\infty} B_{mn} \ . \tag{5.16b}$$

Substituting $C_{2m,n} = A_{mn}$ and $C_{2m+1,n} = B_{mn}$, as in §5.1.2, and putting $W_{2m} = U_m$ and $W_{2m+1} = V_m$, and then k = 2m and k' = 2m+1 gives

$$W_q = \sum_{n=o}^{\infty} C_{q,n} \tag{5.17}$$

where q = k when even and q = k' when odd. Now using (5.15) to express the $C_{q,n}$ in terms of C_{ko} gives

$$W_q = \sum_{k=o}^{\infty} \eta_{qk} C_{k,o} \tag{5.18}$$

where $\eta_{qk} = \sum_{n=o}^{\infty} g_{nqk}$. Since the g_{nqk} (see (5.14) and (5.15)) depend only on the conductivity distribution, so do the η_{qk}.

In matrix notation (5.18) can be written as

$$\underset{\sim}{W} = H\underset{\sim}{C}_o \tag{5.19}$$

where $\left[H\right]_{qk} = \eta_{qk}$, $\left[\underset{\sim}{W}\right]_q = W_q$ and $\left[\underset{\sim}{C}_o\right]_k = C_{k,o}$. Equation (5.19) is used in §5.1.5 to relate the voltage boundary conditions to the current density boundary conditions.

5.1.4 Matching the Current Density Boundary Conditions

The current density boundary conditions are not as easily related to the $C_{k,o}$ as are the voltage boundary conditions, because the conductivity of the surface varies with position. Although the conductivity at the surface is uniquely defined by (5.3), it is convenient here to introduce an alternative representation, i.e.

$$\sigma(1,\theta) = \sum_{p=o}^{\infty} x_p \cos p\theta + y_p \sin p\theta \quad , \tag{5.20}$$

where the x's and y's here depend entirely upon the a's and b's in (5.3). Using (5.20) and (5.2) the current density normal to the boundary at r = 1 (or r' = r_a) is

$$J(r_a,\theta) = -(1/r_a) \sum_{p,m,n=o}^{\infty} (m+n)\left[A_{mn}\cos m\theta + B_{mn}\sin m\theta\right]\left[x_p \cos p\theta + y_p \sin p\theta\right] . \tag{5.21}$$

Matching (5.21) to the boundary condition (5.5) and separating into orthogonal components gives

$$\begin{aligned} -4r_a I_k = 2 &\sum_{q=o}^{k}\sum_{n=o}^{\infty} (q+n)\left[A_{qn}x_{k-q} - B_{qn}y_{k-q}\right] \\ &+ \varepsilon_k \sum_{q=o}^{\infty}\sum_{n=o}^{\infty} (q+n)\left[A_{qn}x_{k+q} + B_{qn}y_{k+q}\right] \\ &+ \varepsilon_k \sum_{q=k}^{\infty}\sum_{n=o}^{\infty} (q+n)\left[A_{qn}x_{q-k} + B_{qn}y_{q-k}\right] \end{aligned} \tag{5.22a}$$

and

$$\begin{aligned} -4r_a J_k = 2 &\sum_{q=o}^{k}\sum_{n=o}^{\infty} (q+n)\left[A_{qn}y_{k-q} + B_{qn}x_{k-q}\right] \\ &+ \varepsilon_k \sum_{q=o}^{\infty}\sum_{n=o}^{\infty} (q+n)\left[A_{qn}y_{k+q} - B_{qn}x_{k+q}\right] \\ &- \varepsilon_k \sum_{q=k}^{\infty}\sum_{n=o}^{\infty} (q+n)\left[A_{qn}y_{q-k} - B_{qn}x_{q-k}\right] \quad . \end{aligned} \tag{5.22b}$$

These equations take the form of a discrete convolution since they are the frequency domain representation of the product of voltage gradient and conductivity.

Equations (5.22a) and (5.22b) are more conveniently written as

$$I_k = \sum_{q=o}^{\infty}\sum_{n=o}^{\infty} f^{(1)}_{kqn} A_{qn} + f^{(2)}_{kqn} B_{qn} \tag{5.23a}$$

and

$$J_k = \sum_{q=o}^{\infty}\sum_{n=o}^{\infty} f^{(3)}_{kqn} A_{qn} + f^{(4)}_{kqn} B_{qn} \tag{5.23b}$$

respectively, where the f's depend upon r_a, the x's and y's, and are chosen so that (5.23a) and (5.23b) are consistent with (5.22a) and (5.22b) respectively. Replacing A_{qn}, B_{qn}, I_k and J_k by $C_{2q,n}$, $C_{2q+1,n}$, K_{2k} and K_{2k+1} respectively, and then putting 2k, 2q, 2k+1 and 2q+1 equal to p, m, p' and m' respectively then gives

$$K_p = \sum_{n=o}^{\infty} \{ \sum_{m=o(2)}^{\infty} f^{(1)}_{\mu\nu n} C_{m,n} + \sum_{m'=1(2)}^{\infty} f^{(2)}_{\mu\nu' n} C_{m',n} \} \tag{5.24a}$$

and

$$K_{p'} = \sum_{n=o}^{\infty} \{ \sum_{m=o(2)}^{\infty} f^{(3)}_{\mu'\nu n} C_{m,n} + \sum_{m'=1(2)}^{\infty} f^{(4)}_{\mu'\nu' n} C_{m',n} \} , \tag{5.24b}$$

where μ, ν, μ' and ν' are $p/2$, $m/2$, $(p'-1)/2$ and $(m'-1)/2$ respectively. The term in parentheses below the summations indicates increments of 2.

Writing (5.24a) and (5.24b) as a single equation gives

$$K_q = \sum_{n=o}^{\infty} \sum_{m=o}^{\infty} f_{qmn} C_{m,n} \tag{5.25}$$

where $q = p$ when even, $q = p'$ when odd and f_{qmn} is either $f^{(1)}_{\mu\nu n}$, $f^{(2)}_{\mu\nu' n}$, $f^{(3)}_{\mu'\nu n}$ or $f^{(4)}_{\mu'\nu' n}$ depending on whether q and m are even or odd. Now using (5.15) to express the $C_{m,n}$ in terms of $C_{p,o}$ yields

$$K_q = \sum_{p=o}^{\infty} \xi_{qp} C_{p,o} \tag{5.26}$$

where $\xi_{qp} = \sum_{n=o}^{\infty} \sum_{m=o}^{\infty} f_{qmn}\, g_{nmp}$. The g_{nmp} (see (5.14) and (5.15)) depend only on the conductivity distribution, and the f_{qmn} depend on both the conductivity distribution at $r' = r_a$ and on the value of r_a. Therefore, apart from the value of r_a, the ξ_{qp} depend only on the conductivity distribution.

In matrix notation (5.26) can be written as

$$\underset{\sim}{K} = \Xi \underset{\sim}{C}_o \tag{5.27}$$

where $[\Xi]_{qp} = \xi_{qp}$, $[\underset{\sim}{K}]_q = K_q$ and $[\underset{\sim}{C}_o]_p = C_{p,o}$. Equation (5.27) is used in §5.1.5 to relate the voltage boundary conditions to the current density boundary conditions.

5.1.5 Relation Between Boundary Voltage and Current Density

The equations derived in §§5.1.3 and 5.1.4 from the voltage and current density boundary conditions can be combined to eliminate the vector $\underset{\sim}{C}_o$, which is common to both. Using (5.19) and (5.27) to eliminate $\underset{\sim}{C}_o$ gives

$$\underset{\sim}{W} = Z \underset{\sim}{K} , \tag{5.28}$$

where the matrix Z equals $H\Xi^{-1}$. The matrix H (see (5.18) and (5.19)) depends only on the conductivity distribution, and the matrix Ξ depends both on the conductivity distribution and the radius $r' = r_a$ of the conductive region. Therefore apart from the value of r_a, Z depends solely upon the conductivity distribution.

Equation (5.28) can be alternatively written as

$$W_m = \sum_{n=o}^{\infty} z_{mn} K_n \qquad (5.29)$$

where $z_{mn} = [Z]_{mn}$. Equation (5.29) is a more general form of (3.6) in §3.1 (the latter treats the cosine and sine Fourier components separately, whereas the former interrelates all components). Both of these equations show that the Fourier components of current density on the boundary S and those of voltage are related by the transfer impedances z_{mn}. The matrix Z, and hence all of the transfer impedances, depend on the size of the conductive region and the conductivity distribution therein.

Here, as in Chapters 3 and 4, the Fourier components of current density on S and those of voltage are linearly related (see (5.29)). Therefore the voltage response of a particular conductivity distribution to the sum of any two current distributions, is equal to the sum of the voltage responses to each current distribution applied separately. The same effect is true for electric networks composed of discrete resistive components (cf. Skilling 1974 Ch.10). For such networks the effect is referred to as superposition. It is not surprising that superposition occurs with both electric networks and conductivity distributions, since a planar electric network (one that can be drawn on a plane with no component crossing another) is a special case of a two-dimensional conductivity distribution. Indeed one approach to impedance imaging is to represent a two-dimensional conductivity distribution by a planar resistive network (cf. Dines and Lytle 1981).

The voltage and current density on the boundary of a circularly symmetric conductivity distribution are related in the spatial domain by a convolution (see §§4.1 and 3.1). No simple spatial domain relationship is apparent for the general conductivity distribution. Furthermore, it is possible with circularly symmetric distributions to fully characterise the electrical response of the region by measuring a single pair of voltage and current distributions (cf. §4.1). This is clearly not possible for a general conductivity distribution because there are more unknowns in the matrix Z than there are measure-

ments in the vectors $\underset{\sim}{W}$ and $\underset{\sim}{K}$ (see (5.28) and (5.29)). However, in the circularly symmetric situation all of the z_{mn} for $m \neq n$ are zero, hence the matrix Z is diagonal and can be uniquely determined from $\underset{\sim}{W}$ and $\underset{\sim}{K}$ using (5.28).

5.1.6 Calculating the Transfer Impedances from Measurements

A single pair of measurements of the voltage distribution $V(r_a,\theta)$ and current density distribution $J(r_a,\theta)$ are not sufficient for calculating the transfer impedances of a general conductivity distribution (see §5.1.5). However these measurements represent only one pair of a set of different pairs of voltage and current density distributions (see §5.1.1). Therefore the vectors $\underset{\sim}{W}$ and $\underset{\sim}{K}$, which contain the Fourier components of $V(r_a,\theta)$ and $J(r_a,\theta)$ respectively, are only one pair of a set of different vectors. Reintroducing the subscript ℓ, used in (5.4) and (5.5) to indicate which pair of the set are being represented, enables (5.28) and (5.29) to be written as

$$\underset{\sim}{W}_\ell = Z\underset{\sim}{K}_\ell \tag{5.30}$$

and

$$W_{m\ell} = \sum_{n=o}^{\infty} z_{mn} K_{n\ell} \tag{5.31}$$

respectively, where $W_{m\ell} = [\underset{\sim}{W}_\ell]_m$ and $K_{n\ell} = [\underset{\sim}{K}_\ell]_n$. Equation (5.31) represents the product of two matrices. Introducing the two matrices V and J, (5.31) may be written as

$$V = ZJ \tag{5.32}$$

where $[V]_{m\ell} = [\underset{\sim}{W}_\ell]_m = W_{m\ell}$ and $[J]_{m\ell} = [\underset{\sim}{K}_\ell]_m = K_{m\ell}$.

When sufficient linearly independent columns $\underset{\sim}{K}_\ell$ of the matrix $\underset{\sim}{J}$ are known then the transfer impedances can be found from (5.32) by

$$Z = VJ^{-1}. \tag{5.33}$$

Clearly it is necessary to have as many linearly independent columns as there are rows in the matrix J for a unique inverse to be found. Having determined Z, any pair of voltage and current density distributions are uniquely related by (5.30). Thus the transfer impedances fully characterise the electrical response of the conductive region. The paired sets of voltage and current measurements represented by the matrices V and J are therefore both necessary and sufficient to fully characterise the electrical response of the conductive region.

Furthermore, it is shown in §5.1.5 that the transfer impedances are related only to the conductivity distribution and the size of the conductive region. Therefore the z_{mn} can be deduced both from the conductivity distribution and from the measurements. However it is not clear whether the conductivity distribution is uniquely determined by the transfer impedances, and hence the measurements, because the conductivity distribution and the z_{mn} are not linearly related.

5.1.7 Receprocity in Relation to the Transfer Impedances

When N linearly independent current distributions $\underset{\sim}{J}_\ell$ (with Fourier components $K_{n\ell}$ for n from 1 to N) are impressed on the surface of a conductive region, and the voltage distributions $\underset{\sim}{V}_\ell$ are measured, then N^2 transfer impedances can be obtained (see (5.31) to (5.33)). Since the transfer impedances fully characterise the electrical response of the conductivity distribution it might appear that N^2 different "pieces of information" about the conductivity distribution have been obtained. However not all of the transfer impedances are independent. This may be shown as follows.

Consider that two current density distributions $\underset{\sim}{J}^{(1)}$ and $\underset{\sim}{J}^{(2)}$ are imposed separately on the boundary S of a conductive region (see Figure 5.2) to which the unit normal vector is $\underset{\sim}{n}$. Their respective voltage responses $V^{(1)}$ and $V^{(2)}$ are measured. Choose, now, the specific current density distributions normal to S, i.e. $\underset{\sim}{J}^{(1)}.\underset{\sim}{n}$ and $\underset{\sim}{J}^{(2)}.\underset{\sim}{n}$, to be K_{p1} ceso$(p\theta)$ and K_{q2} ceso$(q\theta)$ respectively, for which p and q are some predetermined positive integers. The function ceso$(m\theta)$ is defined as $\underline{\cos}(m\theta/2)$ when m is $\underline{\text{even}}$ and $\underline{\sin}((m-1)\theta/2)$ when m is $\underline{\text{odd}}$. Therefore the current distributions K_{p1} ceso$(p\theta)$ and K_{q2} ceso$(q\theta)$ can be represented in terms of their Fourier components by the vectors $\underset{\sim}{K}_1$ and $\underset{\sim}{K}_2$ respectively, in which all elements are zero apart from $\left[\underset{\sim}{K}_1\right]_p = K_{p1}$ and $\left[\underset{\sim}{K}_2\right]_q = K_{q2}$. The voltages $V^{(1)}$ and $V^{(2)}$ may be represented by the Fourier series $\sum_{k=o}^{\infty} W_{k1}$ ceso$(k\theta)$ and $\sum_{k=o}^{\infty} W_{k2}$ ceso$(k\theta)$ respectively. Alternatively they also may be represented in terms of their Fourier components by the vectors $\underset{\sim}{V}_1$ and $\underset{\sim}{V}_2$ respectively, where $\left[\underset{\sim}{V}_1\right]_k = W_{k1}$ and $\left[\underset{\sim}{V}_2\right]_k = W_{k2}$.

The independent source density in the conductive region is zero, so that the divergence theorem can be rearranged to give (cf. Lehr 1972)

$$\int_S V^{(1)} \underset{\sim}{J}^{(2)}.\underset{\sim}{n}\, dS = \int_S V^{(2)} \underset{\sim}{J}^{(1)}.\underset{\sim}{n}\, dS \ , \qquad (5.34)$$

where dS is the elemental length along the boundary S. Substituting the chosen current distributions and the Fourier series for the voltage distribut-

ions into (5.34), and then integrating from $\theta = 0$ to 2π around S gives

$$W_{q1}/K_{p1} = W_{p2}/K_{q2} \quad . \tag{5.35}$$

Using (5.31) it is easy to see for the simple current distributions chosen here that $W_{q1} = z_{qp} K_{p1}$ and $W_{p2} = z_{pq} K_{q2}$. Combining these equations with (5.35) gives

$$z_{pq} = z_{qp} \quad , \tag{5.36}$$

so that the matrix Z is symmetric. However the matrix Z is independent of the current distributions chosen, so in general must always be symmetric. Hence, of the N^2 transfer impedances originally obtained, at most $N(N+1)/2$ are independent.

The transfer impedances of discrete electric networks also observe a symmetry similar to that shown here (cf. Skilling 1966 Ch. 9). In the network situation the symmetry is referred to as receprocity. It is sometimes expressed in terms of the statement: "when a battery and ammeter (or current source and voltmeter respectively) connected to different parts of a circuit are interchanged, the reading on the meter stays the same". The circuit referred to may equally well be a discrete electric network or a conductivity distribution (cf. Lehr 1972). The battery/ammeter statement of symmetry is of little use here. However, (5.36) can be used as a check for consistency when using (5.33) to calculate the z_{pq}. Equation (5.33) does not in itself constrain z_{pq} to equal z_{qp}, so that any errors in the measurements may manifest themselves by making z_{pq} differ from z_{qp}.

5.1.8 Simple Current Distributions for Making Measurements

It is shown in §5.1.6 that a set of linearly independent current distributions can be used to perform measurements which fully characterise the electrical response of a conductivity distribution. It is therefore important to be able to create such current distributions. The method described here to do this is particularly simple, being merely an extension of the technique used for circularly symmetric conductivity distributions, as described in §4.1.1.

Consider the current distributions created when current sources and sinks are alternatively and equally spaced around the circumference of a circular region (see Figure 5.3). The fundamental Fourier components of

the current density distributions correspond to $\cos\theta$, $\sin\theta$, $\cos2\theta$, $\sin2\theta$, and so on for the different distributions. Since the cosine and sine functions are orthogonal, these current distributions must be linearly independent. They are therefore suitable for specifying measurements that fully characterise the electrical response of a conductive region.

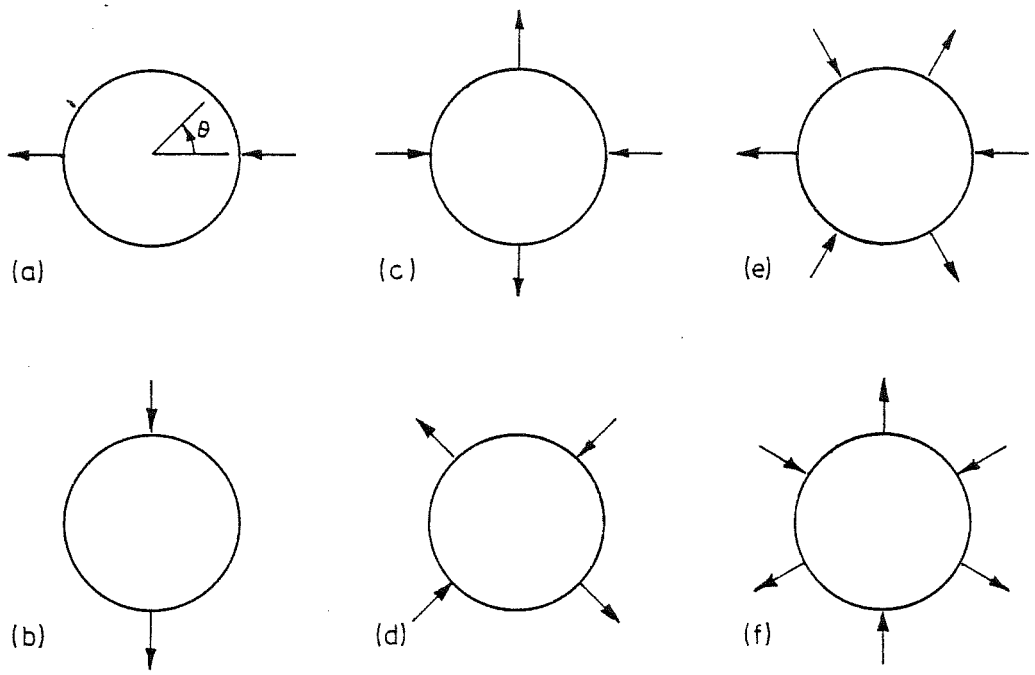

Figure 5.3: Linearly independent current distributions. The inward and outward arrows indicate current sources and sinks respectively. The distributions have the fundamental Fourier components: (a) $\cos\theta$, (b) $\sin\theta$, (c) $\cos2\theta$, (d) $\sin2\theta$, (e) $\cos3\theta$, (f) $\sin3\theta$.

Only two current electrodes need be used at any one time, and those distributions requiring more than two current electrodes can be simulated by using in turn the two available electrodes at different pairs of the electrode positions (cf. §4.1.1). Summing the individual voltage responses then gives the overall response to all electrode pairs simultaneously because the Fourier components of voltage and current density are linearly related by (5.29). This technique can be of practical importance when only one current source and sink are available for making measurements. It was used to obtain the experimental results reported in §5.3. The measurements in that section were obtained using current distributions having fundamental Fourier components corresponding to $\cos k\theta$ and $\sin k\theta$ for k taking values from 1 to 8.

5.2 PIECEWISE CONSTANT DISTRIBUTIONS

Piecewise constant conductivity distributions are in some circumstances more suitable representations of actual conductivity distributions than are smooth conductivity distributions (§5.1). This situation occurs, for instance, when imaging conductivity cross sections of the human body. The conductivities of different regions (e.g. bones, muscle, blood) are essentially constant, with fairly clearly defined boundaries between regions.

5.2.1 The Multiple Offset Anomaly Distribution

Consider the multiple offset anomaly conductivity distribution illustrated in Figure 5.1b. N circular regions (anomalies) are shown imbedded within a circular region which, apart from the anomalies, has a conductivity σ_1. With the appropriate choice of the conductivity, size, position and number of anomalies any two-dimensional conductivity distribution can be represented. In Figure 5.4 the multiple offset anomaly conductivity distribution is reproduced showing, for clarity, only 2 of the N anomalies. The N anomalies are enclosed by curves C_k, for k from 2 to N + 1.

The integral equation approach (cf. §2.6.3) is employed in this section to calculate the relationship between the voltage and current density on the boundary of the multiple offset anomaly conductivity distribution. Used here for this approach are the source point and observation point Q_k and P respectively. Q_k is on the boundary C_k (see Figure 5.4b) and P is anywhere in the region where the conductivity is σ_1. The coordinates of P and Q_k, with respect to the centre of the kth anomaly, are r_k, θ_k and ρ_k, ϕ_k respectively. The distance between P and Q_k is R_k. The radius of the conductive region is $r' = r_a$, which in terms of the normalised coordinates is $r_1 = r'/r_a = 1$ and $\rho_1 = r'/r_a = 1$.

The voltage $V(Q_1)$ at $\rho_1 = 1$ and the current density $J(Q_1)$ normal to the boundary at $\rho_1 = 1$ are represented here by the Fourier series

$$V(Q_1) = \sum_{m=o}^{\infty} U_m \cos m\phi_1 + V_m \sin m\phi_1 \qquad (5.37)$$

and

$$J(Q_1) = \sum_{m=1}^{\infty} I_m \cos m\phi_1 + J_m \sin m\phi_1 \qquad (5.38)$$

respectively (cf. (3.1) and (3.2)). The independent source density within the conductive region is zero so that I_o is zero, and has therefore been

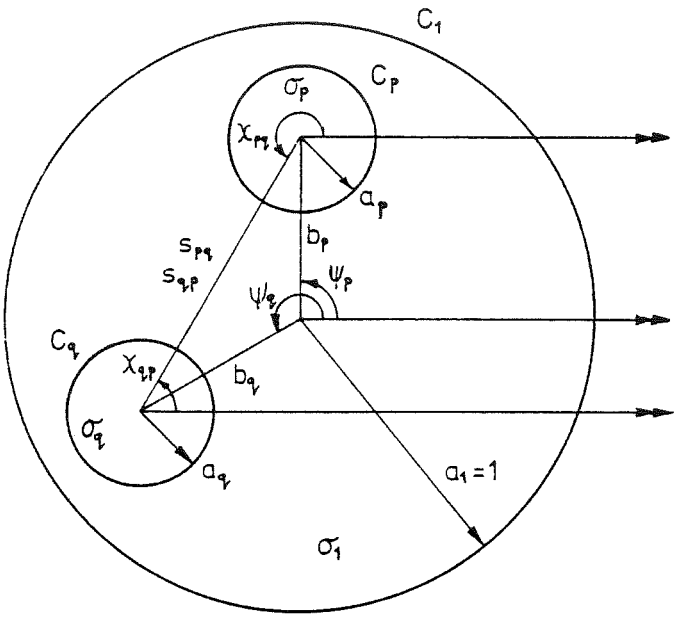

(a)

Figure 5.4: Multiple offset anomaly conductivity distribution.

(a) Curve C_1 encloses a circular region having conductivity σ_1, in which are imbedded N circular regions with conductivity, radius, offset, and angular position σ_k, a_k, b_k and ψ_k respectively (for k from 2 to N + 1). Only the pth and qth regions are shown. The separation S_{pq} (= S_{qp}) between the centres of the pth and qth regions must exceed $a_p + a_q$, and $a_p + b_p$ must be less than a_1.

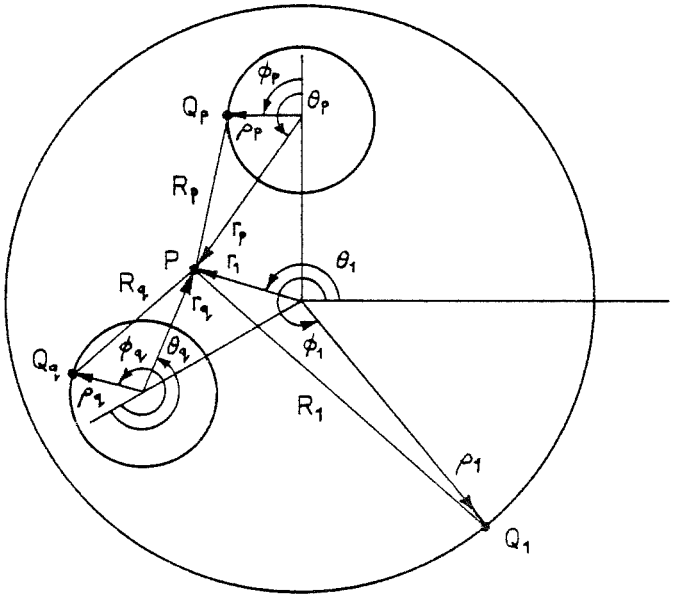

(b)

Figure 5.4: Multiple offset anomaly conductivity distribution.

(b) Observation point P and source point Q_k on curve C_k have coordinates r_k, θ_k and ρ_k, θ_k respectively with respect to the centre of the kth circular region. P is in the region where the conductivity is σ_1. The distance between Q_k and P is R_k.

excluded from (5.38). The voltage gradient normal to the boundary C_p and on the side of C_p where the conductivity is σ_1, is similarly represented by

$$\frac{\partial V}{\partial \rho_p}(Q_p) = \sum_{m=1}^{\infty} A_{pm}\cos m\phi_p + B_{pm}\sin m\phi_p \,. \tag{5.39}$$

Substituting P for Q and θ for ϕ in (5.37) and (5.38) gives similar equations representing the voltage and voltage gradient respectively when the observation point lies adjacent to the boundary C_p.

Using the integral equation (2.79) for the voltage at P gives

$$2\pi V(P) = \int_0^{2\pi} \{ \sum_{n=1}^{\infty} \frac{1}{n} r_1^n \cos n(\theta_1-\phi_1) \frac{\partial V}{\partial \rho_1}(Q_1) + V(Q_1) \sum_{n=0}^{\infty} r_1^n \cos n(\theta_1-\phi_1) \} d\phi_1$$

$$- \sum_{p=2}^{N+1} (\sigma_1-\sigma_p)\frac{1}{\sigma_p} \int_0^{2\pi} \frac{\partial V}{\partial \rho_p}(Q_p) \left[\ln r_p - \sum_{n=1}^{\infty} \frac{1}{n}(a_p/r_p)^n \cos n(\theta_p-\phi_p)\right] a_p d\phi_p \,, \tag{5.40}$$

where the Green's function $-(1/2\pi)\ln R_p$ and its derivative with respect to ρ_p has been expanded in terms of the coordinates r_p, θ_p and ρ_p, ϕ_p (cf. Morse and Feshbach 1953 §10.1). The first integral in (5.40) represents the contribution to the voltage at P due to the voltage and current density boundary conditions on C_1. The second integral represents the contribution due to the change in conductivity at $\rho_p = a_p$. When there is no change, the second term is zero.

5.2.2 Relation Between Boundary Voltage and Current Density

An algebraic expression for the voltage on the boundary of the conductive region illustrated in Figure 5.4 can be obtained by substituting (5.37), (5.38) and (5.39) into (5.40) and integrating. The integration is readily performed using the orthogonal properties of trignometric functions. The resulting expression is

$$V(P) = -(r_a/2\sigma_1) \sum_{m=1}^{\infty} (1/m) r_1^m (I_m \cos m\theta_1 + J_m \sin m\theta_1)$$

$$+ \sum_{m=0}^{\infty} (1/\varepsilon_m) r_1^m (U_m \cos m\theta_1 + V_m \sin m\theta_1)$$

$$+ \sum_{p=2}^{N+1} (a_p/2\sigma_p)(\sigma_1-\sigma_p) \sum_{m=1}^{\infty} (1/m)(a_p/r_p)^m (A_{pm}\cos m\theta_p + B_{pm}\sin m\theta_p) \,, \tag{5.41}$$

where ε_m is the Neumann factor (cf. (5.7)) and the term r_a arises because the current density $J(Q_1)$ is expressed in terms of the unnormalised radial coordinate r'.

Equation (5.41) gives the voltage at any point in the region where the conductivity is σ_1, and in particular it gives the voltage when P approaches C_1. Similarly the derivative of (5.41) with respect to ρ_q gives the voltage gradient normal to curve C_q as P approaches C_q. On C_1 the former is (cf. (5.37))

$$V(P) = \sum_{m=o}^{\infty} U_m \cos m\theta_1 + V_m \sin m\theta_1 \quad , \tag{5.42}$$

and on C_q the latter is (cf. (5.39))

$$\frac{\partial V}{\partial \rho_q}(P) = \sum_{m=1}^{\infty} A_{qm} \cos m\theta_q + B_{qm} \sin m\theta_q \quad . \tag{5.43}$$

Expressing the factors $r_p^{-m}\cos m\theta_p$ and $r_p^{-m}\sin m\theta_p$ in (5.41) in terms of the coordinates r_1 and θ_1, and then evaluating (5.41) at $r_1 = 1$ and matching to the boundary condition (5.42), gives an equation which has the orthogonal components

$$U_m = -(r_a/m\sigma_1) I_m + \sum_{p=2}^{N+1} (\sigma_1 - \sigma_p)\frac{1}{\sigma_p} \sum_{n=1}^{m} \binom{m-1}{n-1} \frac{1}{n} a_p^{n+1} b_p^{m-n} (A_{pn} \cos m\psi_p - B_{pn} \sin m\psi_p) \tag{5.44a}$$

and

$$V_m = -(r_a/m\sigma_1) J_m + \sum_{p=2}^{N+1} (\sigma_1 - \sigma_p)\frac{1}{\sigma_p} \sum_{n=1}^{m} \binom{m-1}{n-1} \frac{1}{n} a_p^{n+1} b_p^{m-n} (A_{pn} \sin m\psi_p - B_{pn} \cos m\psi_p) . \tag{5.44b}$$

The angle ψ_p (see Figure 5.4a) arises when the factors containing r_p and θ_p are expressed in terms of the coordinates r_1 and θ_1. This is achieved by expanding $\{r_1 \exp[i(\theta_1 - \psi_p)] - b_p\}^{-m}$ in terms of a binomial power-series, and then equating the resulting real and imaginary parts to those of $\{r_p \exp[i\theta_p]\}^{-m}$. The notation $\binom{k}{\ell}$ is used here to represent the binomial coefficients.

After similarly expressing the factors $r_1^m \cos m\theta_1$, $r_1^m \sin m\theta_1$, $r_p^{-m}\cos m\theta_p$ and $r_p^{-m}\sin m\theta_p$ in (5.41) in terms of r_q and θ_q, equation (5.41) can be differentiated with respect to r_q, evaluated at $r_q = a_q$ and matched to the boundary condition (5.43). This gives an equation which has the orthogonal components

$$A_{qm} = \left[\sigma_q/(\sigma_1+\sigma_q)\right] m a_q^{m-1} \{(-r_a/\sigma_1) \sum_{n=m}^{\infty} \binom{n}{m} \frac{1}{n} b_q^{n-m} \left[I_n \cos n\psi_q + J_n \sin n\psi_q\right]$$

$$+ \sum_{n=m}^{\infty} \binom{n}{m} b_q^{n-m} \left[U_n \cos n\psi_q + V_n \sin n\psi_q\right]$$

$$+ (-1)^m \sum_{\substack{p=2 \\ p\neq q}}^{N+1} \left[(\sigma_1-\sigma_p)/\sigma_p\right] \sum_{n=1}^{\infty} \binom{m+n-1}{m} \frac{1}{n} a_p^{n+1} S_{pq}^{-n-m}$$

$$\left[A_{pn} \cos(n(\psi_p-\chi_{pq})+m(\psi_q-\chi_{pq})) - B_{pn} \sin(n(\psi_p-\chi_{pq})+m(\psi_q-\chi_{pq}))\right]\} \quad (5.45a)$$

and

$$B_{qm} = \left[\sigma_q/(\sigma_1+\sigma_q)\right] m a_q^{m-1} \{-(r_a/\sigma_1) \sum_{n=m}^{\infty} \binom{n}{m} \frac{1}{n} b_q^{n-m} \left[-I_n \sin n\psi_q + J_n \cos n\psi_q\right]$$

$$+ \sum_{n=m}^{\infty} \binom{n}{m} b_q^{n-m} \left[-U_n \sin n\psi_q + V_n \cos n\psi_q\right]$$

$$+ (-1)^m \sum_{\substack{p=2 \\ p\neq q}}^{N+1} \left[(\sigma_1-\sigma_p)/\sigma_p\right] \sum_{n=1}^{\infty} \binom{m+n-1}{m} \frac{1}{n} a_p^{n+1} S_{pq}^{-n-m}$$

$$\left[-A_{pn} \sin(n(\psi_p-\chi_{pq})+m(\psi_q-\chi_{pq})) - B_{pn} \cos(n(\psi_p-\chi_{pq})+m(\psi_q-\chi_{pq}))\right]\}. \quad (5.45b)$$

The angle χ_{pq} is defined in Figure 5.4a.

Equations (5.44a), (5.44b), (5.45a) and (5.45b) are more conveniently written using the complex quantities $K_m = I_m + iJ_m$, $W_m = U_m + iV_m$ and $D_{qm} = A_{qm} + iB_{qm}$. They may then be written as the single pair of equations

$$W_m = -(r_a/m\sigma_1) K_m + \sum_{p=2}^{N+1} (\sigma_1-\sigma_p) \frac{1}{\sigma_p} e^{im\psi_p} \sum_{n=1}^{m} \binom{m-1}{n-1} \frac{1}{n} a_p^{n+1} b_p^{m-n} D_{pn} \quad (5.46a)$$

and

$$D_{qm} = \left[m\sigma_q/(\sigma_1+\sigma_q)\right] \{a_q^{m-1} \sum_{n=m}^{\infty} \binom{n}{m} b_q^{n-m} e^{-in\psi_q} (W_n - r_a K_n/n\sigma_1)$$

$$+ (-1)^m \sum_{\substack{p=2 \\ p\neq q}}^{N+1} \left[(\sigma_1-\sigma_p)/\sigma_p\right] e^{-im(\psi_q-\chi_{pq})} (a_q/S_{pq})^{m-1}$$

$$\sum_{n=1}^{\infty} \frac{1}{n} \binom{m+n-1}{m} (a_p/S_{pq})^{n+1} e^{-in(\psi_p-\chi_{pq})} D_{pn}^* \}, \quad (5.46b)$$

where the asterisk denotes the complex conjugate. Equation (5.46a) gives the Fourier components of the voltage W_m at r = 1 in terms of the Fourier components of current density K_m at r = 1, and the Fourier components of the voltage gradients D_{pn} at the surface of each of the anomalies.

There are sufficient equations in (5.46a) and (5.46b) to eliminate all of the D_{pm} and thus to relate the voltage at r = 1 to the current density alone. This can be achieved by first substituting (5.46a) into (5.46b), which then forms a system of linear equations in the D_{qm} and D^*_{qm}. Once this set of equations is solved for the D_{qm} (by rearrangement and matrix inversion), the D_{pn} in (5.46a) can be eliminated by substitution. After the D_{pn} are eliminated the W_m are related to the K_m alone.

5.2.3 Three Components Contributing to Boundary Voltage

Equations (5.46a) and (5.46b) are best interpreted by viewing the contribution to the voltage W_m in terms of three components. The first component can be observed when the conductivity is uniform throughout the entire conductive region. In this situation (5.46a) reduces to $W_m = W_m^{(u)} = -(r_a/m\sigma_1)K_m$. Here this component of voltage is called the uniform conductivity component.

Suppose, now, there is one anomaly present in the region. In addition to $W_m^{(u)}$ there is now another component contributing to the voltage W_m (see 5.46a). The additional component depends on the voltage gradients D_{pm} at the surface of the anomaly. It is convenient in this situation to consider W_m as being the sum of two components $W_m^{(u)}$ and $W_m^{(s)}$. The component $W_m^{(s)}$ is called the single anomaly component.

When there is more than one anomaly, the voltage is contributed to by $W_m^{(u)}$, by a single anomaly component for every anomaly present $W_{pm}^{(s)}$, and by yet another component. The source of the latter component can be seen by examining the D_{pm} in (5.46b). The D_{pm} of one anomaly is altered by the presence of every other anomaly, as indicated by the sum over p in (5.46b). Physically this happens because each anomaly alters the current flow throughout the entire conductive region, and therefore affects the voltage gradients D_{pm} at all other anomalies. It is therefore sensible to call this third component contributing to W_m the coupling component $W_m^{(c)}$.

Expressing the voltage W_m in terms of all three contributing components now gives

$$\underset{\sim}{W} = \underset{\sim}{W}^{(u)} + \sum_{p=2}^{N+1} \underset{\sim}{W}_p^{(s)} + \underset{\sim}{W}^{(c)} \tag{5.47}$$

where $\left[\underset{\sim}{W}\right]_m = W_m$, $\left[\underset{\sim}{W}^{(u)}\right]_m = W_m^{(u)}$, $\left[\underset{\sim}{W}_p^{(s)}\right]_m = W_{pm}^{(s)}$ and $\left[\underset{\sim}{W}^{(c)}\right]_m = W_m^{(c)}$. It is interesting to observe that the magnitude of the coupling component tends towards zero as the separation S_{pq} between anomalies increases, and as the size of the anomalies decreases (see 5.46b). It is reasonable, therefore, to expect that in some circumstances the coupling component may be small enough in comparison to the other components for it to be neglected. In order to evaluate the relative sizes of the coupling and the single anomaly components in (5.47) they are compared in §§5.3.3 and 5.3.4 for some simple conductivity distributions.

5.2.4 The Single Offset Anomaly Distribution

When there is only one anomaly present (i.e. N=2) equations (5.46a) and (5.46b) can be readily combined to relate the Fourier components of voltage W_m, to those of current density K_m. In this situation the summation over p in (5.46b) is zero so that substituting (5.46b) into (5.46a) gives

$$W_m = \sum_{n=1}^{\infty} T_{mn}(nW_n - r_a K_n/\sigma_1) - r_a K_m/m\sigma_1 \ , \tag{5.48}$$

where

$$T_{mn} = \frac{1}{n}\frac{\sigma_1-\sigma_2}{\sigma_1+\sigma_2} e^{i(m-n)\psi_2} b_2^{m+n} \sum_{p=1}^{<(m,n)} \binom{m-1}{p-1}\binom{n}{p}(a_2/b_2)^{2p} \tag{5.49}$$

in which $<(m,n)$ means the lesser of m and n. Equation (5.48) is more conveniently written in matrix notation as

$$\underset{\sim}{W} = TD\underset{\sim}{W} - (r_a/\sigma_1)T\underset{\sim}{K} - (r_a/\sigma_1)D^{-1}\underset{\sim}{K} \tag{5.50}$$

where the vectors $\underset{\sim}{W}$ and $\underset{\sim}{K}$, and the matrix T have elements $\left[\underset{\sim}{W}\right]_m = W_m$, $\left[\underset{\sim}{K}\right]_m = K_m$ and $\left[T\right]_{mn} = T_{mn}$ respectively. D is a diagonal matrix having elements $\left[D\right]_{mn} = m\delta_{mn}$, where δ_{mn} is the Kronecker delta. Rearranging (5.50) to express the voltage $\underset{\sim}{W}$ explicitly in terms of current density $\underset{\sim}{K}$ gives

$$\underset{\sim}{W} = Z\underset{\sim}{K} \ , \tag{5.51}$$

where

$$Z = -(r_a/\sigma_1)(I-TD)^{-1}(I+TD)D^{-1} \tag{5.52}$$

in which I is the identity matrix.

Equations (5.51) and (5.52) give a direct technique for calculating the voltage from the current density when there is only one anomaly present. In that situation they represent an alternative to the more complicated technique described in §5.2.2. It is interesting to note that the structure of (3.5), which applies here when the anomaly is centred at r = 0 (i.e. b_2 = 0), is similar to the structure of (5.52). The matrix operations in the latter equation appear as the equivalent scalar operations in the former. When b_2 is zero, the matrix T is a diagonal matrix and (5.52) reduces to the uncoupled set of equations (3.5).

Equation (5.51) has the same form as (5.30) in §5.1.6, although the individual elements of the respective vectors and matrices are different because here the equations are expressed in terms of complex numbers, whereas in §5.1.6 real numbers are used. The complex matrix Z here is one half the size of the real matrix Z in §5.1.6, however the former cannot represent totally general conductivity distributions as can the latter. Nevertheless, the same reasoning used in §5.1.6 to show that Z can be deduced from a set of linearly independent measurements $\underset{\sim}{W}_\ell$ and $\underset{\sim}{K}_\ell$ applies equally well here to the complex matrix Z. Therefore the latter matrix can be obtained from the measurements by (cf. (5.33))

$$Z = VJ^{-1} , \tag{5.53}$$

where $[V]_{m\ell} = [\underset{\sim}{W}_\ell]_m$ and $[J]_{m\ell} = [\underset{\sim}{K}_\ell]_m$.

5.2.5 Direct Inversion for a Single Offset Anomaly

When the conductivity distribution is comprised of a single offset anomaly it is possible from voltage and current measurements to deduce the position, size and conductivity of the anomaly. The first step is to obtain the matrix Z from the measurements using (5.53). The matrix T can then be obtained by rearranging (5.52) to give

$$T = -D^{-1}\left[I+(\sigma_1/r_a)DZ\right]\left[I-(\sigma_1/r_a)DZ\right]^{-1} . \tag{5.54}$$

It is interesting to note that according to (5.49) the matrix T is complex conjugate symmetric. This symmetry provides a useful check, since if T is calculated from measurements using (5.54) and is not complex conjugate symmetric then it is inappropriate to interpret the conductivity distribution as a single offset anomaly.

Having determined the elements T_{mn} from (5.54) the nonlinear equations given by (5.49) must be solved in order to obtain the unknowns σ_2, a_2, b_2 and ψ_2. The most simply found of these unknowns is ψ_2. Taking the ratio of imaginary (IM) to real (RE) parts of any element T_{mn} and rearranging gives

$$(m-n)\psi_2 = \tan^{-1}\left[IM(T_{mn})/RE(T_{mn})\right] . \tag{5.55}$$

When evaluated, the right hand side of (5.55) yields many possible values for $(m-n)\psi_2$. There are therefore many possible values for ψ_2. Only when m-n is 1 or -1 are all of these values separated by integral multiples of 2π. In this situation, which corresponds to choosing T_{mn} from one of the diagonals adjacent to the leading diagonal, the angular position represented by all of the values of ψ_2 is unique.

Once ψ_2 is deduced, the offset b_2 is easily calculated using the ratio of any two elements from the first column of T, i.e.

$$b_2 = (T_{m1}/T_{k1})^{1/(m-k)} e^{-i\psi_2} . \tag{5.56}$$

A similar equation can be found using elements from the first row of T because of its complex conjugate symmetry.

Having calculated b_2, the radius of the anomaly a_2 can be found by solving for the roots of a polynomial in a_2^2. There are many polynomials from which to choose, each formed by taking the ratio of one element of T to another. When pairs of elements from the first three elements in the leading diagonal are used, the polynomials formed are either linear or quadratic. Solving these polynomials for a_2^2 gives

$$a_2^2 = 2(T_{22}/T_{11} - b_2^2) \tag{5.57a}$$

$$a_2^2 = (6b_2^4 + 3T_{33}/T_{11})^{1/2} - 3b_2^2 \tag{5.57b}$$

and

$$a_2^2 = \left[5b_2^4 + (3T_{33}/4T_{22} - b_2^2)^2\right]^{1/2} + 3T_{33}/4T_{22} - 3b_2^2 . \tag{5.57c}$$

Any of these equations can be used to calculate a_2 provided the values of their respective right hand sides are greater than zero.

After finding a_2, the ratio σ_2/σ_1 can be determined using any element in the matrix T. Choosing an element from the leading diagonal gives

$$\sigma_1/\sigma_2 = -(T_{mm} - \tau_m)/(T_{mm} + \tau_m) \tag{5.58a}$$

where

$$\tau_m = \frac{1}{m} b_2^{2m} \sum_{p=1}^{m} \binom{m-1}{p-1} \binom{m}{p} (a_2/b_2)^{2p} \quad . \tag{5.58b}$$

Equations (5.53) to (5.58) represent a direct technique for imaging a single circular offset anomaly.

Inspection of (5.54) shows that the matrix T is diagonal when Z is diagonal, as happens when the conductivity distribution is circularly symmetric (see Chapter 4). Therefore, for the single offset conductivity distribution, T is diagonal when the offset b_2 is zero. In this situation ψ_2 as given by (5.55) is indeterminate. However, any value of ψ_2 is then appropriate because the distribution is circularly symmetric. Similarly b_2 given by (5.56) may be indeterminate when T is diagonal. The simplest way to avoid this difficulty is to choose T_{k1} to be T_{11} in the denominator of (5.56). Equations (5.57) and (5.58) do not suffer from indeterminacy when T is diagonal because they have been specifically chosen to involve only the diagonal elements of T. There are other equations giving a_2 and σ_2/σ_1 in terms of off diagonal elements, but they may become indeterminate when T is diagonal.

In §5.4 equations (5.53) to (5.58) are employed to determine ψ_2, b_2, a_2 and σ_2/σ_1, using experimental measurements obtained from conductivity distributions consisting of a single offset anomaly.

5.3 CASE STUDIES

Case studies are useful for confirming that theoretical expressions and the experimental measurements they supposedly represent are in agreement. Such confirmation supports the theoretical approach, and enables the theoretical expressions to be used with confidence. Even when theoretical expressions are available, it is often impossible to settle general questions directly from them. Here, it is desired to draw general conclusions about impedance imaging from the expressions derived in §§5.1 and 5.2. A variety of case studies have been performed in order to do this.

Four different studies are presented in this section. The first is concerned with data gathering and with how the measurements are related to the transfer impedances (see §§5.1.5 and 5.1.6). In the second study, the visibility, defined in Chapter 3, is reintroduced. The visibility is shown

to be particularly useful when comparing measurements made on different conductivity distributions. The third study relates to the component of the measurements due to coupling between the anomalies (see §5.2.3). In the final study, the relative importance of the coupling component is examined.

The experimental measurements reported here were obtained using the technique described in §5.1.8 and the equipment described in Appendices 1 and 2. All measurements were made on conductivity distributions of the multiple offset anomaly type, as illustrated in Figure 5.1b.

5.3.1 Voltage Measurements and Transfer Impedances

Measurements are reported here for a uniform conductivity distribution, in order to both demonstrate the experimental technique and to introduce a method for representing the transfer impedances calculated from such measurements.

Voltage Measurements

Different current distributions were applied to the circumference of a uniform conductivity distribution and the corresponding voltage distributions were sampled at thirty-two equally spaced points. The current distributions were of the simple point current and sink type described in §5.1.8 (see Figure 5.3).

The voltage distributions measured for the current sources and sinks indicated in Figures 5.3b, d and f, are shown in Figure 5.5a, b and c respectively. Figure 5.5d shows the voltage distribution measured for current sources at 22.5^{o}, 112.5^{o}, 202.5^{o} and 292.5^{o}, and current sinks at 67.5^{o}, 157.5^{o}, 247.5^{o} and 337.5^{o}. At the current sources and sinks the gradient of the voltage abruptly changes sign. These abrupt changes occur because the electrodes used to inject and remove the current approximate point electrodes (see Figure 4.5a), around which the voltage varies logarithmically with the distance from the electrodes (cf. §§2.6.1 and 2.7.1).

Transfer Impedances

In order to calculate the transfer impedances from particular voltage distributions it is first necessary to calculate their Fourier components. The transfer impedances can then be calculated using (5.33). There is a practical difficulty in estimating the Fourier components of the voltage distributions shown in Figure 5.5. This difficulty arises because the

voltage gradient is very steep near the current sources and sinks, so that the voltage has appreciable high spatial-frequency Fourier components. However to estimate these components needs more than the 32 voltage samples measured here for each of the voltage distributions. It is therefore necessary to estimate extra voltage samples before calculating the transfer impedances.

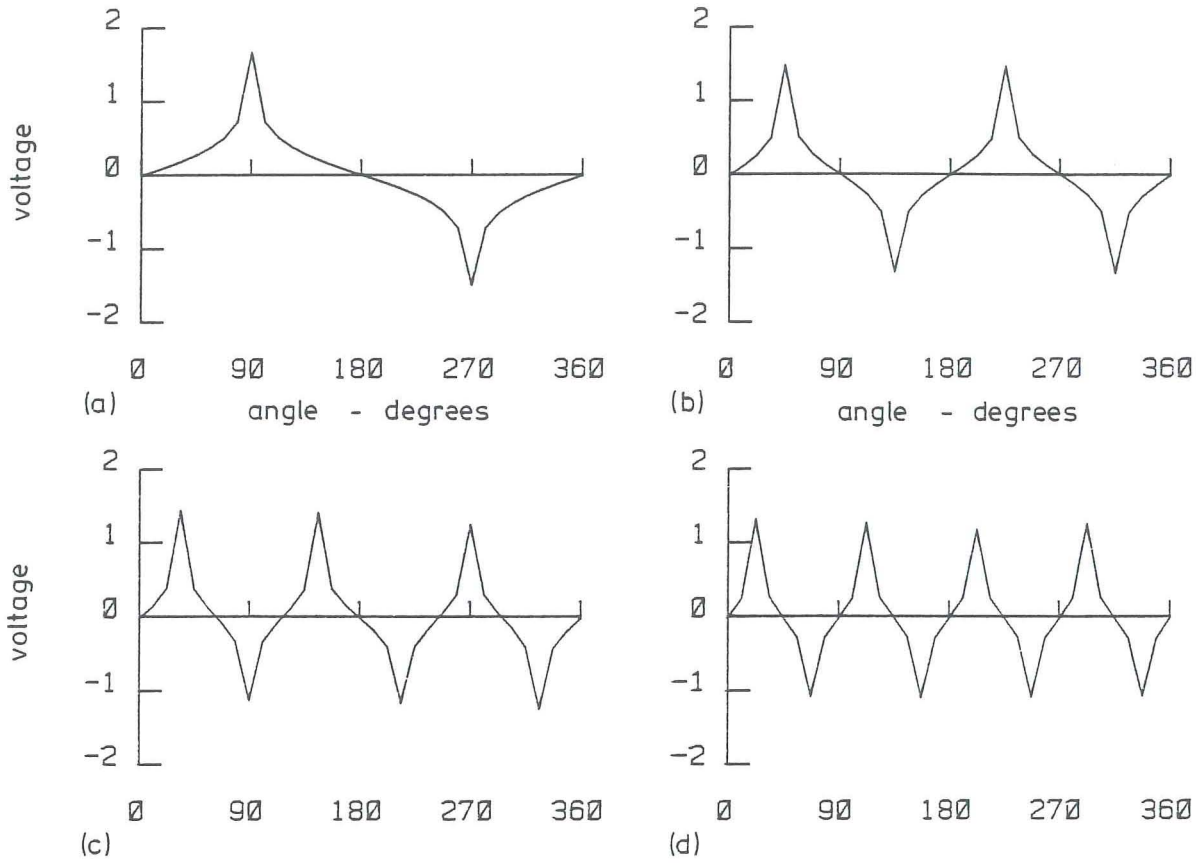

Figure 5.5: Voltage distributions measured on a uniform conductivity distribution using from 1 to 4 pairs of current sources and sinks. The current sources and sinks coincide with the voltage maxima and minima respectively.

For the particular current distributions used here, the injection and removal of current is performed alternately as a function of angle. Therefore the voltage must vary monotonically between any two adjacent electrodes. Extra voltage samples, which vary in this way, can be obtained by using straight line interpolation between adjacent electrodes. Therefore, this type of interpolation was used here to estimate 96 extra voltage samples. The Fourier components of the voltage distributions were then estimated from both the original 32 voltage samples and the 96 extra samples.

Figure 5.6a shows the transfer impedances calculated from experimental measurements made on a uniform conductivity distribution. For comparison, Figure 5.6b shows the theoretical values of the transfer impedances. In Figures 5.6a and 5.6b the values of the transfer impedances z_{xy} are represented in perspective as the height above the x,y plane. They have been scaled by -1 so that the peaks appear above the x,y plane. This permits visual evaluation without the need for making numerical comparisons. The origin is on the left of each plot, from which the x and y axes run towards and away from the observer respectively. Remember that the transfer impedances are expected to be symmetric about the leading diagonal (cf. §5.1.7), which in these diagrams runs from left to right across the page. The origin corresponds to the transfer impedance z_{22} in the notation of (5.29). Each axis covers the range x (or y) from 2 to 18, corresponding to the transfer impedances for the Fourier components $\cos\theta, \sin\theta, \ldots \cos 8\theta$, and $\sin 8\theta$. For visual clarity, continuous plots are presented even though the z_{xy} exist only at discrete values of x and y.

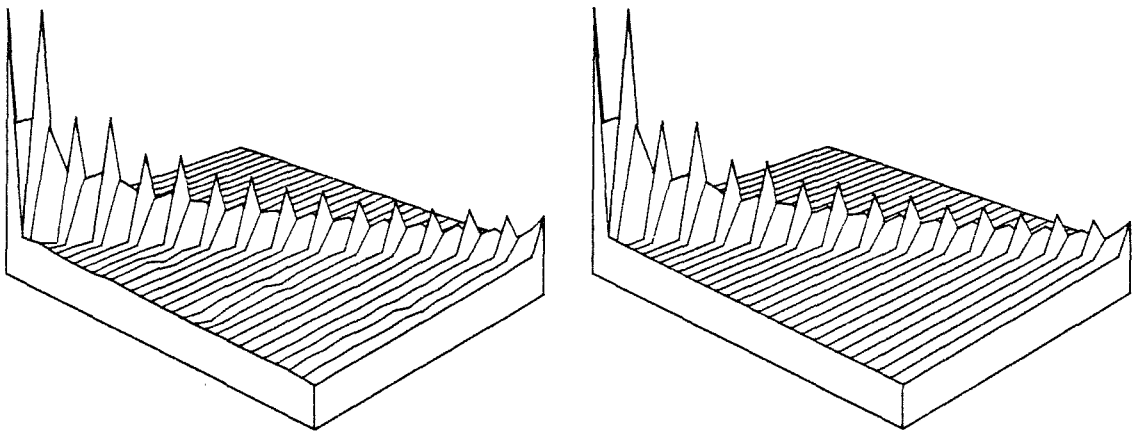

Figure 5.6: Transfer impedances of a uniform conductivity distribution displayed as a perspective plot (see §5.3.1).
(a) experimental, (b) theoretical.

The measured transfer impedances (Figure 5.6a) compare favourably with the calculated values (Figure 5.6b). The experimental conductivity distribution was supposed to be circularly symmetric so that all terms off the leading diagonal should have been zero. The effects of measurement noise and asymmetry in the conductivity distribution are manifested by small non-zero values for the off diagonal terms.

5.3.2 Transfer Impedances and Visibilities

The transfer impedances have been shown to fully characterise the electrical response of any conductivity distribution (see §§5.1.5 and 5.1.6). They may therefore be used to compare the measurements obtained from different conductivity distributions. Consider, for example, the two conductivity distributions illustrated in Figure 5.7. In each distribution a single nonconducting anomaly is offset by 0.551 of the radius of the conducting region, and itself has a radius of either 0.312 or 0.197. The transfer impedances calculated from experimental measurements are shown in Figure 5.8.

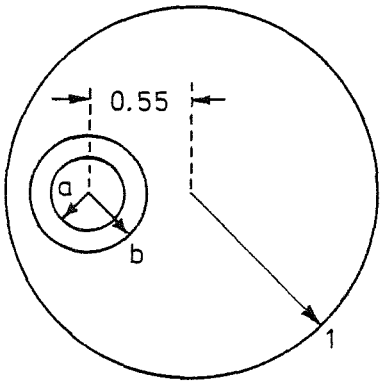

Figure 5.7: Conductivity distribution consisting of a single nonconducting offset anomaly. The sizes of the anomaly are either (a) 0.20 or (b) 0.31.

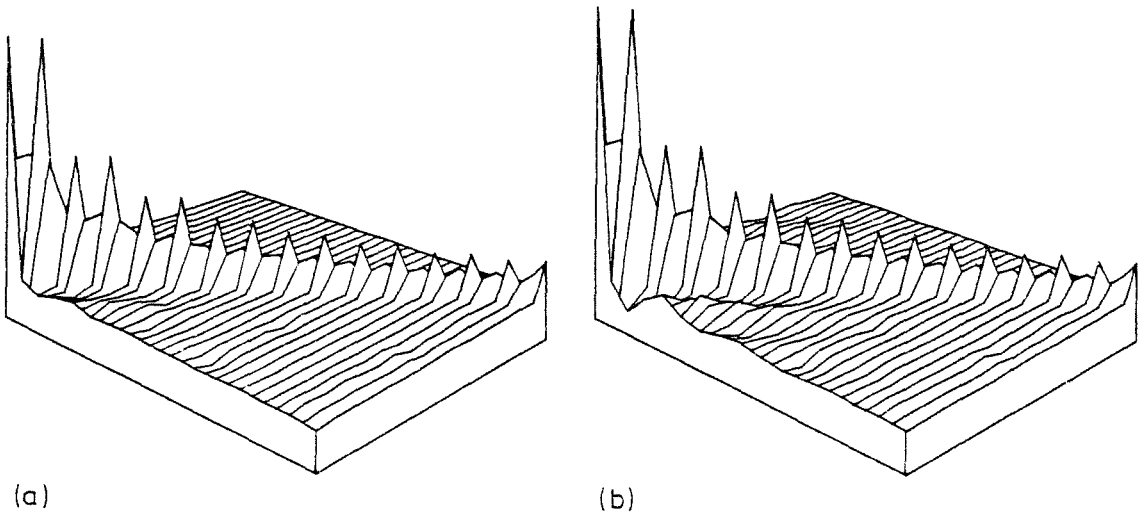

Figure 5.8: Transfer impedances calculated using experimental measurements from the conductivity distributions (a) and (b) shown in Figure 5.7.

It is clear from Figure 5.8b that the transfer impedances for the large anomaly are different from those for a uniform conductivity distribution (cf. Figure 5.6a). The same cannot be said with such confidence of the transfer impedances for the smaller anomaly (cf. Figure 5.8a).

In order to emphasise the difference between the measurements made on different conductivity distributions, it is less convenient to examine the transfer impedances themselves than the visibility defined in terms of them through (3.8). The visibilities calculated from the transfer impedances displayed in Figure 5.8 are shown in Figure 5.9. The vertical scale is enlarged 5 times in comparison to the plots of the transfer impedances.

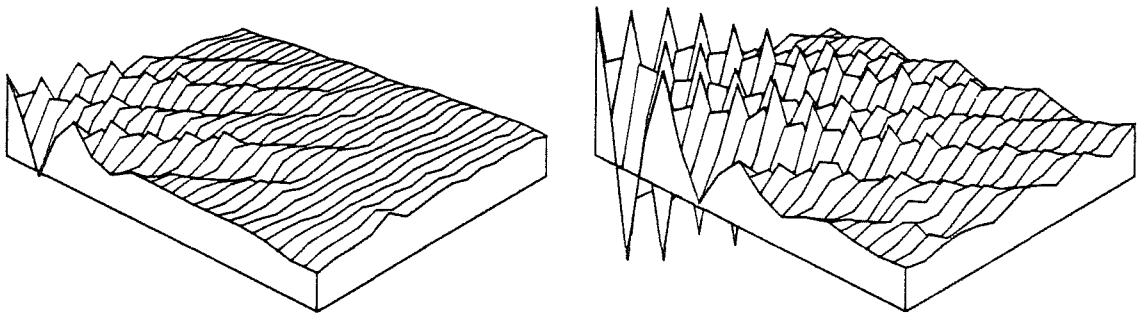

Figure 5.9: Visibilities calculated using experimental measurements from the conductivity distributions (a) and (b) shown in Figure 5.7.

The visibilities of a uniform conductivity distribution are all identically zero (see (3.8)). It is therefore clear from the visibilities shown in Figure 5.9 that neither of the experimental conductivity distributions is truly uniform. Note the wavelike pattern in Figure 5.9a, in which the crests of the waves are parallel to the leading diagonal. Now observe that the same feature is evident in Figure 5.9b, except that the waves are of greater amplitude. This similarity between the visibilities appears to reflect the similarity between the conductivity distributions themselves. Shown in Figure 5.10, for comparison, are the theoretical visibilities calculated using (5.48) for the same conductivity distributions. The experimental and theoretical values agree well, thereby confirming that the experimental technique is adequate and that the theoretical description is appropriate.

The visibilities, displayed in the manner used here, enable the measurements from different conductivity distributions to be compared more clearly than do the transfer impedances. The visibilities are therefore used exclusively in the remaining subsections of this section (i.e. §5.3).

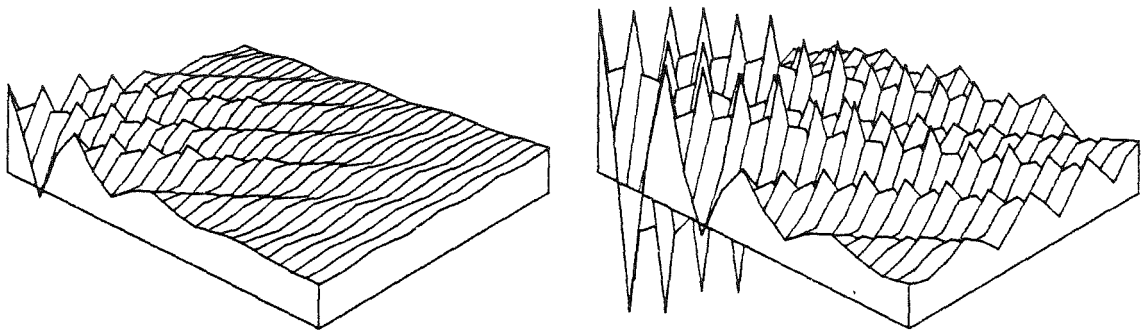

(a) (b)

Figure 5.10: Theoretical visibilities calculated for the conductivity distributions (a) and (b) shown in Figure 5.7.

5.3.3 Coupling Effects Between Two Anomalies

In §5.2.3 the voltage distribution associated with a conductivity distribution consisting of multiple offset anomalies (see Figure 5.1b) is interpreted in terms of three components. They are a uniform conductivity component $\underset{\sim}{W}^{(u)}$, a sum of single anomaly components $\underset{\sim}{W}_p^{(s)}$ and a component $\underset{\sim}{W}^{(c)}$ representing the coupling between anomalies (see (5.47)). The sum of these components is $\underset{\sim}{W}$, which is related to the voltage distribution by Fourier transformation. The conductivity distributions examined in §5.3.2 consist of a single anomaly. In that situation $\underset{\sim}{W} = \underset{\sim}{W}^{(u)} + \underset{\sim}{W}_p^{(s)}$, because the coupling term is zero (cf.§§5.2.3). In this subsection it is desired to examine the visibilities in the alternate case where $\underset{\sim}{W} = \underset{\sim}{W}^{(u)} + \underset{\sim}{W}^{(c)}$.

The visibilities are defined in terms of the transfer impedances through (3.8). Therefore consider first the transfer impedances Z, $Z^{(u)}$, $Z_p^{(s)}$ and $Z^{(c)}$ calculated from linearly independent sets of the vectors $\underset{\sim}{W}$, $\underset{\sim}{W}^{(u)}$, $\underset{\sim}{W}_p^{(s)}$ and $\underset{\sim}{W}^{(c)}$ respectively (see §5.1.6). It follows directly from (5.47) and (5.28) that

$$Z = Z^{(u)} + \sum_{p=2}^{N+1} Z_p^{(s)} + Z^{(c)} \qquad (5.59)$$

where N is the number of anomalies. When measurements are made on a uniform conductivity distribution the transfer impedances $Z = Z^{(u)}$ can be calculated since the terms $Z_p^{(s)}$ and $Z^{(c)}$ in (5.59) are zero. Similarly, when the conductivity distribution consists of a single anomaly then $Z = Z^{(u)} + Z_p^{(s)}$. Therefore the transfer impedances corresponding to the term $\underset{\sim}{W}^{(u)} + \underset{\sim}{W}^{(c)}$ can be calculated from measurements after rearranging (5.59) to give

$$Z^{(u)}+Z^{(c)} = Z - \sum_{p=2}^{N+1} (Z^{(u)}+Z_p^{(s)}) + NZ^{(u)} . \qquad (5.60)$$

Using (5.60) and (3.8) the visibilities corresponding to the term $Z^{(u)} + Z^{(c)}$ can then be calculated.

In §5.2.3 it is reasoned that the coupling effect decreases as the size of the anomalies decreases and as the separation between them increases. Consider therefore the four conductivity distributions illustrated in Figure 5.11. Each of the four distributions consists of two anomalies. One of these anomalies is centred at a radius of 0.551 and an angle of 30°. The other anomaly is centred at one of two positions and has one of two radii. These radii are 0.275 and 0.312, which are referred to as "small" and "big" respectively. The two positions are at 90° and 180°, which are referred to as "near" and "far" respectively.

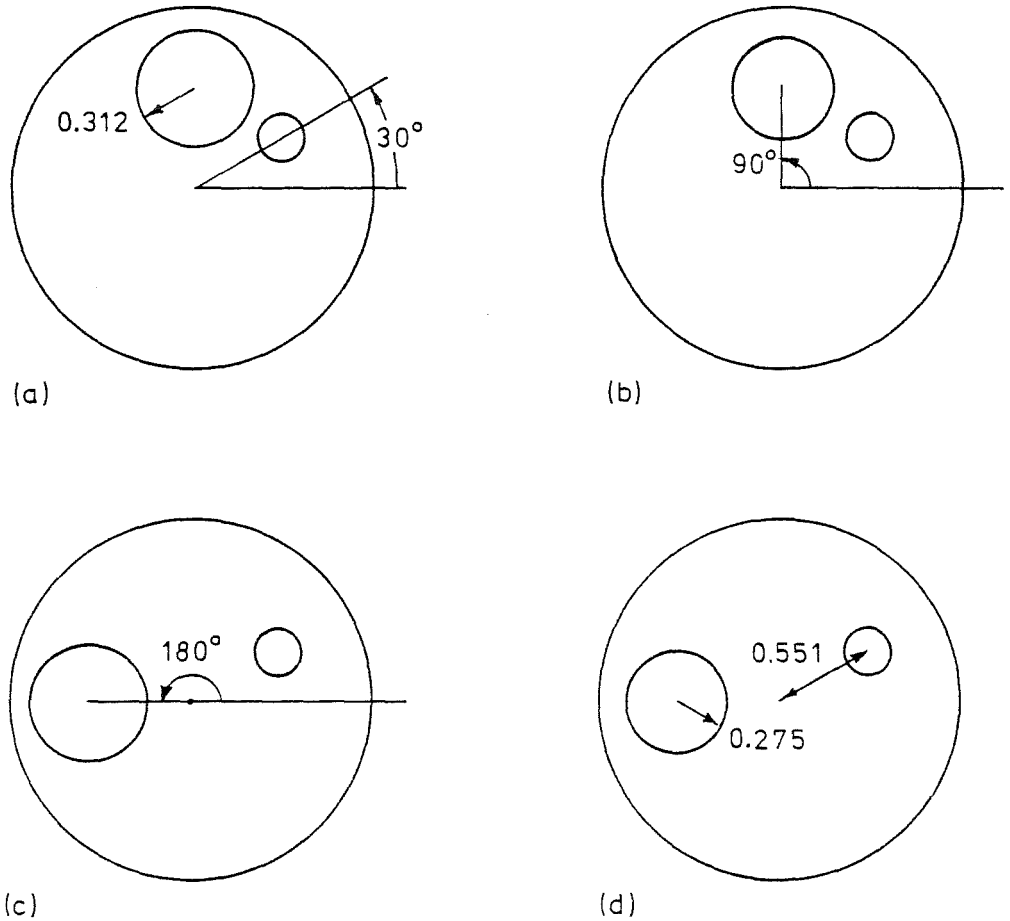

Figure 5.11: Dual anomaly conductivity distributions.
(a) big near, (b) small near, (c) big far,
(d) small far, (see §5.3.3).

Figure 5.12 shows the visibilities calculated from $Z^{(u)} + Z^{(c)}$ using (5.60) and experimental measurements. Figure 5.13 shows, for comparison, the theoretical values calculated using (5.46) and (5.60). Comparing Figure 5.13 with Figure 5.12 shows significant differences, which are due to experimental noise in the latter. This difference is much larger than the difference between the experimental and theoretical visibilities shown in Figures 5.9 and 5.10 respectively. The larger difference results from calculating $Z^{(u)} + Z^{(c)}$ using (5.60) when there is noise in the measurements. In that situation the number of anomalies N times the error in $Z^{(u)}$ is accumulated and added to the errors in each of the $Z_p^{(s)}$. In Figures 5.12a, b and c these errors have reinforced each other, whereas in Figure 5.12d they appear to have cancelled.

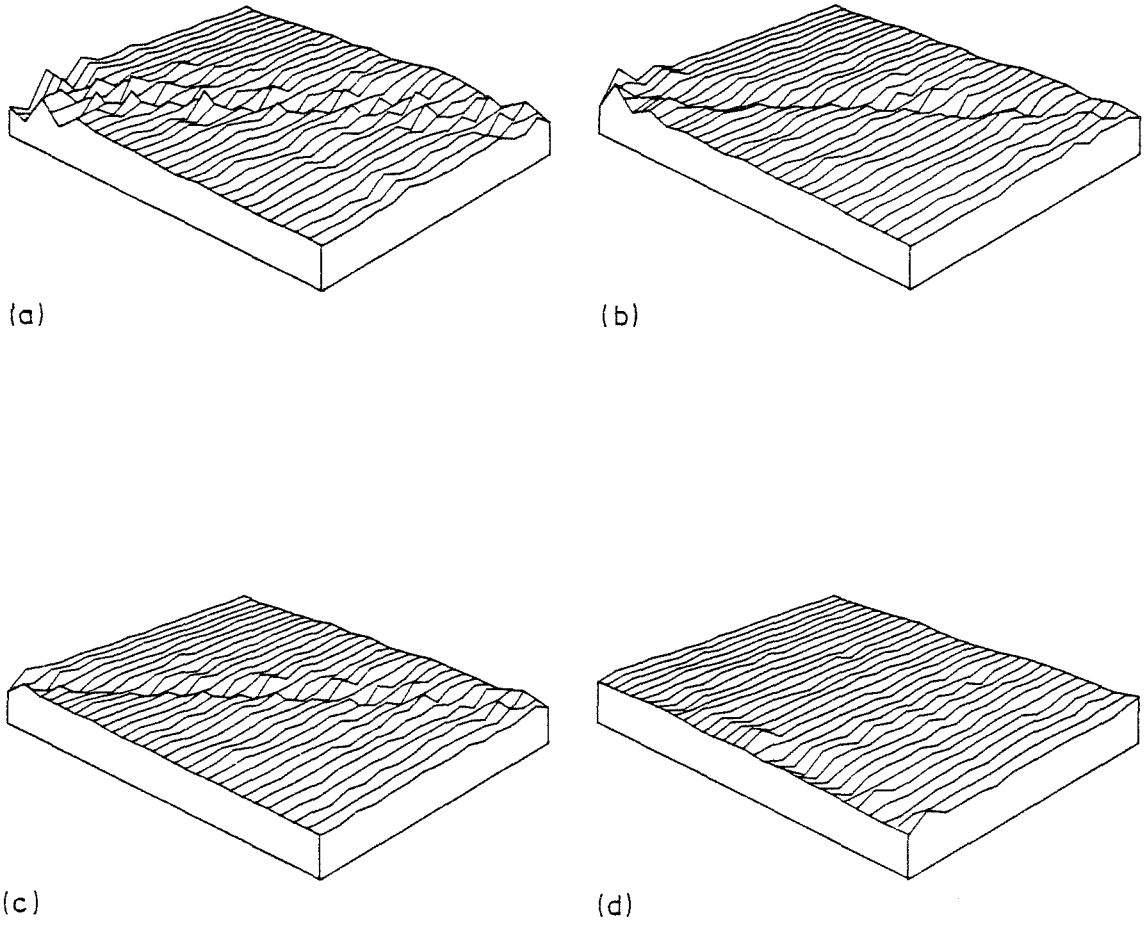

Figure 5.12: Visibilities, due to coupling between the anomalies shown in Figure 5.11, calculated from experimental measurements.

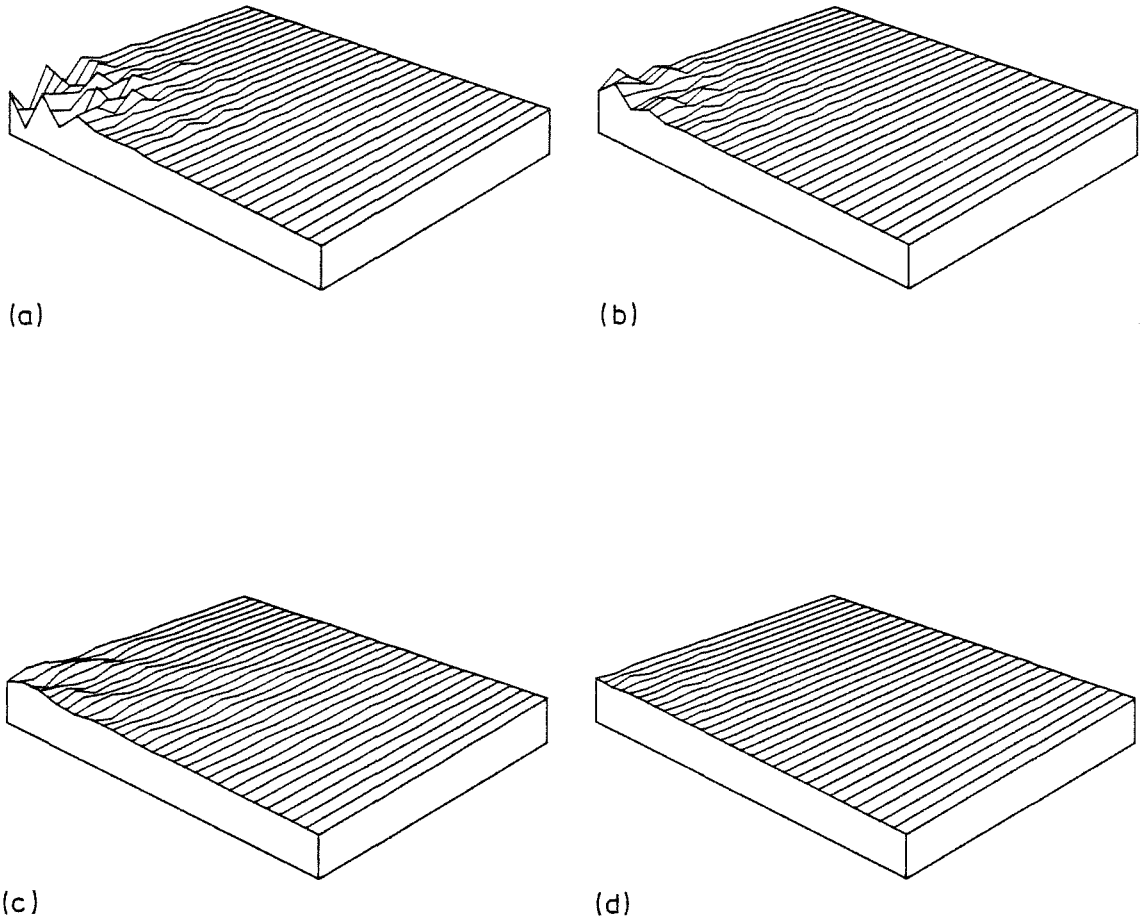

Figure 5.13: Visibilities, due to coupling between the anomalies shown in Figure 5.11, calculated from theory.

In spite of the errors, careful comparison of the left hand corner of each of the plots shown in Figure 5.12 with the corresponding plots in Figure 5.13 does show that the theoretical and experimental values for the coupling are in close agreement. Also as expected, the coupling of the "near" conductivity distributions (a) and (b) is higher than that of the corresponding "far" distributions, (c) and (d) respectively (see Figure 5.13). Similarly, the "big" distributions (a) and (c) have higher coupling than the small distributions (b) and (d) respectively. Furthermore, the visibilities due to coupling shown in Figure 5.12c are significantly less than the visibilities of the "big" anomaly alone (cf. Figure 5.9b). In this situation the coupling term appears, in comparison, to be negligible.

5.3.4 Multiple Offset Anomalies and Coupling

It would simplify matters greatly if the contribution to the transfer impedances, due to coupling between anomalies, was negligible, because the effect on the measurements of each anomaly could then be treated separately. Consider, therefore, the conductivity distribution illustrated in Figure 5.14. This distribution approximates the conductivity cross section of the human leg at calf level. In the distribution there are two "bones" having effectively zero conductivity, and two "superficial blood vessels" and a "group of deep blood vessels" all having effectively infinite conductivity.

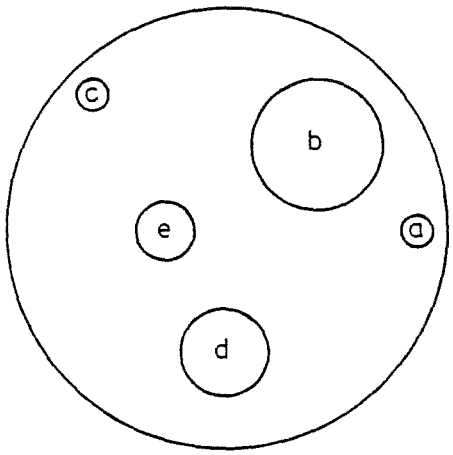

Figure 5.14: Model representing the conductivity cross-section of the human leg at calf level.
(a) & (c) superficial vessels,
(b) & (d) bones,
(e) group of deep vessels.
The conductivity of the vessels, bones, and rest of the limb are taken to be infinity, zero, and unity respectively.

The visibilities obtained when each of the anomalies (a) to (e) (see Figure 5.14) are treated separately, are shown in Figures 5.15a to 5.15e respectively. Figure 5.15f shows the visibility due to coupling between the anomalies calculated using the approach described in §5.3.3. All of these visibilities are deduced from theoretically calculated measurements.

The visibilities of the bones (b) and (d) clearly exceed those due to coupling (f). The visibilities of the superficial vessels, (a) and (c), also exceed those due to coupling, although not by as much as the bones. The visibilities of the deep vessels (e) are of much the same size as those due to coupling. This demonstrates that the visibility due to coupling can be significant in comparison to that of anomalies which are both smaller and

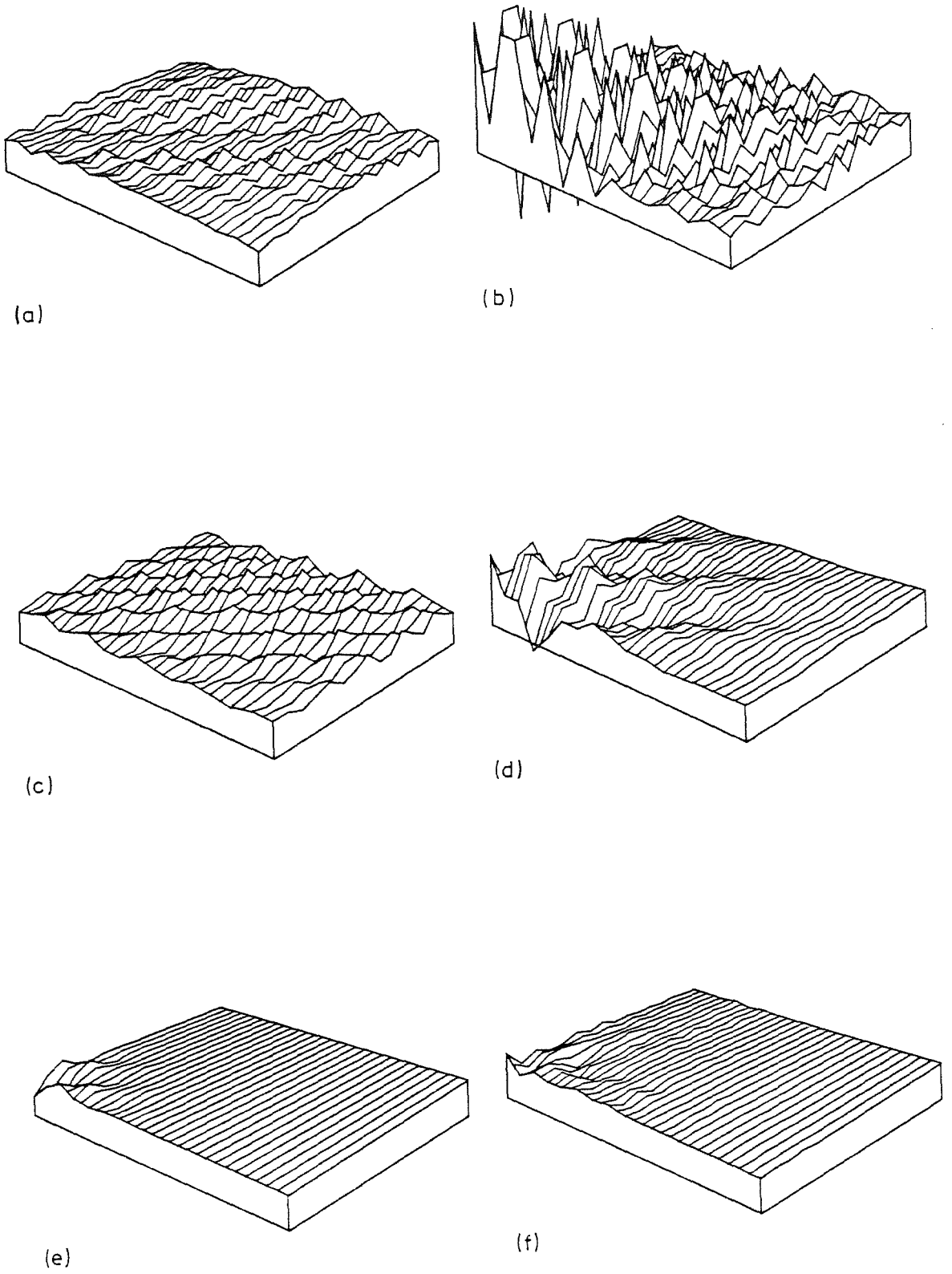

Figure 5.15 (a) to (e): Visibility of individual anomalies (a) to (e) shown in Figure 5.14.

(f): Visibility due to coupling between the anomalies shown in Figure 5.14.

deeper, whereas it may be insignificant in comparison to larger or more superficial anomalies. Depending on which anomalies are of interest, it may therefore be possible to neglect the coupling term. It appears, for the conductivity distribution examined here, that the coupling term can be neglected provided it is not desired to detect the group of deep vessels (e).

5.4 SINGLE OFFSET ANOMALY RECONSTRUCTIONS

Either of the methods developed in §§5.1 and 5.2 can be used to calculate the transfer impedances for any two-dimensional conductivity distribution. However it is not obvious how to adapt these methods to solve directly for such a conductivity distribution from the transfer impedances. Since the equations relating the conductivity distribution and the transfer impedances are nonlinear, it is not even clear if a unique solution for the conductivity distribution exists. However, it is shown in §5.2.5 that a direct solution is possible in terms of a single offset anomaly. In this section that direct solution is examined.

Consider, therefore, the conductivity distribution shown in Figure 5.16. A single nonconducting anomaly having a radius of 0.312 is offset by 0.551 at 180°. Both experimental and simulated measurements were obtained for this conductivity distribution, and the corresponding transfer impedances were calculated using (5.33). Gaussian noise was added to the simulated measurements. The root mean square value of the added noise was 1% of the root mean square value of the measurements. The angle of offset, distance of offset, radius and conductivity of the anomaly were calculated from the transfer impedances using (5.54) to (5.58).

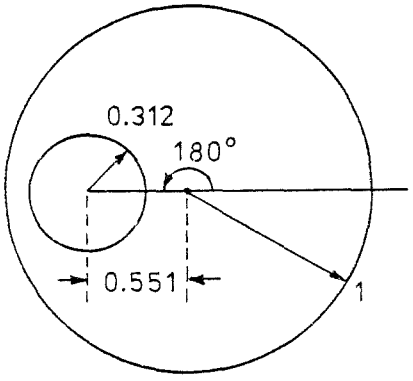

Figure 5.16: Conductivity distribution consisting of a single offset anomaly. The anomaly is characterised by the parameters: angle = 180°, offset = 0.551, radius = 0.312, conductivity = 0.

Listed in Table 5.1 are the values of the parameters calculated from the transfer impedances. The different values of the parameters were obtained from different elements T_{mn} of the matrix T (see §5.2.5). It should be remembered that when calculating the values of the parameters, using (5.54) to (5.58), the angle, offset, radius and conductivity are found in that order. The value calculated for each of these parameters depends upon the values of the preceding parameters. Therefore from all the possibilities of a particular parameter given in Table 5.1, one must be chosen before all possibilities of the next parameter can be calculated. It appears on inspection of Table 5.1 that the values calculated from the elements T_{mn} having the lowest indices m and n are those least affected by noise in the measurements. Therefore the best estimate for the value of an individual parameter is here chosen to be the average of the first three values in the list of alternatives. This choice, indicated in Table 5.1 by an asterisk, is adopted when calculating the values of the subsequent parameters.

Furthermore, since the values of the parameters depend on the values chosen for the preceding parameters, any error in the value of one parameter propagates through to the following parameters. It is expected, therefore, that the angle, offset, radius and conductivity are determined with decreasing accuracy in that order. The percentage errors in the values of these parameters calculated from the experimental measurements are 2%, 11%, 50% and 100% respectively. The errors in the values deduced from the simulated measurements are much lower, but follow the same trend.

Consider now the four conductivity distributions illustrated in Figure 5.17. Each distribution consists of a single offset anomaly having zero conductivity (solid line). The centre of each of these anomalies is marked by an "o". Experimental measurements were obtained from these conductivity distributions, and the best estimates of the parameters representing the conductivity distributions were obtained as described above. The dotted lines in Figure 5.17 indicate the imaged anomalies, alongside which the conductivity, ideally zero, is written. The centre of each imaged anomaly is marked by an "x".

The position of the centre of all the anomalies is imaged reasonably accurately in the sense that it lies within the region occupied by the actual anomaly. However the conductivity and radius are not accurately imaged. The values of the parameters deduced for the larger anomalies (a) and (b), are more accurate than the corresponding values deduced for the smaller

TABLE 5.1: Parameters deduced for the single offset anomaly distribution shown in Figure 5.16 from both experimental and simulated measurements. The indices m and n of the T_{mn} used to calculate the values are also listed.

Indices m,n	Experimental	Simulated 1% noise
	Angle (180^{o})	
2,1	176.9	-179.7
3,2	176.9	-179.1
4,3	171.3	-180.0
5,4	167.8	-177.7
6,5	131.6	-163.4
7,6	30.9	-167.8
8,7	48.0	179.2
*	176.4	-179.6
	Offset (0.551)	
2,1 & 1,1	0.472	0.550
3,1 & 1,1	0.593	0.545
4,1 & 1,1	0.428	0.558
5,1 & 1,1	0.553	0.505
6,1 & 1,1	0.645	0.707
7,1 & 1,1	0.380	0.472
8,1 & 1,1	-0.125	0.428
*	0.498	0.551
	Radius (0.312)	
2,2 & 1,1	0.655	0.293
3,3 & 1,1	0.622	0.327
3,3 & 2,2	0.596	0.345
*	0.624	0.322
	Conductivity (0.000)	
1,1	0.638	0.028
2,2	0.625	0.041
3,3	0.640	0.021
4,4	0.664	0.073
5,5	0.671	0.056
6,6	0.696	-0.027
7,7	0.727	0.064
8,8	0.755	0.881
*	0.634	0.030

anomalies (c) and (d) respectively. This is consistent with larger anomalies having higher sensitivity and visibility (see Chapter 3).

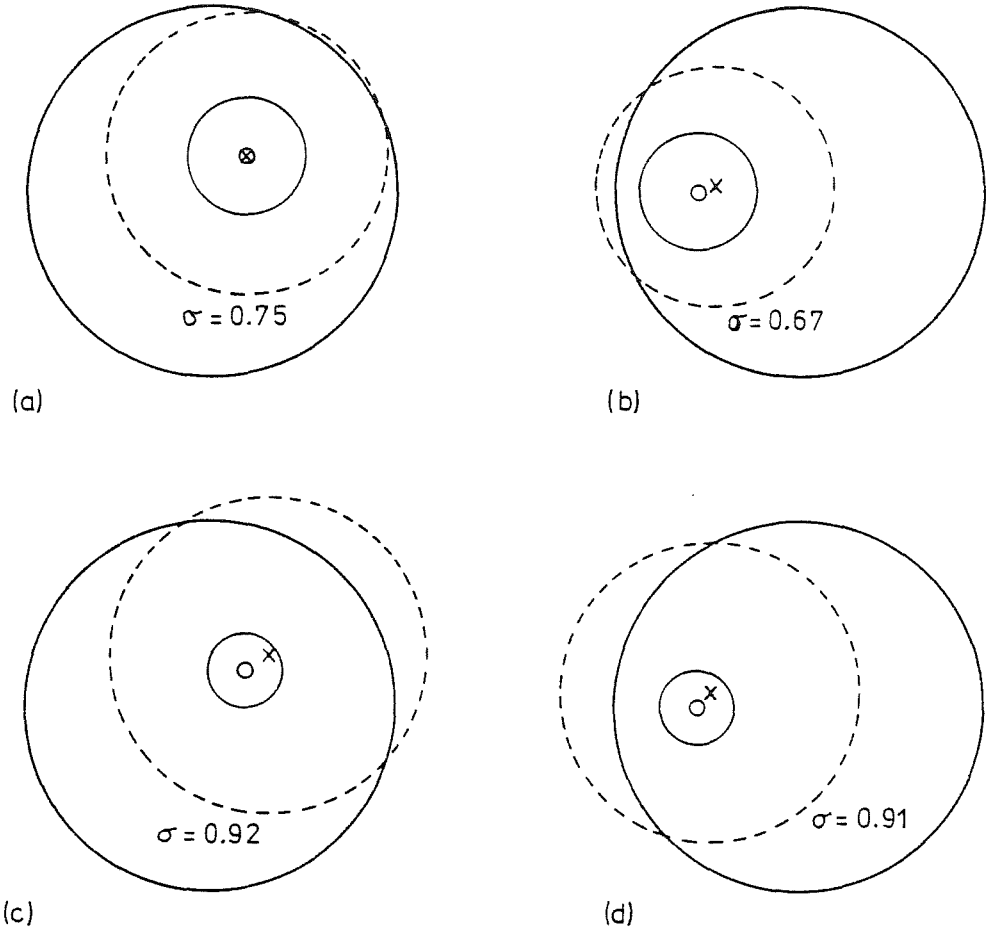

Figure 5.17: Conductivity distributions consisting of single offset anomalies (solid lines) centred at "o". The conductivity of the anomalies is zero, and that of the surrounding region is 1. Imaged anomalies are shown (dashes) with the conductivity written alongside, and are centred at "x".

The method employed here to image these single anomaly conductivity distributions uses only some of the elements of the matrix T (see §5.2.5). The particular elements chosen were those which appear the least sensitive to noise (see above). These elements are therefore the most likely to give an accurate image of the conductivity. However the imaged anomalies extend beyond the surface of the conductive region (see Figure 5.17), which is physically impossible. It may be possible to resolve this difficulty by using more of the elements of the matrix T.

5.5 DISCUSSION

It is shown in §5.1.8 how to make measurements which fully characterise the electrical response of a conductivity distribution. In this chapter such measurements are represented as the transfer impedances (see §§5.1.5 and 5.1.6). These transfer impedances can be calculated from either the experimental measurements or from any conductivity distribution. The geophysical kernel (cf. Keller and Frischnecht 1966; Szaraniec 1976) has similar properties to the transfer impedances. It fully characterises the electrical response of any region which is flat and stratified (see Figure 1.3). It is significant that the conductivity distribution of such a region can be directly calculated from the geophysical kernel (Coen 1981). This suggests that it may be possible to calculate a two-dimensional conductivity distribution from the transfer impedances, although it is not clear in general how this may be done. However, when the transfer impedances are those of a single offset anomaly, the conductivity distribution can be uniquely calculated from them (see §5.2.5).

Since the transfer impedances do uniquely characterise the voltage response of any conductivity distribution, it is possible to use them to compare the measurements gained from different conductivity distributions (cf. 5.3.2). Such comparisons could be used as the basis of an iterative modelling procedure in order to deduce a conductivity distribution from measurements. Smooth and piecewise constant conductivity distributions could be modelled using the expressions developed in §§5.1 and 5.2 respectively.

The direct reconstruction technique developed in §5.2.5 reproduces exactly a conductivity distribution consisting of a single offset anomaly, when used to interpret measurements simulated from such a distribution. If noise is added to these measurements, the reconstruction is degraded (see Table 5.1). When the noise in experimental measurements is large enough, the technique can yield conductivity distributions which are physically impossible (see Figure 5.17). It appears that the sensitivity of the technique to noise, results from using only some of the available information contained in the matrix T (see §5.2.5). It is likely that, by using more of the available information, the technique can be substantially improved.

It is shown in §§5.3.3 and 5.3.4 that under certain conditions the coupling effects between anomalies may be neglected. These conditions are when the anomalies are large or near the surface. Whether coupling effects can be neglected therefore depends on the conductivity of the distribution being probed. The significance of neglecting coupling depends largely on the particular situation. For instance, when probing the earth for orebodies, neglecting coupling means it is likely that only the larger or shallower of the orebodies are detected. These orebodies are potentially more economically viable to recover than any smaller and deeper orebodies which may not have been detected. In this situation it seems appropriate to neglect coupling. It would be possible to establish in advance whether coupling could be neglected if some a priori knowledge about the conductivity distribution was available. This is particularly relevant to medical probing, since much is known in advance about the anatomy of the region being probed. In that situation it would even seem likely that the coupling effects could be estimated on the basis of the anatomy, and rather than neglecting the coupling effects some compensation could be introduced to make allowance for them.

CHAPTER 6

MODELLING LIMB VOLUME CHANGES MEASURED DURING VENOUS OCCLUSION PLETHYSMOGRAPHY

Venous occlusion plethysmography is a technique for measuring the changes in limb volume over an interval during which venous bloodflow is temporarily interrupted (see §1.3.3). These changes in volume are useful in the detection of a medical condition called venous thrombosis (cf. Sumner 1978). Descriptions of venous thrombosis, and another important condition which can arise from it, are given in §6.1.

In §6.2 a simple model is developed to interpret the changes in volume measured during venous occlusion plethysmography. Results are reported of three studies which have been carried out in order to evaluate the model. Firstly, the physiological changes predicted by the model are compared with those measured on human limbs. In the second study, the relationships between the parameters used in the model and particular physiological variables of the limb are examined. Finally, it is demonstrated by example that the model can be used effectively to monitor changes in these physiological variables.

6.1 VENOUS THROMBOSIS AND PULMONARY EMBOLISM

Venous thrombosis and pulmonary embolism are two medical conditions which occur in the circulatory system. This system transports blood around the body. It consists of the pulmonary circulation and the systemic circulation, which are interconnected by the heart. The pulmonary circulation comprises the blood vessels which make up the lungs, and the vessels connecting the lungs to the heart. The systemic circulation is comprised of all other blood vessels in the body.

Blood usually coagulates only when in the presence of damaged tissue. However under various abnormal circumstances it can coagulate in a blood vessel even when the latter is not damaged. Such abnormal coagulation is called thrombosis, and the coagulated blood is called a thrombus (the plural of which is thrombi) (cf. Guyton 1971, Ch.10). Patients who are undergoing surgery or who are immobile for long periods are particularly susceptible to venous thrombosis in the veins of the calf muscles (cf. Caro et al 1978, Ch. 10). There is an increased likelihood of thrombi forming when the

bloodflow decreases. Disturbances of the mechanisms which control coagulation can also lead to venous thrombosis.

A thrombus may sometimes be dislodged from its site of formation and be transported through the veins towards the heart. Such a free floating thrombus is called an embolus. After passing through the heart the embolus enters the arteries of the pulmonary circulation. These arteries branch and get smaller in size, so that the embolus becomes lodged in the pulmonary circulation. This condition is referred to as a pulmonary embolism. If the embolus blocks both of the main arteries of the pulmonary circulation, which are called the pulmonary arteries, then death follows immediately. If only one of the pulmonary arteries or a smaller arterial branch is blocked then death may not occur immediately, but the function of the lungs is usually dangerously impaired. Further growth of such an embolus can subsequently lead to death (cf. Guyton 1971, Ch.10).

6.2 THE MODEL OF THE LIMB CIRCULATION

The model depicted in Figure 6.1 is used here to represent the circulatory system within the limb. The networks of arteries, capillaries and veins which make up the limb circulation are each represented in the figure by a single blood vessel. The model cuff represents an actual cuff that is placed circumferentially around the limb, so that when it is inflated the bloodflow through the veins is interrupted. The arterial pressure P_a forces blood, at a flow rate Q_a, through the resistance of the arterioles R_a and into the capillaries and veins. The venous pressure P_v forces the blood, at a flow rate Q_v, through the veins and out of the limbs. The resistance to bloodflow out of the limb is the venous resistance R_v when the cuff is deflated, and is R_v plus the cuff resistance R_c when the cuff is inflated.

It is assumed that the presure drop ΔP across any resistance R is proportional to the flow Q through the resistance, and that changes in the volume of the veins ΔV are proportional to changes in venous pressure ΔP_v. These relations are written

$$\Delta P = QR \tag{6.1}$$

and

$$\Delta V = C_v \Delta P_v \tag{6.2}$$

respectively, where C_v is the venous compliance (cf. Noordergraaf 1978, p.25).

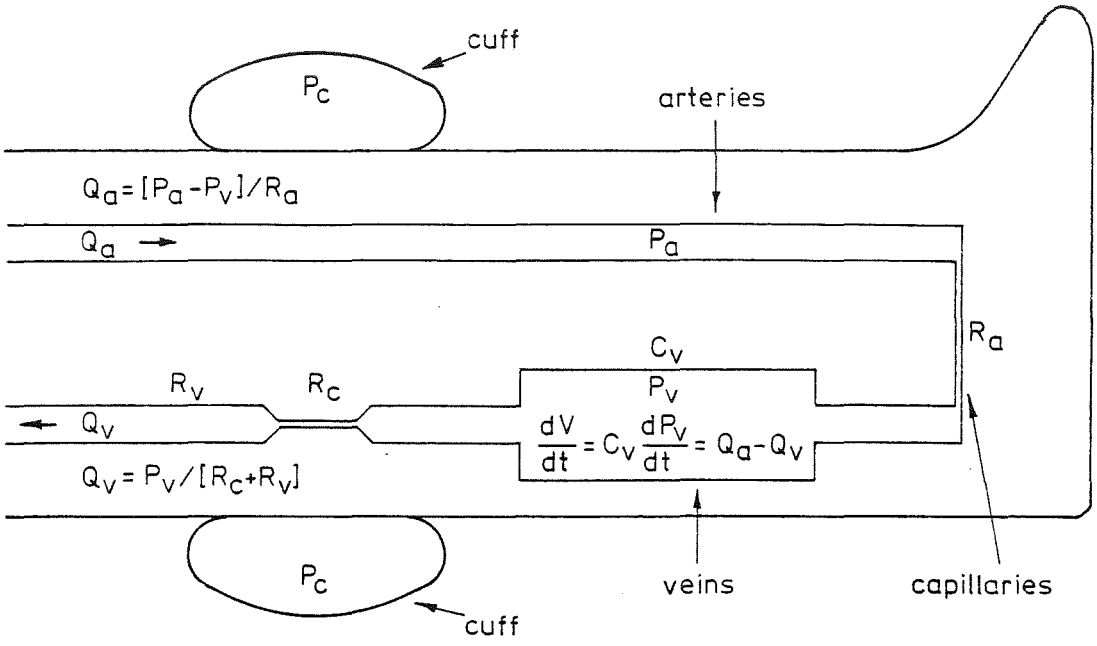

Figure 6.1: Model of limb circulation during venous occlusion.

Q_a = arterial bloodflow — Q_v = venous bloodflow

P_a = mean arterial pressure — P_v = venous pressure

R_a = arteriolar resistance — R_v = venous resistance

P_c = cuff pressure — C_v = venous compliance

R_c = cuff resistance — dV/dt = changes in venous volume with respect to time.

When venous occlusion is released both P_c and R_c are zero.

In plethysmography, volume changes are often expressed as volume changes per unit volume of tissue (cf. Sumner 1978) in terms of the units "cc/100cc" or "ml/100ml" or "%". It is therefore convenient here to define $C_u = C_v/V$ as the venous compliance per unit volume of tissue. Suppose, now, that the venous bloodflow is first occluded by inflating the cuff at t = 0, and is subsequently restored by deflating the cuff at t = T. Solving the differential equation shown in Figure 6.1 then gives the volume change resulting from the alterations to the venous bloodflow. The fractional volume change per unit volume $\Delta V/V$ is

$$\Delta V/V = P'C_u\left[1-\exp(-t/R_1C_u)\right] \quad ; \quad 0<t<T \qquad (6.3)$$

and

$$\Delta V/V = V(T)\exp\left[(T-t)/R_2C_u\right] \quad ; \quad t>T \qquad (6.4)$$

where V(T) is the fractional change in volume reached just before cuff release,

$$R_1 = R_a(R_c+R_v)/(R_a+R_v+R_c) \tag{6.5}$$

$$R_2 = R_aR_v/(R_a+R_v) \tag{6.6}$$

and

$$P' = P_aR_1/R_a \ . \tag{6.7}$$

P' is the venous pressure which would be reached if the cuff was inflated indefinitely.

6.2.1 Using the Model to Represent Measurements

The parameters of the model which are of particular interest are the venous resistance R_v, the venous compliance per unit volume of tissue C_u, and the bloodflow per unit volume of tissue Q_a/V. When t = 0 the value of Q_a/V is the same as the limb bloodflow before occlusion. Specific values of these parameters represent particular volume changes as a function of time. In order to use the model to represent particular limb volume changes, the values of these parameters must be calculated from the volume changes.

The first step in determining the values of the parameters involves fitting exponential curves of the form "volume = A+Bexp[-Ct]" to the measurements. Fitting one exponential from t = 0 to t = T gives the values A_1, B_1 and C_1, say, for A, B and C (see Figure 6.2). Fitting another exponential for t > T gives the new values A_2, B_2 and C_2, say, for A, B and C. An effective procedure for fitting exponentials to measured data is described in §6.3.

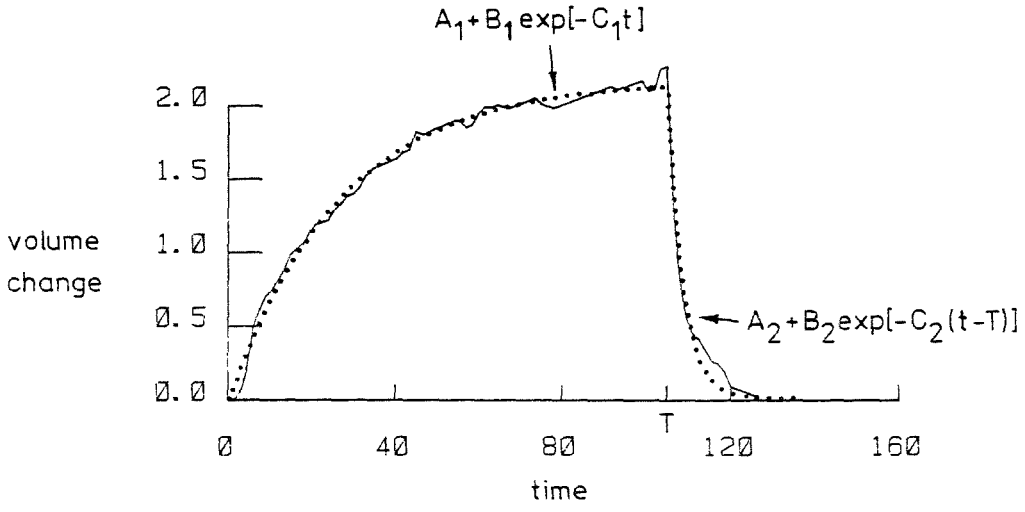

Figure 6.2: Exponentials (dotted) fitted to measurements (solid)

Once the exponentials are fitted to the measurements then the values of the model parameters may be determined. Equating B_1 and C_2 to the corresponding terms in (6.3) and (6.4) respectively gives

$$P'C_u = -B_1 \tag{6.8}$$

and

$$R_2C_u = 1/C_2 \ . \tag{6.9}$$

Similarly, equating the time derivative of (6.3) with that of $A_1+B_1\exp[-C_1t]$ and evaluating the resulting expression at t = 0 (written as $|_{t=o}$) gives

$$d(\Delta V/V)/dt\big|_{t=o} = (Q_a-Q_v)/V\big|_{t=o} = -B_1C_1 \ . \tag{6.10}$$

It is found in practice that the bloodflow calculated using the left hand side of (6.10) usually agrees well with the arterial bloodflow $Q_a/V|_{t=o}$ measured directly (cf. Raman et al 1973). Therefore, the leakage of blood through the veins, under the cuff and out of the limb, immediately following cuff inflation, is comparatively small. Hence $Q_v/V|_{t=o} << Q_a/V|_{t=o}$. Therefore using (6.10), the arterial bloodflow before cuff inflation can be calculated from the measurements using

$$Q_a/V\big|_{t=o} \simeq -B_1C_1 \ . \tag{6.11}$$

Assuming now that P' is known, the value of the venous compliance C_u is given from (6.8) by

$$C_u = -B_1/P' \ . \tag{6.12}$$

Ordinarily, the venous pressure in the limb of a supine subject is about 10 mmHg* and the mean arterial pressure is about 85 mmHg (cf. Rushmer 1970 Ch. 6). In terms of the model this means $R_a \simeq 7.5R_v$. Hence, from (6.6), $R_2 \simeq R_v$. Using (6.8) and (6.9) therefore gives an estimate of the venous resistance to be

$$R_v \simeq -P'/B_1C_2 \ . \tag{6.13}$$

---

* 100 mmHg = 7.501 kPa.

6.3 EXPERIMENTAL STUDIES

This section describes three experimental studies in which the model has been invoked. The first study compares the changes in venous pressure and limb volume predicted by the model with those measured on human limbs. The second study is based on a "limb" which is a physical model of a real limb. Using this "limb" enables the three physiological quantities limb bloodflow, limb compliance and limb resistance to be varied independently. The volume changes of the "limb" are interpreted in terms of the three model parameters Q_a/V, C_u and R_v (see §6.2.1) in order to relate them to the physiological quantities. The third study describes measurements made on a patient in a clinical environment.

In all of these studies the impedance plethysmograph described in Appendix 2 was used to measure the volume changes of the limbs (both those of humans and of the model "limb" described in §6.3.2). Exponential curves were iteratively fitted to these volume changes by minimising the root mean square difference between the exponentials and the measurements. The particular iterative procedure employed was a modified Newton algorithm (see Appendix 3), which requires initial estimates of the exponential curves. Initial estimates were obtained directly from the measurements as described in Appendix 6. The values of the model parameters Q_a/V, C_u and R_v were then calculated using (6.11) to (6.13).

6.3.1 Comparison of Model of Limb Circulation with Human Limbs

Method

Venous occlusion plethysmography was performed on two resting supine subjects. A pneumatic cuff was applied just above the knee for interrupting venous bloodflow. Each subject had a venous catheter inserted in the foot. The venous pressure was measured using a strain gauge connected to the catheter. The venous bloodflow was interrupted by suddenly inflating the pneumatic cuff to a preselected pressure in the range from 20 to 100 mmHg. That cuff pressure was maintained until the venous pressure ceased rising. The cuff was then suddenly deflated. Both the venous pressure and the changes in limb volume were recorded from before the inflation of the cuff until approximately thirty seconds after it had been deflated. Measurements of pressure and volume changes were obtained under different conditions of cuff pressure on three legs. Each of these measurements was duplicated to check that the results were repeatable.

Results

The changes in volume measured on one limb are shown in Figure 6.3a. The exponential curves which were fitted to these changes in volume are shown in Figure 6.3b. The values of the model parameters which correspond to these curves are listed in the caption of Figure 6.3b. Comparing Figure 6.3a to Figure 6.3b shows qualitatively that the changes in limb volume can be accurately represented by the model. This accuracy is quantified here in terms of the root mean square difference between corresponding curves in Figures 6.3a and 6.3b. This difference varies between 3.1% and 4.1% of the maximum value reached by the respective changes in volume. The average root mean square difference between all eleven of the measured and modelled changes in volume is 4.1% with a standard deviation of 2.7%.

The changes in venous pressure measured on the limb are shown in Figure 6.4a. The changes in venous pressure represented by the model, for the model parameters listed in the caption to Figure 6.3b, are illustrated in Figure 6.4b.

Figure 6.5 shows the changes in limb volume measured on three limbs plotted as a function of venous pressure. The venous compliance per unit volume of tissue is the slope of the curves shown. The venous compliance decreases as the pressure in the veins increases.

Figure 6.6 shows the value at which the venous pressure stabilised (i.e. P'), for three limbs, plotted as a function of cuff pressure. Over the range of cuff pressures commonly used in venous occlusion plethysmography (i.e. 40 mmHg to 60 mmHg) the maximum venous pressure is approximately one half of the cuff pressure.

6.3.2 Relating the Model Parameters to Physiological Quantities

Method

The model "limb" depicted in Figure 6.7 consists of four functional parts. These are (i) a pump to circulate saline, (ii) a section which expands when flow is interrupted downstream, (iii) a section on which interruption of flow can be performed and (iv) a narrow orifice to provide resistance to flow.

The pump (Bio-console model 520A, Bio-medicus Inc) circulated a 0.9% sodium chloride solution at flow rates of 125,250 and 375 cc/min. It was operated under servo control, using feedback from an electromagnetic flow-

meter, with the aim of maintaining a constant flow independent of the resistance to flow.

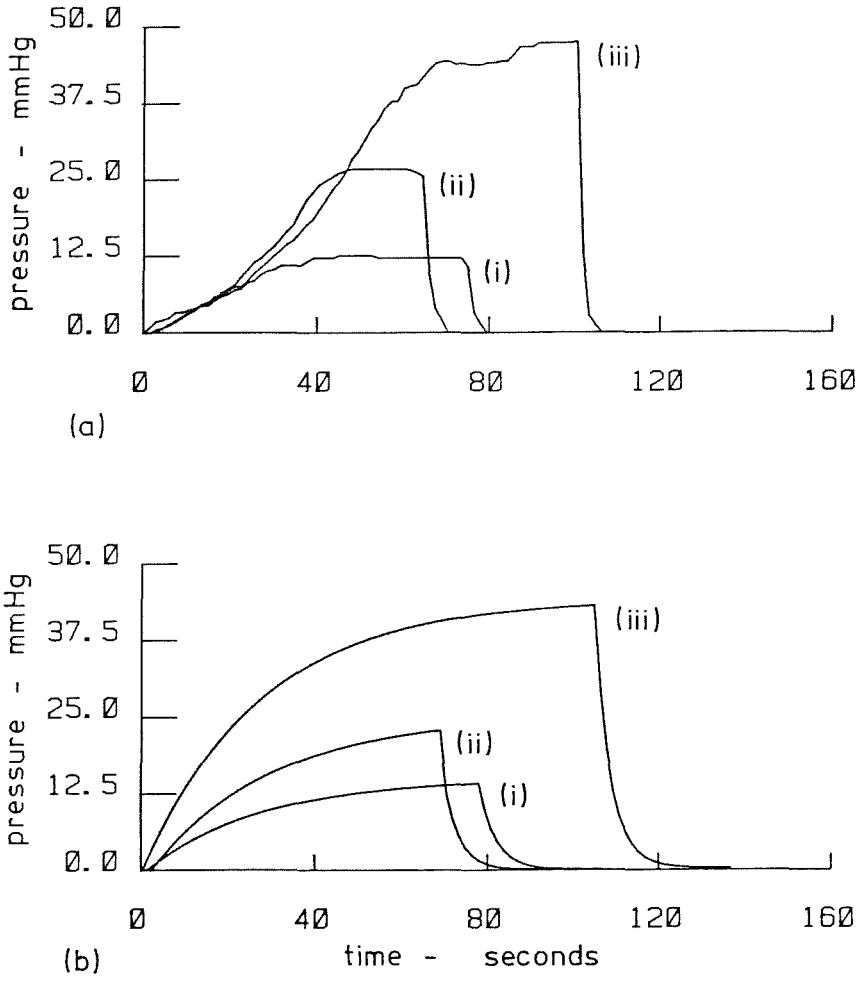

Figure 6.3: (a) Volume changes measured at different cuff pressures on one limb.

P_c = (i) 30, (ii) 50, (iii) 80 mmHg.

(b) Volume changes predicted by the model having parameters:

$Q_a/V|_{t=o}$ = (i) 0.067, (ii) 0.077, (iii) 0.083 %/s.

C_u = (i) 0.11, (ii) 0.076, (iii) 0.054 %/mmHg.

R_v = (i) 35.5, (ii) 46.1, (iii) 68.1 mmHg/(%/s)

P' = (i) 15, (ii) 25, (iii) 40 mmHg.

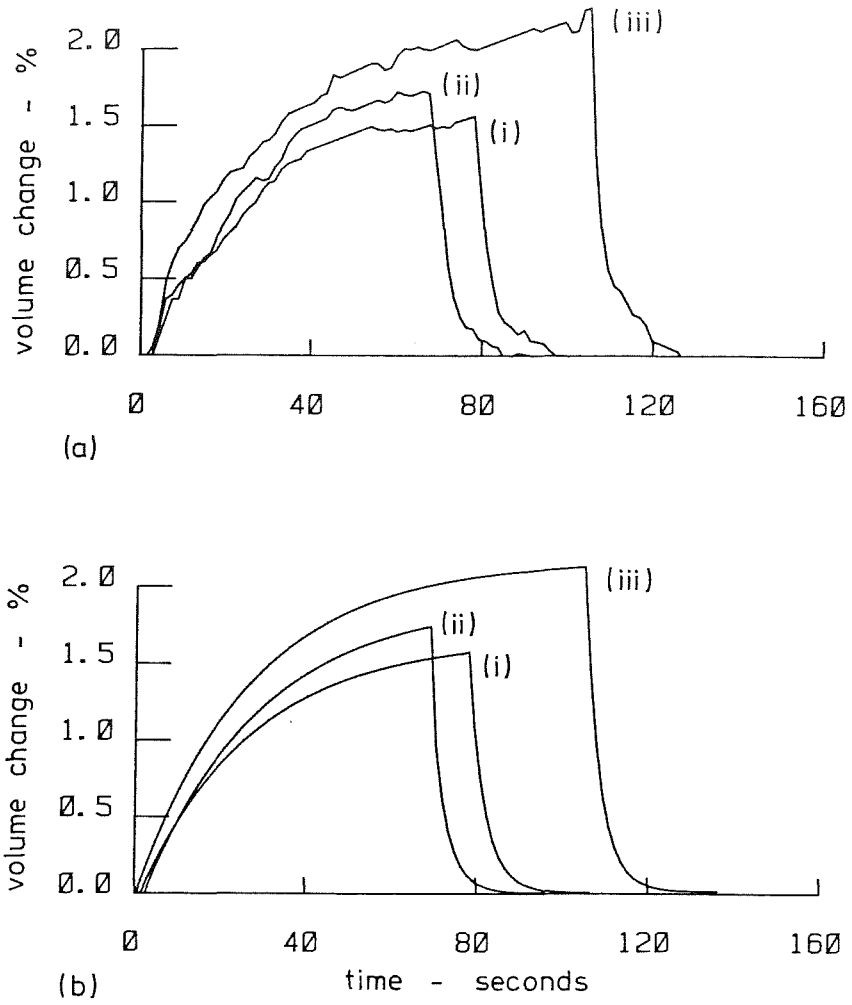

Figure 6.4: (a) Venous pressure changes measured at the same time as the volume changes shown in Figure 6.3a.

(b) Venous pressure changes predicted by the model having the parameters as given in the caption to Figure 6.3b.

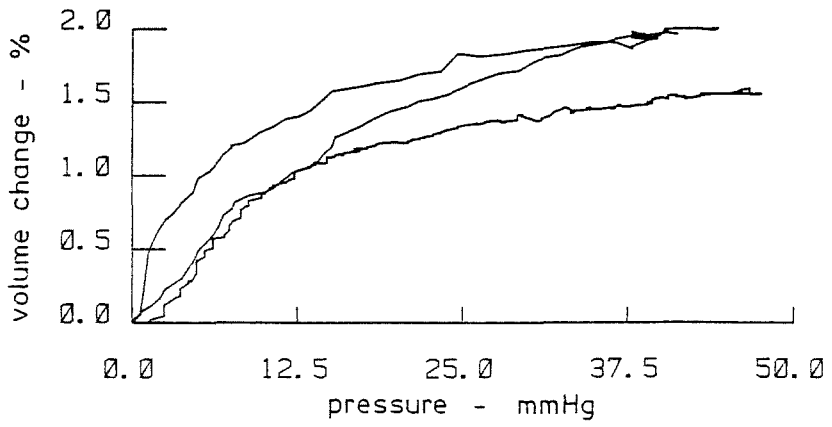

Figure 6.5: Limb volume change plotted as a function of venous pressure for three limbs. The venous compliance per unit volume of tissue is the slope of the curves shown.

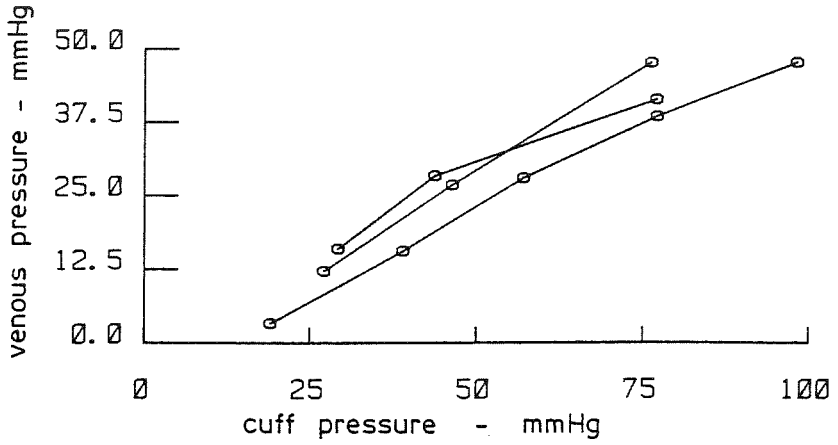

Figure 6.6: Maximum venous pressure obtained after indefinite occlusion for three limbs over a range of cuff pressures.

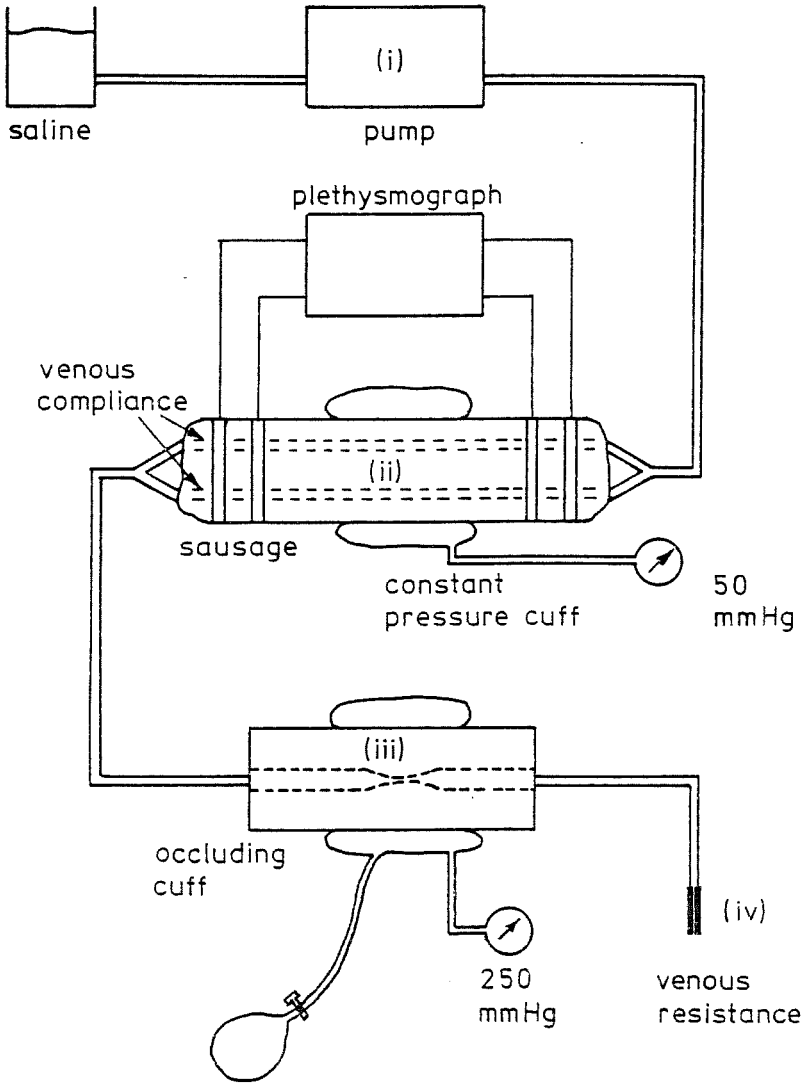

Figure 6.7: Model "limb" used for investigating the controlled variation of flow, compliance and resistance (see text).

A large sausage 45 cm long and 10 cm in diameter was used to model the flesh of the limb. Veins were simulated by two parallel lengths of dog intestine threaded internally down the length of the sausage. Changes in compliance were effected by clamping off one of the lengths of intestine. The electrical impedance plethysmograph (see Appendix 2) was connected to the sausage to measure changes in its volume. Tissue elasticity was simulated by maintaining a fixed pressure of 50 mmHg in a pneumatic cuff encircling the sausage. This was necessary to ensure the sausage returned to its original volume following any experiment.

The second section of the "limb" comprised a length of thin walled (0.1 mm) rubber tube mounted concentrically within a semi-rigid rubber-impregnated canvas pipe. The space between the tube and pipe was filled with water. A pneumatic cuff encircling this section was employed to interrupt the flow of saline, using the method for occluding flow described in §6.3.1.

The resistance to outflow from the "limb" was changed by altering the size of the orifice downstream. Three different sizes of orifice were employed.

A control condition for the "limb" was chosen to be a flow rate of 250 cc/min., a compliance corresponding to both vessels open, and a resistance corresponding to the intermediate-sized orifice. The flow and resistance were each independently changed to higher and lower values compared to the control condition. The compliance was changed only to a lower value.

The cuff encircling the second section of the "limb" was inflated to 250 mmHg, and then deflated when there was no further apparent increase in the volume of the sausage. This was repeated for all of the various conditions of flow, compliance and resistance. For each condition the changes in volume of the sausage were measured. The model parameters for which the model described in §6.3.2 mimicked these changes were calculated.

Results

Table 6.1 shows the model flow, compliance and resistance calculated when the "limb" flow was 125, 250 and 375 cc/min. respectively, and the "limb" compliance and resistance remained at their control values. Each model parameter is the average of duplicate experiments, and is normalised to the average of its respective control value. Table 6.2 records the variations of the three model parameters when the "limb" compliance was

changed, and Table 6.3 shows the effect of altering "limb" resistance.

Table 6.1: Relative changes in model parameters in response to changes in "limb" flow.

"Limb" Quantity Flow x 250 cc/min.	Model Parameter		
	Flow	Compliance	Resistance
0.50	0.53	1.01	0.76
1.00	1.00	1.00	1.00
1.50	1.47	0.98	1.81

Table 6.2: Relative changes in model parameters in response to changes in "limb" compliance.

"Limb" Quantity Compliance	Model Parameter		
	Flow	Compliance	Resistance
1 vessel	0.94	0.61	1.22
2 vessels	1.00	1.00	1.00

Table 6.3: Relative changes in model parameters in response to changes in "limb" resistance.

"Limb" Quantity Resistance	Model Parameter		
	Flow	Compliance	Resistance
low	0.96	1.03	0.20
medium	1.00	1.00	1.00
high	1.03	0.86	5.41

The standard deviations of the model parameters are 0.07, 0.08 and 0.09 for the flow, compliance and resistance respectively in the control experiments. The overall standard deviation of all the model parameters in Tables 6.1 to 6.3 taken together is 0.07. This suggests that a change of less than 0.07 in any of the model parameters is insignificant. In Table 6.1 there are significant changes in the values of both model flow and resistance. In Tables 6.2 and 6.3 there are significant changes in the values of both model compliance and resistance.

6.3.3 Monitoring Limb Bloodflow, Compliance and Resistance

Method

Venous occlusion plethysmography was used to record changes in limb volume before, during and after surgery. The particular surgery for which volume changes were recorded was an abdominal hysterectomy. The surgery was performed with the patient under an epidural plus a light general anaesthesia. The values of the model parameters were calculated from the measured changes in volume.

Results

Figure 6.8 shows the variations of limb bloodflow, compliance and resistance plotted as a function of time. The preoperative values of the parameters were bloodflow = 0.082%/s, compliance = 0.083%/mmHg = 1.1%/kPa, and resistance = 35 mmHg/(%/s) = 2.6 kPa/(%/s). (Remember that "%" means "cc of blood per 100 cc of tissue"). Reference to Figure 6.8 shows that there were pronounced changes in the values of all of these parameters during the surgical procedure.

6.4 DISCUSSION

The model described in §6.2 can closely mimic the changes in limb volume measured during venous occlusion plethysmography (see Figure 6.3 and §6.3.1). Therefore the model parameters can be used to accurately represent such changes in volume. These changes in volume can be interpreted to detect venous thrombosis (cf. Barnes et al 1972; Johnson and Kakkar 1974; Jaffrin 1976; Wheeler et al 1974). It therefore follows that it is also possible to interpret the model parameters, for which the model mimics these changes, to detect venous thrombosis. Indeed the model parameters are directly related to the variables used by Barnes et al (1972), Johnson and Kakkar (1974), Jaffrin (1976) and Wheeler et al (1974) for detecting venous thrombosis (see Table 6.4).

The venous pressure P', which would be reached if the cuff was left inflated indefinitely, (see (6.7)) is needed in order to find the values of the model parameters C_u and R_v from the changes in limb volume (see §6.2.1). It is seen from Figure 6.6, for the experiments described in §6.3.1, that P' was approximately one half of the cuff pressure. It therefore seems, for the particular cuff used in these experiments (10 cm x 86 cm Zimmer torniquet cuff), that a good estimate for P' is one half of the cuff pressure.

This estimate was used in the experiments described in §§6.3.2 and 6.3.3, since it was not convenient in those experiments to measure the venous pressure.

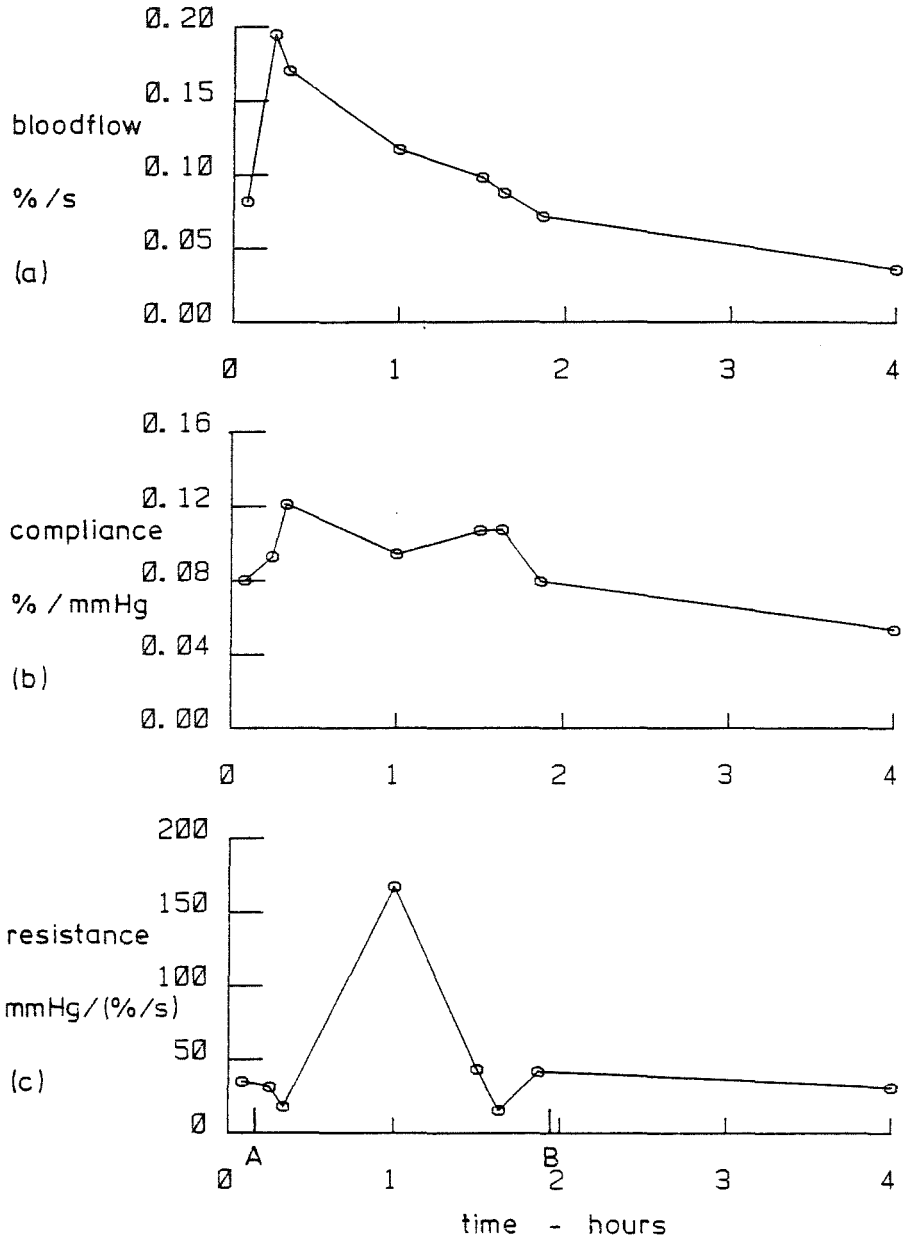

Figure 6.8: Variations in the (a) bloodflow, (b) compliance and (c) resistance measured on the leg of a patient undergoing surgery. The time from A to B is the period during which the patient was in theatre.

Table 6.4: Variables used to detect venous thrombosis in previous studies, in terms of the parameters of the model used here. (See also Figure 1.6).

Variable(s)	In Terms of the Model	Reference
Maximum venous outflow	$-V(T)/R_vC_u$	Barnes et al (1972)
Drop in 2s over rise	$1-\exp(-2/R_vC_u)$	Johnson & Kakkar (1974)
Half life	$R_vC_u\ln 2$	Jaffrin (1976)
Drop in 3s	$V(T)\left[1-\exp(-3/R_vC_u)\right]$	Wheeler et al (1974)
and rise	$V(T)$	Wheeler et al (1974)

Inspection of Table 6.1 shows that changes in the "limb" bloodflow (see §6.3.2) correspond to changes in the flow deduced with the aid of the model. The values of the latter flow agree within experimental error with the respective values of the former flow. There are no significant changes in the compliance of the model. However the resistance of the model shows even more variation than does the flow. This is because the resistance to turbulent flow through pipes is nonlinearly related to flow, as is the resistance to bloodflow through vessels (cf. Berne and Levy 1972 pp 44-59; Caro et al 1978 Ch.5, 14). In both of these situations the resistance increases as the flow increases. The changes of the resistance shown in Table 6.1 are therefore consistent with the changes in flow.

Altering the "limb" compliance produced significant changes in both the compliance and the resistance deduced using the model (see Table 6.2). The change in compliance was effected by clamping off one vessel, thereby blocking one passage through which saline flowed. This action also altered the resistance, which accounts for the increase in resistance accompanying the decrease in compliance shown in Table 6.2.

Increasing the "limb" resistance, by altering the size of the orifice (see Figure 6.8), produced an increase in the model resistance and a decrease in the model compliance (see Table 6.3). When the resistance is increased, with the flow remaining the same, the pressure in the "limb" prior to interruption of the flow is also increased. In this situation the vessels are more fully distended. However the compliance of a full vein is lower than that of one which is empty (cf. Moreno et al 1970). It therefore follows that the compliance of the vessels in the "limb" decreases as the flow increases. Hence the changes in compliance shown in Table 6.3 are consistent with the respective changes in resistance.

Tables 6.1 to 6.3 together suggest that changes in each of the "limb" quantities of flow, compliance and resistance accord with similar changes in the corresponding model parameters. In actual limbs it is observed that an increase in flow causes an increase in resistance, and an increase in pressure causes a decrease in compliance (cf. Berne and Levy 1972 pp 44-59; Moreno et al 1970). As discussed above, the values of the resistance and compliance deduced from measurements on the "limb" increased and decreased respectively when the flow and pressure respectively increased. This suggests that the model described in §6.2 is particularly suitable for monitoring changes in the venous compliance and venous resistance of real limbs. Figure 6.8 shows the changes in flow, compliance and resistance monitored on one human limb during surgery. These changes are clearly large enough to be detected with the aid of the model. Monitoring changes in bloodflow during surgery is of particular relevance to the detection of venous thrombosis, since reduced bloodflow is one of the factors related to the formation of the thrombi. Patients who are undergoing surgery are particularly susceptible to venous thrombosis.

The model described in §6.2 can closely mimic the changes in limb volume measured during venous occlusion plethysmography (see Figure 6.2 and §6.3.1), but it does not seem to be capable of accurately representing changes in venous pressure (see Figure 6.3). This is because the model compliance is assumed independent of the volume of the veins (i.e. (6.2)) whereas, as mentioned earlier, the compliance of veins depends on their volume. This dependence may be deduced from Figure 6.4. There the compliance per unit volume of tissue is represented by the slope of the plots of change in volume against change in pressure. The slope decreases as the volume or pressure increases.

The compliance deduced with the aid of the model is nevertheless directly related to the compliance of veins. The latter compliance C' can be written as

$$C' = dV/dP \ . \tag{6.14}$$

Consider the mean value of C' over the range of venous pressures from P_1 to P_2. This mean value is

$$C'_{mean} = \int_{P_1}^{P_2} \left[C'/(P_2-P_1)\right] dP \ = (V_2-V_1)/(P_2-P_1) \tag{6.15}$$

where V_1 and V_2 are the volumes of the veins at pressures P_1 and P_2 respectively. Suppose now that P_1 and P_2 are the venous pressures just before the cuff is inflated and deflated respectively. Reference to (6.2) then shows that

$$C'_{mean} = C_v \tag{6.16}$$

so that

$$C_u = C_v/V = C'_{mean}/V\,. \tag{6.17}$$

Therefore the venous compliance per unit volume C_u, found by using the model, is precisely the mean value of the compliance C' of the veins, per unit volume of tissue, over the range of venous pressures occurring during occlusion.

Both the venous and arteriolar resistances, and the venous compliance are assumed here to be constant during the measurement of the changes in limb volume. However it is argued by Caro et al (1970) that the vascular bed dilates actively shortly after cuff release. This is sometimes observed as a transient increase in volume some 5 to 10 seconds following cuff release (Lewes and Grant 1925). In the model introduced here, dilation of the vascular bed can be represented by a change in the value of the parameter R_a. When a transient increase in volume is observed following cuff release, it may therefore be useful to model R_a as a function of time following cuff release.

Zicot et al (1970) deduce flow, resistance and compliance using a different technique from that described here. They measure the changes in limb volume caused by increased external pressure on the limb. This differs from venous occlusion plethysmography, in which the changes in volume are due to increasing internal (i.e. venous) pressure. The average values of the parameters obtained by Zicot et al on 11 resting subjects are: flow per unit volume = 0.054%/s, compliance per unit volume = 1.1%/kPa, and resistance = 3.8 kPa/(%/s). These values compare favourably with the preoperative values of the parameters shown in Figure 4.7 (i.e. Q_a/V = 0.082%/s, C_u = 1.1%/kPa and R_v = 2.6 kPa/(%/s)).

There appear to be three particularly useful applications for the model described in §6.2. Firstly, the model parameters deduced from changes in limb volume, and the equations listed in Table 6.4 can be used to calculate the quantities employed by others when detecting venous thrombosis (cf. Barnes et al 1972; Johnson and Kakkar 1974; Wheeler et al 1974;

Anderson and Wheeler 1979). These quantities can then be invoked to detect venous thrombosis. Secondly, the values of the model parameters themselves can be used directly to represent the condition of the circulation within the limb. The values of the model parameters which represent particular conditions, such as thrombosis, have yet to be established. Finally, it is particularly important to note that changes in the compliance and resistance deduced with the aid of the model exhibit a dependency on pressure and flow respectively which is characteristic of the compliance and resistance of blood vessels. This suggests that a particularly appropriate application for the model is to use changes in the model parameters to monitor changes in the condition of limb circulation.

CHAPTER 7

CONCLUSIONS AND SUGGESTIONS FOR FUTURE RESEARCH

7.1 LIMITATIONS ON IMPEDANCE IMAGING

Limits on the spatial resolution and conductivity resolution of impedance imaging systems are developed in Chapter 3. These limits are useful for estimating the accuracy with which a conductivity distribution can be imaged. Both the spatial resolution and conductivity resolution can be found from them. The limits are developed for both circular and half plane regions, so that they have application to both medical and geophysical probing. With the aid of conformal transformations, similar limits could also be found for regions of other shapes.

A preliminary estimate of the accuracy of an imaged conductivity distribution is particularly important when using an iterative imaging technique, since the convergence of any such technique is often open to question. Many of the techniques commonly employed to interpret geophysical probing measurements are iterative, so that the limits developed in this thesis may be of use in geophysics.

The spatial resolution and conductivity resolution of a particular impedance image depend upon several factors. The former resolution is related to the accuracy of the measurements, and the latter is related to both the spatial resolution and the accuracy of the measurements. Both of these resolutions also depend upon the conductivity of the image, the position within the image and the particular geometry of the impedance imaging system. All of these factors should be taken into account when designing such a system. It is significant that, for a particular accuracy of the measurements, the spatial and conductivity resolutions for all positions in a circular conductive region are better (i.e. higher) than a particular value. This means that the entire region can be imaged to whatever accuracy is desired by making the measurements to the appropriate accuracy. However for half plane regions the situation is different. For such regions the conductivity and spatial resolution decrease without limit as the distance increases from the boundary where measurements are made. In this respect impedance imaging can be expected to achieve better results in medical applications than it can in geophysical applications.

The limits on spatial and conductivity resolutions developed in Chapter 3 associate all of the errors in the measurements with one small region of the image. In this respect they yield a pessimistic estimate of the accuracy of the image. An alternative approach is to assume that the errors in the measurements are associated with errors in the image over its entire extent. By distributing the error as evenly as possible, an overly optimistic estimate is likely to be obtained. In practice, the actual accuracy is probably somewhere between these two extremes. It would therefore be worthwhile exploring ways of calculating optimistic estimates of this kind. It would also be particularly useful to compare optimistic and pessimistic estimated accuracies with actual accuracies achieved when imaging a variety of conductivity distributions.

7.2 CIRCULARLY SYMMETRIC CONDUCTIVITY DISTRIBUTIONS

Two methods for interpreting electrical probing measurements, in terms of two-dimensional circularly symmetric conductivity distributions, are developed in Chapter 4. Variables called driving point impedances are introduced as a convenient way of representing the measurements. They are particularly useful for this purpose because they depend on the conductivity distribution and are independent of the particular current or voltage distributions used to make the measurements. It is shown that the driving point impedances fully characterise the electrical response of any circularly symmetric conductivity distribution. In this respect they are similar to the geophysical kernel (cf. Keller and Frischnecht 1966 §23a; Szaraniec 1976), which fully characterises the electrical response of a region in which the conductivity varies in only one dimension.

It is shown in §4.2.2 how to reconstruct a smooth circularly symmetric conductivity distribution directly from the driving point impedances. The method uses only two of the driving point impedances, so that the distribution it yields is not usually the same as the actual conductivity distribution. However, the two distributions do have the same overall character. In this respect the method developed in §4.2.2 is useful for providing an initial estimate of the conductivity distribution, which may then be refined to provide a more accurate estimate.

It is usually possible to iteratively refine such an initial estimate until a distribution is found which mimics the measurements to an accuracy of the same order as the experimental error (cf. §§4.3.1 and 4.3.2). However,

it is apparent that such a distribution can be significantly different from the actual conductivity distribution. Two such distinct distributions which correspond to the same measurements, to within some specified accuracy, are referred to as being equivalent. A similar equivalence is encountered when interpreting geophysical probing measurements (cf. §1.2.5), which are often interpreted in terms of conductivity distributions which vary in only one dimension. This type of conductivity distribution can be mapped onto a circularly symmetric conductivity distribution using a conformal transformation. It is therefore to be expected that many of the characteristics of the methods of interpretation developed in Chapter 4 should also apply to popular methods used for interpreting geophysical probing measurements.

Care must be taken when performing impedance imaging since many equivalent conductivity distributions can be found which correspond effectively to the same measurements. In view of this, the following three points should be considered when reconstructing an image. Firstly, it is critical that the distribution which is reconstructed should fit the measurements as closely as is practically possible, in order to reduce the number of conductivity distributions equivalent to it. Secondly, it makes little difference whether a smooth or piecewise constant distribution is fitted to the measurements (cf. §§4.3.3 and 4.3.5). Thirdly, even when a particular distribution has been identified as best fitting the measurements, quantitatively, it must be considered as being open to further, qualitative, interpretation.

Suppose that a number of equivalent conductivity distributions are found consistent with some particular measurements. It is then necessary to use some independent information to decide which distribution is closest to the actual distribution. Such independent information is routinely invoked in geophysics. There the information might be derived, for instance, from seismic or gravity surveys. In medical contexts, independent information is available as knowledge of the human anatomy, but it is not yet clear how to make use of it. Further study of how such information may be incorporated into imaging techniques is warranted.

7.3 GENERAL CONDUCTIVITY DISTRIBUTIONS

In Chapter 5, relationships are developed which symbolize the electrical measurements which can be made on arbitrary two-dimensional conductivity distributions. Transfer impedances, which are generalisations of the driving point impedances used in Chapter 4, are introduced as a convenient way of representing such measurements. The transfer impedances fully characterise the electrical response of a two-dimensional conductivity distribution. It is shown that in order to calculate the transfer impedances from measurements, the measurements must be linearly independent. Such measurements are necessary, when imaging a general two-dimensional conductivity distribution, to ensure that the reconstructed image may be unique. This explains why an impedance imaging approach based on conventional back projection techniques (cf. Lewitt et al 1978) is not appropriate (cf. Schomberg 1980; Bates et al 1980).

The relationships between the conductivity distribution and the measurements are not linear. As developed in Chapter 5 they can be used to calculate the measurements for any conductivity distribution. However it is not clear if they can in general be rearranged to permit the reconstruction of a particular conductivity distribution from the measurements. It would therefore be worthwhile attempting to devise an appropriate iterative procedure for fitting a conductivity distribution to the measurements. Either the smooth or the piecewise constant conductivity distributions examined in §§5.1 and 5.2 respectively would be suitable for fitting in this manner.

The direct inversion technique developed in §5.2.5 shows that single offset anomalies can be deduced uniquely from measurements. It is found, when using this technique, that larger anomalies are more accurately imaged than smaller ones. This is consistent with the ideas, developed in Chapter 3, about spatial resolution and conductivity resolution. The same technique could be modified, by incorporating conformal transformations, to image circular anomalies beneath a flat surface. This may have application in geophysical probing for locating tunnels or pipes buried under the earth.

When a conductivity distribution consists of multiple offset anomalies it is possible to identify one component of the measurements as being caused by coupling between the anomalies (§5.2.3). In certain circumstances this component can be negligible (§§5.3.3 and 5.3.4). Neglecting coupling is equivalent to assuming that each anomaly does not significantly affect the current flowing through the other anomalies. Neglecting coupling makes it

easier to interpret measurements in terms of conductivity distributions. Exhaustive computational and experimental studies would be useful to determine whether such distributions resemble the actual distributions.

7.4 CONSERVATIVE FIELD IMAGING

It is shown in Chapter 2 that conservative field theory describes the flow of electrical current through conductive regions. It is also shown that the same theory has much wider application. What has gone before in this chapter therefore applies to a whole class of imaging techniques, which are here bracketed under the portmanteau term "conservative field imaging". Included in this class are the electrical techniques of geophysical probing and medical probing, which deduce the conductivity as a function of position. References to Table 2.1 shows that conservative field imaging also can be used to determine spatial distributions of electric permittivity, magnetic permeability, fluid permeability, thermal conductivity, and coefficient of molecular diffusion. These physical parameters are of importance in a wide range of scientific and technical disciplines. A useful exercise might be to relate the results of this thesis in detail to each of these disciplines.

7.5 MODELLING LIMB VOLUME CHANGES MEASURED DURING VENOUS OCCLUSION PLETHYSMOGRAPHY.

A model is developed in Chapter 6 for interpreting the changes in limb volume measured during venous occlusion plethysmography. The parameters of the model are chosen to relate, as closely as possible, to physiological variables within the limb. The interpretation of these parameters is, therefore, straightforward. An experiment described in §6.3.2 demonstrates how changes in the parameters correspond to changes in important physiological variables.

There are at least three uses for the model. Firstly, it can aid in the interpretation of changes in limb volume for the detection of venous thrombosis. Secondly, the parameters of the model can represent the physiological condition of the circulation within the limb. Thirdly, the model can be used to monitor changes in the limb circulation under conditions of particular interest, such as during surgery.

In order for the model to be of maximum use it is necessary to establish the ranges of the model parameters which correspond to particular conditions of limb circulation. It would be helpful to determine these ranges under normal conditions, after exercise, for various vascular diseases, and in response to certain drugs. This requires a clinical study of a large number of limbs. As part of such a study it would also be particularly useful to examine the model in relation to alternative methods for interpreting changes in limb volume (cf. Figure 1.6).

APPENDIX 1

SYSTEM FOR ELECTRICALLY PROBING CONDUCTIVITY DISTRIBUTIONS

The equipment used to make experimental measurements on conductivity distributions is illustrated in Figure A1.1. The conductivity distributions were composed of a circular tank containing saline solution, in which were placed metal or PVC pipes. Current was passed through any such distribution between two electrodes on its circumference. The resulting voltage distribution was measured at electrodes around the circumference using the impedance plethysmograph and multiplexer described in Appendix 2. The output of the plethysmograph was converted from analogue to digital and stored in a computer. The computer also controlled which of the multiplexer's inputs was connected to the plethysmograph.

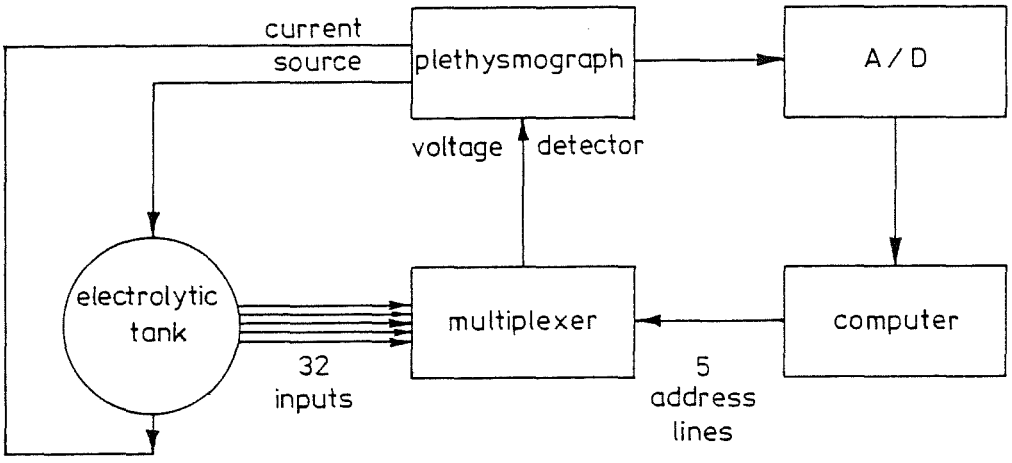

Figure A1.1: System used to make electrical probing measurements on conductivity distributions (see text).

The electrolytic tank was 185 mm in diameter, and was filled with saline to between 40 mm and 50 mm in depth. The current source produced a 0.1 mA peak sinusoidal waveform (see Appendix 2). The depth and concentration of the saline were chosen so that the greatest voltage measured on the circumference was less than 0.1V. The voltage was measured at either 32 or 128 electrodes depending on the particular experiment (see §§3.3.3, 4.1.1 and 5.3.1). The electrodes were equally spaced around the circumference of the tank.

APPENDIX 2

INSTRUMENTATION

Two items of instrumentation were constructed for use in the experimental studies described in this thesis. These items, being an impedance plethysmograph and an analogue multiplexer, are described below.

A2.1 IMPEDANCE PLETHYSMOGRAPH

A2.1.1 Specifications

Current source:		waveform	sinusoidal
		amplitude	1 mA peak
		frequency	62.5 kHz
		maximum load	10 kΩ
Voltage detectors:		2 differential channels	
		centre frequency	62.5 kHz
		maximum input	0.1V differential
Outputs:	(a)	Basal (2 channels)	
		sensitivity	0.1V/Ω
		frequency response (3dB)	DC to 25 Hz
	(b)	Venous (2 channels)	
		sensitivity	-5V/Ω
		frequency response (3dB)	0.0016 Hz to 0.25 Hz
	(c)	Arterial (2 channels)	
		sensitivity	-100V/Ω
		frequency response (3dB)	0.25 Hz to 25 Hz.
Calibration levels:		Basal	10 Ω to 60 Ω
		Venous	1 Ω to 0 Ω
		Arterial	0.05 Ω to 0 Ω

A2.1.2 Circuitry

Figures A2.1 to A2.8 show the circuitry of the impedance plethysmograph. Power supply connections to active components are not shown. The following notes are of relevance to the circuits indicated.

Front Panel (Figure A2.2)

When the "operate" position is selected the function switch (9 poles 4 positions) connects the patient, via leads connected to the sockets, to the plethysmograph. The other three positions allow for calibration of the outputs of the plethysmograph (see A2.1.1) when used in conjunction with the pushbutton. The meter (1 mA DC full scale deflection) displays the magnitude of the basal impedance (0 to 100 Ω) on left or right channels as selected by the "meter select" switch. The LED indicates when the impedance exceeds 100 Ω. The basal impedance is monitored at all times, whereas changes in impedance can be monitored with either the venous or arterial outputs as selected by the "waveform select" switch. The "set zero" switch sets all outputs to zero.

Mains Power Supply (Figure A2.3)

The transformer has two 20V 0.5A RMS secondaries. The transformer has a single electrostatic shield.

Isolated Power Supply (Figure A2.4)

The transformer (Phillips E20/3E1) is ferrite cored. The primary winding has 20 turns of 32SWG copper wire. Each secondary has 30 turns of the same wire. The primary and secondary windings are side by side and are separated by a 1.5 mm plastic wall. This reduces the capacitance between the primary and the secondaries to about 3 pF.

Current Source (Figure A2.5)

The transformer (Phillips E20/3E1) is ferrite cored. Primary and secondary windings are each 200 turns of 36SWG copper wire. They are wound side by side and separated by a plastic wall (see above).

Voltage Detector (Figure A2.6)

The transformer is the same as that used in the current source. The common mode rejection of the stage before the transformer can be maximised

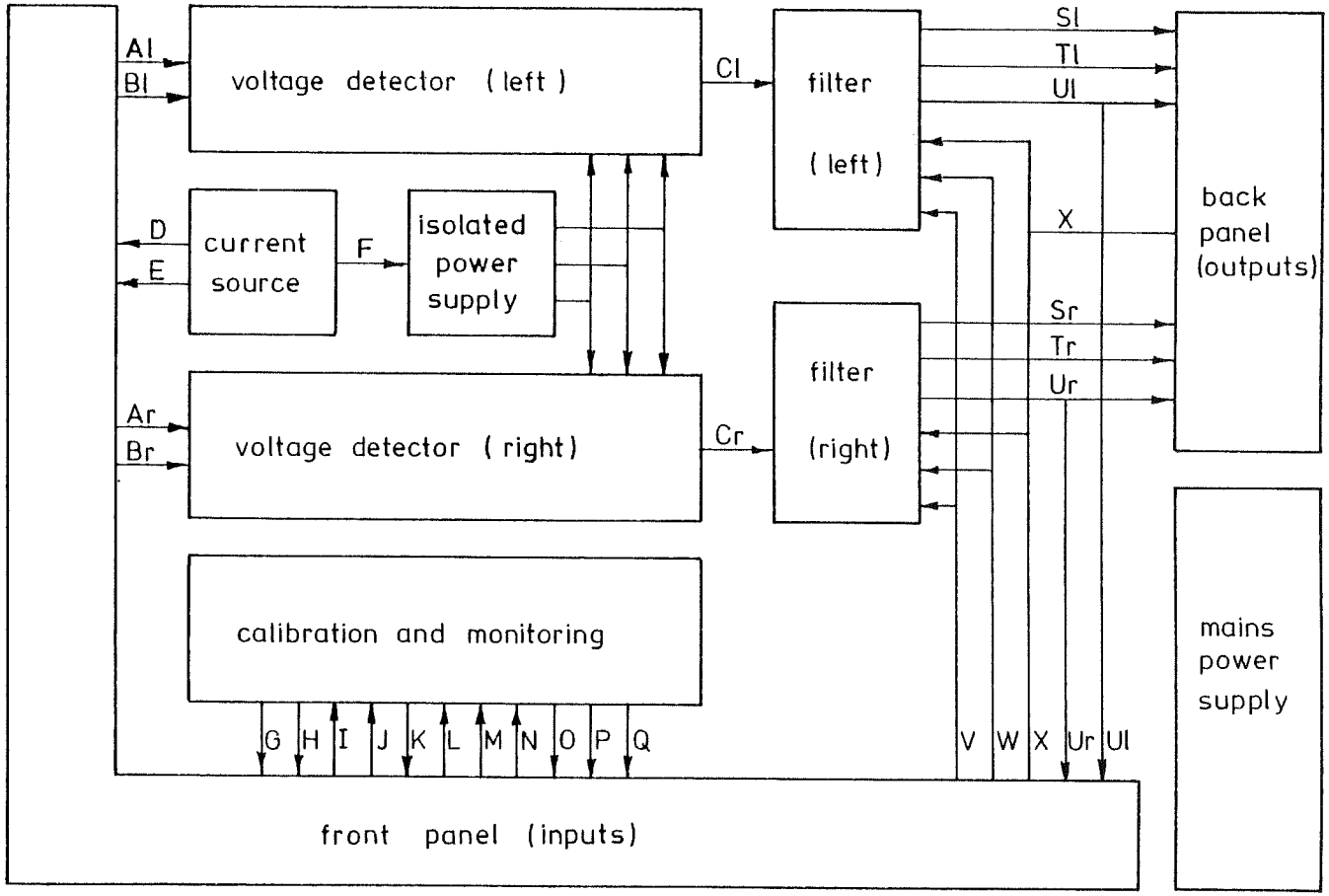

Figure A2.1: Block diagram of plethysmograph.

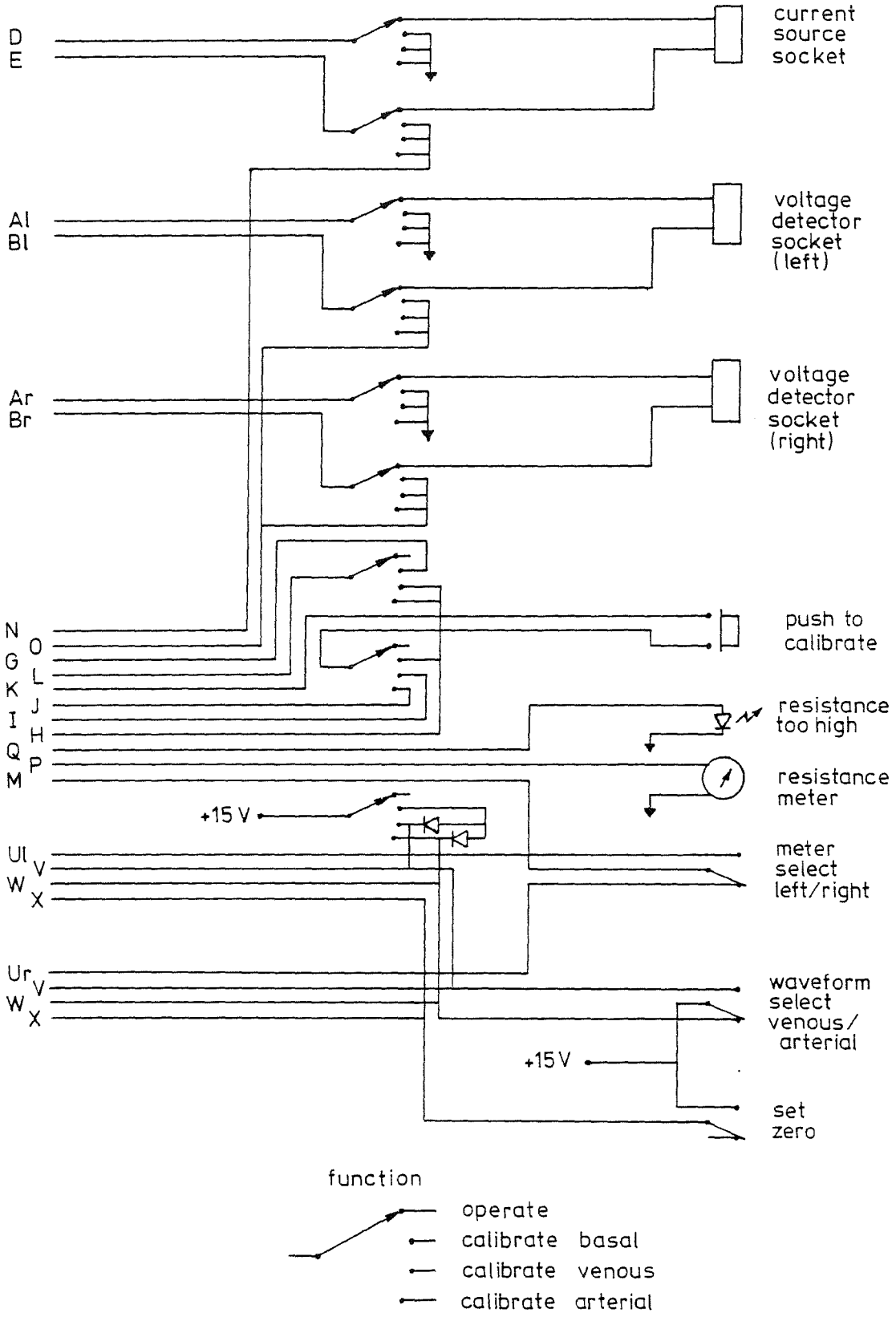

Figure A2.2: Front panel circuit.

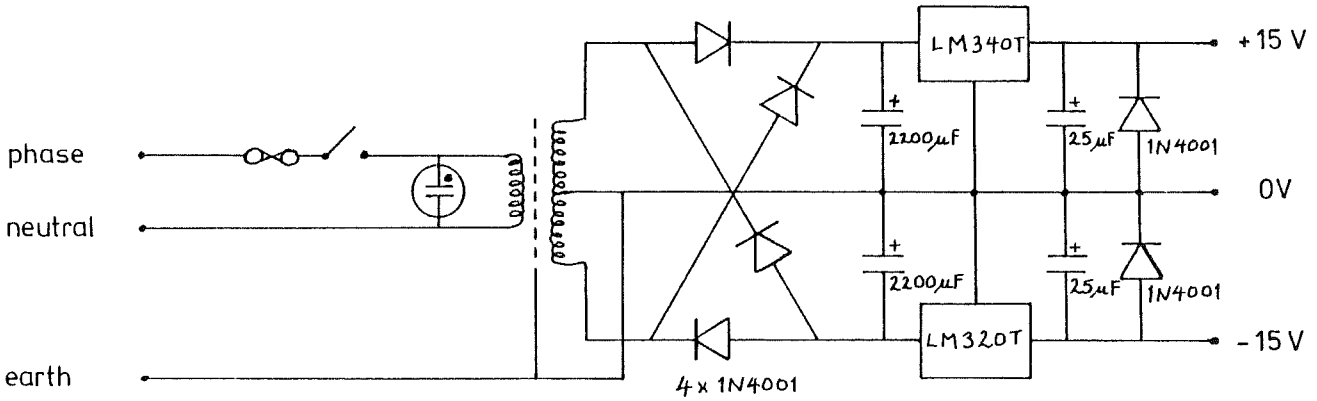

Figure A2.3: Mains power supply circuit.

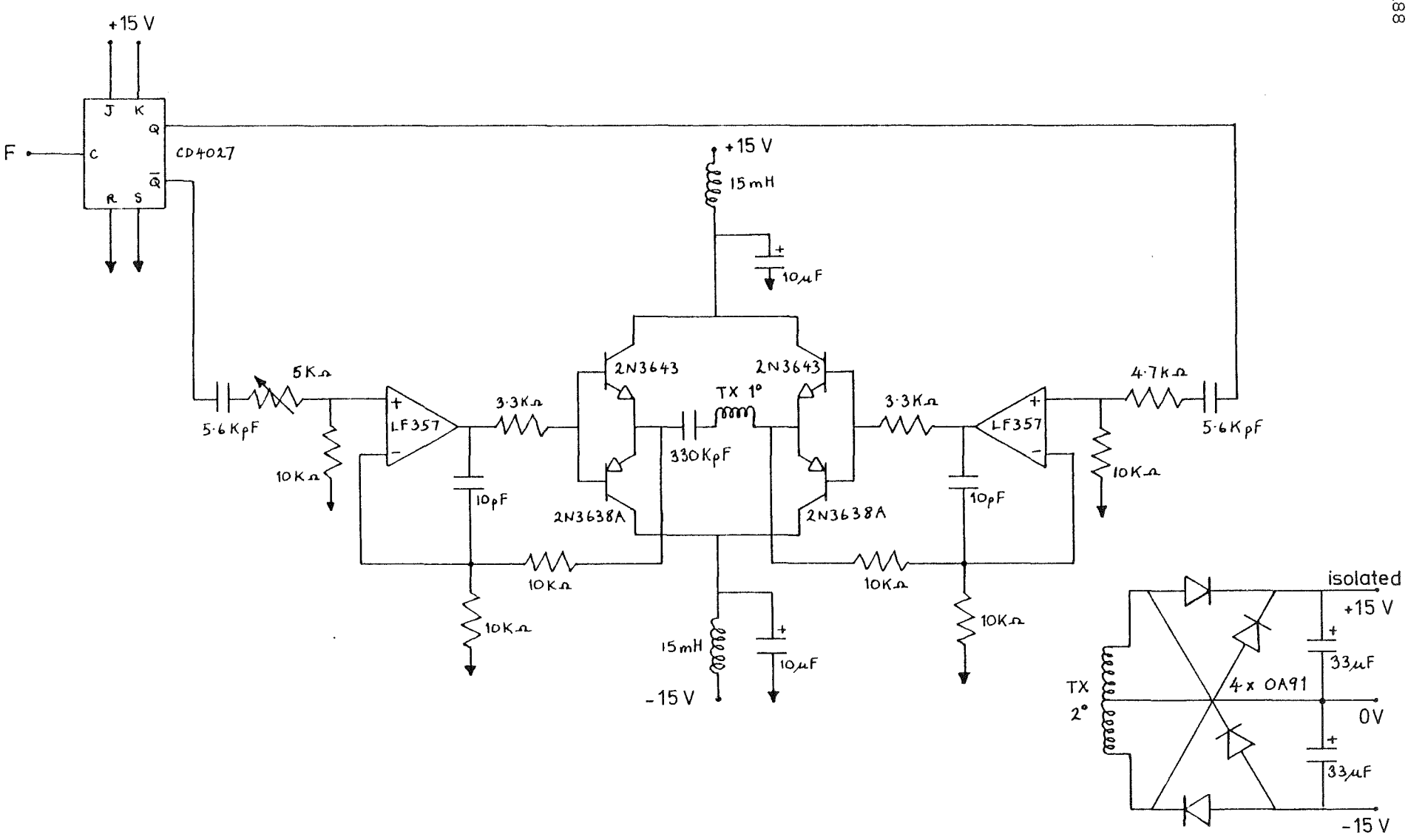

Figure A2.4: Isolated power supply circuit.

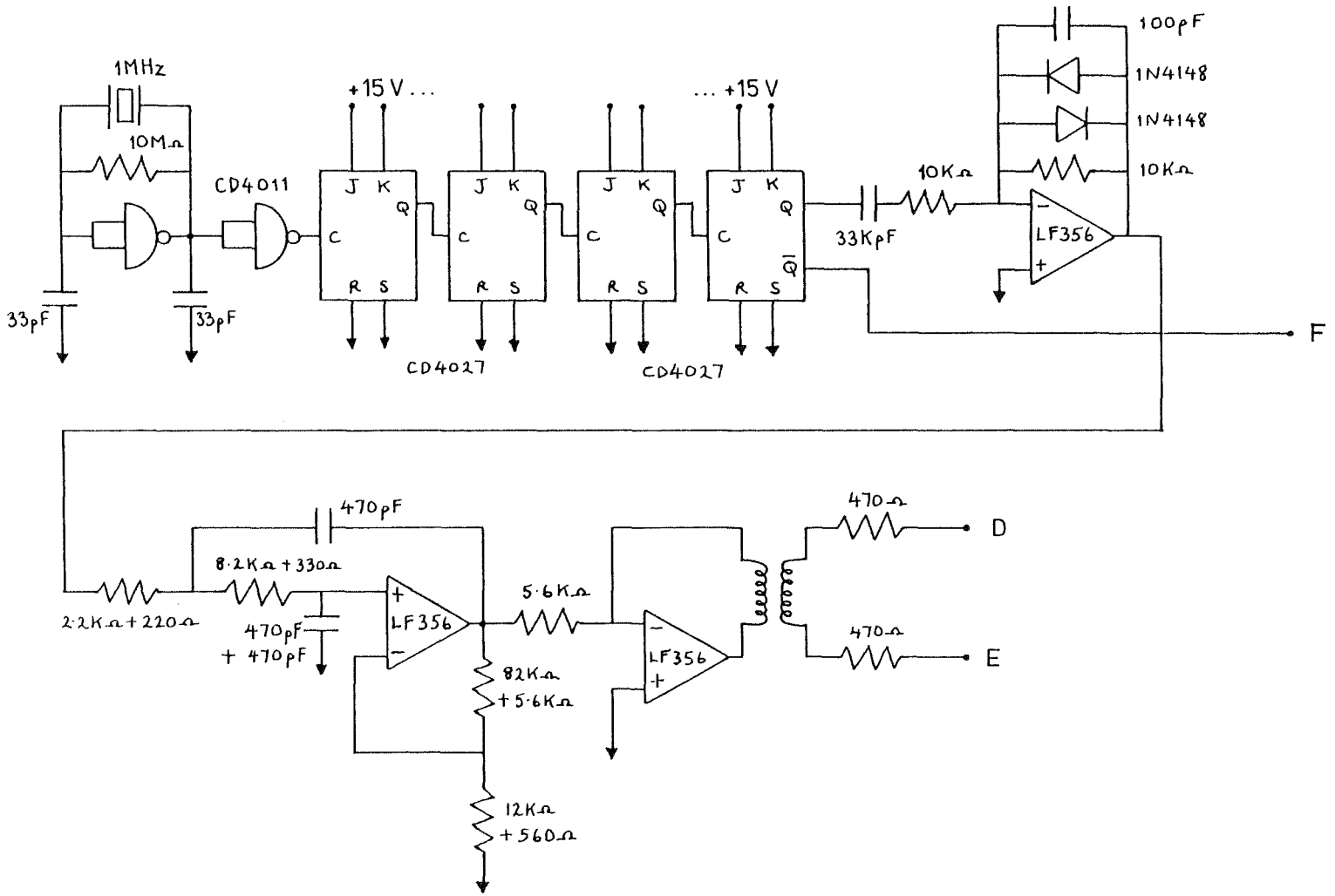

Figure A2.5: Current source circuit.

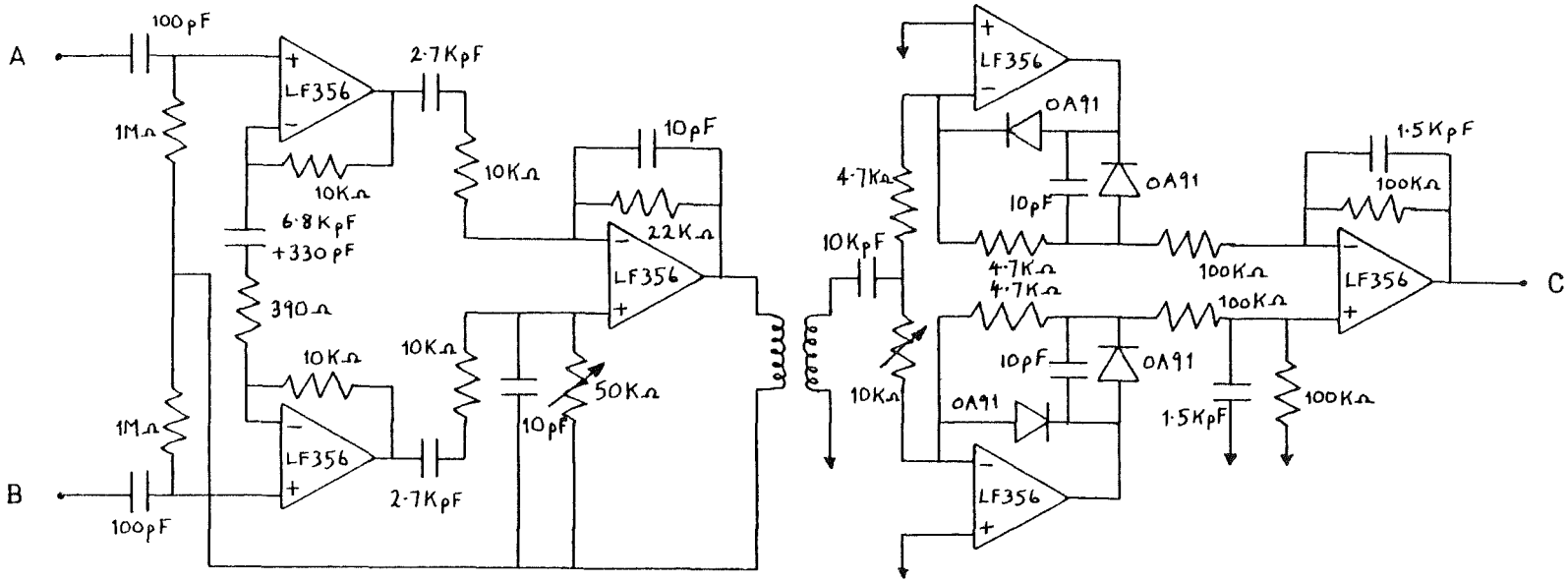

Figure A2.6: Voltage detector circuit.

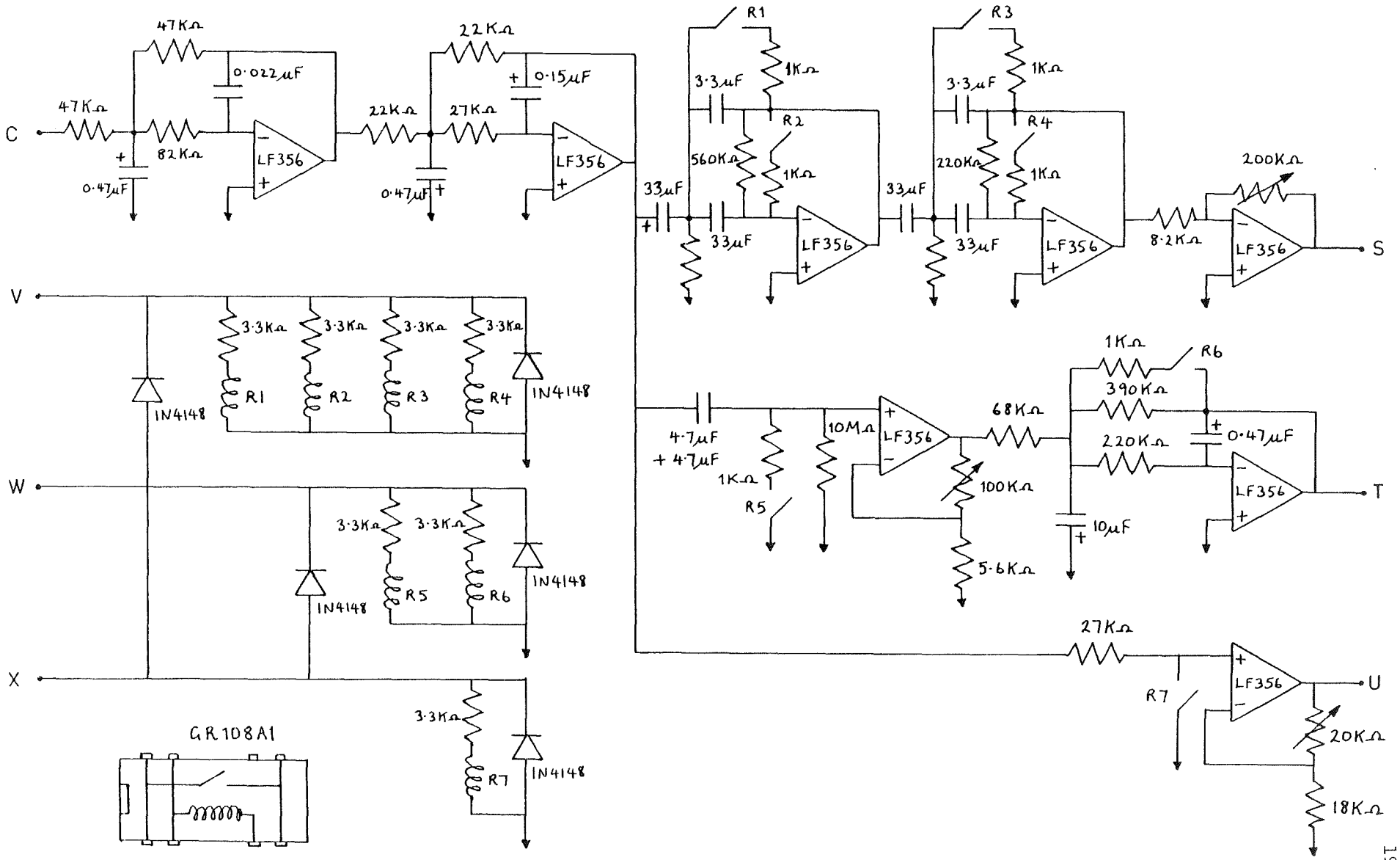

Figure A2.7: Filter circuit.

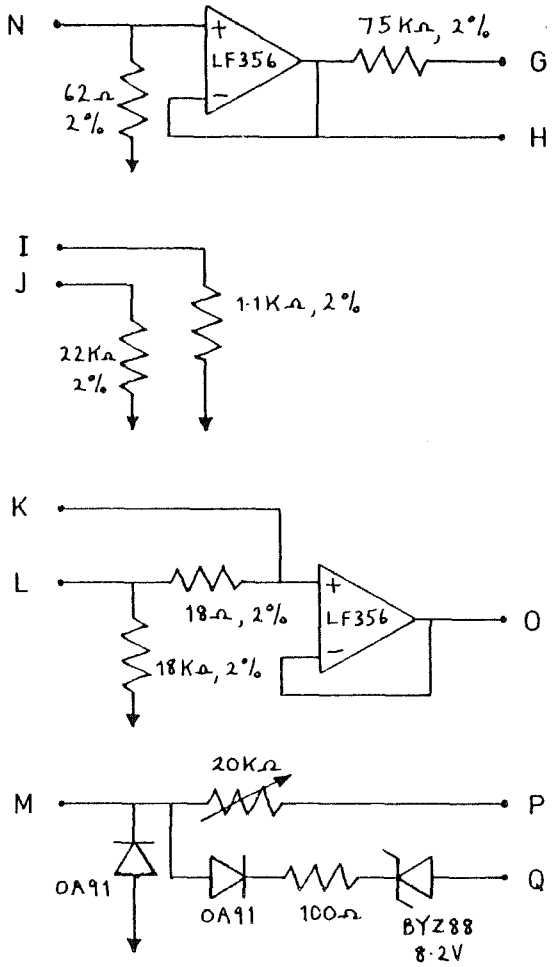

Figure A2.8: Calibration and Monitoring circuit.

by adjusting the 50 kΩ variable resistor. The full wave rectifier following the transformer can be balanced by adjusting the 10 kΩ variable resistor. The circuitry before (to the left) of the transformer is powered by the isolated power supply.

Filter (Figure A2.7)

The two 4.7 μF capacitors must have a DC resistance much higher than the 10 MΩ bias resistor. Shizuki metallised polyester film capacitors type TME are used. The relays (GR108A1) are normally open.

Calibration and Monitoring (Figure A2.8)

The accuracy of the calibration levels is determined by the accuracy of the resistors used. Resistors with 2% accuracy are used here.

A2.2 ANALOGUE MULTIPLEXER

Figure A2.9 shows the circuitry of the analogue multiplexer. This instrument was designed, constructed and originally used by Chan (1981).

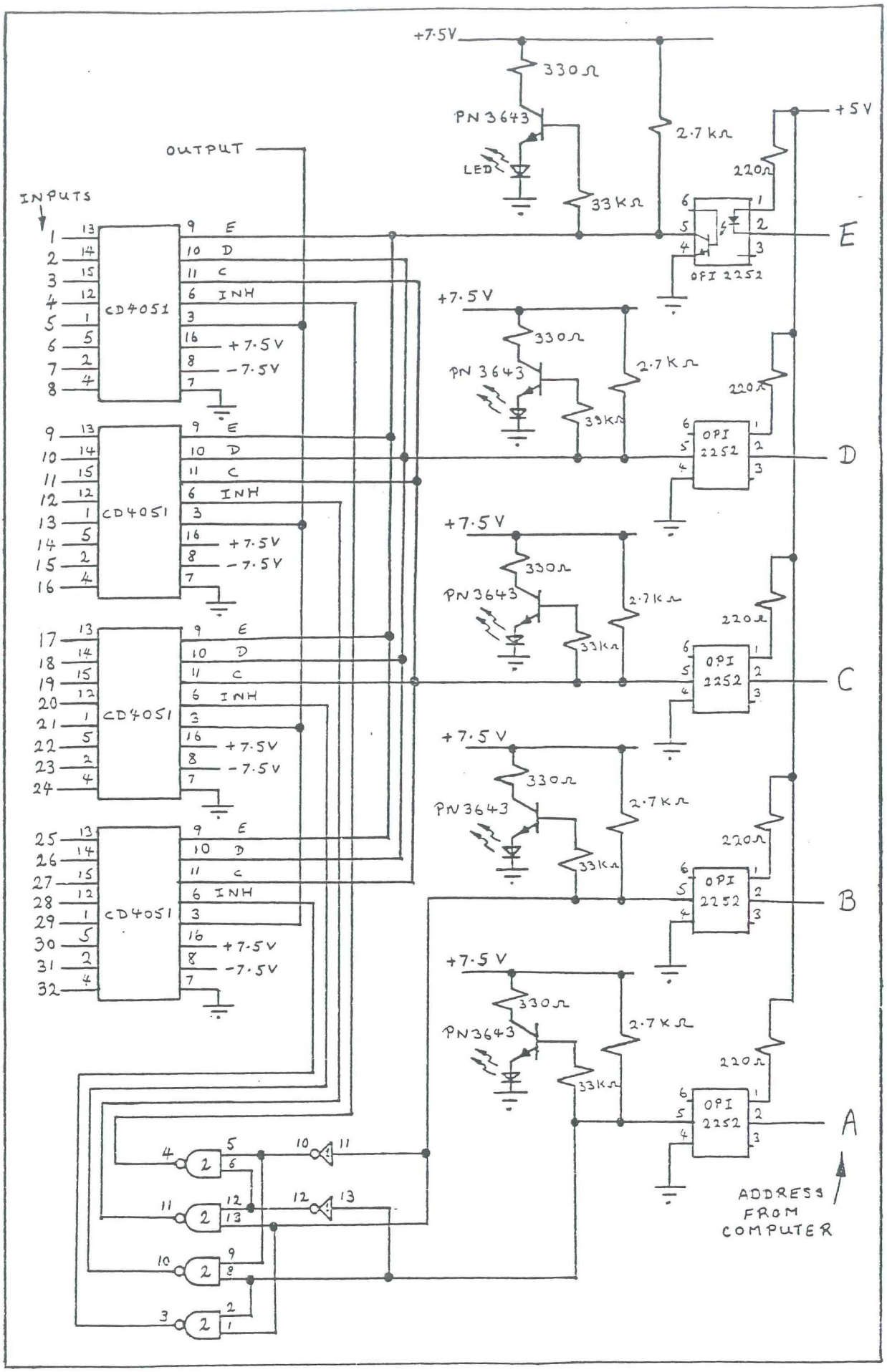

Figure A2.9: Circuit diagram of the Multiplexer. (from Chan 1981).

APPENDIX 3

TECHNIQUES EMPLOYED FOR MODEL FITTING

A3.1 NEWTON METHODS (cf. Murray 1972)

In order to find the values of parameters $\underset{\sim}{x}$ for which a particular model mimics certain measurements $\underset{\sim}{b}$ it is often necessary to solve a system of nonlinear equations

$$\underset{\sim}{F}(\underset{\sim}{x}) = \underset{\sim}{b} \tag{A3.1}$$

where $\underset{\sim}{F}$ is a nonlinear function. An exact solution may not be possible, however a least squares solution can be found by minimising the square of the Euclidean length of the residual vector

$$\underset{\sim}{r} = \underset{\sim}{F}(\underset{\sim}{x}) - \underset{\sim}{b} \tag{A3.2}$$

which is $\underset{\sim}{r}^T\underset{\sim}{r}$. At the minimum, the gradient of $\underset{\sim}{r}^T\underset{\sim}{r}$ with respect to the parameters $\underset{\sim}{x}$ is zero, i.e.

$$\nabla(\underset{\sim}{r}^T\underset{\sim}{r}) = \underset{\sim}{0} \ . \tag{A3.3}$$

Expanding the function $\underset{\sim}{F}$ in its Taylor series gives

$$\underset{\sim}{F}(\underset{\sim}{x}) = \underset{\sim}{F}(\underset{\sim}{x}-\Delta\underset{\sim}{x}) + A\Delta\underset{\sim}{x} + O^2(\Delta\underset{\sim}{x}) \ , \tag{A3.4}$$

where matrix A has elements $[A]_{ij} = \partial F_i(\underset{\sim}{x})/\partial x_j$, which are the derivatives of the components $F_i = [\underset{\sim}{F}]_i$ of the function with respect to the parameters $x_j = [\underset{\sim}{x}]_j$. The factor $O^2(\Delta\underset{\sim}{x})$ represents the 2nd and higher order terms. Approximating $\underset{\sim}{F}$ with a linear function in the neighbourhood around $\underset{\sim}{x}$ by neglecting the terms $O^2(\Delta\underset{\sim}{x})$, and then substituting the resulting equation into (A3.3) gives

$$\underset{\sim}{r}^T\underset{\sim}{r} \simeq (A\Delta\underset{\sim}{x}-\Delta\underset{\sim}{b})^T(A\Delta\underset{\sim}{x}-\Delta\underset{\sim}{b}) \tag{A3.5}$$

where

$$\Delta\underset{\sim}{b} = \underset{\sim}{b} - \underset{\sim}{F}(\underset{\sim}{x}-\Delta\underset{\sim}{x}) \ . \tag{A3.6}$$

Differentiating (A3.5) with respect to the parameters $\underset{\sim}{x}$ and equating the derivative to zero gives

$$\underset{\sim}{0} = 2A^TA\Delta\underset{\sim}{x} - 2A^T\Delta\underset{\sim}{b} \ . \tag{A3.7}$$

An approximate solution to (A3.3) can then be found by solving the set of linear equations (A3.7). The solution is given explicitly by

$$\Delta\underset{\sim}{x} = (A^TA)^{-1}A^T\Delta\underset{\sim}{b} \quad . \tag{A3.8}$$

The matrix A^TA is called the Hessian. When (A3.8) is used to find $\underset{\sim}{x}$ by generating successive corrections $\Delta\underset{\sim}{x}$, it is called Newton's method. When this method is modified by taking some fraction of $\Delta\underset{\sim}{x}$ as the correction, it is called a quasi (or modified) Newton method.

When the Hessian is nonsingular its inverse can be calculated and then $\Delta\underset{\sim}{x}$ can be obtained using (A3.8). If the derivatives of all of the F_i with respect to one of the x_j are zero, the Hessian is singular. This occurs when using the variable radii model (see §4.1.2) in the situation where two radii have the same value or two adjacent rings have the same conductivity. There are then an unlimited number of corrections $\Delta\underset{\sim}{x}$ consistent with (A3.7). Assuming that the last estimate of $\underset{\sim}{x}$ was close to the solution for $\underset{\sim}{x}$, it is then sensible to choose the particular correction $\Delta\underset{\sim}{x}$ which has the least Euclidean length. This solution for $\Delta\underset{\sim}{x}$ is called the minimal least squares solution.

A3.2 THE MOORE PENROSE GENERALISED INVERSE (cf. Noble 1976)

The minimal least squares solution of a system of linear equations

$$A\Delta\underset{\sim}{x} = \Delta\underset{\sim}{b} \tag{A3.9}$$

is given by

$$\Delta\underset{\sim}{x} = A^{\dagger}\Delta\underset{\sim}{b} = C^{\dagger}B^{\dagger}\Delta\underset{\sim}{b} \tag{A3.10}$$

where

$$A = BC \tag{A3.11}$$

$$C^{\dagger} = C^T(CC^T)^{-1} \tag{A3.12}$$

$$B^{\dagger} = (B^TB)^{-1}B^T \tag{A3.13}$$

and B and C are both of full rank (which here means the rank of B equals the number of columns in B and the rank of C equals the number of rows in C). $A^{\dagger}$ is called the Moore Penrose generalised inverse. Substituting (A3.12) and (A3.13) into (A3.10) gives

$$\Delta\underset{\sim}{x} = C^T(CC^T)^{-1}(B^TB)^{-1}B^T\Delta\underset{\sim}{b} \quad . \tag{A3.14}$$

When the rank of A equals the number of columns in A then C can be chosen to equal the identity matrix, so that B=A. Thus when the system of equations is overdetermined (A3.14) reduces to (A3.8). In this situation both (A3.14) and (A3.8) give the least squares solution for $\Delta\underset{\sim}{x}$. When the system of

equations is underdetermined (A3.8) cannot be used and (A3.14) gives the minimal least squares solution.

A3.3 ORTHOGONAL DECOMPOSITION (cf. Broyden 1975)

The evaluation of (A3.14) can be formed with numerical stability and efficiency using orthogonal decomposition. The matrix B can always be factorised into the product

$$B = Q_1^T \begin{bmatrix} U \\ \cdots \\ 0 \end{bmatrix} \tag{A3.15}$$

where Q_1 is an orthogonal matrix, and $\begin{bmatrix} U \\ \cdots \\ 0 \end{bmatrix}$ is upper triangular above the dots and zero below them. Similarly, C can always be factorised into the product

$$C = [L:0]Q_2^T \tag{A3.16}$$

where Q_2 is orthogonal and $[L:0]$ is lower triangular to the left of the dots and zero to the right. These factorisations may be performed directly with the use of what are called Householder transformations (or matrices) (see the reference cited above). Substituting for B, C, B^T and C^T in (A3.14) using (A3.15) and (A3.16) gives

$$\Delta\underset{\sim}{x} = Q_2 \begin{bmatrix} I \\ \cdots \\ 0 \end{bmatrix} L^{-1}U^{-1}[I:0]Q_1\Delta\underset{\sim}{b} \tag{A3.17}$$

where I is the identity matrix. The operations L^{-1} and U^{-1} represent forward and back substitutions respectively, which can be carried out more conveniently than the inverses in (A3.14).

As a further simplification, the choice of the matrices B and C, into which A is factorised, can be made concurrently with the orthogonal decomposition. There are four different choices, which depend on the number of rows and columns in A and on the rank of A.

Suppose first that the number of rows in A exceeds the number of columns. Then A may be decomposed to give

$$Q_1^T \begin{bmatrix} I \\ \cdots \\ 0 \end{bmatrix} U\Delta\underset{\sim}{x} = \Delta\underset{\sim}{b} . \tag{A3.18}$$

If now A is of full rank then U is also of full rank. Putting $B = Q^T \begin{bmatrix} I \\ \cdots \\ 0 \end{bmatrix}$ and C=U into (A3.14) then gives

$$\Delta\underset{\sim}{x} = U^{-1}[I:0]Q_1\Delta\underset{\sim}{b} . \tag{3.19}$$

However, if A is not of full rank then neither is U. Rather than being upper triangular, U is upper trapezoidal. Decomposing U now gives

$$Q_1^T \begin{bmatrix} I \\ \cdots \\ 0 \end{bmatrix} \begin{bmatrix} I' \\ \cdots \\ 0 \end{bmatrix} L \left[I' : 0 \right] Q_2^T \Delta \underset{\sim}{x} = \Delta \underset{\sim}{b} \qquad \text{(A3.20)}$$

where I' is another identity matrix whose dimension is different from that of I. The dimension of I' is the same as the rank of both U and L. Putting $B = Q_1^T \begin{bmatrix} I \\ \cdots \\ 0 \end{bmatrix} \begin{bmatrix} I' \\ \cdots \\ 0 \end{bmatrix}$ and $C = L \left[I' : 0 \right] Q_2^T$ into (A3.14) then gives

$$\Delta \underset{\sim}{x} = Q_2 \begin{bmatrix} I' \\ \cdots \\ 0 \end{bmatrix} L \left[I' : 0 \right] \left[I : 0 \right] Q_1 \Delta \underset{\sim}{b} \; . \qquad \text{(A3.21)}$$

Suppose now that the number of columns in A exceeds the number of rows. Then A may be decomposed to give

$$L \left[I : 0 \right] Q_2^T \Delta \underset{\sim}{x} = \Delta \underset{\sim}{b} \quad . \qquad \text{(A3.22)}$$

If now A is of full rank then L is also of full rank. Putting B = L and $C = \left[I : 0 \right] Q_2^T$ into (A3.14) then gives

$$\Delta \underset{\sim}{x} = Q_2 \begin{bmatrix} I \\ \cdots \\ 0 \end{bmatrix} L^{-1} \Delta \underset{\sim}{b} \; . \qquad \text{(A3.23)}$$

However, if A is not of full rank then neither is L. Rather than being lower triangular, L is lower trapezoidal. Decomposing L now gives

$$Q_1^T \begin{bmatrix} I' \\ \cdots \\ 0 \end{bmatrix} U \left[I' : 0 \right] \left[I : 0 \right] Q_2^T \Delta \underset{\sim}{x} = \Delta \underset{\sim}{b} \; . \qquad \text{(A3.24)}$$

The dimension of I' is the same as the rank of both L and U. Putting $B = Q_1^T \begin{bmatrix} I' \\ \cdots \\ 0 \end{bmatrix} U$ and $C = \left[I' : 0 \right] \left[I : 0 \right] Q_2^T$ into (A3.14) then gives

$$\Delta \underset{\sim}{x} = Q_2 \begin{bmatrix} I \\ \cdots \\ 0 \end{bmatrix} \begin{bmatrix} I' \\ \cdots \\ 0 \end{bmatrix} U \left[I' : 0 \right] Q_1 \Delta \underset{\sim}{b} \; . \qquad \text{(A3.25)}$$

Either (A3.19), (A3.21), (A3.23) or (A3.25) may be used instead of (A3.17) in the four circumstances as described above. The particular circumstance for any matrix A becomes evident as the decompositions are performed. It is not necessary to factorize A into the product BC before performing these decompositions.

A3.4 THE PROCEDURES EMPLOYED

Iterative model fitting was used for two purposes in this thesis. In §4.1.2 models are described which were iteratively fitting to measurements from circularly symmetric conductivity distributions. In §6.2

another model is described which was iteratively fitted to measurements from limbs. For the models described in §4.1.2 the iterative procedure comprised the following steps:

(a) calculate the derivatives (the matrix A) at the current parameter values $\underset{\sim}{x}$,

(b) calculate the correction $\Delta\underset{\sim}{x}$ using (A3.19), (A3.21), (A3.23) or (A3.25),

(c) search for the value k between 0 and 1 for which $k\Delta\underset{\sim}{x}$ minimises $\underset{\sim}{r}^T\underset{\sim}{r}$,

(d) update $\underset{\sim}{x}$ using the correction $k\Delta\underset{\sim}{x}$,

(e) repeat from (a).

For the model described in §6.2 the iterative procedure comprised the following steps:

(a) calculate the derivatives (the matrix A) at the current parameter values $\underset{\sim}{x}$,

(b) calculate the correction $\Delta\underset{\sim}{x}$ using (A3.19), (A3.21), (A3.23) or (A3.25),

(c) search from k = 1 to k = 0 for the first value of k for which $k\Delta\underset{\sim}{x}$ reduces $\underset{\sim}{r}^T\underset{\sim}{r}$,

(d) update $\underset{\sim}{x}$ using the correction $k\Delta\underset{\sim}{x}$,

(e) repeat from (a).

Each of these procedures was terminated when no value of k could be found to reduce $\underset{\sim}{r}^T\underset{\sim}{r}$.

The only difference between the two procedures is step (c). It was found for the models described in §4.1.2 that step (a) took more time than any of the other steps. It was therefore sensible once $\Delta\underset{\sim}{x}$ had been found, to determine the best possible correction before returning to step (a). For the model described in §6.2, step (a) was not significantly longer than any other step. In that situation it was more sensible to repeat step (a) as soon as a correction $k\Delta\underset{\sim}{x}$ was found which reduced $\underset{\sim}{r}^T\underset{\sim}{r}$.

APPENDIX 4

A POWER SERIES REPRESENTATION FOR THE QUOTIENT OF TWO POWER SERIES

Consider here how the quotient Q of two infinite power series may be resolved into a single power series. Let the quotient be

$$Q = \frac{\sum_{n=o}^{\infty} a_{mn} x^n}{\sum_{k=o}^{\infty} b_k x^k} \quad . \tag{A4.1}$$

Dividing the demoninator into the numerator gives

$$Q = \frac{a_{mo}}{b_o} + x\left[\frac{\sum_{n=o}^{\infty} a_{m+1,n} x^n}{\sum_{k=o}^{\infty} b_k x^k}\right] \tag{A4.2}$$

where

$$a_{m+1,n} = a_{m,n+1} - a_{mo} b_{n+1}/b_o \quad . \tag{A4.3}$$

Expanding the bracket in (A4.2) using (A4.1) gives

$$Q = \frac{a_{mo}}{b_o} + x\left[\frac{a_{m+1,o}}{b_o} + \frac{\sum_{n=o}^{\infty} a_{m+2,n} x^n}{\sum_{k=o}^{\infty} b_k x^k}\right] \quad . \tag{A4.4}$$

Continuing the expansion indefinitely gives

$$Q = \frac{a_{mo}}{b_o} + x\left[\frac{a_{m+1,o}}{b_o} + x\left[\frac{a_{m+2,o}}{b_o} + x\left[\, . \ . \ . \,\right]\right]\right]$$

$$= (1/b_o) \sum_{k=o}^{\infty} a_{m+k,o} x^k \quad . \tag{A4.5}$$

Thus using (A4.1), (A4.3) and (A4.5) the quotient of two infinite power series can be resolved into a single power series, provided that it converges.

APPENDIX 5

DETAIL OF SECTION 5.1.2

In this appendix the steps taken to transform (5.6a) and (5.6b) into (5.7a) to (5.7d) are given. The individual steps involve either substituting a new variable as a combination of 2 old variables (and discarding one of the old variables), or transposing the order with which two of the summations take effect, i.e. changing $\sum_m \sum_n$ to $\sum_n \sum_m$. The latter step requires careful consideration of how the variables of summation interact. The object of the various substitutions and transpositions is to reduce terms in (5.6b) of the type $r^{m+n+p+q-2}\cos p\theta$ to terms of the type $r^{x+y}\cos x\theta$. The coefficients of the latter terms are then equal to the coefficients of the corresponding terms in (5.6a). Equations (5.6a) and (5.6b) can then be reduced to equations in the coefficients alone, so that the terms of the radius and angle are eliminated.

Firstly, restating (5.6a) and (5.6b) gives

$$\nabla^2 V = \sum_{m=o}^{\infty} \sum_{n=o}^{\infty} r^{m+n-2}\left[(m+n)^2-m^2\right]\left[A_{mn}\cos m\theta+B_{mn}\sin m\theta\right] \qquad (A5.1)$$

and

$$\nabla V.\nabla \ln\sigma = \sum_{m,n,p,q=o}^{\infty} r^{m+n+p+q-2}$$

$$\{(m+n)(p+q)\left[A_{mn}\cos m\theta+B_{mn}\sin m\theta\right]\left[a_{pq}\cos p\theta+b_{pq}\sin p\theta\right]$$

$$+ mp\left[-A_{mn}\sin m\theta+B_{mn}\cos m\theta\right]\left[-a_{pq}\sin p\theta+b_{pq}\cos p\theta\right]\} . \qquad (A5.2)$$

Multiplying out the square brackets in (A5.2), then using trignometric identities to change the products of trignometric functions into sums of trignometric functions, and collecting like terms gives

$$\nabla V.\nabla \ln\sigma = (S1+S2)/2 \qquad (A5.3)$$

where

$$S1 = \sum_{m,n,p,q=o}^{\infty} r^{m+n+p+q-2}\left[(m+n)(p+q)-mp\right]$$

$$\{\left[A_{mn}a_{pq}-B_{mn}b_{pq}\right]\cos(m+p)\theta + \left[A_{mn}b_{pq}+B_{mn}a_{pq}\right]\sin(m+p)\theta\} \qquad (A5.4)$$

and

$$S2 = \sum_{m,n,p,q=o}^{\infty} r^{m+n+p+q-2}\left[(m+n)(p+q)+mp\right]$$

$$\{\left[A_{mn}a_{pq}+B_{mn}b_{pq}\right]\cos(m-p)\theta - \left[A_{mn}b_{pq}-B_{mn}a_{pq}\right]\sin(m-p)\theta\} . \quad (A5.5)$$

Introducing the new variables $k = m+p$ and $\ell = n+q$ into (A5.4) to eliminate p and q respectively, and transposing the order of the sums over m and k, and over n and ℓ respectively gives

$$S1 = \sum_{k,\ell=o}^{\infty} \sum_{m=o}^{k} \sum_{n=o}^{\ell} r^{k+\ell-2}\left[(m+n)(k-m+\ell-n)-m(k-m)\right]$$

$$\{\left[A_{mn}a_{k-m,\ell-n}-B_{mn}b_{k-m,\ell-n}\right]\cos k\theta+\left[A_{mn}b_{k-m,\ell-n}+B_{mn}a_{k-m,\ell-n}\right]\sin k\theta\} . \quad (A5.6)$$

Equation (A5.6) has radial and angular dependence of the same form as (A5.1).

Introducing $k = m-p$ into (A5.5) to eliminate p, and transposing the order of the sums over m and k gives

$$S2 = (S3+S4)/2 \quad (A5.7)$$

where

$$S3 = \sum_{k=o}^{\infty} \varepsilon_k \sum_{m=k}^{\infty} \sum_{n,q=o}^{\infty} r^{2m+n+q-k-2}\left[(m+n)(m-k+q)+m(m-k)\right]$$

$$\{\left[A_{mn}a_{m-k,q}+B_{mn}b_{m-k,q}\right]\cos k\theta-\left[A_{mn}b_{m-k,q}-B_{mn}a_{m-k,q}\right]\sin k\theta\} \quad (A5.8)$$

and

$$S4 = \sum_{k=o}^{-\infty} \varepsilon_k \sum_{m=o}^{\infty} \sum_{n,q=o}^{\infty} r^{2m+n+q-k-2}\left[(m+n)(m-k+q)+m(m-k)\right]$$

$$\{\left[A_{mn}a_{m-k,q}+B_{mn}b_{m-k,q}\right]\cos k\theta-\left[A_{mn}b_{m-k,q}-B_{mn}a_{m-k,q}\right]\sin k\theta\} , \quad (A5.9)$$

in which the Neumann factor ε_k is introduced so the term when $k = 0$ is not added twice. ($\varepsilon_o = 1$ and $\varepsilon_k = 2$ when $k \neq 0$). Introducing $p = m-k$ and $\ell = n+m-k$ into (A5.8) to eliminate m and n respectively, and transporing the order of the sums over p and ℓ gives

$$S3 = \sum_{k=o}^{\infty} \varepsilon_k \sum_{\ell=o}^{\infty} \sum_{p=o}^{\ell} \sum_{q=o}^{\infty} r^{p+k+\ell+q-2}\left[(k+\ell)(p+q)+p(p+k)\right]$$

$$\{\left[A_{p+k,\ell-p}a_{pq}+B_{p+k,\ell-p}b_{pq}\right]\cos k\theta-\left[A_{p+k,\ell-p}b_{pq}-B_{p+k,\ell-p}a_{pq}\right]\sin k\theta\} . \quad (A5.10)$$

Introducing $p = -k$ and $\ell = m+n$ into (A5.9) to eliminate k and n respectively, and transposing the order of the sums over m and ℓ gives

Equations (A5.14) and (A5.15) now have the same angular and radial dependence as (A5.6) and (A5.1).

Taking the Fourier transform splits (5.1) into its angular components. Using (A5.1), (A5.3), (A5.6), (A5.7), (A5.14) and (A5.15), the angular components of (5.1) can be written as series in powers of r. Equating the coefficients of the terms, in these series, having the same powers of r gives

$$
\begin{aligned}
&-4\left[(\mu+\nu)^2-\mu^2\right]A_{\mu\nu} = \\
&2\sum_{m=0}^{\mu}\sum_{n=0}^{\nu}\left[(m+n)(\mu-m+\nu-n)-m(\mu-m)\right]\left[A_{mn}a_{\mu-m,\nu-n}-B_{mn}b_{\mu-m,\nu-n}\right] \\
&+\varepsilon_{\mu}\sum_{\ell=0}^{\nu}\sum_{m=0}^{<(\nu-\ell,\ell)}\left[(\nu-\ell)(\mu+\ell)+m(m+\mu)\right]\left[A_{m+\mu,\ell-m}a_{m,\nu-\ell-m}+B_{m+\mu,\ell-m}b_{m,\nu-\ell-m}\right] \\
&+\varepsilon_{\mu}\sum_{\ell=0}^{\nu}\sum_{m=0}^{<(\nu-\ell,\ell)}\left[\ell(\nu-\ell+\mu)+m(m+\mu)\right]\left[A_{m,\ell-m}a_{m+\mu,\nu-\ell-m}+B_{m,\ell-m}b_{m+\mu,\nu-\ell-m}\right]
\end{aligned}
\tag{A5.16}
$$

and

$$
\begin{aligned}
&-4\left[(\mu+\nu)^2-\mu^2\right]B_{\mu\nu} = \\
&2\sum_{m=0}^{\mu}\sum_{n=0}^{\nu}\left[(m+n)(\mu-m+\nu-n)-m(\mu-m)\right]\left[A_{mn}b_{\mu-m,\nu-n}+B_{mn}a_{\mu-m,\nu-n}\right] \\
&+\varepsilon_{\mu}\sum_{\ell=0}^{\nu}\sum_{m=0}^{<(\nu-\ell,\ell)}\left[(\nu-\ell)(\mu+\ell)+m(m+\mu)\right]\left[-A_{m+\mu,\ell-m}b_{m,\nu-\ell-m}+B_{m+\mu,\ell-m}a_{m,\nu-\ell-m}\right] \\
&+\varepsilon_{\mu}\sum_{\ell=0}^{\nu}\sum_{m=0}^{<(\nu-\ell,\ell)}\left[\ell(\nu-\ell+\mu)+m(m+\mu)\right]\left[A_{m,\ell-m}b_{m+\mu,\nu-\ell-m}-B_{m,\ell-m}a_{m+\mu,\nu-\ell-m}\right].
\end{aligned}
\tag{A5.17}
$$

Transposing the order of the sums over ℓ and m in both (A5.16) and (A5.17) gives $\sum_{m=0}^{\nu/2}\sum_{\ell=m}^{\nu-m}$, where $\nu/2$ is truncated to an integer value when ν is odd. Introducing $n = \ell-m$ and $p = m+\mu$ to eliminate ℓ and m in the second double sum in (A5.16), and introducing $m = \ell-m$ to eliminate ℓ in the third double sum in (A5.16) then gives

$$
\begin{aligned}
&-4\left[(\mu+\nu)^2-\mu^2\right]A_{\mu\nu} = \\
&2\sum_{m=0}^{\mu}\sum_{n=0}^{\nu}\left[(m+n)(\mu-m+\nu-n)-m(\mu-m)\right]\left[A_{mn}a_{\mu-m,\nu-n}-B_{mn}b_{\mu-m,\nu-n}\right] \\
&+\varepsilon_{\mu}\sum_{p=\mu}^{\mu+\nu/2}\sum_{n=0}^{\nu-2p+2\mu}\left[(\mu-p+\nu-n)(p+n)+(p-\mu)p\right]\left[A_{pn}a_{p-\mu,\nu+2\mu-2p-n}\right. \\
&\qquad\qquad\left.+B_{pn}b_{p-\mu,\nu+2\mu-2p-n}\right] \\
&+\varepsilon_{\mu}\sum_{m=0}^{\nu/2}\sum_{n=0}^{\nu-2m}\left[(m+n)(\nu-n+\mu-m)+m(m+\mu)\right]\left[A_{mn}a_{m+\mu,\nu-2m-n}+B_{mn}b_{m+\mu,\nu-2m-n}\right].
\end{aligned}
\tag{A5.18}
$$

Substituting m to replace p in (A5.18) gives

$$-4\left[(\mu+\nu)^2-\mu^2\right]A_{\mu\nu} =$$

$$2\sum_{m=o}^{\mu}\sum_{n=o}^{\nu}\left[(m+n)(\mu-m+\nu-n)-m(\mu-m)\right]\left[A_{mn}a_{\mu-m,\nu-n}-B_{mn}b_{\mu-m,\nu-n}\right]$$

$$+\varepsilon_\mu\sum_{m=\mu}^{\mu+\nu/2}\sum_{n=o}^{\nu-2m+2\mu}\left[(m+n)(\mu-m+\nu-n)-m(\mu-m)\right]\left[A_{mn}a_{m-\mu,\nu-n-2m+2\mu}\right.$$

$$\left.+B_{mn}b_{m-\mu,\nu-n-2m+2\mu}\right]$$

$$+\varepsilon_\mu\sum_{m=o}^{\nu/2}\sum_{n=o}^{\nu-2m}\left[(m+n)(\mu-m+\nu-n)+m(\mu+m)\right]\left[A_{mn}a_{m+\mu,\nu-n-2m}+B_{mn}b_{m+\mu,\nu-n-2m}\right] . \quad \text{(A5.19)}$$

Applying to (A5.17) the same operations used when deriving (A5.19) from (A5.16) gives

$$-4\left[(\mu+\nu)^2-\mu^2\right]B_{\mu\nu} =$$

$$2\sum_{m=o}^{\mu}\sum_{n=o}^{\nu}\left[(m+n)(\mu-m+\nu-n)-m(\mu-m)\right]\left[A_{mn}b_{\mu-m,\nu-n}+B_{mn}a_{\mu-m,\nu-n}\right]$$

$$+\varepsilon_\mu\sum_{m=\mu}^{\mu+\nu/2}\sum_{n=o}^{\nu-2m+2\mu}\left[(m+n)(\mu-m+\nu-n)-m(\mu-m)\right]\left[-A_{mn}b_{m-\mu,\nu-n-2m+2\mu}\right.$$

$$\left.+B_{mn}a_{m-\mu,\nu-n-2m+2\mu}\right]$$

$$+\varepsilon_\mu\sum_{m=o}^{\nu/2}\sum_{n=o}^{\nu-2m}\left[(m+n)(\mu-m+\nu-n)+m(\mu+m)\right]\left[A_{mn}b_{m+\mu,\nu-n-2m}+B_{mn}a_{m+\mu,\nu-n-2m}\right] . \quad \text{(A5.20)}$$

Equations (A5.19) and (A5.20) together form a set of linear equations in the $A_{\mu\nu}$ and $B_{\mu\nu}$. They are further manipulated in Chapter 5.

APPENDIX 6

A DIRECT METHOD FOR ESTIMATING A SINGLE EXPONENTIAL CURVE FROM MEASUREMENTS

Consider the exponential curve

$$y = Ae^{-Bx} + C \tag{A6.1}$$

illustrated in Figure A6.1. The area under the curve, measured from x = 0, is

$$Y = \int y dx = (A/B)\left[1-e^{-Bx}\right] + Cx \ . \tag{A6.2}$$

Combining (A6.1) and (A6.2) to eliminate the exponential term gives

$$BY = A - y + C(1+Bx) \ . \tag{A6.3}$$

Suppose now that measurements of y have been obtained as a function of x. Let y_1, y_2 and y_3 be measured values corresponding to x_1, x_2 and x_3 respectively. Let Y_1, Y_2 and Y_3 be estimates of the area under the curve, calculated from the measurements, from x = 0 to $x = x_1$, $x = x_2$ and $x = x_3$ respectively. Substituting these values into (A6.3) gives

$$\left.\begin{aligned} BY_1 &= A - y_1 + C(1+Bx_1) \\ BY_2 &= A - y_2 + C(1+Bx_2) \\ BY_3 &= A - y_3 + C(1+Bx_3) \end{aligned}\right\} \ . \tag{A6.4}$$

Solving the set of equations in (A6.4) for A, B and C gives

$$B = \frac{(y_2-y_3)(x_1-x_2)-(y_1-y_2)(x_2-x_3)}{(Y_1-Y_2)(x_2-x_3)-(Y_2-Y_3)(x_1-x_2)} \tag{A6.5a}$$

$$C = \frac{(y_2-y_3)(Y_1-Y_2)-(y_1-y_2)(Y_2-Y_3)}{(y_2-y_3)(x_1-x_2)-(y_1-y_2)(x_2-x_3)} \tag{A6.5b}$$

and

$$\begin{aligned} A = \{&(x_2-x_3)\left[C(Y_2-Y_1+x_2y_1-x_1y_2)+(Y_1y_2-Y_2y_1)\right] \\ &-(x_1-x_2)\left[C(Y_3-Y_2+x_3y_2-x_2y_3)+(Y_2y_3-Y_3y_2)\right]\} \\ &/\{(x_2-x_3)(Y_1-Y_2)-(x_1-x_2)(Y_2-Y_3)\} \ . \end{aligned} \tag{A6.5c}$$

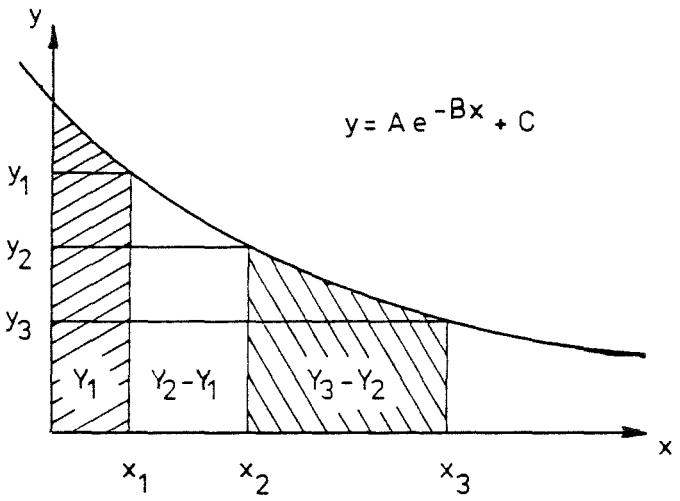

Figure A6.1: Exponential curve which is characterised by the parameters A, B and C.

Equations (A6.5a) to (A6.5c) yield A, B and C directly from the measurements. They avoid evaluation of the exponential function.

REFERENCES

AHLFORS, L. V. 1953. "Complex Analysis", McGraw Hill, New York.

ANDERSON, F. A., Penney, B. C., Patwardhan, N. A., Wheeler, H. B., 1980.
"Impedance Plethysmography: the Origin of Electrical Impedance Changes Measured in the Human Calf".
Medical and Biological Engineering and Computing. V18 #2 Mar. p234-240.

ANDERSON, F. A., Wheeler, H. B., 1979.
"Venous Occlusion Plethysmography for the Detection of Venous Thrombosis".
Medical Instrumentation. V13 #6 p350-354.

APPARAO, A., Gangadhara, Rao. T., 1974.
"Depth Investigation in Resistivity Methods Using Linear Electrodes".
Geophysical Prospecting. V22, #2, June. p211-223.

AVOLIO, A. P., 1980.
"Multi-branched Model of the Human Arterial System".
Medical and Biological Engineering and Computing. V18 #6, Nov. p709-718.

BACKUS, G., Gilbert, F., 1968.
"The Resolving Power of Gross Earth Data".
Geophysical Journal of the Royal Astronomical Society. V16, p169-205.

BADEN Fuller A. J., 1973.
"Engineering Field Theory".
Pergamon Press, Oxford.

BAKER, L. E., 1971.
"Biomedical Applications of Electrical Impedance Measurements".
Medical Electronics Monographs 1-6.
Watson, B. W. (Ed.), Peter Peregrinus, London.

BARNES, R. W., Collicott, P. E., Mosersky, D. J., Sumner, D. S., Strandness, D. E., 1972.
"Noninvasive Quantitation of Maximum Venous Outflow in Acute Thrombophlebitis".
Surgery. V2, #6, Dec. p971-979.

BATES, R. H. T., McKinnon, G. C., 1980.
"Possible Applications of Inverse Scattering Concepts to Ultrasonic Imaging".
Research Techniques in Non-Destructive Testing 4. Ch3, p71-85.
Sharp, R. J. (Ed.), Academic Press, London.

BATES, R. H. T., McKinnon, G. C., Seagar, A. D., 1980.
"A Limitation on Systems for Imaging Electrical Conductivity Distributions".
IEEE Transactions on Biomedical Engineering. V27, #7, Jul. p418-420.

BERNE, R. M., Levy, N. M., 1972.
"Cardiovascular Physiology".
C. V. Mosby, Saint Louis.

BRASS, G., Flathe, H., Schulz, R., 1981.
"Resistivity Profiling with Different Electrode Arrays over a Graphite Deposit".
Geophysical Prospecting. V29, #4 Aug. p589-600.

BROWN, B. H., Pryce, W. I. J., Baumber, D., Clarke, R. G., 1975.
"Impedance Plethysmography: Can it Measure Changes in Limb Bloodflow".
Medical and Biological Engineering. V13, #5, Sep. p674-682.

BROWN, J. M., Nahorski, Z. T., Woodcock, J. P., 1978.
"Transfer Function Modelling of Arteries".
Medical and Biological Engineering and Computing. V16, #2, Mar. p161-164.

BROYDEN, C. G., 1975.
"Basic Matrices".
MacMillan Press, London.

CAGNIARD, L., 1953.
"Basic Theory of the Magnetotelluric Method of Geophysical prospecting".
Geophysics. V18, #3, Jul. p605-635.

CARO, C. G., Pedley, T. J., Schroter, R. C., Seed, W. A., 1978.
"The Mechanics of the Circulation".
Oxford University Press, Oxford.

CASE, C. C., 1980.
"The Use of Impedance Plethysmography in the Measurement of Cardiac Output".
Australasian Physical and Engineering Sciences in Medicine. V3, #5, p223-226.

CHAN, L. S., 1981.
"Computed Tomography with Low Frequency Electric Currents".
Electrical Engineering Department Project Report, University of Canterbury, Christchurch, New Zealand.

COEN, S., Wang-Ho Yu, M., 1981.
"The Inverse Problem of the Direct Current Conductivity Profile of a Layered Earth".
Geophysics., V46, #12, Dec. p1702-1713.

COGGON, J. H., 1971.
"Electromagnetic and Electrical Modelling by the Finite Element Method".
Geophysics. V36, #1, Feb. p132-155.

CRANK, J., 1970.
"The Mathematics of Diffusion".
Oxford University Press, London.

CROFT, D. R., Lilley, D. G., 1977.
"Heat Transfer Equations using Finite Difference Equations".
Applied Science, London.

CROMWELL, L., Weibell, F. J., Pfeiffer, E. A., Usselman, L. B., 1973.
"Biomedical Instrumentation and Measurements".
Prentice Hill, New Jersey.

DESCHAMPS, G. A., Cabayan, H. S., 1972.
"Antenna Synthesis and Solution of Inverse Problems by Regularisation Methods".
IEEE Transactions on Antennas and Propagation. V20, #3, May, p268-274.

DEY, A., Morrison, H. F., 1979.
"Resistivity Modelling for Arbitrarily Shaped 3 Dimensional Structures".
Geophysics. V44, #4, Apr. p753-780.

DEY, A., Ward, S. H., 1970.
"Inductive Sounding of a Layered Earth with a Horizontal Magnetic Dipole".
Geophysics, V35, #4, Aug. p660-703.

DINES, K. A., Lytle, R. J., 1979.
"Computerised Geophysical Tomography".
Proceedings of the IEEE. V67, #7, Jul. p1065-1072.

DINES, K. A., Lytle, R. J., 1981.
"Analysis of Electrical Conductivity Imaging".
Geophysics. V46, #7, Jul. P1025-1036.

FREWER, R. A., 1974.
"The Electrical Conductivity of Flowing Blood".
Biomedical Engineering. V9, #12, Dec. p552-555.

FRISCHKNECHT, F. C., 1971.
"Electromagnetic Scale Modelling".
Electromagnetic Probing in Geophysics.
Wait, J. R. (Ed.), Golem Press, Boulder Colorado.

GEDDES, L. A., Baker, L. E., 1967.
"The Specific Resistance of Biological Material - A Compendium of Data for the Biomedical Engineer and Physiologist".
Medical and Biological Engineering. V5, #3, May, p271-293.

GEDDES, L. A., Baker, L. E., Moore, A. G., Coulter, T. W., 1969.
"Hazards in the use of Low Frequencies for the Measurement of Physiological Events by Impedance".
Medical and Biological Engineering. V7, #3, May, p289-296.

GEDDES, L. A., 1965.
"Electronarcosis".
Medical and Biological Engineering. V3, #1, Jan. p11-26.

GELFAND, I. M., Levitan, B. M., 1955.
"On the Determination of a Differential Equation from its Spectral Function".
American Mathematical Society Translations. Series 2 V1, p253-304.

GILL, P. E., Murray, W. (Eds), 1974.
"Numerical Methods for Constrained Optimisation".
Academic Press, London.

GLENN, W. E., Ryu, J., Ward, S. H., Peeples, W. J., Phillips, R. J., 1973.
"The Inversion of Vertical Magnetic Dipole Sounding Data".
Geophysics. V38, #6, Dec. p1109-1129.

GREENLEAF, J. F., Johnson, S. A., Lee, S. L., Herman, G. T., Wood, E. H. 1974.
"Algebraic Reconstruction of Spatial Distributions of Acoustic Absorption within Tissue from their Two Dimensional Acoustic Projections".
Acoustic Holography 5. p591-603.
Green, P. S., (Ed.), Plenum Press, New York.

GREENLEAF, J. F., Johnson, S. A., Samayoa, W. F., and Duck, F. A., 1975.
"Algebraic Reconstruction of Spatial Distributions of Acoustic Velocities in Tissues from their Time of Flight Profiles".
Acoustic Holography 6. p71-90.
Booth, N. (Ed.), Plenum Press, New York.

GUYTON, A. C., 1971.
"Basic Human Physiology: Normal Function and Mechanisms of Disease".
Saunders, Philadelphia.

HENDERSON, R. P., Webster, J. G., 1978.
"An Impedance Camera for Spatially Specific Measurements of the Thorax".
IEEE Transactions on Biomedical Engineering. V25, #3, May, p250-254.

HILL, D. A., Wait, J. R., 1981.
"HF Ground Wave Propagation over Mixed Land Sea and Sea Ice Paths".
IEEE Transactions on Geoscience and Remote Sensing. V19, #4, Oct. p210-216.

HILL, D. W., Lowe, H. J., 1973.
"The Use of the Electrical Impedance Technique for the Monitoring of Cardiac Output and Limb Bloodflow During Anaesthesia".
Medical and Biological Engineering. V11, #5, Sep. p534-545.

INMAN, J. R., 1975.
"Resistivity Inversion with Ridge Regression".
Geophysics. V40, #5, Oct. p798-817.

INMAN, J. R., Ryu, J., Ward, S. H., 1973.
"Resistivity Inversion".
Geophysics, V38, #6, Dec. p1088-1108.

JAFFRIN, M. Y., 1976.
"Rationale of Plethysmographic Detection of Deep Vein Thrombosis".
29th Annual Conference in Medicine and Biology, Boston, Massachusetts, 6-10 Nov. 1976. p317.

JAFFRIN, M. Y., Vanhoutte, C., 1979.
"Quantitative Interpretation of Arterial Impedance Plethysmographic Signals".
Medical and Biological Engineering and Computing. V17, #1, Jan. p2-10.

JOHNS, P. B., Rowbotham, T. R., 1981.
"Solution of Resistive Meshes by Deterministic and Monte Carlo Transmission-line modelling".
IEEE Proceedings Part A. V128, #6, Sep. p453-462.

JOHNSON, K. W. Kakkar, V. V., 1974.
"Plethysmographic Diagnosis of Deep Vein Thrombosis".
Surgery, Gynecology and Obstetrics. V139, p41-44.

JUPP, D. L. B., Vozoff, K., 1975.
"Stable Iterative Methods for the Inversion of Geophysical Data".
Geophysical Journal of the Royal Astronomical Society, V42, #3, Sep. p957-976.

KAK, A. C., 1979.
"Computerised Tomography with X-ray, Emission and Ultrasonic Sources".
Proceedings IEEE. V67, #9, Sep. p1245-1271.

KATZ, B., 1966.
"Nerve, Muscle and Synapse".
McGraw Hill, New York.

KAUFMANN, W., 1963.
"Fluid Mechanics".
McGraw Hill, New York.

KELLER, G. V., 1971.
"Electrical Characteristics of the Earth's Crust".
Electromagnetic Probing in Geophysics.
Wait, J. R. (Ed.), Golem Press, Boulder Colorado.

KELLER, G. V., Frischknecht, F. C., 1966.
"Electrical Methods in Geophysical Prospecting".
Pergamon Press, Oxford.

KINSNER, W., Della Torre, E., 1974.
"An Iterative Approach to the Finite Element Method in Field Problems".
IEEE Transactions on Microwave Theory and Techniques. V22, #3, Mar. p221-228.

KOEFOED, O., 1976.
"Progress in the Direct Interpretation of Resistivity Soundings: An Algorithm".
Geophysical Prospecting. V24, #2, Jun. p233-240.

KOEFOED, O., 1979.
"Resistivity Sounding on an Earth Model containing Transition Layers with Linear Change of Resistivity with Depth".
Geophysical Prospecting. V27, #4, Dec. p862-868.

KREYSZIG, E., 1972.
"Advanced Engineering Mathematics".
Wiley, New York (3rd edition).

LANGER, R. E., 1933.
"An Inverse Problem in Differential Equations"
Bulletin of the American Mathematical Society. V39, #10, Oct. p814-820.

LANGER, R. E., 1936.
"On the Determination of Earth Conductivity from Observed Surface Potentials".
Bulletin of the American Mathematical Society. V42, #10, Oct. p747-754.

LARSEN, J. C., 1981.
"A New Technique for Layered Earth Magnetotelluric Inversion".
Geophysics. V46, #9, Sep. p1247-1257.

LEE, K. H., Pridmore, D. F., Morisson, H. F., 1981.
"A Hybrid 3-D Electromagnetic Modelling Scheme".
Geophysics. V46, #5, May. p796-805.

LEHR, J., 1972.
"A Vector Derivation Useful in Impedance Plethysmography Field Calculations".
IEEE Transactions on Biomedical Engineering. V19, #3, Mar. p156-157.

LEWES, T., Grant, R., 1925.
"Observations upon Reactive Hyperaemia in Man".
Heart. V12, p73-120.

LEWITT, R. M., Bates, R. H. T., 1978a.
"Image Reconstruction from Projections I: General Theoretical Considerations".
Optik. V50, #1, Feb. p19-33.

LEWITT, R. M., Bates, R. H. T., 1978b.
"Image Reconstruction from Projections III: Projection Completion Methods (Theory)".
Optik. V50, #3, Apr. p189-204.

LEWITT, R. M., Bates, R. H. T., 1978c.
"Image Reconstruction from Projections IV: Projection Completion Methods (Computational Examples)".
Optik. V50, #4, May. p269-278.

LEWITT, R. M., Bates, R. H. T., Peters, T. M., 1978.
"Image Reconstruction from Projections II: Modified Back Projection Methods".
Optik. V50, #2, Mar. p85-109.

LI, J. K. J., Melbin, J., Campbell, K., Noordergraaf, A., 1980.
"Evaluation of a Three Point Pressure Method for Determination of Arterial Transmission Characteristics".
Journal of Biomechanics. V13, #12, Dec. p1023-1029.

LYTLE, R. J., Dines, K. A., 1978.
"An Impedance Camera: A System for Determining the Spatial Variation of Electrical Conductivity".
Lawrence Livermore Laboratory, University of California, report #UCRL-52413 Jan.

LYTLE, R. J., Dines, K. A., 1980.
"Iterative Ray Tracing Between Boreholes for Underground Image Reconstruction".
IEEE Transactions on Geoscience and Remote Sensing. V18, #3, Jul. P234-240.

LYTLE, R. J., Lager, D. L., Laine, E. F., 1976.
"Subsurface Probing by High Frequency Measurements of the Wave Tilt of Electromagnetic Surface Waves".
IEEE Transactions on Geoscience Electronics. V14, #4, Oct. p244-249.

MAINI, R., Iskander, M. F., Durney, C. H., 1980.
"On the Electromagnetic Imaging using Linear Reconstruction Techniques".
Proceedings of the IEEE. V68, #12, Dec. p1550-1552.

MALEY, S. W., 1971.
"Radio Wave Methods for Measuring the Electrical Parameters of the Earth".
Electromagnetic Probing in Geophysics.
Wait, J. R., (Ed.), Golem Press, Boulder Colorado.

MALLICK, K., Roy, A., 1968.
"Resistivity Sounding on a 2-Layer Earth with Transitional Boundary".
Geophysical Prospecting. V16, #4, Dec. p436-446.

MARQUARDT, D. W., 1963.
"An Algorithm for Least Squares Estimation of Nonlinear Parameters".
Journal of the Society of Industrial and Applied Mathematics.
V11, #2, June, p431-441.

MARTIN, R. O., Pilkington, T. C., 1972.
"Unconstrained Inverse Electrocardiography: Epicardial Potentials".
IEEE Transactions on Biomedical Engineering. V19, #4, Jul. p276-285.

McDONALD, D. A., 1979.
"Blood Flow in Arteries".
Edward Arnold, London.

McKINNON, G. C., Bates, R. H. T., 1980.
"A Limitation on Ultrasonic Transmission Tomography".
Ultrasonic Imaging. V2, #1, Jan. p 48-54.

MEINARDUS, H. A., 1970.
"Numerical Interpretation of Resistivity Soundings over Horizontal Beds".
Geophysical Prospecting. V18, #3, Sep. p415-433.

METZ, W. C., Pilkington, T. C., 1969.
"The Utilisation of Integral Equations for Solving Three Dimensional Time Invariant Conservative Fields".
International Journal of Engineering Science. V7, #2, Feb. p183-208.

MIYAMOTO, Y., Takahashi, M., Tamura, T., Nakamura, T., Hiura, T., Mikami, M., 1981.
"Continuous Determination of Cardiac Output during Exercise by the use of Impedance Plethysmography".
Medical and Biological Engineering and Computing. V19, #5, Sep. p638-644.

MORENO, A. H., Katz, A. I., Gold, L. D., Reddy, R. V., 1970.
"Mechanics of Distension of Dog Veins and other Thin Walled Structures".
Circulation Research. V27, p1069-1080.

MORSE, P. M., Feshbach, H., 1953.
"Methods of Theoretical Physics".
McGraw Hill, New York, (2 parts).

MUFTI, I. R., 1976.
"Finite Difference Resistivity Modelling for Arbitrarily Shaped Structures".
Geophysics. V41, #1, Feb. p62-78.

MUFTI, I. R., 1978.
"A Practical Approach to Finite Difference Resistivity Modelling"
Geophysics. V43, #5, Aug. p930-942.

MURRAY, W., (Ed.), 1972.
"Numerical Methods for Unconstrained Optimisation".
Academic Press, London.

NOBLE, B., 1976.
"Methods for Computing the Moore-Penrose Generalised Inverse and Related Matters".
Generalised Inverses and Applications. p245-302.
Nashed, M. Z. (Ed.), Academic Press, New York.

NOORDERGRAAF, A., 1978.
"Circulatory System Dynamics".
Academic Press, New York.

NOWOTNY, R., Nowotny, C., 1980.
"Determination of Electrode Impedance with an FFT Spectrum Analyser".
Medical and Biological Engineering and Computing. V18, #6, Nov. p779-782.

NYOBER, J., 1970.
"Electrical Impedance Plethysmography".
Thomas, Springfield, Illinois, (2nd Edition).

OGUNADE, S. O., 1981.
"Electromagnetic Response of an Embedded Cylinder for Line Current Excitation".
Geophysics. V46, #1, Jan. p45-52.

OLDENBURG, D. W., 1978.
"The Interpretation of Direct Current Resistivity Measurements".
Geophysics. V43, #3, Apr. p610-625.

OLDENBURG, D. W., 1979.
"One Dimensional Inversion of Natural Source Magnetotelluric Observations".
Geophysics. V44, #7, Jul. p1218-1244.

PARKER, R. L., 1971.
"The Inverse Problem of Electromagnetic Conductivity in the Mantle".
Geophysical Journal of the Royal Astronomical Society. V22, #2, Feb. p121-138.

dE PATER, L., van den Berg, J. W., 1964.
"An Electrical Analogue of the Entire Human Circulatory System".
Medical Electronics and Biological Engineering. V2, #2, Apr. p161-166.

PEKERIS, C. L., 1940.
"Direct Method of Interpretation in Resistivity Prospecting".
Geophysics. V2, #1, Jan. p31-42.

PELTON, W. H., Rijo, L., Swift, C. M., 1978.
"Inversion of 2 Dimensionsl Resistivity and Induced Polarisation Data".
Geophysics. V43, #4, June, p788-803.

PENNEY, B. C., Narducci, L. M., Peura, R. A., Anderson, F. A., Wheeler, H. B., 1979.
"The Impedance Plethysmographic Sampling Field in the Human Calf".
IEEE Transactions on Biomedical Engineering. V26, #4, Apr. p193-198.

PETRICK, W. R., Pelton, W. H., Ward, S. H., 1977.
"Ridge Regression Inversion Applied to Crustal Resistivity Sounding Data from South Africa".
Geophysics. V42, #5, Aug. p995-1005.

PETRICK, W. R., Sill, S. R., Ward, S. H., 1981.
"Three Dimensional Resistivity Inversion using Alpha Centres".
Geophysics. V46, #8, Aug. p1148-1162.

PEURA, R. A., Penney, B. C., Arcuri, J., Anderson, F. A., Wheeler, H. B., 1978.
"Influence of Erythrocyte Velocity on Impedance Plethysmographic Measurements".
Medical and Biological Engineering and Computing. V16, #2, Mar. p147-154.

PLONSEY, R., 1969.
"Bioelectric Phenomena".
McGraw Hill, New York.

PRICE, L. R., 1979.
"Electrical Impedance Computed Tomography: A New Imaging Technique".
IEEE Transactions on Nuclear Science. V26, #2, Apr. p2736-2739.

PRIDMORE, D. F., Hohmann, G. W., Ward, S. H., Sill, W. R., 1981.
"An Investigation of Finite Element Modelling for Electrical and Electromagnetic Data in 3 Dimensions".
Geophysics. V46, #7, Jul. p796-805.

RAINES, J. K., 1978.
"Use of the Pulse Volume Recorder in Peripheral Arterial Disease".
Noninvasive Diagnostic Techniques in Vascular Disease. p304-314.
Bernstein, E. F. (Ed.), C. V. Mosby, St. Louis.

RAMAN, E. R., Vanhuyse, V. J., Jaseneau, A. H., 1973.
"Comparison of Plethysmographic and Electromagnetic Flow Measurements".
Physics in Medicine and Biology. V18, #5, Sep. p704-711.

RAMO, S., Whinnery, J. R., van Duzer, T., 1965.
"Fields and Waves in Communications Electronics".
Wiley, New York.

RIJO, L., Pelton, W. H., Feitosa, E. C., Ward, S. H., 1977.
"Interpretation of Apparent Resistivity Data from Apodi Valley, Rio Grande Do Norte, Brazil".
Geophysics. V42, #4, June. p811-822.

ROY, A., Apparao, A., 1971.
"Depth Investigation in Direct Current Methods".
Geophysics. V36, #5, Oct. p943-959.

RUBAL, B. J., Baker, L. E., Poder, T. C., 1980.
"Correlation between Maximum dZ/dt and Parameters of Left Ventricular Performance".
Medical and Biological Engineering and Computing. V18, #5, Sep. p541-548.

RUSHMER, R. F., 1970.
"Cardiovascular Dynamics".
W.B. Saunders, Philadelphia.

SCHOMBERG, H., 1980.
"Nonlinear Image Reconstruction from Projections of Ultrasonic Travel Times and Electric Current Densities".
Presented at Conference on Mathematical Aspects of Computerised Tomography, Mathematics Research Institute, Oberwolfach, Blackforest FRG, 10-16 Feb.

SEIGEL, H. O., 1959.
"A Theory for Induced Polarisation Effects".
Overvoltage Research and Geophysical Applications.
Wait, J. R., (Ed.), Pergamon Press, London.

SKIDMORE, R., Woodcock, J. P., 1980.
"Physiological Interpretation of Doppler-shift Waveforms - I. Theoretical Considerations".
Ultrasound in Medicine and Biology. V6, #1, p7-10.

SKILLING, H. H., 1974.
"Electric Networks".
Wiley, New York.

SLICHTER, L. B., 1933.
"The Interpretation of the Resistivity Prospecting Method for Horizontal Structures".
Physics. V4, Sep. p307-322.

SNYDER, D. D., 1976.
"A Method for Modelling the Resistivity and IP Response of Two Dimensional Bodies".
Geophysics. V41, #5, Oct. p977-1015.

SPIEGEL, M. R., 1968.
"Mathematical Handbook".
McGraw Hill, New York.

STEFANESCO, S., Schlumberger, C., Schlumberger, M., 1930.
"Sur la Distribution Electrique Potentielle autour d'une Prise de Terre Ponctuelle dans un Terrain a Couches Horizontales Homosenes at Isotropes".
le Journal de Physique et le Radium. series 7, V1, #4, April. p132-141.

STEFANESCU, S., Stefenescu, D., 1974.
"Mathematical Models of Conducting Ore Bodies for Direct Current Electrical Prospecting".
Geophysical Prospecting. V22, #2, June. p246-260.

SUMNER, D. S., 1978.
"Volume Plethysmography in Vascular Disease: an Overview".
Noninvasive Diagnostic Techniques in Vascular Disease. p68-92.
Bernstein, E. F. (Ed.), C. V. Mosby, St. Louis Illinois.

SWANSON, D. K., Webster, J. G., 1976.
"Origin of the Electrical Impedance Pulse in the Limbs"
29th Annual Conference of Engineering in Medicine and Biology,
Boston, Massachusetts, 6-10 Nov. V18, p324.

SZARANIEC, E., 1976.
"Fundamental Functions for Horizontally Stratified Earth".
Geophysical Prospecting. V24, #3, Sep. p528-548.

SZARANIEC, E., 1980.
"Direct Resistivity Interpretation by Accumulation of Layers".
Geophysical Prospecting. V28, #2, Apr. p257-268.

TARJAN, P. P., McFee, R., 1968.
"Electrodeless Measurements of Effective Resistivity of the Human Torso and Head by Magnetic Induction".
IEEE Transactions on Biomedical Engineering. V15, #4, Oct. p266-278.

TING, S. C., Hohmann, G. W., 1981.
"Integral Equation Modelling of 3-D Magnetotelluric Response".
Geophysics. V42, #2, Feb. p182-197.

VOZOFF, K., 1958.
"Numerical Resistivity Analysis: Horizontal Layers".
Geophysics. V23, #3, Jul. p536-556.

VOZOFF, K., Jupp, D. L. B., 1975.
"Joint Inversion of Geophysical Data".
Geophysical Journal of the Royal Astronomical Society. V42, #3, Sep. p977-991.

WAIT, J. R., 1959.
"The Variable Frequency Method".
Overvoltage Research and Geophysical Applications.
Wait, J. R. (Ed.), Pergamon Press, London.

WAIT, J. R., 1962.
"Electromagnetic Waves in Stratified Media".
Pergamon Press, Oxford.

WAIT, J. R., 1981a.
"Towards a General Theory of Induced Polarisation in Geophysical Exploration".
IEEE Transactions on Geoscience and Remote Sensing. V19, #4, Oct. p231-234.

WAIT, J. R., 1981b.
"Wave Propagation Theory".
Pergamon Press, New York.

WANG, C. C., 1979.
"Mathematical Principles of Mechanics and Electromagnetism. Part B: Electromagnetism and Gravitation".
Plenum Press, New York.

WEIDELT, P., 1972.
"The Inverse Problem of Geomagnetic Induction".
Journal of Geophysics - Zeitschrift fur Geophysik. V38, p257-289.

WHEELER, H. B., O'Donnell, J. A. Anderson, F. A., Benedict, K., 1974.
"Occlusive Impedance Phlebography: A Diagnostic Procedure for Venous Thrombosis and Pulmonary Embolism".
Progress in Cardiovascular Diseases. V17, #3, Nov/Dec. p199-205.

WU, F. T., 1968.
"Inverse Problem of Magnetotelluric Sounding".
Geophysics. V33, #6, Dec. P972-979.

YUNGUL, S. H., 1966.
"Telluric Sounding - A Magnetotelluric Method Without Magnetic Measurements".
Geophysics. V16, #1, Feb. p185-191.

ZICOT, M., Parker, K. H., Caro, C. G., 1977.
"Effect of Positive External Pressure on Calf Volume and Local Venous Haemodynamics".
Physics in Medicine and Biology. V22, #6, p1146-1159.